Constraining Northern Cordilleran lithosphere thickness and xenolith residence times using mantle xenolith geochemistry

by

Yuzhe Gan
Bachelor of Science (Honours.), Acadia University, 2023

A Thesis Submitted in Partial Fulfillment of the
Requirements for the Degree of

Master Of Science

in the School of Earth and Ocean Sciences

© Yuzhe Gan, 2024
University of Victoria

All rights reserved. This thesis may not be reproduced in whole or in part, by photocopy or other means, without the permission of the author.

We acknowledge and respect the Lək^{w}əŋən (Songhees and Esquimalt) Peoples on whose territory the university stands, and the Lək^{w}əŋən and W̱ SÁNEĆ Peoples whose historical relationships with the land continue to this day.

Constraining Northern Cordilleran lithosphere thickness and xenolith residence times using mantle xenolith geochemistry

by

Yuzhe Gan
Bachelor of Science (Honours.), Acadia University, 2023

Supervisory Committee

Dr. Dante Canil, Supervisor
School of Earth and Ocean Sciences

Dr. Lucinda Leonard, Department Member
School of Earth and Ocean Sciences

Dr. Ruohong Jiao, Department Member
School of Earth and Ocean Sciences

Abstract

This study re-examines 28 mantle peridotite xenoliths and their Quaternary host lavas from near Llangorse, northwest British Columbia to determine the thickness, and reconstruct the thermal history of the Cordilleran mantle lithosphere, as well as to discover the residence time of mantle xenoliths within the host magma. Based on the equilibrium textures, the Llangorse mantle xenoliths can be separated into three distinct groups: non-sieved, weakly sieved, and strongly sieved. The sieved samples are defined by partially melted pyroxenes, with weakly sieved samples exhibiting melted rims under 50 μm wide and strongly sieved samples exhibiting broader rims. Both weakly and strongly sieved samples exhibit strong Ca zoning in olivine, with Ca concentrations increasing from core to rim, indicative of substantial heating. Closure temperatures for the xenoliths were calculated using T_{Al}, T_{BKN}, and T_{REE}, and varied between 829 to 941 °C, 811 to 1004 °C, and 847 to 1084 °C respectively. Depth estimates for the xenoliths obtained through Ca-in-olivine barometry (P_{SC}) show that only non-sieved samples and a few sieved samples yield reasonable depths between 34 and 65 (± 6) km. These depths align with both adjacent seismic measurements and the depth of equilibration of the host lava derived from SiO_2 barometry. Based on the most robust xenolith samples, I construct a model geotherm consistent with a surface heat flow of 76 (± 3) mW/m² and heat production of 1.1 (± 0.2) mW/m³. This model geotherm intersects the peridotite solidus with 300 ppm H_2O, corresponding to a lithosphere-asthenosphere boundary at 1280 (± 15) °C and 74 (± 6) km depth. Diffusion chronometry is applied to Ca zoning profiles in olivine. The results show that all the sieved samples have been heated over timescales ranging from several years to hundreds of years depending on the assumed heat source temperatures and uncertainties in the diffusion coefficient for Ca in olivine. This timescale is consistent with typical magma storage time of several years to

thousands of years observed from modern volcanoes in Iceland and Hawaii. The sieved xenolith samples either have been entrained by ascending magma at an early stage, with the magma subsequently stored in the upper mantle or crustal level, or underwent heating prior to being sampled by the ascending magma.

Table of Contents

Supervisor Committee ..... **ii**

Abstract ..... **iii**

Table of Contents ..... **v**

List of Tables ..... **vii**

List of Figures ..... **viii**

List of Abbreviations ..... **xiii**

Acknowledgements ..... **xv**

CHAPTER 1: Introduction **1**

1.1 Introduction 1

1.2 Canadian Cordillera 1

1.3 Rationale and Purpose of Study 4

1.4 Geologic Setting 6

1.4.1 Terranes 6

1.4.2 Neogene-Quaternary volcanism in Cordillera 6

1.4.3 Lithosphere Structure of the Canadian Cordillera 8

1.5 Mantle Xenoliths 9

1.5.1 Previous Work on Cordilleran Xenoliths 9

1.5.2 Mantle Thermobarometry 10

1.6 Llangorse Volcanic Field 15

1.7 Samples for Study 15

1.8 Methods of Study 16

CHAPTER 2: Petrography **18**

2.1 Mantle Xenoliths 18

2.2 Host Lava 19

CHAPTER 3: Mineral Chemistry 25

3.1 Major Element Chemistry 25

3.2 Olivine Trace Element Chemistry 28

3.3 Zoning in Olivine 31

3.4 Pyroxene Trace Element Chemistry 33

CHAPTER 4: Geothermobarometry 36

4.1 Data Selection 36

4.2 Geothermometry 39

4.3 Geobarometry 46

4.4 Host Lava Temperature 50

CHAPTER 5: Discussion 54

5.1 Lithosphere Mantle Origin 54

5.2 Geotherm and Lithosphere Thickness 56

5.3 Heating and Residence Time of the Xenoliths in Magma 72

5.4 Cooling History of Cordilleran Lithosphere 78

CHAPTER 6: Conclusions 80

References 84

Appendix A: Mineral analyses by electron microprobe in weight %. 97

Appendix B: Mineral analyses by LA-ICP-MS in ppm. 120

Appendix C: LA-ICP-MS analysis locations. 139

Appendix D: EPMA analysis locations. 196

Appendix E: Olivine Al, Ca zoning profiles 234

Appendix F: Best fitted olivine Ca zoning profiles 250

List of Tables

Table. 1. Geothermobarometers used in this study. 14

Table. 2. Modal mineralogy, rock type and assigned group of all the samples used in this study 21

Table. 3. Geothermobarometry results for all samples. All the temperatures are reported in °C. Both T_{Al} and T_{Ca} habe inherent uncertainty ± 20 °C, and T_{BKN} has inherent uncertainty ± 15 °C. The P_{Sc} is reported in kbar and depth is reported in km. P_{Sc} mean are calculated by using average Ca. P_{Sc} preferred are calculated using average Ca for non-sieved samples, MH-02-04, and MH-02-109, and minimum Ca for sieved samples.. 40

Table. 4. Calculated host lava temperatures in °C 53

Table. 5. Parameters used in modelling geotherm 61

Table. 6. Diffusion coefficients (Coogan et al. 2005) used in fitting olivine zoning profile 73

Table. 7. Calculated heating timescales for six sieved samples using olivine Ca zoning profiles. Distances are from the boundary of the grain, which is defined by the point where the Al concentration begins to change, to the core of the grain. C_1 is the initial concentration at the grain boundary (where $x = 0$). C_2 is the original concentration at the core 76

List of Figures

Fig. 1. Relief map of the northern Cordilleran showing mantle xenolith localities. Blue star shows the location of Llangorse locality. Also shown major faults, the Aleutian trench, Rocky Mountain Trench (RMT), Queen Charlotte transform fault (QCF). Figure made with GeoMapApp (Ryan et al. 2009)... 5

Fig. 2. Projection of xenolith T_{BKN} temperature to a model geotherm... 12

Fig. 3. Various geothermobarometers are used to recover the temperature and pressure conditions for Llangorse xenoliths. The element exchange of the different geothermometers (fast vs. slow) depends on the diffusion rate of the elements involved within each system.....14

Fig. 4. Modal mineralogy of Llangorse locality xenoliths (Harder and Russell 2006) plotted on a peridotite classification diagram 20

Fig. 5. Photomicrographs of harzburgite xenolith MH-02-125. The sample contains orthopyroxene and clinopyroxene with narrow sieved rims. Image on left is in plane polarized light (PPL) and image on the right is with crossed polars (XP) 22

Fig. 6. Photomicrographs of lherzolite xenolith MH-02-18B. The sample contains entirely and partially sieved orthopyroxene and clinopyroxene grains. Image on left is in plane polarized light (PPL) and image on the right is with crossed polars (XP) 22

Fig. 7. Photomicrographs of lherzolite xenoliths MH-02-18B (A, B) and MH-02-04 (C, D). (A, B) Photomicrographs showing thick melt veinlet cross-cutting olivine grains. (C, D) Photomicrographs showing spinel with reaction rim. Images on left are in plane polarized light (PPL) and images on the right are with crossed polars (XP).....23

Fig. 8. Photomicrographs of lherzolite xenolith MH-02-109. This sample has been heavily invaded by melts, and all the crystal boundaries have been filled with melts. Image on left is in plane polarized light (PPL) and image on the right is with crossed polars (XP).....23

Fig. 9. Backscattered electron image of lava sample MH-02-101. Image shows the olivine phenocryst with cpx relict core 24

Fig. 10. Plots of SiO_2 vs major element oxides in olivine from Llangorse xenoliths. Blue dots are analyses from this study, orange dots are analyses from Harder and Russell (unpublished). (A) FeO vs SiO_2. (B) MgO vs SiO_2. (C) NiO vs SiO_2. (D) MnO vs SiO_2 26

Fig. 11. Plots of SiO_2 vs Mg# in olivine phenocrysts 26
Fig. 12. Trivalent Cr-Al-Fe^{3+} ternary diagram (Stevens 1944) showing the composition of spinel inclusions in olivine phenocrysts. The apfu stands for atom per formula unit in the spinel structure.....27
Fig. 13. Plot of Al vs Ca of all olivines from xenoliths based on their equilibrium texture 29
Fig. 14. Plot of Al vs Ca in each olivine trace element analysis based on their equilibrium texture. Open coloured symbols are published data for other Cordilleran xenoliths (Canil and Russell 2022) Open uncoloured symbols are from the literature (Gregoire et al. 2000; Mallmann et al. 2009; De Hoog et al. 2010; Lin et al. 2023).....29
Fig. 15. Plot of Ca vs trace element in olivine from xenoliths based on their equilibrium texture 30
Fig. 16. Olivine Al and Ca zoning profiles. All the zoning profiles start from the core of the grains (0 micron) to the rim then into the adjacent spinel grain (hundreds micron). (A, B) Al and Ca zoning profiles of non-sieved sample MH-02-108. (C, D) Al and Ca zoning profiles of weakly sieved sample MH-02-100B showing strong Ca zoning. (E, F) Al and Ca zoning profiles of strongly sieved sample MH-02-18B showing strong Ca zoning 32
Fig. 17. Chondrite-normalized rare earth element (REE) diagrams for cpx from Llangorse harzburgite and lherzolite samples. Plots are averages of four to seven grains in each sample, with one standard deviation of the mean plotted as error bars. (A) Chondrite-normalized REE patterns for cpx in harzburgite samples. (B) Chondrite-normalized REE pattern for cpx in lherzolite samples. Literature data are from other Cordilleran xenolith localities (Shi et al. 1998). Black lines with circle symbols are residual cpx REE composition after (1, 5, 10, 15 %) partial melting from a depleted mantle cpx source REE composition. They are calculated using melting model and partition coefficients given in Warren (2016). Chondrite normalized values are from Sun and McDonough (1989).....34
Fig. 18. Chondrite-normalized rare earth element (REE) diagrams for opx from Llangorse harzburgite and lherzolite samples. Plots are averages of three to six grains in each sample, with one standard deviation of the mean plotted as error bars. Literature data are from other spinel lherzolite and harzburgite within Coast Range ophiolite (Jean and Shervais 2017). Chondrite normalized values are from Sun and McDonough (1989) 35
Fig. 19. Plot of Al and Ca 1 standard deviations in ppm for each sample 37

Fig. 20. Plot of average ppm Al vs selected Ca in each Llangorse sample based on their equilibrium texture. Hollow symbols are published data for xenoliths from elsewhere in the Cordillera (Canil and Russell 2022) and worldwide (Gregoire et al. 2000; Mallmann et al. 2009; De Hoog et al. 2010; Lin et al. 2023) 38

Fig. 21. Plot comparing various temperatures with the petrographic textures in samples. (A) T_{Al}. (B) T_{Ca}. (C) T_{FeMg}. (D) T_{BKN} at 15 kbar. (E) T_{REE} at 15 kbar 41

Fig. 22. Plot comparing calculated temperatures with lithology. (A) T_{Al}. (B) T_{Ca}. (B) T_{FeMg}. (C) T_{BKN} result at 15 kbar. (D) T_{REE} at 15 kbar 42

Fig. 23. Plot of difference between temperature estimates among all five geothermometers. (A) T_{Al} vs T_{BKN}. (B) T_{Ca} vs T_{BKN}. (C) T_{REE} vs T_{BKN}. (D) T_{Al} vs T_{FeMg}. (D) T_{Al} vs T_{Ca}. Error bars for T_{Al} are calculated using 1 standard deviation of Al and Ca concentration. Error bars for T_{REE} are derived from the REE inversions (Liang et al. 2013).....44

Fig. 24. Plot of filtered 'mean' depth in km vs T_{Al} in degrees. The Moho depth is at 33 km (Audet et al. 2019). Samples with Ca standard deviation above 80 ppm are filtered out. Horizontal error bars are calculated T_{Al} uncertainties using Al 1 standard deviation. Error bars are uncertainty in experimental calibration (± 1.5 kbar) for the P_{SC} barometer.....47

Fig. 25. Plot of preferred depth in km vs T_{Al} in degrees. The Moho depth is at 33 km (Audet et al. 2019). Horizontal error bars are calculated T_{Al} uncertainties using 1 standard deviation for Al in olivine. Error bars are uncertainty in experimental calibration (± 1.5 kbar) for the P_{SC} barometer.....48

Fig. 26. Plot of depth (km) vs T_{Al} in °C for xenolith samples. The T_{Al} temperature and depth are calculated using minimum Ca and selected Al in olivine. The Moho depth is at 33 km (Audet et al. 2019). Error bars are uncertainty in experimental calibration (± 1.5 kbar) for the P_{SC} barometer. Only samples giving positive depths are plotted (two strongly sieved samples which plotted above ground, are excluded from this plot).....49

Fig. 27. Rhodes diagram (Dungan et al. 1978; Rhodes et al. 1979) showing the Mg# of olivine phenocryst cores and rims vs Mg# of liquid from melt (Abraham et al. 2001; Harder et al. 2003). Only the samples within the dashed lines are in equilibrium with the melt 51

Fig. 28. The % difference in highly incompatible elements concentrations between measured whole rock powders (Harder and Russell 2006) and reconstructed samples of Llangorse xenoliths.....55

Fig. 29. Model geotherms calculated at various surface heat flow and crustal heat production compared with T-depth of Llangorse samples. Uncertainties of (± 6 km) are in experimental calibration. Dry and wet (with 150 and 300 ppm H_2O) mantle peridotite solidus (ppm is parts per million) are from Hirschmann et al. (2009). (A) Model geotherms calculated using average Cordilleran crustal heat production (A_0 = 1.6 μW/m³) (Lewis et al. 2013) and various surface heat flow. (B) Model geotherms calculated using average Cordilleran surface heat flow (q_0 = 73 mW/m²) (Lewis et al. 2013) and various crustal heat production 63

Fig. 30. Model geotherms calculated assuming surface heat flow (q_0 = 76 mW/m²) and crustal heat production (A_0 = 1.1 μW/m³). Dry and wet (with 150 and 300 ppm H_2O) mantle peridotite solidus lines are from Hirschmann et al. 2009. Uncertainties are in experimental calibration of the barometer (± 6 km). The average LAB depth of Canadian Cordillera is 65 ± 10 km (Hyndman and Canil 2021).....64

Fig. 31. Reconstructed geotherms following (Harder and Russell 2006). Only the purple geotherm can reasonably align with the T-depth array. A_0 is crustal heat production. q_0 is surface heat flow. Dry and wet (with 150 and 300 ppm H_2O) mantle peridotite solidus are from Hirschmann et al. 2009. Uncertainties are in experimental calibration of the barometer (± 6 km). LAB depth is from Hyndman and Canil (2021).....65

Fig. 32. Model geotherms calculated using surface heat production where A_0 = 1.1 μW/m³ and various surface heat flow. Uncertainties are in experimental calibration of the barometer (± 6 km). Dry and wet (with 150 and 300 ppm H_2O) mantle peridotite solidus are from Hirschmann et al. (2009). Other Cordilleran xenoliths are from (Canil and Russell 2022). The average Moho depth is from Audet et al. (2020). LAB depth is from Hyndman and Canil (2021) 67

Fig. 33. Plot of depth in km vs T_{Al} in °C. Hollow symbols are published data for xenoliths from elsewhere in the Cordillera (Canil and Russell 2022) and worldwide (Gregoire et al. 2000; Mallmann et al. 2009; De Hoog et al. 2010; Lin et al. 2023). The average spinel-garnet peridotite transition depth for continental off-craton mantle lithosphere is at 73 ± 6 km (Canil et al. 2021a) 68

Fig. 34. Plot of temperature and Ca dependence of P_{SC} barometry. (A) temperature vs P_{SC} when X_{Mo} fixed at 0.001. (B) X_{Mo} vs P_{SC} when temperature is fixed at 850 °C 68

Fig. 35. Plot of depth in km vs T_{Al} in °C. The depths are converted from P_{Lin}. Hollow symbols are published data for xenoliths from elsewhere in the Cordillera (Canil and Russell 2022) and worldwide (Gregoire et al. 2000; Mallmann et al. 2009; De Hoog et al. 2010; Lin et al. 2023). Superimposed on the array of xenoliths is a best

fit geotherm calculated using surface heat flow (q_0) of 97 mW/m² and heat production (A_0) of 2.2 μW/m³. Also shown is the mantle solidus for dry (solid) and 150, 300 ppm water (dashed) after Hirschmann et al. (2009). The spinel-garnet peridotite transition field is from Canil et al. (2021a) 71

Fig. 36. Fit of Equation 6 to the measured zoning profile from sample MH-02-100B. C_1 is the initial concentration at the grain boundary (where $x = 0$). C_2 is the original concentration at the core 73

Fig. 37. Measured zoning profile for sample MH-02-100B. The olivine grain boundary is defined by the beginning of abrupt increase of Al concentration 74

List of Abbreviations

Minerals

cpx = clinopyroxene

gt = garnet

ol = olivine

opx = orthopyroxene

sp = spinel

Others

APFU = atom per formula weight

BLOD = below limit of detection

EPMA = electron probe microanalysis

HREE = heavy rare earth element

LA-ICP-MS = laser ablation inductively coupled plasma mass spectrometry

LAB = lithosphere-asthenosphere boundary

LREE = light rare earth element

OIB = oceanic island basalt

PPL = plane polarized light

P_{SC} = Ca in olivine barometer

SEM = scanning electron microscope

STD = standard deviation

T_{Al} = Al in olivine thermometer

T_{BKN} = pyroxene major elements thermometer

T_{Ca} = Ca in olivine thermometer

T_{FeMg} = Fe-Mg in olivine thermometer

T_{Mg} = olivine-melt thermometer based on Mg partitioning

T_{Ni} = olivine-melt thermometer based on Ni partitioning

T_{REE} = pyroxene rare earth element and Y thermometer

XP = cross polarized light

Acknowledgements

First and foremost, I would like to thank my supervisor Dr. Dante Canil, for giving me the chance to work on this dream project and guiding me throughout. His knowledge, passion, and understanding has been a huge inspiration throughout this degree. I am also grateful to Dr. Rebecca Morris for answering my endless questions and giving me solid advice during my stay at UVic. I would also like to thank Dr. Jody Spence for assistance with the LA-ICP-MS work, and Anette von der Handt for her help and guidance through EPMA works. And thanks Dr. Kelly Russell for donating the Llangorse samples for this study.

I want to acknowledge the Earth and Environmental Science Department at Acadia University and every faculty member there. Thanks for letting me use the petrography camera for the images in this thesis. It always felt like home when I am sitting at that cozy lounge at third floor of Huggins. I am incredibly grateful to my Honours supervisor Dr. Sandra Barr who has been the most passionate, supportive and dedicated mentor. Her encouragement and guidance through both my degrees at Acadia and UVic has been invaluable. I would like to thank Dr. Mo Snyder who is the coolest and my favorite professor, thanks for being a great listener and helping me through the toughest moments. And thanks for letting me join your fun labs and field trips whenever I felt down or needed accompany. I would also like to thank Dr. Rob Raeside who encouraged me to pursue Honours and Masters degrees in geology.

To my friends from my first year at Acadia: Imran Iqbal, Yi Pan, Junmo Eum, and Julia Toma. Cannot believe it’s been over half a decade! I am grateful for every memory we have shared.

I would also like to shout out my friends at the home department Parker Ingham, Jesse Demaries-Smith, Cameron Greaves, Jessica Beckwith, Zoe Mathurin, Mitch Maracle and all the

others I could not name here. Thanks for the laughs, late nights, and all the great memories at Wolfville and the geo conferences. Special thanks to my best friend Parker Ingham who generously offered all my stays in Nova Scotia and being supportive in the past year.

To my friends in Victoria, Matthew Wilson and Katie Withrow, thank you for your support, for listening, and for being here for me.

Last but certainly not least, my heartfelt thanks to my family for their constant encouragement and support.

Finally, I would like to dedicate this thesis to the memory of Katharine Baldwin, who passed away three weeks before my defense. Thank you for caring for me and treating me like your own son over the past five years. Your unwavering encouragement and support guided me through the most challenging season of my life. I hope to see you again at the end of this journey.

CHAPTER 1: Introduction

1.1 Introduction

The study of the mantle lithosphere is critical for understanding the fundamental processes that shape the Earth. The lithosphere, which consists of the Earth's rigid outer shell, plays a central role in plate tectonics, which drives the movement of continents, the formation of mountains, and the generation of earthquakes and volcanic activity. Beneath the lithosphere, the mantle contains essential information about the planet's composition, temperature, and dynamic behavior over geological history. Understanding the mantle lithosphere is crucial because it provides insights into the thermal and chemical evolution of the Earth, as well as the nature of its deep structure and interaction with the underlying asthenosphere.

Mantle xenoliths are fragments of the mantle lithosphere that are brought to the surface by volcanic activity, providing a rare and direct window into the deep interior of the Earth. These pieces of mantle rock, typically embedded in alkalic basalt or kimberlites, offer valuable insights into the composition, structure, and processes occurring within the mantle lithosphere. By studying the mantle xenoliths, we can calculate the depth, reconstruct the thermal history, and derive the ‘paleogeotherm’ of mantle lithosphere (e.g., Harder and Russell 2006; Francis et al. 2010; Canil et al. 2021b; Canil and Russell 2022). Then the results can be compared with the current geothermal state measured or estimated by geophysical methods.

1.2 Canadian Cordillera

Intensive petrological and geophysical research has been conducted in the Canadian Cordillera to investigate the chemical and physical properties of the Cordilleran lithosphere, to understand the origin of the underlying mantle, and elucidate the mechanisms of crustal

amalgamation (e.g., Lewis et al. 2003; Hyndman and Canil 2021). Geophysical observations reveal that the Cordilleran lithosphere is hot and thin compared to the adjacent craton (e.g., Currie and Yu 2023), but the origin of such thin and hot lithosphere is still unclear and is an ongoing topic of debate.

One hypothesis is that the thin Cordilleran lithosphere is a long-lived structure and has existed for more than 100 million years. The lithosphere may have been partially inherited from the old Laurentia craton. In this model, the mantle lithosphere of the Laurentia craton was first thinned by a rifting event in the formation of Rodinia (e.g., Monger and Price 2002), then was overthrust by allochthonous terranes during terrane accretion that built the Cordillera (e.g., Cook and Erdmer 2005). Alternatively, a second model is that the entire lithosphere was added, originated as allochthonous terranes, and emplaced when those terranes collided with the Laurentia craton margin (e.g., Johnston 2008; Sigloch and Mihalynuk 2013). At the same time, the Farallon plate was subducting under the western edge of the Cordillera. The subducting slab released water that lowered the viscosity of the above mantle wedge creating small-scale convection (e.g., Honda and Saito 2003; Dixon et al. 2004) to maintain the high back arc temperature of the Cordillera lithosphere and preventing it from further thickening (Hyndman and Currie 2011).

A third hypothesis is that the thin and hot lithosphere is created and maintained by a slab window (Thorkelson et al. 2011), a gap created by the subduction of a mid ocean ridge (Dickinson and Snyder 1979; Thorkelson and Taylor 1989). When an ocean ridge subducts under the plate, it will separate and create a slab window which is bounded by thin slab edges that can be easily deformed and eroded by high temperature (Thorkelson and Breitsprecher 2005). When the slab window opens, the hot anhydrous asthenosphere mantle will ascend from below the slab

to fill the void (Thorkelson et al. 2011). The uprising mantle will undergo decompression melting and thermally erode the overlying Cordilleran lithospheric mantle (Thorkelson et al. 2011) to create thin and hot lithosphere. At the same time, arc volcanism above the region will transition to intraplate volcanism (Hole et al., 1991; Thorkelson 1996) due to the change of melting source from the hydrous mantle wedge above the subducted slab to anhydrous asthenosphere or lithospheric mantle below (Carignan et al. 1994; Edwards and Russell 2000). Thorkelson et al. (2011) compiled geochemical data of the Neogene to Holocene volcanic rocks in a transect from the Cascade Arc to Aleutian Arc. Based on the intraplate character of the volcanic centers, Thorkelson et al. interpret the presence of a 1500 km slab window beneath almost all of the Canadian Cordillera.

The fourth hypothesis is that the Cordilleran lithosphere was originally thicker but has undergone thermal erosion or gravitational removal in the past 55 million years, and that the weaker lower lithosphere was decoupled from strong upper lithosphere. Bao et al. (2014) proposed that there was a wholesale lithosphere removal, "delamination" or foundering at around 55 Ma, based on geological evidence of rapid surface uplift, extension, and magmatism in the Cordillera. They suggested delamination was likely triggered by subduction edge-driven convection, with the lower part of the lithosphere being delaminated along the weak zone to sink into the deeper mantle (Bao et al. 2014). A high-velocity anomaly zone at 200 km depth in a seismic tomography model was interpreted to be the detached Cordillera lower lithosphere (Bao et al. 2014). According to Audet et al. (2019), thermal modelling suggests that the Cordilleran lithosphere north of 60° N have been through replacement and subsequent cooling, with new mantle lithosphere only formed in the past 25 to 5 million years. Other studies suggest that the Cordilleran lithosphere might have been through gradual convection erosion or removal which

was caused by subduction induced mantle flow rather than wholesale removal or delamination (e.g., Currie et al. 2008; Hardebol et al. 2012).

1.3 Rationale and Purpose of Study

The main purpose of this study is to investigate the thickness and thermal history of mantle lithosphere in the northern Canadian Cordillera (Fig. 1) to provide constraints on the hypotheses described above. Many previous mantle xenolith studies in this region were focused on the trace element and isotopic composition of these rocks (Carignan et al. 1994; Peslier et al. 2002; Francis et al. 2010). Earlier work described the xenoliths and calculated equilibrium temperatures to interpret the conditions of Cordilleran mantle lithosphere (e.g., Fujii and Scarfe 1982; Ross 1983; Brearley et al. 1984; Harder and Russell 2006). In this thesis, I present new geochemical information and petrographic descriptions on mantle derived xenoliths and their host dykes from the Llangorse Mountain locality. I apply various improved geothermometers to calculate closure temperatures of mantle xenoliths and interpret the cooling rate of the mantle lithosphere. I use geobarometry to directly calculate the pressure conditions to interpret the thickness of the Cordilleran lithosphere. Additionally, I apply diffusion chronometry to calculate the zoning timescale and recover the thermal history of Llangorse xenoliths and host lava. Finally, I combine these temperature, pressure conditions and thermal history of Llangorse xenoliths with other published datasets to constrain the origin of the lithospheric mantle underlying the Canadian Cordillera.

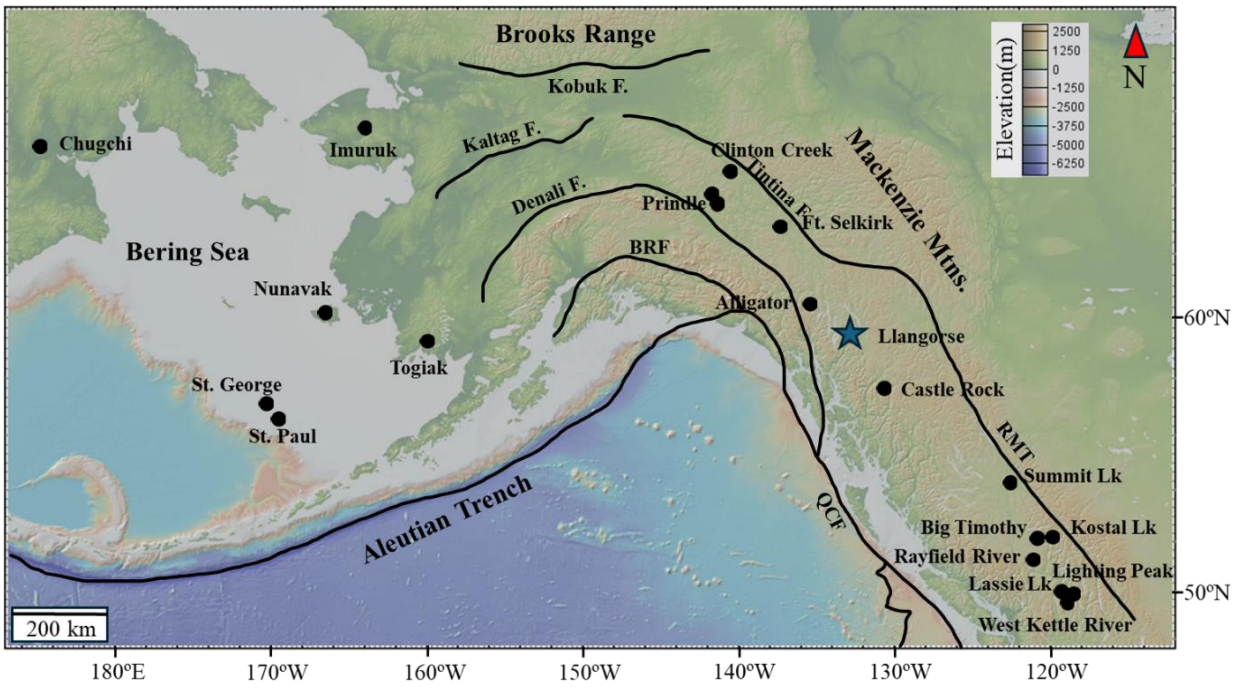

Fig. 1. Relief map of the northern Cordilleran showing mantle xenolith localities. Blue star shows the location of Llangorse locality. Also shown major faults, the Aleutian trench, Rocky Mountain Trench (RMT), Queen Charlotte transform fault (QCF). Figure made with GeoMapApp (Ryan et al. 2009).

1.4 Geologic Setting

1.4.1 Terranes

The Canadian Cordillera is a relatively youthful mobile belt located along the western margin of the North American plate. In this thesis the 'Canadian Cordillera' refers to the Canadian portion of the larger North American Cordillera that occurs in Western United State, British Columbia, Yukon, and Alaska. The Canadian Cordillera consists of five major tectonic belts from east to west: the Foreland, Omineca, Intermontane, Coastal, and Insular belts (Monger and Price 2002). The formation of this mobile belt can be attributed to the accretion of allochthonous oceanic and island-arc terranes onto the ancient Laurentia craton margin during the Mesozoic (Monger and Price 2002) or by the westward moving North American plate colliding with exotic terranes (Sigloch and Mihalynuk 2013).

1.4.2 Neogene-Quaternary volcanism in Cordillera

Neogene-Quaternary volcanism is widespread along the western margin of North America, from Alaska to Mexico. These young alkaline volcanic centers have erupted behind the Cascade arc, likely triggered by either opening of a slab window (Thorkelson et al. 2011) or Miocene and modern plate movements and plate stresses (Valentine and Perry 2007; Russell et al. 2023). More than 100 volcanic centers erupted in the Canadian Cordillera. These volcanic centers range in age from 28 million years to 200 years (Edward and Russell 2000). Early Neogene volcanic centers are mainly located in the northern and central part of the Canadian Cordillera (Edwards and Russell 2000). In contrast, more recent volcanism is distributed throughout the entire Cordillera (Edwards and Russell, 2000). The peak of magmatism which occurred between 9 and 7 Ma coincides with a net extension event along the plate boundary

between the North American and Pacific plates, which indicates volcanism might be triggered by transtension in the Cordillera (Edwards and Russell 2000).

According to Edwards and Russell (2000), alkali olivine basalt and hawaiite are the most abundant volcanic rock types erupted, followed by basanite and olivine nephelinite. They also document more evolved alkaline rock types such as phonolite, trachyte, and comendite (Edwards and Russell, 2000). Crustal and mantle xenoliths, megacrysts, and cognate inclusions have been observed in Neogene-Quaternary volcanic units throughout the entire Canadian Cordillera (Edwards and Russell 2000).

Geochemical data show that the most primitive rock types such as nephelinite, basanite and alkali basalt are highly enriched in incompatible elements (Ba, Rb, K, Nb, La, Ce, Sr, P, Nd, Zr, Sm) as much as 100X, and have slight enrichment in more compatible elements (Ti, Y, Yb) of about 10X compared to primitive mantle (Edwards and Russell 2000). The similar enrichment trends of these three rock types indicate they have a common origin (Edwards and Russell 2000). Neogene-Quaternary lavas exhibit similar trace element patterns to the average oceanic island basalt composition. Most of the samples exhibit ε_{Nd} values greater than +5 and $^{87}Sr / {}^{86}Sr <$ 0.705. This isotopic composition is typical of OIB or the most radiogenic end of the mid-ocean ridge basalt. This suggests that they are likely derived from same source as the normal oceanic island basalt (Edwards and Russell 2000). Furthermore, the isotopic ratios of the lavas are consistent across the entire Canadian Cordillera. Given the highly heterogeneous nature of the lithosphere beneath the region, along with supporting trace element and isotopic data, it is likely that these volcanic rocks were derived from an asthenosphere source (Edwards and Russell 2000). Canil et al. (2021a) used the $aSiO_2$ barometer to calculate the depth of equilibration of most mantle-xenolith bearing alkaline lavas of 65 ± 10 km, which is also consistent with a

mainly asthenosphere origin. However, other studies interpret that these alkaline lavas originated in the mantle lithosphere, and are derived from partial melting of amphibole-bearing veins hosted in peridotitic mantle (e.g., Francis and Ludden 1995; Abraham et al. 2005).

1.4.3 Lithosphere Structure of the Canadian Cordillera

The western boundary of the Canadian Cordillera has experienced subduction since the early Triassic. Transcurrent motion of the overlying plate began in the mid Eocene (Dickinson 2004). Currently in the southern part of the western boundary, the Juan de Fuca plate and other smaller plates which are remnants of the Farallon plate, are subducting under the North American plate to form the Cascade arc (Dickinson 2004). In British Columbia, subduction was cut off by the Queen Charlotte fault and replaced by transcurrent motion, with the Pacific plate starting to move dextrally along this fault since around 43 Ma (Dickinson 2004). In the east, the Cordillera is separated from the Laurentia craton by the Cordillera deformation front (Currie and Yu 2023). Topographically, the Cordillera exhibits a higher average elevation of 1.5 km, whereas the craton is flat and has low mean elevation near sea level.

Compared to the adjacent Laurentian craton, the Canadian Cordillera has a relatively thin lithosphere. Many geophysical surveys in the Canadian Cordillera region have been undertaken to investigate the lithosphere structure under the Cordillera. This work is summarized in Currie and Yu (2023). The Cordillera exhibits a high heat flow of 75 ± 15 mW/m^2 compared to 42 ± 10 mW/m^2 in the craton. Compared to the craton, the Cordillera also has relatively low mantle seismic velocities (e.g., Clowes et al. 1995; Bao et al. 2014; Schaeffer and Lebedev 2014) and low mantle electrical resistivities (e.g., Rippe et al. 2013). Seismic data reveal a subvertical to west-dipping step in the lithosphere, which is interpreted as the Cordillera-craton boundary underlying the Rocky Mountain Trench and the Tintina Fault system (e.g., Schaeffer and

Lebedev 2014; Chen et al. 2019). Based on these geophysical features and other observations, the Canadian Cordillera lithosphere is interpreted to be hot and thin, with a Moho temperature around 800 to 900 °C at 27 to 43 km in depth with mean and standard deviations (std) of 33 and 3 km (Postlethwaite et al. 2014; Audet et al. 2020), and a lithosphere thickness around 60 to 70 km (e.g., Hyndman and Lewis 1999; Currie and Hyndman 2006; Hyndman 2010; Canil et al. 2021a; Hyndman and Canil 2021a). These results are broadly consistent with the study of mantle xenoliths in the region (e.g., Harder and Rusell 2006; Francis et al. 2010) but the xenoliths' sampling depths are open to question, as will be described below.

1.5 Mantle Xenoliths

1.5.1 Previous Work on Cordilleran Xenoliths

In British Columbia, mantle xenoliths were first reported by Soregoreli (1968) in the Boss Mountain area and were subsequently studied by Littlejohn and Greenwood (1974). Over the past decades, mantle xenoliths hosted in alkaline lavas have been discovered at more than 30 localities throughout the Canadian Cordillera (Some xenolith localities next to each other have been combined on the figure) (Fig.1). They are parts of the mantle lithosphere brought up to the surface by Neogene and younger alkaline volcanism. Based on their mineral chemistry and assemblages, these xenoliths can be separated into two distinct series which are lherzolite and wehrlite (Francis et al. 2010). The majority of mantle xenoliths belong to the chromian-diopside lherzolite series (Frey and Prinz 1978). Within the lherzolite series, xenoliths can be subdivided into unimodal and bimodal suites. The unimodal suites contain only relatively fertile spinel lherzolites whereas bimodal suites have both spinel lherzolites and refractory spinel harzburgites (Shi et al., 1998). On average, the fertile lherzolite xenoliths are rich in clinopyroxene and consist of 39 to 40 wt% MgO and 3 to 3.5 wt% Al_2O_3, and refractory spinel harzburgites are

poor in clinopyroxene, and have a higher MgO of about 45 to 46 wt% and lower Al_2O_3 contents of about 0.5 to 1 wt% (Francis et al. 2010). The wehrlite series xenoliths mainly comprise dark green augite and olivine (Francis et al., 2010), and have been interpreted as cumulates derived from the reaction between alkaline melt and mantle lherzolite (Peslier et al. 2002)

1.5.2 Mantle Thermobarometry

The thermal history of mantle xenoliths is important, because temperature is the main constraint on mantle rheology and plate strength (Ranalli 1980). The first mantle thermobarometry studies in the Canadian Cordillera were done in the early 80s. Those early studies were mainly focussed on describing the texture and composition of the mantle xenoliths and calculating pyroxene equilibrium temperatures (e.g., Fujii and Scarfe 1982; Ross 1983; Brearley et al. 1984). Previous studies used the major element composition of the coexisting clinopyroxene and orthopyroxene to calculate the equilibrium temperature of mantle xenoliths. The results range from 800 °C to 1100 °C (e.g., Harder and Russell 2006; Francis et al. 2010). The minimum xenolith temperatures have been interpreted as maximum Moho temperature, and the maximum xenolith temperatures indicate the minimum lithosphere-asthenosphere boundary temperature (Harder and Russell 2006). By projecting xenolith equilibrium temperatures to the model regional geotherm (Fig.2), previous studies (Fujii and Scarfe 1982; Brearley et al. 1984; Harder and Russell 2006) concluded that the Cordilleran mantle lithosphere is at least 16 to 30 km thick, and the lithosphere-asthenosphere boundary is at 52 to 66 km depth.

However, using the xenoliths' temperatures to project to a model geotherm and derive depth (Fig.2) is not a direct method and is inaccurate. The model geotherm is based on a presumed surface heat flow, crustal heat production, and thermal conductivity of crustal rocks, and there are uncertainties and local variations on these values (Chapman and Pollock 1985).

These uncertainties will be inherited by the depth projection. In addition, most geothermometers only record the closure temperature during cooling of the mantle (Dodson 1973), which is based on diffusion parameters of the chemical exchange involved. For example, for rocks having coexisting cpx and opx the geothermometer T_{BKN} (Brey and Köhler 1990) is based on Ca-Mg-Fe exchange between, and this system closes to diffusion at lower temperature than T_{REE} (Liang et al. 2013) which is based on REE exchange between the same two minerals. At a given cooling rate, T_{REE} will typically always record higher temperature than T_{BKN}. If different thermometers are used on the same sample and then projected to the model geotherm, the thermometer with higher closure temperature will always yield a deeper depth, interpreted as thicker lithosphere. In contrast, a recent study (Canil and Russell 2022) applied the independent barometer P_{Ca} (Kohler and Brey 1990; Shejwalkar and Coogan 2013) based on exchange of Ca and Al between olivine and clinopyroxene on samples from Summit Lake locality to calculate the depth and thickness of underlying lithosphere. Compared to the geotherm projection method, the lithosphere thickness calculated by barometry is 10-20 km thinner, which indicates these samples might be lying on a much hotter geotherm than the model geotherm (Canil and Russell 2022). That work also shows that there is some regional variation on the geotherm gradients and that the geotherm projection method is inaccurate.

Differences between geothermometers can also be used to infer the thermal history of the mantle lithosphere, not just its thickness. A recent study (Canil et al. 2021b) has applied coexisting T_{BKN} and T_{REE} to xenoliths from the Mt. Timothy xenolith locality to interpret the cooling history of Cordilleran lithosphere. Results show that the difference between the closure temperatures of these two geothermometers is less than 80 °C which is statistically insignificant, indicating that these mantle xenoliths have a cooling rate less than 10^{-5} °C / Myr.

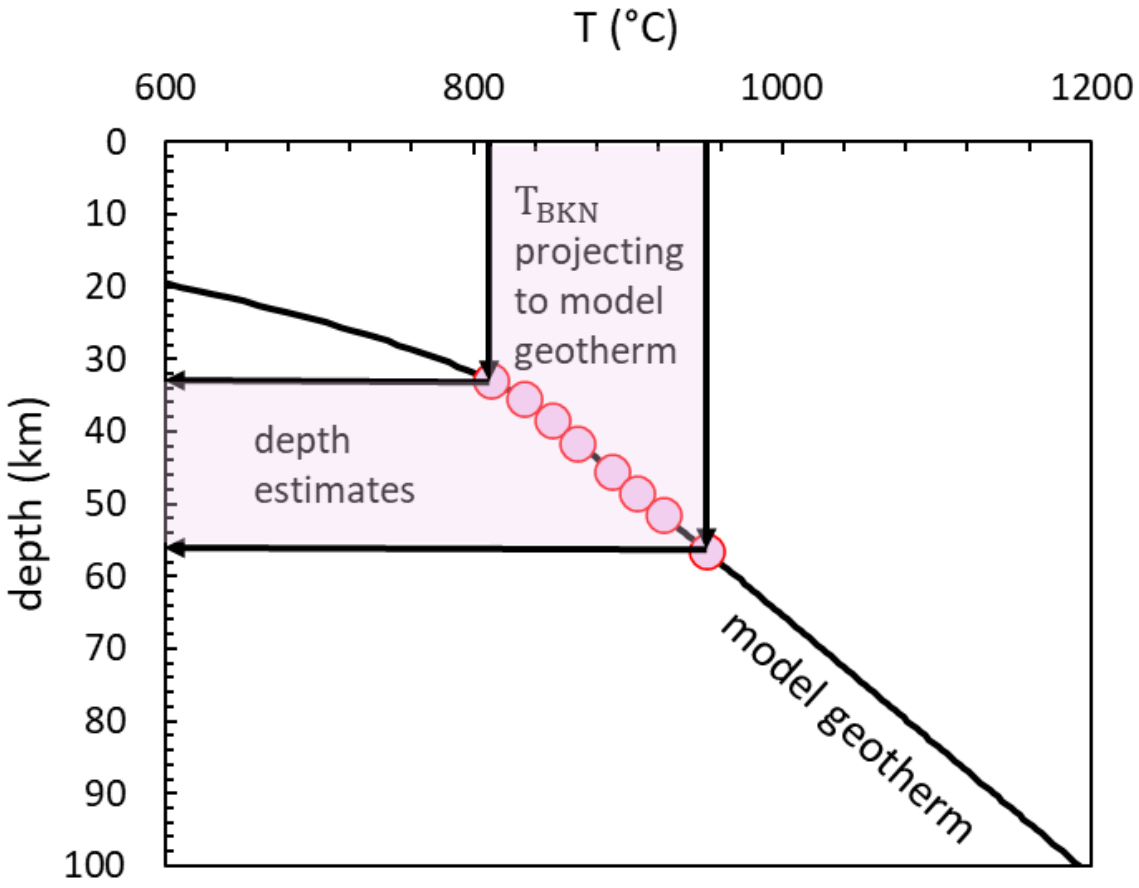

Fig. 2. Projection of xenolith T_{BKN} temperature to a model geotherm.

This cooling rate is far less than the required cooling rate (> 10° C / Myr) for delamination or for the replacement of lithosphere process as proposed by Bao et al (2014) or Audet et al. (2019) (Canil et al. 2021b).

Several different thermobarometers (Table.1, Fig.3) can be used to recover the equilibrium conditions and thermal history of the mantle lithosphere represented by the xenoliths. T_{BKN} is a well calibrated and commonly used pyroxene major element thermometry developed based on Ca-Mg-Fe exchange reaction between coexisting clinopyroxenes and orthopyroxenes by Brey and Köhler (1990). T_{REE} is a newly developed pyroxene trace element thermometer, based on partitioning of all REE and Y between coexisting cpx and opx to calculate the equilibrium temperature (Liang et al. 2013). Compared to the pyroxene major element thermometers, T_{REE} normally records higher closure temperatures, because the REE in pyroxenes have much slower diffusion rates than the major elements. Both T_{Al} and T_{FeMg} are thermometers based on Al and Fe-Mg exchange reactions, respectively, between coexisting olivine and Cr spinel (Li et al. 1995; Coogan et al. 2014). In general, the Fe and Mg cations have much faster diffusion rates than the Al, hence the T_{FeMg} thermometer is more prone to be affected by later thermal events. Lastly, the Ca exchange reaction between olivine and clinopyroxene was used as a geobarometer (P_{SC}) to directly calculate the equilibrium pressure. However the Ca exchange reaction is both affected by the temperature and pressure, and Ca has high diffusivity in olivine, so the P_{SC} can be affected by heating of the xenoliths in host magmas. For this reason, P_{SC} can be coupled with T_{Al} to get more precise results (D'Souza et al, 2020).

In this thesis, I measure and examine the equilibrium condition and thermal history of the lithospheric mantle represented by mantle xenoliths at Llangorse, located in northern British

Table. 1. Geothermobarometers used in this study.

short form	mineral	exchange
T_{BKN}	cpx and opx	based on Ca-Mg-Fe exchange between cpx and opx
T_{REE}	cpx and opx	based on REE and Y exchange between cpx and opx
T_{Al}	olivine	based on Al exchange between olivine and spinel
T_{FeMg}	olivine	based on Fe-Mg exchange between olivine and spinel
T_{Ca}	olivine	based on Ca exchange between olivine and cpx
P_{SC}	olivine	based on Ca exchange between olivine and cpx
T_{Mg}	olivine-melt	based on Mg partitioning between olivine phenocryst and melt
T_{Ni}	olivine-melt	based on Ni partitioning between olivine phenocryst and melt

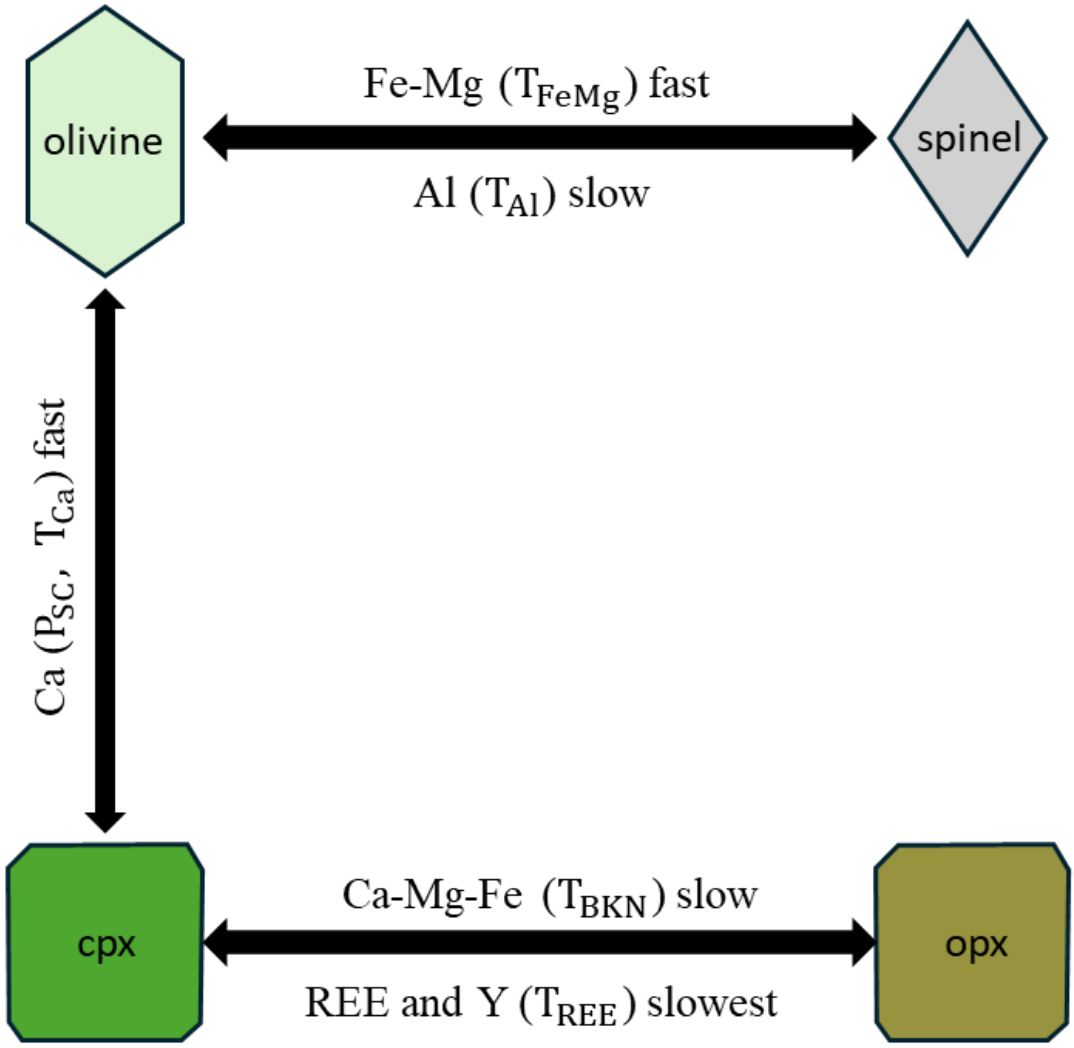

Fig. 3. Various geothermobarometers are used to recover the temperature and pressure conditions for Llangorse xenoliths. The element exchange of the different geothermometers (fast vs. slow) depends on the diffusion rate of the elements involved within each system.

Columbia (Fig.1). These data will be used to interpret thickness and cooling rate of the Cordilleran mantle lithosphere and derive the regional geotherm. The resulting cooling rate can be used to test various proposed models for the Cordilleran lithosphere. The derived geotherm can be compared with the geotherms from other xenolith localities and the model calculated geotherm using local heat flow.

1.6 Llangorse Volcanic Field

Llangorse volcanic field is located southeast of Atlin, BC (Fig.1). It is part of the Atlin volcanic district, which was first mapped by Aitken (1959). It consists of 7 volcanic localities which are Llangorse Mountain, Table Hill, Lone Point, Hidden Ridge, Hirschfeld Creek, Mt. Sanford, and Chikoida Mountain (Harder et al. 2003). The entire volcanic field is located within the Intermontane Belt near the boundary between the Intermontane and Coast Belt. These volcanic rocks were extruded on Llangorse Mountain batholith and Cache Creek Group cherts (Harder and Russel 2006). Based on previous study (Harder et al. 2003), the Llangorse volcanic field mainly consists of three types of Miocene to Holocene volcanic rocks which are alkali-olivine basalts, basanites and olivine-nephelinites. Most of these volcanic rocks are aphanitic and non-porphyritic with abundant amount of mantle xenoliths ranging from 1 cm to 10s cm in size and xenocrysts (Harder and Russel 2006).

1.7 Samples for Study

Thirty-six polished standard thin section samples collected by Harder (2002) from Llangorse Mountain locality were examined (kindly donated for further study by Kelly Russell, UBC). All these samples were used for detailed petrographic study at the University of Victoria. Thirty-two samples (28 xenolith samples and 4 host lava samples) were chosen for mineral chemical analysis.

1.8 Methods of Study

Major element compositions of olivine in 22 samples and spinel in 5 samples were analyzed using a JEOL JXA-iHP200F field emission electron microprobe (EPMA) at the University of British Columbia. The system was operating in wavelength dispersive mode with an accelerating voltage of 15kV, a beam current of 40nA and a beam size of 1 μm. The counting times for Si peak were 10 s, for Ni, Fe, Ca, Mn, Cr, Ti peaks were 15 s, and for Al, Mg peaks were 20 s. Data reduction was done using the Super High Precision (six terms) correction method (Donovan et al. 2023).

Trace elements in olivine (28 samples), and co-existing clinopyroxene and orthopyroxene (7 samples) were analyzed by laser ablation ICP MS system (LA-ICP-MS) at the University of Victoria. The LA-ICP-MS system consists of a Teledyne LSX-213 G2+ laser and an Agilent 8800 QQQ ICP MS operated in double quadrupole mode. The operating conditions for olivine included: spot of 100 μm circle; laser output of 5.10 J/cm^2; and scan speed of 20 μm/s. The operating conditions for pyroxene were spot of 65 μm square; laser output of 7.14 J/cm^2; and scan speed of 10 μm/s. For some smaller cpx grains a spot of 50 μm was used instead. Ideally the laser was rastered along a line of 200 μm length twice to avoid surface contamination. But for some smaller pyroxene grains, the raster line for the laser was shorter. Any visible inclusions, cleavage planes, and crystal boundaries were avoided as well except for some pyroxene analysis which was impossible to avoid all cleavages. The MPI DING komatiite glasses GOR-128 and GOR-132 (Jochum et al. 2006) were used as external standards, with Si determined by EPMA as the internal standard. A mantle olivine standard (MONG - Batanova et al. 2019) and BCR2g glass were analyzed as unknowns three times in each session to check for accuracy and precision for trace elements in olivine and pyroxene. For olivine, the isotopes ^{25}Mg, ^{27}Al, ^{29}Si, ^{40}Ca, ^{45}Sc,

^{47}Ti, ^{51}V, ^{52}Cr, ^{55}Mn, ^{57}Fe, ^{59}Co, ^{60}Ni, ^{63}Cu, ^{66}Zn, ^{89}Y, ^{172}Yb were measured, with ^{29}Si as the internal standard. In able to measure the ^{40}Ca, the ICP MS was operating in MS/MS H_2 mode to remove potential interference from $^{40}Ar^{+}$. For pyroxene, the isotopes ^{27}Al, ^{29}Si, ^{42}Ca, ^{43}Ca, ^{47}Ti, ^{51}V, ^{52}Cr, ^{60}Ni, ^{88}Sr, ^{89}Y, ^{90}Zr, ^{93}Nb, ^{137}Ba, ^{139}La, ^{140}Ce, ^{141}Pr, ^{146}Nd, ^{147}Sm, ^{151}Eu, ^{157}Gd, ^{159}Tb, ^{163}Dy, ^{165}Ho, ^{166}Er, ^{169}Tm, ^{172}Yb, ^{175}Lu were measured.

A check for zoning in Al and Ca in olivine in 8 samples was measured using the same LA-ICP-MS system. The operating conditions included: spot of 50 μm circle; laser output of 7.14 J/cm^2; and scan speed of 10 μm/s. The laser was rastered along a line from the core to the rim of individual olivine grains. Any visible inclusions, cleavage planes, and crystal boundaries were avoided. The MPI DING glasses GOR-128, GOR-132 (Jochum et al. 2006) were used as the external standard.

CHAPTER 2: Petrography

2.1 Mantle Xenoliths

The petrography of xenoliths and host lava at the Llangorse locality have been previously described in Harder (2004 thesis) and Harder and Russell (2006). All the mantle xenolith samples comprise olivine, cpx, opx and spinel; hence they are spinel-bearing peridotites. Based on the model mineralogy (Harder and Russell 2006), these samples can be further subdivided as lherzolites and harzburgites (Fig.4, Table 2). Most olivine and orthopyroxene grains are coarse grained in size, from approximately 2 mm to 15 mm. Clinopyroxene grains are smaller and they are medium grain in size. Spinel grains are mostly anhedral, and have various sizes from 1 mm to 5 mm.

Some of the samples show equilibrium granoblastic texture with triple junction grain boundaries. Other samples show signs of textural disequilibrium. As illustrated in Figure 5, the rim of the pyroxenes in some samples appears to have broken down or partially melted to form a region filled with inclusions and glass pockets, referred to as ‘sieve texture’. Even in a few samples, the smaller pyroxenes have been partially melted to form sieved grains (Fig.6). Other signs of disequilibrium include invasions of melt (now glass) and spinel with obvious reaction rims (Fig.7). One of the lherzolite samples MH-02-109 has been heavily invaded by melt (Fig.8), wherein all grain boundaries contain glass. Based on the textures, these xenoliths, with the exception of MH-02-109 can be subdivided into three groups: non-sieved, weakly sieved and strongly sieved (Table 2). The non-sieved samples show perfect equilibrium textures. The weakly sieved samples have narrow sieved rims (less than 50 micron) around pyroxene grains. The strongly sieved group included samples with wide sieved rims (more than 50 micron) or

entirely sieved grains. There is no other visible texture difference between these three groups other than disequilibrium textures.

2.2 Host Lava

The Llangorse lava samples are medium to fine-grained with a porphyritic texture (Fig.9). The groundmass consists of glass, fine-grained cpx, olivine, opaque, and medium- to fine-grained plagioclase. The phenocrysts are medium-grained, euhedral to subhedral olivine and cpx, ranging from 1 to 3 mm in diameter. These samples also contain coarse-grained olivine xenocrysts which are typically larger than the phenocryst olivine and exhibit reaction rims. Both the phenocryst and xenocryst olivine show strong zoning and contain tiny spinel inclusions (2 to 15 microns in diameter). In addition, some olivine phenocrysts have a relic cpx core (Fig.9).

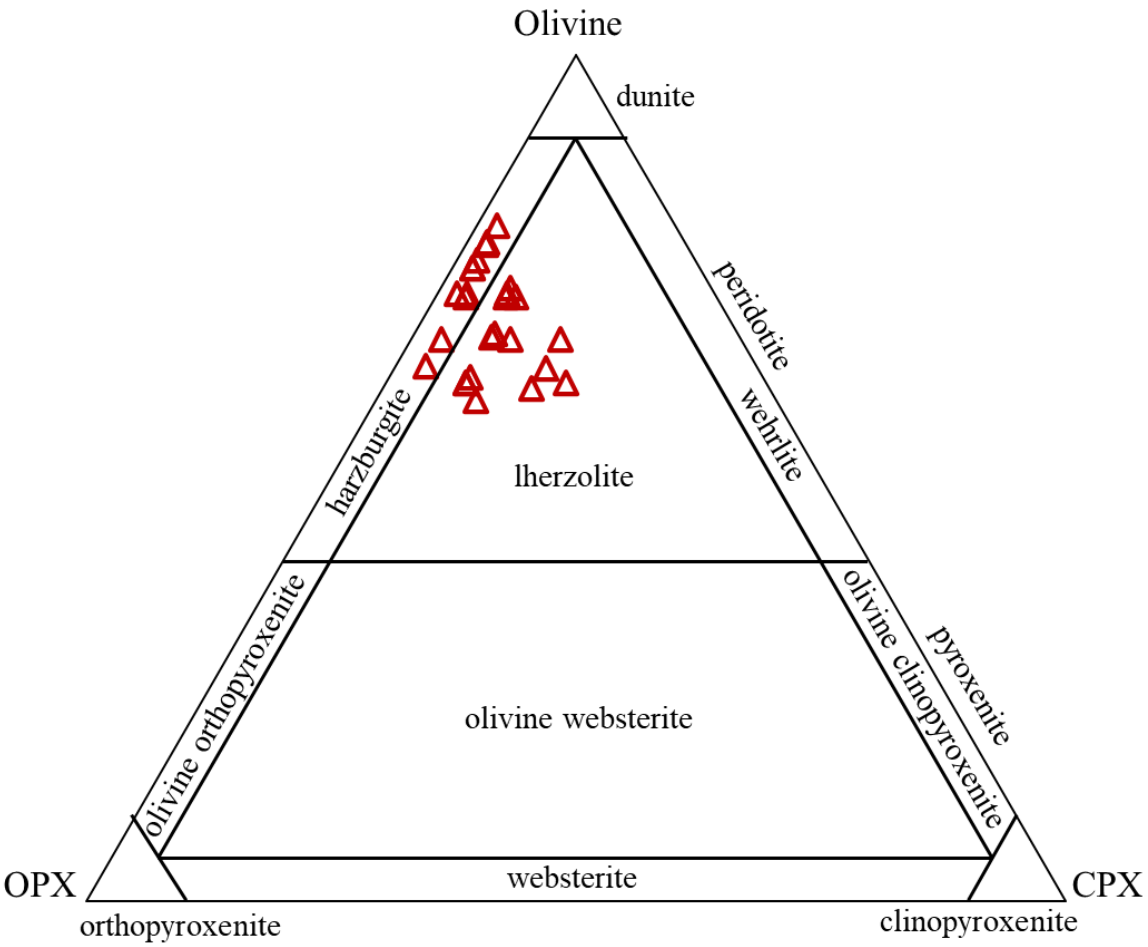

Fig.4. Modal mineralogy of Llangorse locality xenoliths (Harder and Russell 2006) plotted on a peridotite classification diagram.

Table. 2. Modal mineralogy, rock type and assigned group of all the samples used in this study.

Sample Names	Mode Olivine %	Mode OPX %	Mode CPX %	Mode Spinel %	Rock Type	Texture
MH-02-121	65	23	10	2	lherzolite	no sieve
MH-02-10B	58	30	10	2	lherzolite	no sieve
MH-02-10	60	20	18	2	lherzolite	no sieve
MH-02-108	71	21	7	1	lherzolite	no sieve
MH-02-100	74	23	2	1	harzburgite	no sieve
MH-02-117-1	70	20	8	2	lherzolite	weakly sieve
MH-02-116	66	25	8	1	lherzolite	weakly sieve
MH-02-111	61	21	15	3	lherzolite	weakly sieve
MH-02-04	65	24	8	3	lherzolite	weakly sieve
MH-02-9B	65	30	3	2	harzburgite	weakly sieve
MH-02-10C	62	33	3	2	harzburgite	weakly sieve
MH-02-125	79	18	2	1	harzburgite	weakly sieve
MH-02-115	70	25	3	2	harzburgite	weakly sieve
MH-02-117-2	71	26	2	1	harzburgite	weakly sieve
95LM1	76	20	2	2	harzburgite	weakly sieve
MH-02-100B						weakly sieve
MH-02-20	65	18	15	2	lherzolite	strongly sieve
MH-02-102	60	24	15	1	lherzolite	strongly sieve
MH-02-15	60	30	8	2	lherzolite	strongly sieve
MH-02-18B	60	30	8	2	lherzolite	strongly sieve
MH-02-12-1	60	29	8	3	lherzolite	strongly sieve
MP-02-10D	71	20	7	2	lherzolite	strongly sieve
MH-02-19	71	25	3	1	harzburgite	strongly sieve
MH-02-114	77	20	2	1	harzburgite	strongly sieve
MH-02-112	75	22	2	1	harzburgite	strongly sieve
MH-02-115B	74	23	2	1	harzburgite	strongly sieve
MH-02-14						strongly sieve
MH-02-109	70	21	7	2	lherzolite	

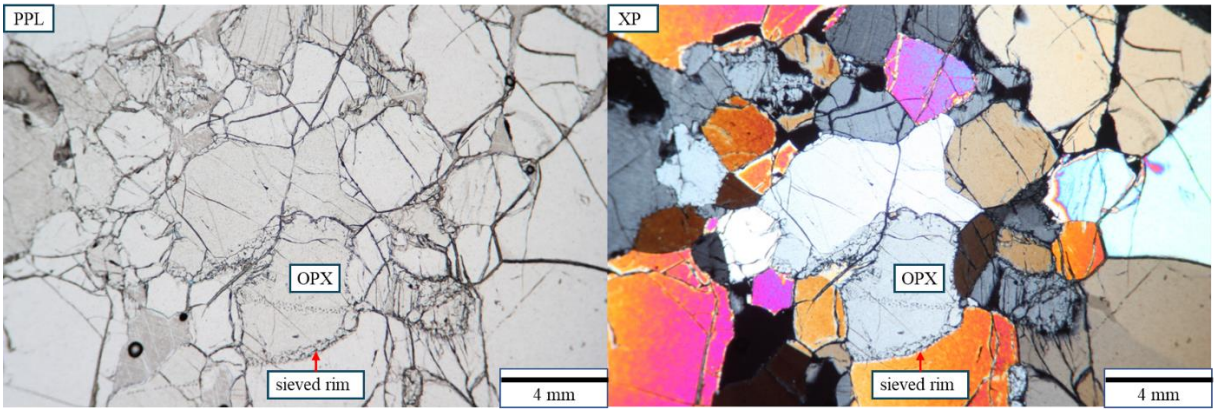

Fig. 5. Photomicrographs of harzburgite xenolith MH-02-125. The sample contains orthopyroxene and clinopyroxene with narrow sieved rims. Image on left is in plane polarized light (PPL) and image on the right is with crossed polars (XP).

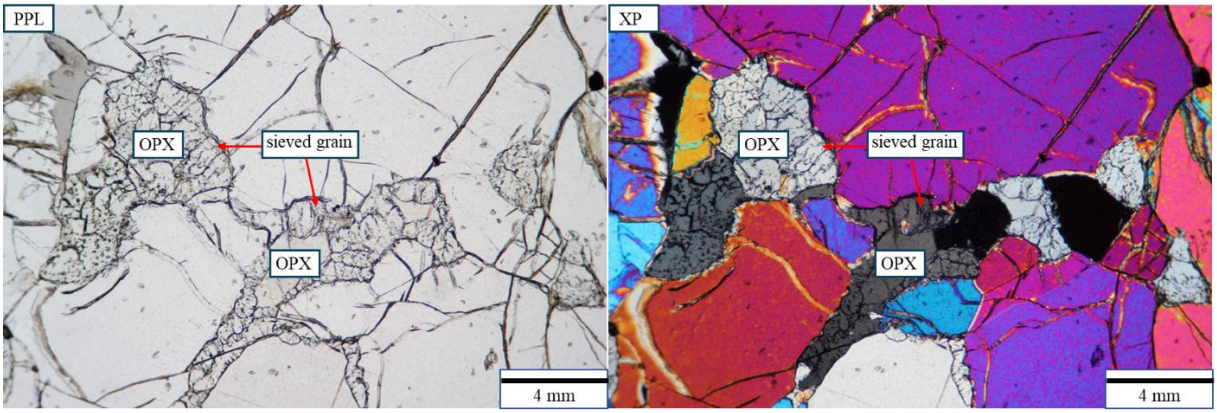

Fig. 6. Photomicrographs of lherzolite xenolith MH-02-18B. The sample contains entirely and partially sieved orthopyroxene and clinopyroxene grains. Image on left is in plane polarized light (PPL) and image on the right is with crossed polars (XP).

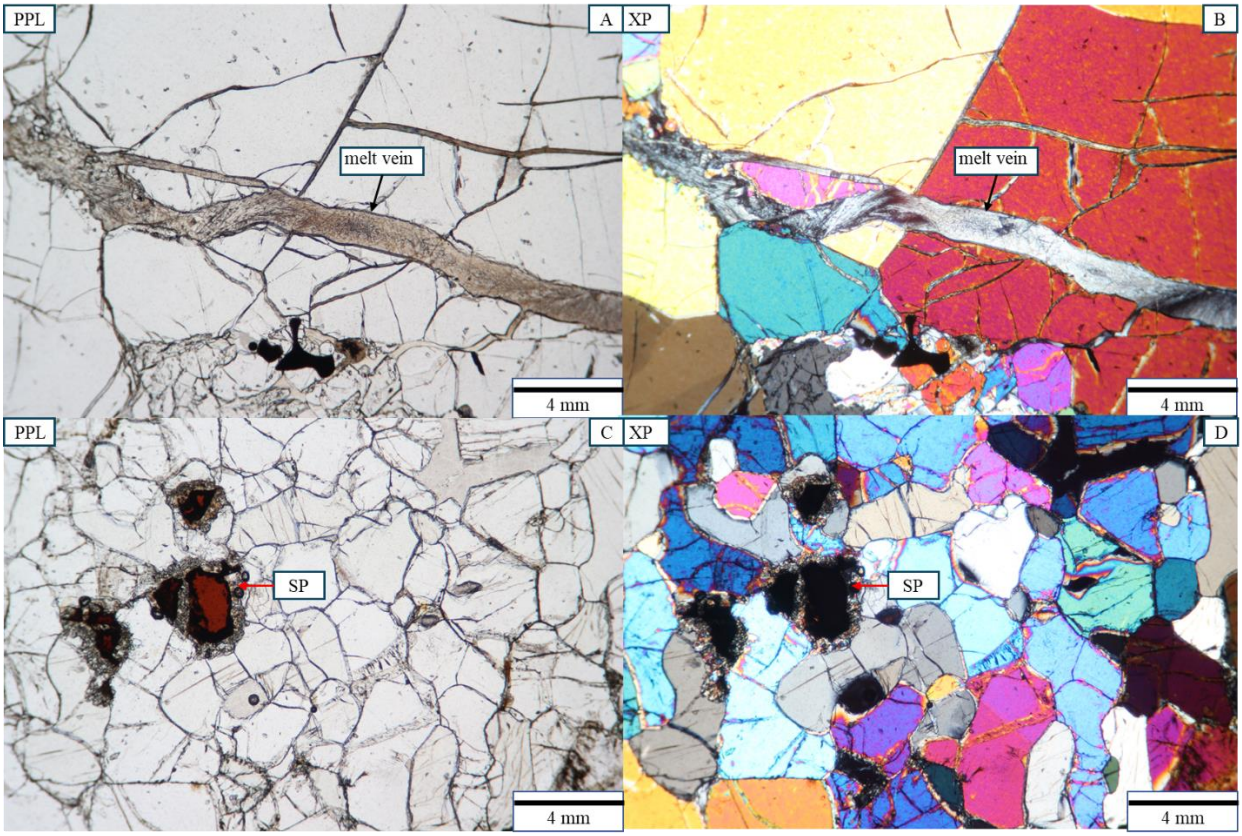

Fig. 7. Photomicrographs of lherzolite xenoliths MH-02-18B (A, B) and MH-02-04 (C, D). (A, B) Photomicrographs showing thick melt veinlet cross-cutting olivine grains. (C, D) Photomicrographs showing spinel with reaction rim. Images on left are in plane polarized light (PPL) and images on the right are with crossed polars (XP).

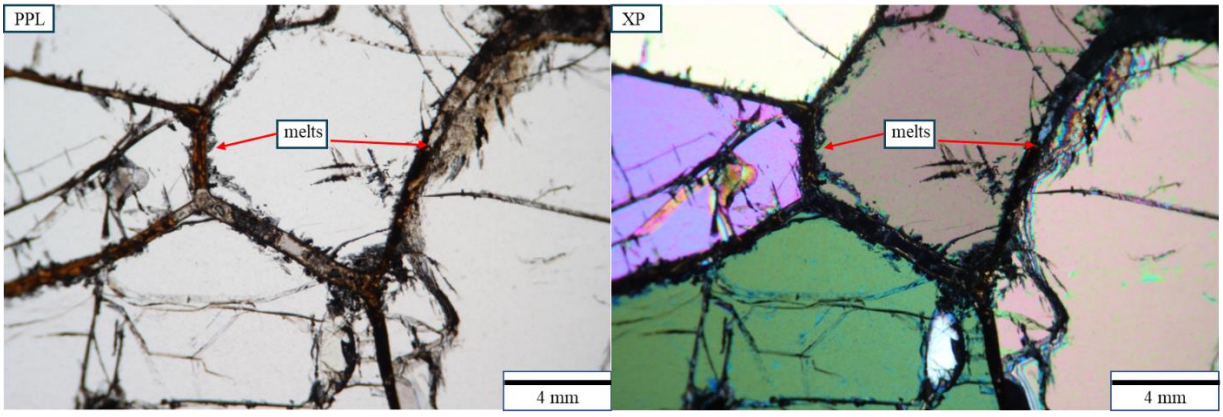

Fig. 8. Photomicrographs of lherzolite xenolith MH-02-109. This sample has been heavily invaded by melts, and all the crystal boundaries have been filled with melts. Image on left is in plane polarized light (PPL) and image on the right is with crossed polars (XP).

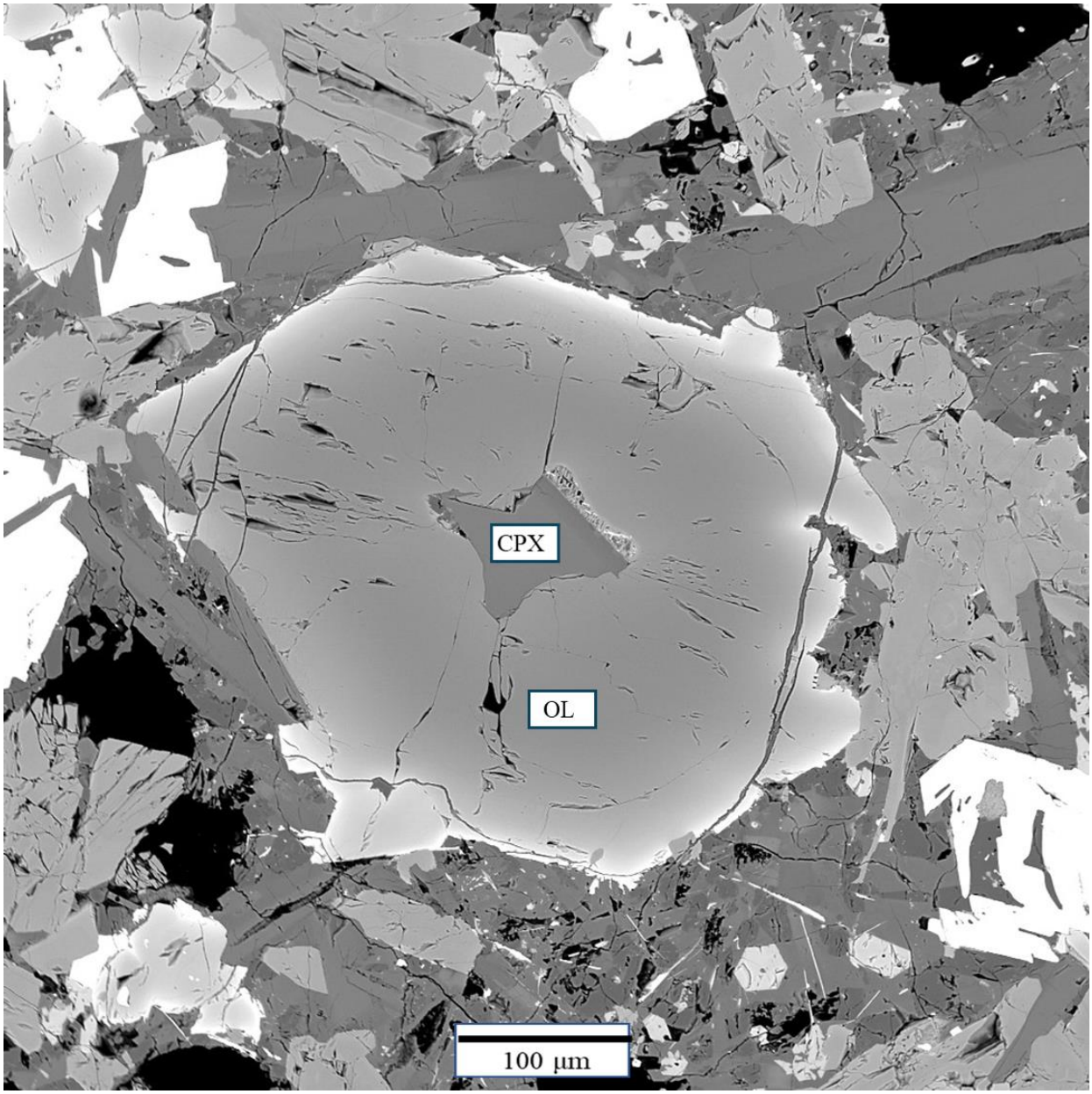

Fig. 9. Backscattered electron image of lava sample MH-02-101. Image shows the olivine phenocryst with cpx relict core.

CHAPTER 3: Mineral Chemistry

3.1 Major Element Chemistry

In each xenolith sample, 6 to 10 olivine grains in direct contact with cpx or spinel were selected, and their core and rim were analyzed using EPMA to determine mineral chemistry. The complete dataset of major mineral chemistry for the olivine grains is provided in Appendix A1. No significant intra-sample grain variation was observed. Additionally, no notable zoning or variations in major elements were detected within individual grains, except for the Cr_2O_3 content, which was significantly higher in the rim analysis near spinel grains. This might indicate the Cr exchange between the contacting olivine and spinel. Alternatively, it is an analytical artefact due to secondary fluorescence effect, because these rim analyses are only five microns away from the olivine-spinel grain boundary. Combined with unpublished olivine major chemistry data from Harder and Russell (2006), the average major element oxides in each sample are plotted against SiO_2 (Fig.10). The olivine grains in the Llangorse locality have a restricted range of magnesium number (Mg# = Mg / (Mg + Fe) molar) between 0.899 and 0.917 except for one sample MH-02-111 which has a lower Mg number at 0.887.

Olivine phenocrysts from four Llangorse lava samples are measured. Their major element chemistry is presented in Appendix A2. Compared to the olivine from xenoliths, all the olivine phenocrysts display much higher concentrations of Al_2O_3, FeO, MnO, CaO, along with lower concentrations of NiO and MgO. Additionally, all the phenocrysts exhibit chemical zoning patterns with higher Mg# in the cores. The olivine phenocrysts from three of the lava samples (MH-02-124A, MH-02-14, and MH-02-16) show relatively uniform composition. The average Mg# for rim analyses from these three samples are 0.671, 0.660, and 0.657, respectively, while core analyses show slightly higher magnesium numbers at 0.684, 0.682, and 0.664. In contrast,

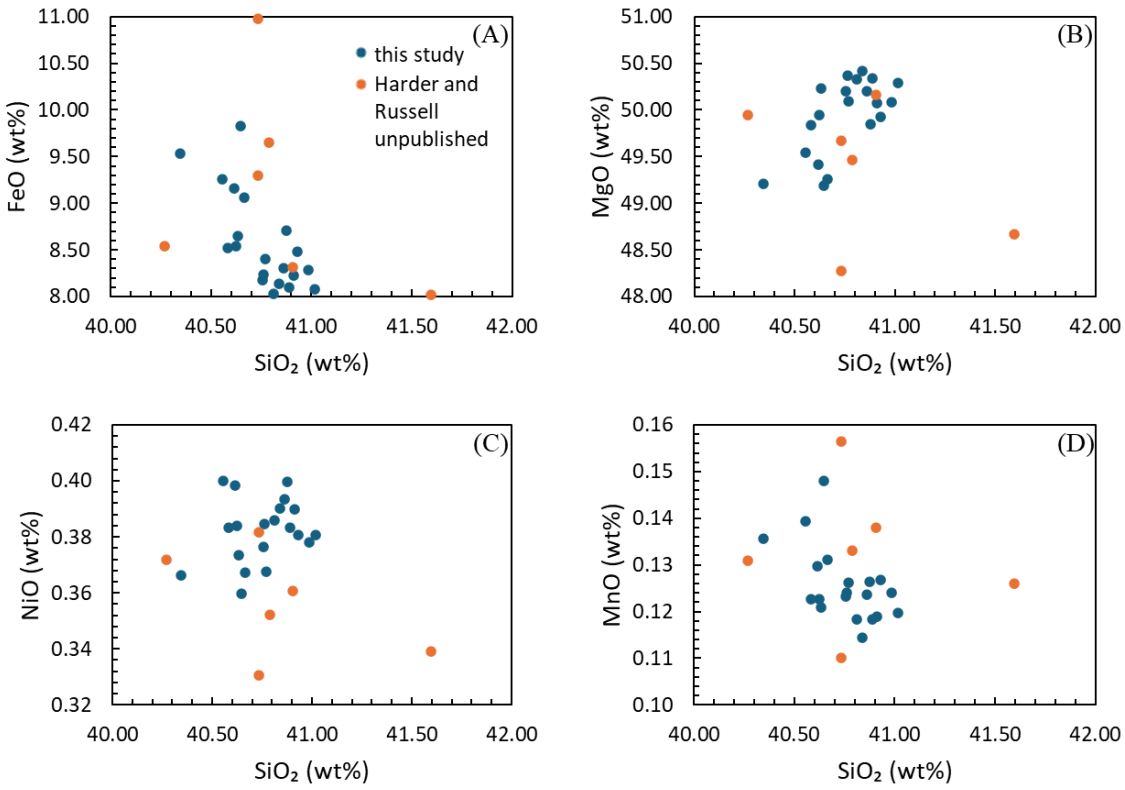

Fig. 10. Plots of SiO_2 vs major element oxides in olivine from Llangorse xenoliths. Blue dots are analyses from this study, orange dots are analyses from Harder and Russell (unpublished). (A) FeO vs SiO_2. (B) MgO vs SiO_2. (C) NiO vs SiO_2. (D) MnO vs SiO_2.

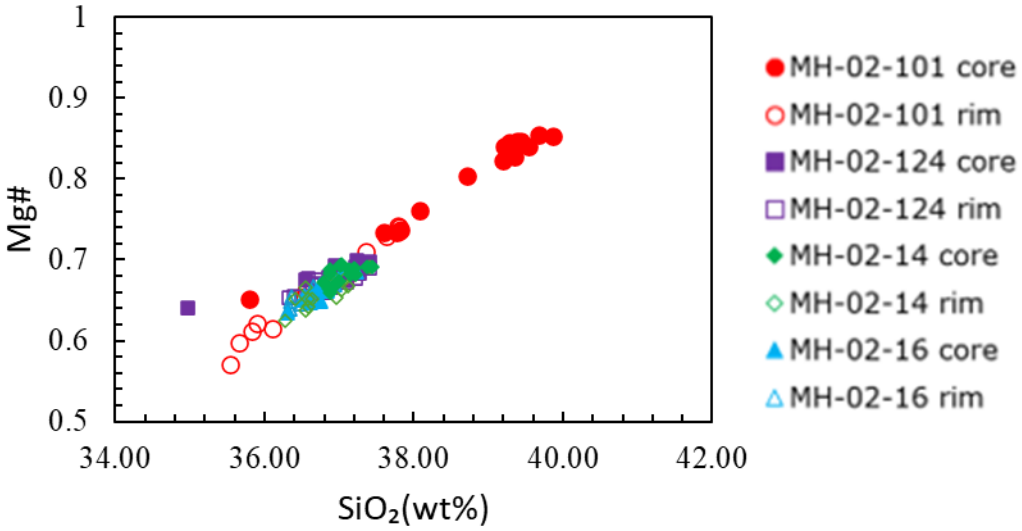

Fig. 11. Plots of SiO_2 vs Mg# in olivine phenocrysts.

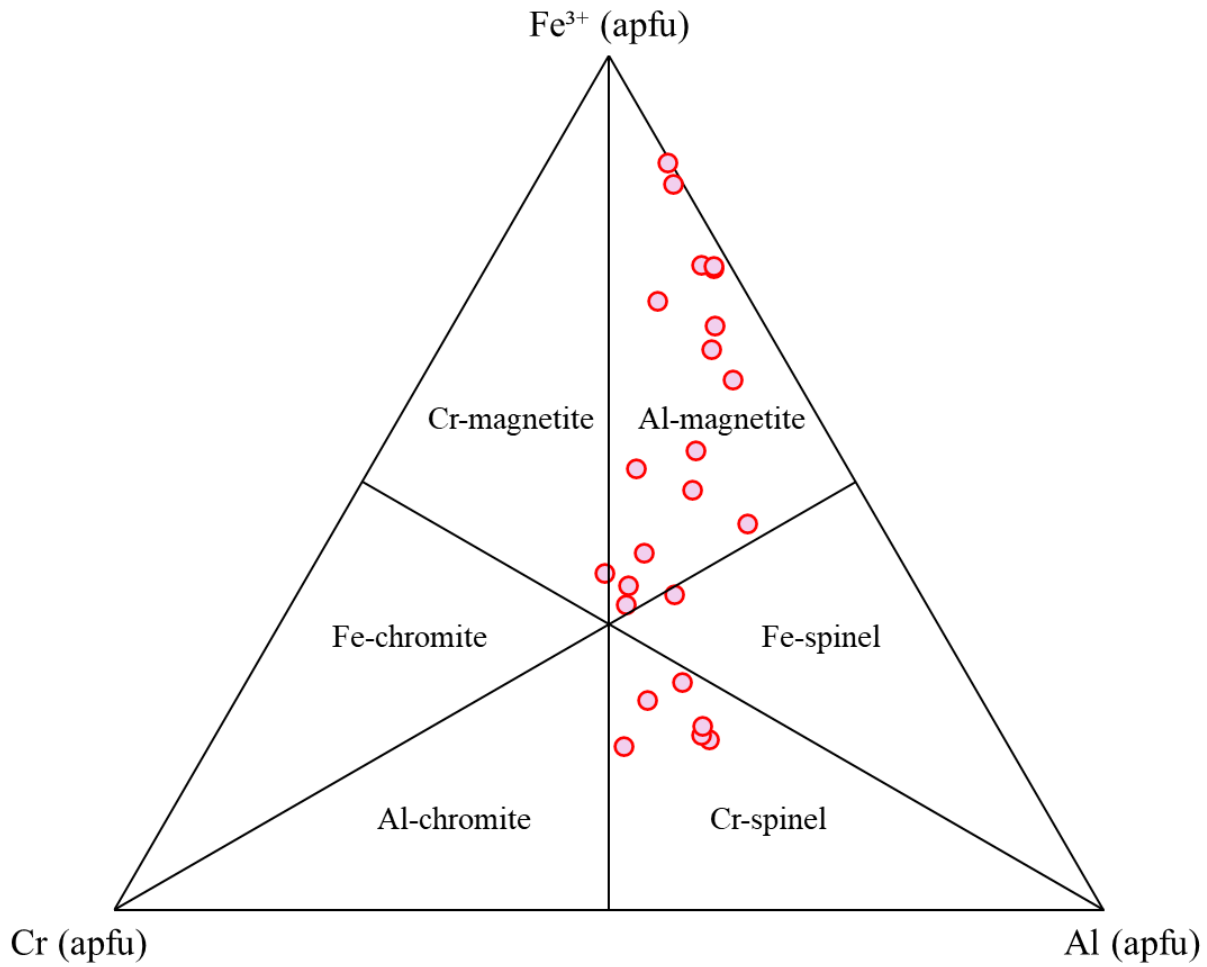

Fig. 12. Trivalent Cr-Al-Fe^{3+} ternary diagram (Stevens 1944) showing the composition of spinel inclusions in olivine phenocrysts. The apfu stands for atom per formula unit in the spinel structure.

the phenocrysts from sample MH-02-101 exhibit a wide range of rim and core compositions with a strong zoning pattern. Their magnesium numbers for the rims and cores range from 0.570 to 0.742 and 0.652 to 0.854, respectively (Fig.11).

The tiny spinel inclusions in the olivine phenocrysts are also analyzed with their mineral chemistry reported in Appendix A4. These spinel inclusions exhibit a wide range of compositions. The Cr, Al, and Fe^{3+} atoms per formula units (apfu) are calculated and plotted on a trivalent Cr-Al-Fe^{3+} ternary diagram (Fig.12) (Stevens 1944). The plot shows that the majority of the spinel inclusions are Al-magnetite, with a few Cr-spinel, Fe-spinel and Cr-magnetite present.

3.2 Olivine Trace Element Chemistry

The trace element composition of olivine grains from 28 samples was analyzed using LA-ICP-MS in seven sessions (Appendix B1). The MONG olivine standard (Batanova et al. 2019) was measured to verify the quality of results for Ca and Al - both important elements to the thermobarometry of the samples. The results for the MONG olivine standard in six sessions, gave Ca and Al results consistently 5 to 10% lower, but within uncertainty of the reference value (Appendix B4) (Batanova et al.2019). However, in the first LA-ICP-MS session, the MONG olivine standard results for Al and Ca results are 12 and 20 % lower than the preferred value (Appendix B1).

The results from each olivine analysis are plotted according to the equilibrium texture (Fig.13, Fig.15). The plot shows that all Llangorse olivines have Al content ranging from 18 to 58 ppm, except for sample MH-02-109, which has an Al above 80 ppm. Samples without sieve texture exhibit a narrow Ca concentration range, between 144 and 305 ppm except one analysis from MH-02-100 which has Ca concentration at 348 ppm, with each sample displaying uniform Ca compositions (Fig.13). However, samples with weak and strong sieve texture show

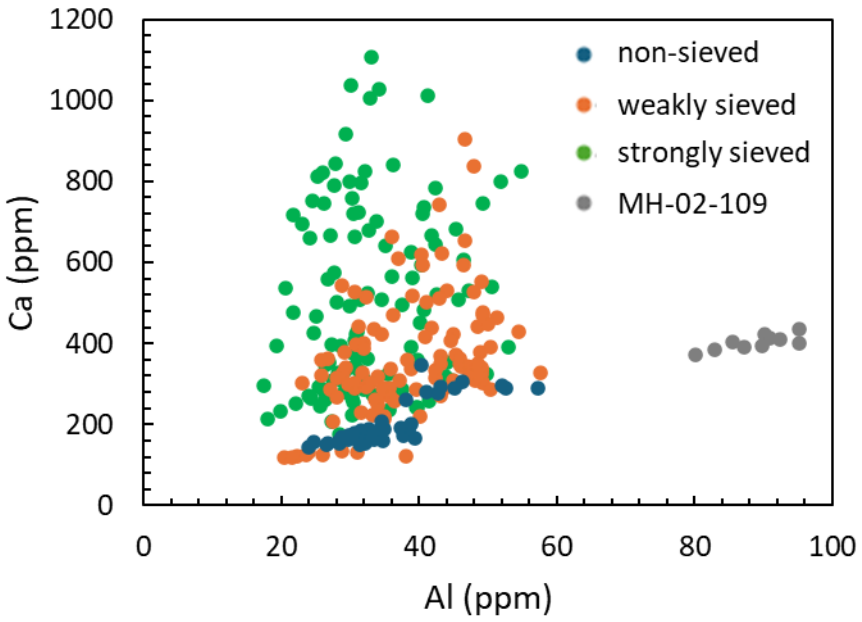

Fig. 13. Plot of Al vs Ca of all olivines based on their equilibrium texture.

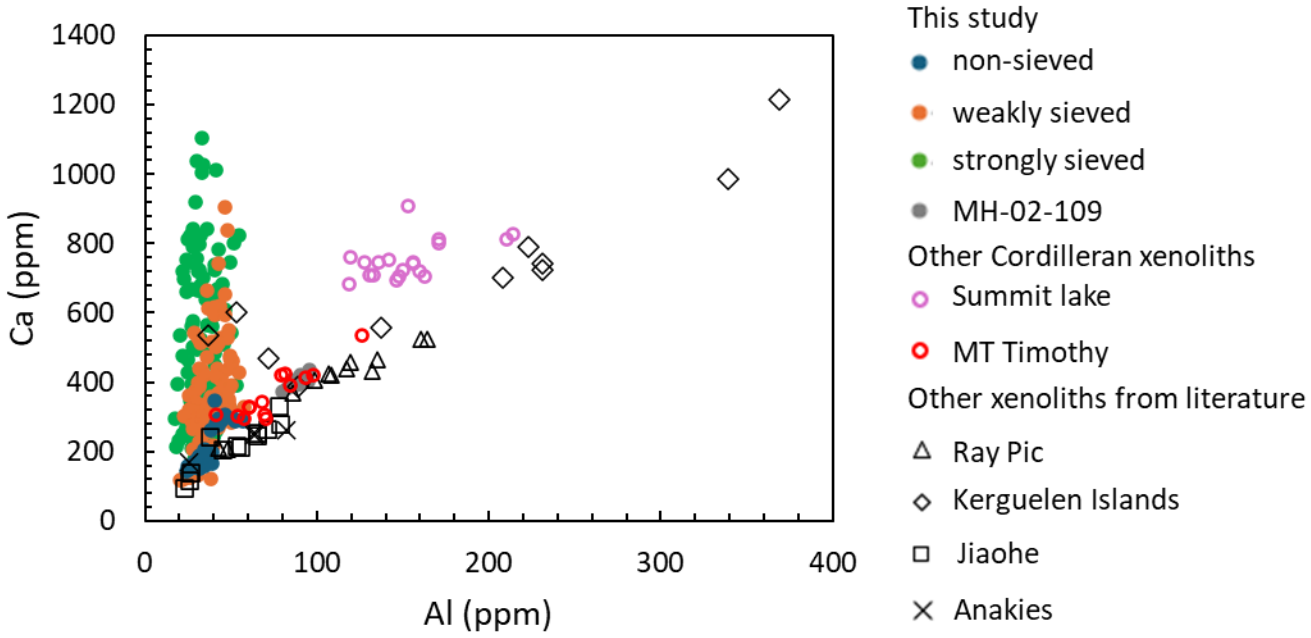

Fig. 14. Plot of Al vs Ca in each olivine trace element analysis based on their equilibrium texture. Open coloured symbols are published data for other Cordilleran xenoliths (Canil and Russell 2022) Open uncoloured symbols are from the literature (Gregoire et al. 2000; Mallmann et al. 2009; De Hoog et al. 2010; Lin et al. 2023).

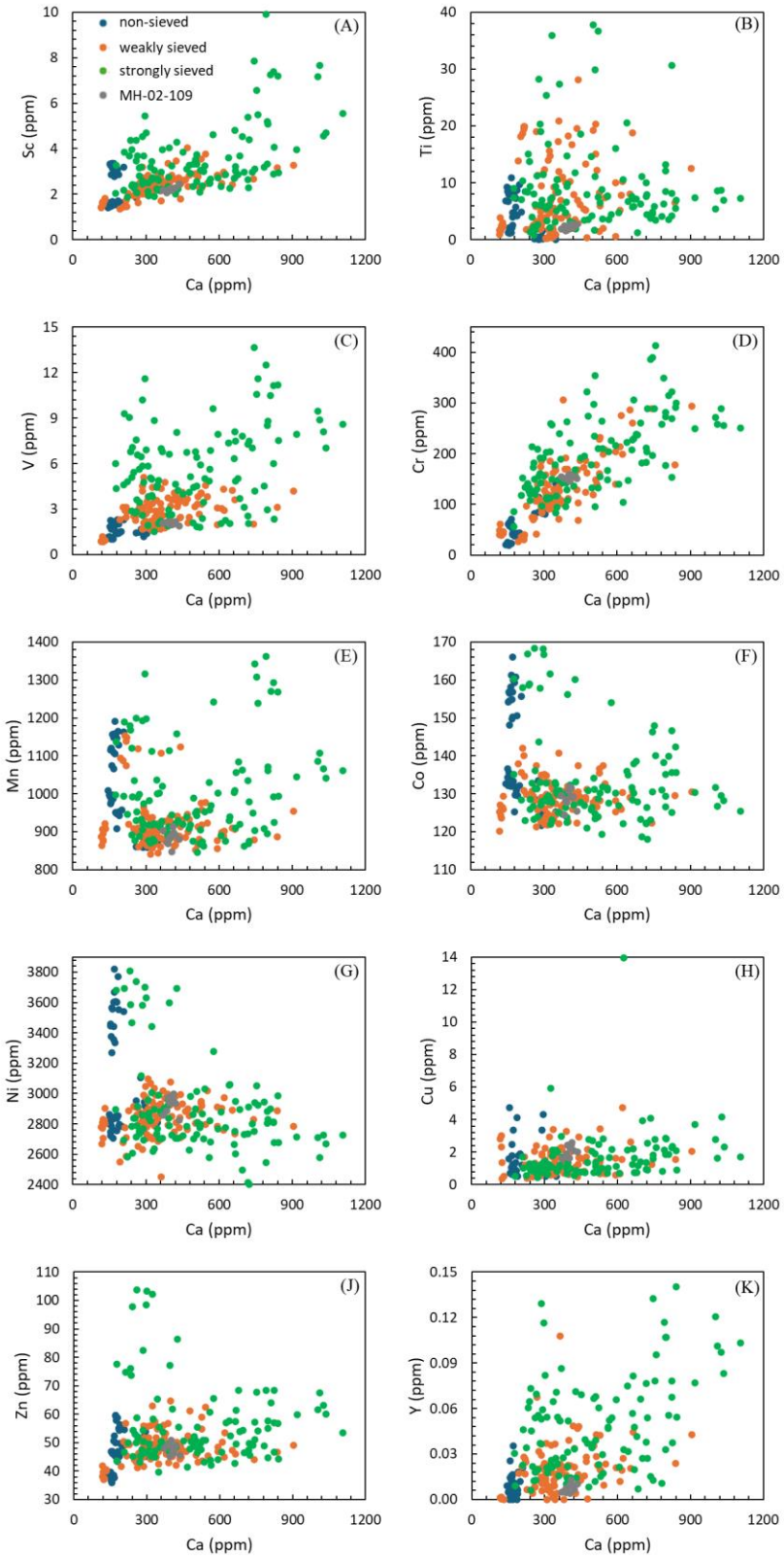

Fig. 15. Plot of Ca vs trace element in each olivine analysis based on their equilibrium texture.

significantly higher Ca concentrations, ranging from 117 to 905 ppm and 176 to 1106 ppm, respectively (Fig.13). Additionally, the Ca content in each sieved sample exhibits a wide concentration range (Appendix B1), and highly elevated Ca compared to other spinel peridotite xenoliths reported in literature (Fig.14). Based on the literature data, there is a positive and linear trend between Al and Ca; however, only the non sieved samples and a few analyses from sieved samples show this trend (Fig.14). In contrast, the Ca in most sieved samples shows a near vertical trend against Al (Fig.14). Figure 15 shows that Sc, Ti, V, Cr, and Y all have a strong positive correlation with Ca concentration, while other trace elements do not exhibit any significant correlation with Ca. Due to this positive correlation, sieved samples exhibit wider ranges of concentrations in Sc, Ti, V, Cr, and Y compared to non-sieved samples.

3.3 Zoning in Olivine

The zoning profiles for Ca and Al for olivine from the three different texture groups were measured using LA-ICP-MS with the results plotted in Figure 16 and Appendix E. No Al zoning is observed in any of the Llangorse olivine (Fig.16A, 16C, 16E). The non-sieved samples show no evidence of Ca zoning (Fig.16B). However, the samples with sieve textures display strong Ca zoning, characterized by significantly higher Ca concentration near the rim compared to the core (Fig.16D, 16F). Additionally, some smaller olivine grains show abnormally high Ca concentration in both the core and rim of the grains. When the laser intersects cracks in the grains, it yields abnormal peaks in the zoning profiles (Fig.16E, 16F).

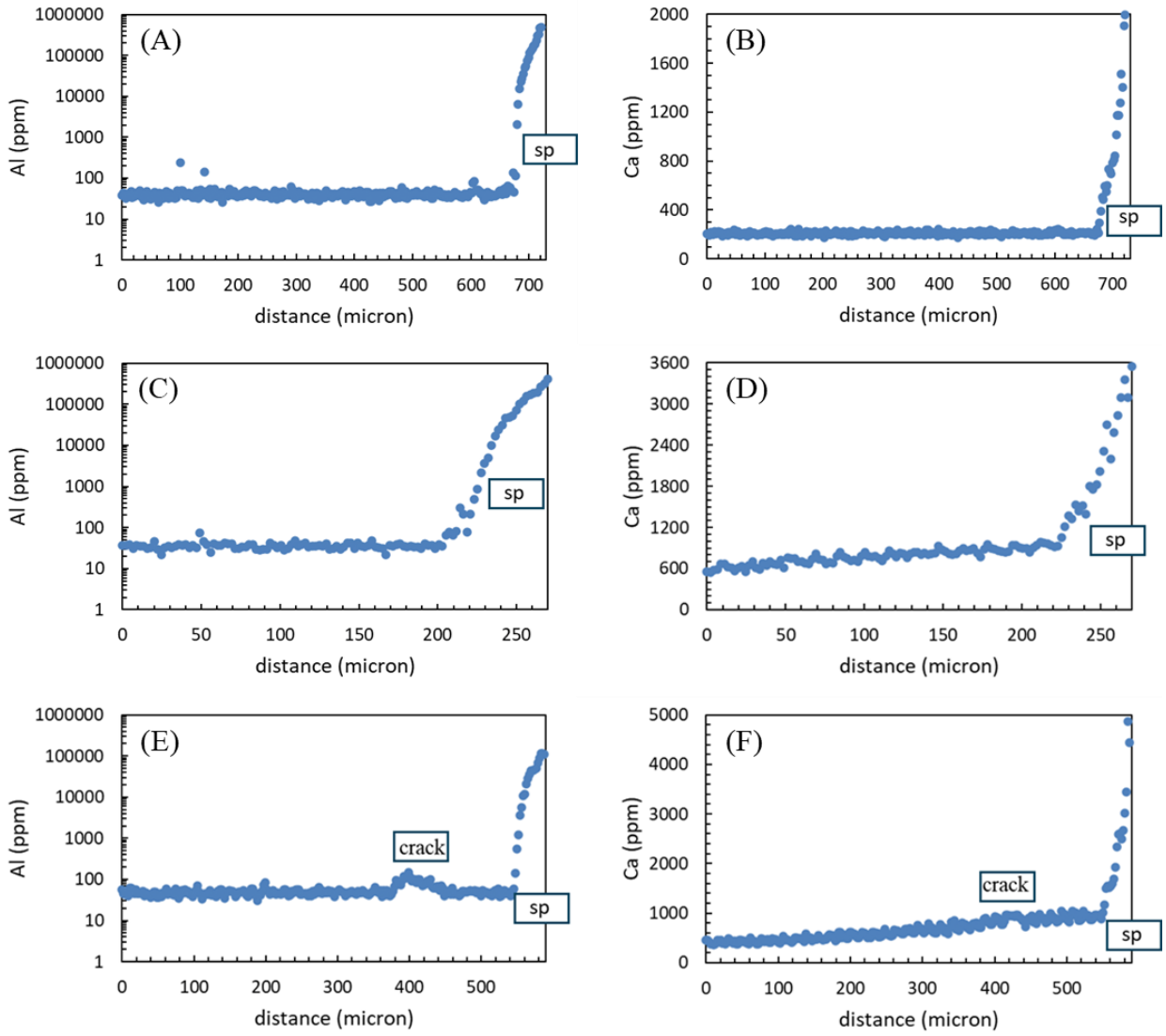

Fig. 16. Olivine Al and Ca zoning profiles. All the zoning profiles start from the core of the grains (0 micron) to the rim then into the adjacent spinel grain (hundreds micron). (A, B) Al and Ca zoning profiles of non-sieved sample MH-02-108. (C, D) Al and Ca zoning profiles of weakly sieved sample MH-02-100B showing strong Ca zoning. (E, F) Al and Ca zoning profiles of strongly sieved sample MH-02-18B showing strong Ca zoning.

3.4 Pyroxene Trace Element Chemistry

Trace and rare earth element compositions of pyroxenes in seven samples were analyzed using LA-ICP-MS in two sessions, with BCR2G glass used as an unknown to measure accuracy. The results on BCR2G standard agree with the reference values within 5%. All the pyroxene trace element data for pyroxenes are presented in Appendices B2, and B3. No significant intrasample REE variation is observed, and all the patterns are uniform. The average rare earth element (REE) abundances are chondrite-normalized (Sun and McDonough 1989) and plotted (Fig.17, 18) comparing with pyroxene compositions in spinel peridotites from other xenoliths in the northern Cordillera and other regions (Shi et al. 1998; Jean and Shervais 2017). Figure 17A shows that the cpx in harzburgite samples are strongly enriched in light rare earth element (LREE) (La between 20 to 79 times chondrite values). Two lherzolite samples (MH-02-10 and MH-02-108) display normal REE patterns with slight enrichment in all REE. The other two samples (MH-02-121 and MH-02-15) show a spoon-shape pattern with depleted LREE and slightly enriched heavy rare earth element (HREE). These cpx patterns are consistent with those observed in other Cordilleran mantle xenolith samples (Shi et al. 1998). The normalized La/Yb values for cpx in harzburgites are 66, 18, and 144. In comparison, the cpx in lherzolite has normalized La/Yb values between 0.0 and 0.1 Figure 18 shows that opx in harzburgites has relatively flat REE patterns. This flat pattern is similar to that of opx in enriched harzburgites reported in the literature (Jean and Shervais 2017). However, the opx in enriched harzburgites are less depleted in HREE compared to those from Llangorse. In contrast, the opx in lherzolite samples display the same pattern as opx from literature lherzolites (Jean and Shervais 2017), but with lower concentrations of LREE.

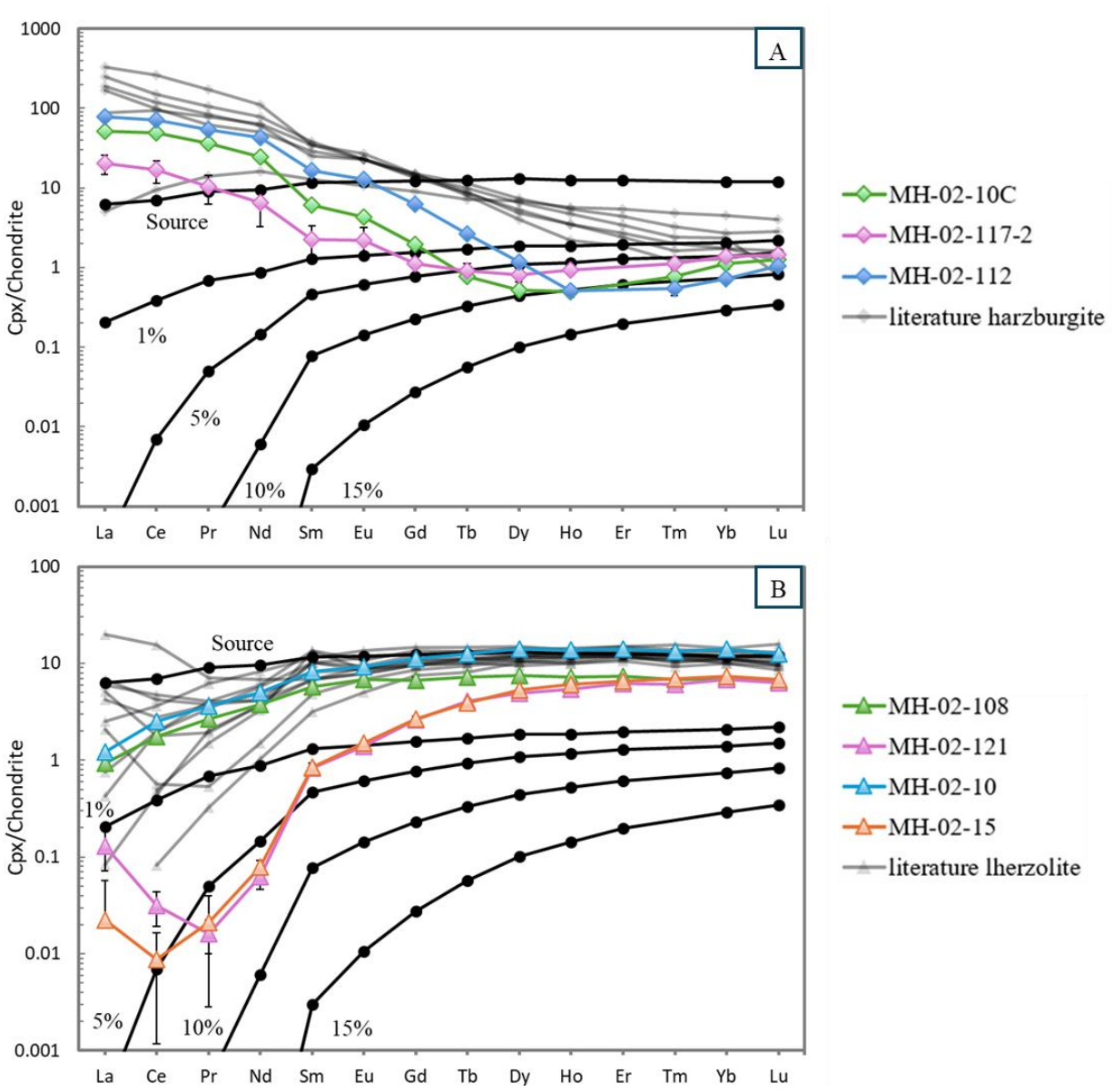

Fig. 17. Chondrite-normalized rare earth element (REE) diagrams for cpx from Llangorse harzburgite and lherzolite samples. Plots are averages of four to seven grains in each sample, with one standard deviation of the mean plotted as error bars. (A) Chondrite-normalized REE patterns for cpx in harzburgite samples. (B) Chondrite-normalized REE pattern for cpx in lherzolite samples. Literature data are from other Cordilleran xenolith localities (Shi et al. 1998). Black lines with circle symbols are residual cpx REE composition after (1, 5, 10, 15 %) partial melting from a depleted mantle cpx source REE composition. They are calculated using melting model and partition coefficients given in Warren (2016). Chondrite normalized values are from Sun and McDonough (1989).

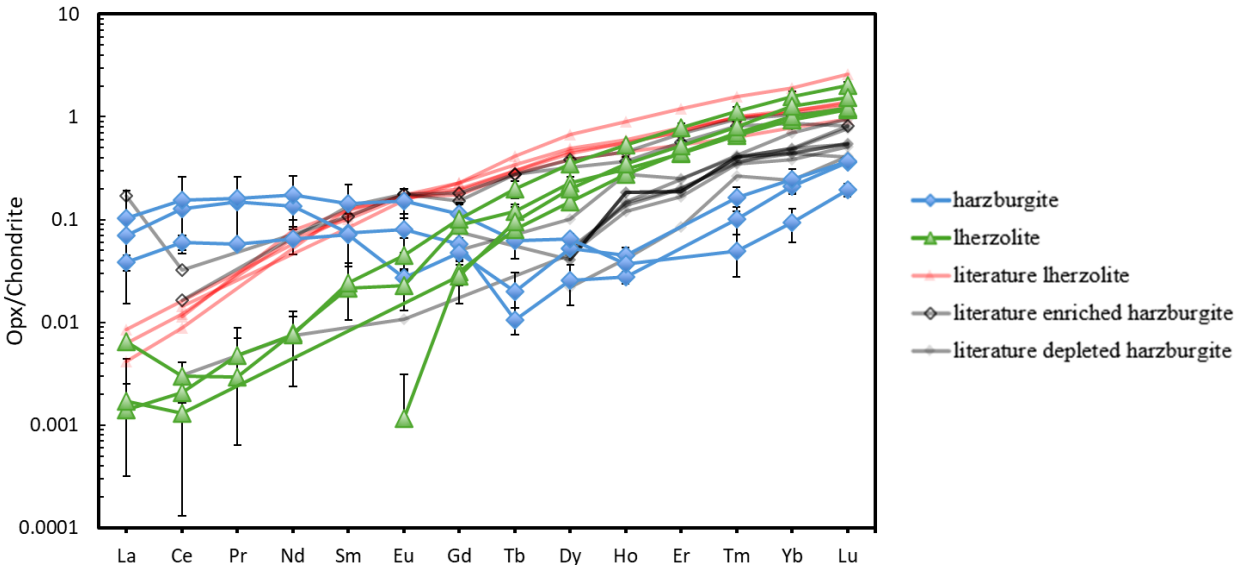

Fig. 18. Chondrite-normalized rare earth element (REE) diagrams for opx from Llangorse harzburgite and lherzolite samples. Plots are averages of three to six grains in each sample, with one standard deviation of the mean plotted as error bars. Literature data are from other spinel lherzolite and harzburgite within Coast Range ophiolite (Jean and Shervais 2017). Chondrite normalized values are from Sun and McDonough (1989).

CHAPTER 4: Geothermobarometry

4.1 Data Selection

The standard deviation of Al and Ca measurements for olivine in each xenolith sample are calculated and plotted in Figure 19. The results show that all non-sieved samples have small standard deviations, approximately 10%, this is within analytical uncertainty according to standards. However, the sieved samples exhibit much higher standard deviations for both Al and Ca in olivine. Despite this, the average Al concentrations in the sieved samples are likely still reliable, as their standard deviations remain within 15% for most samples. In contrast, the Ca standard deviations far exceed 20% in most sieved samples, indicating heterogeneity and strong zoning.

To obtain the P-T conditions of Llangorse xenolith samples, the major element compositions of olivine and spinel obtained in this study are combined with compositions of pyroxene, olivine and spinel reported by Harder and Russell (2006; unpublished) in thermobarometry calculations (T_{Al}, T_{FeMg}, T_{Ca}, T_{BKN}, T_{REE}, and P_{SC}). Since no major element zoning or intrasample variations are observed in the Llangorse xenolith samples, the average mineral compositions are used. For the non-sieved samples, MH-02-04 and MH-02-109, the average olivine major element compositions are coupled with the average of high precision Al and Ca measurements from LA-ICP-MS to calculate closure temperature (T_{Al} and T_{Ca}) and pressure (P_{SC} coupled with T_{Al}) conditions. However, for the samples with the sieve texture, the minimum Ca in olivine is used instead of the average, except MH-02-04 which has uniform Ca measurements. As discussed in section 3.3, the sieved samples exhibit strong Ca zoning, with lower concentrations in the core and abnormally high concentrations near the rim (Fig.16D, 16F). Ca in olivine is highly temperature-dependent; as the temperature increases, the Ca

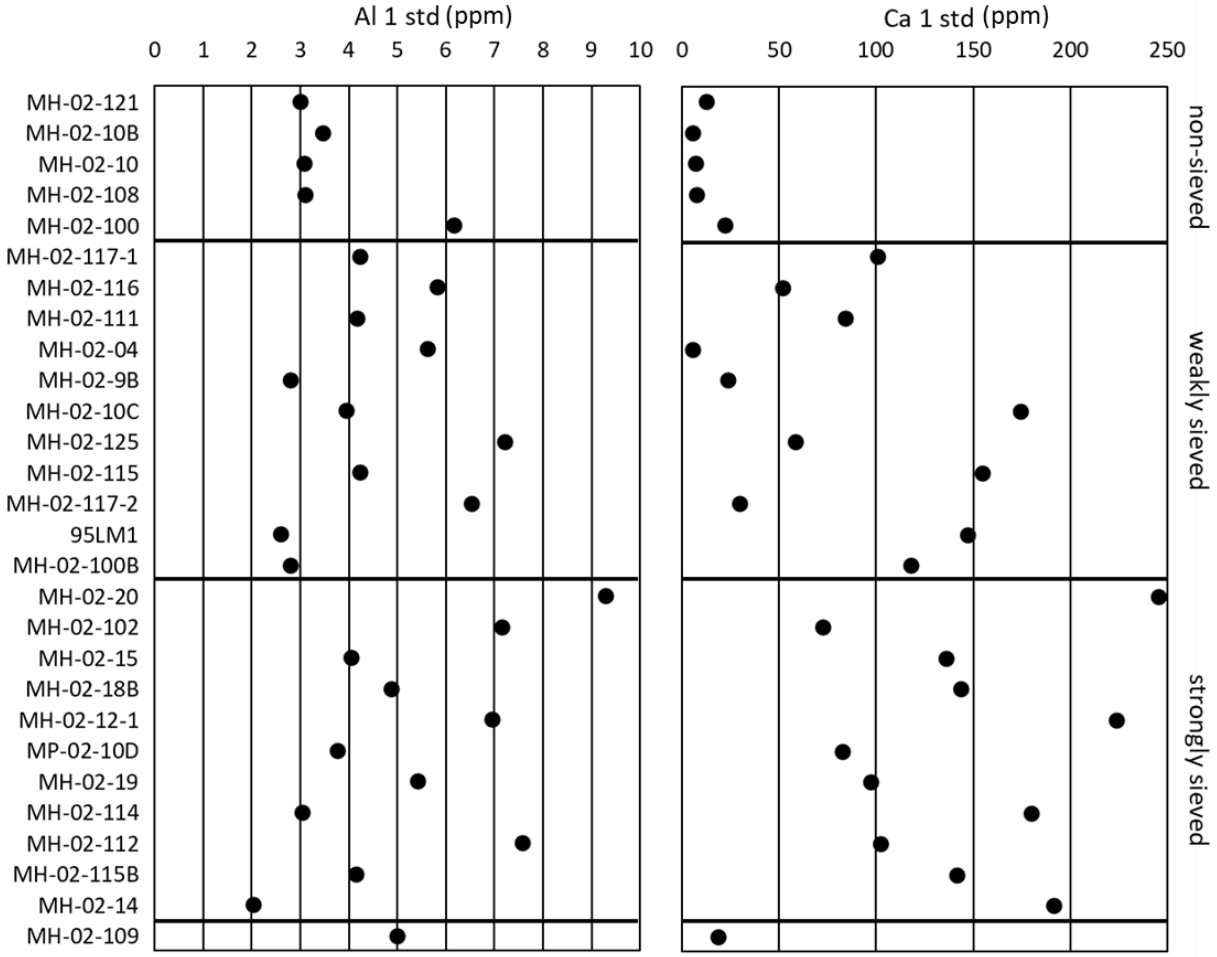

Fig. 19. Plot of Al and Ca 1 standard deviations in ppm for each sample.

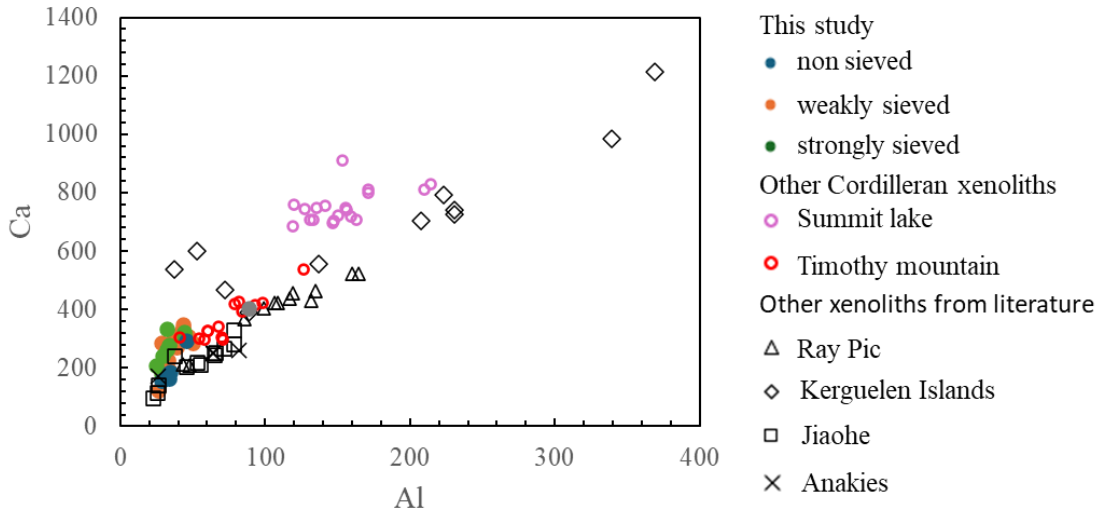

Fig. 20. Plot of average ppm Al vs selected Ca in each Llangorse sample based on their equilibrium texture. Hollow symbols are published data for xenoliths from elsewhere in the Cordillera (Canil and Russell 2022) and worldwide (Gregoire et al. 2000; Mallmann et al. 2009; De Hoog et al. 2010; Lin et al. 2023).

concentration rises correspondingly (Shejwalkar and Coogan 2013). Due to the relatively high diffusivity of Ca and its sensitivity to temperature, these samples were likely affected by later thermal events, resulting in abnormally high Ca in olivine, as is discussed further below in Section 5.3. The core of the olivine which is farther from grain boundaries is less affected by diffusion and is more likely to record the T or P conditions before later thermal events. As the cores consistently show lower Ca concentration, the lowest Ca values in olivine is more likely to record the maximum pressure, before any thermal resetting.

Figure 20 shows the average Al and selected Ca in olivine compared with literature data. When using the minimum Ca in sieved samples, all Llangorse samples now align with the positive linear Al-Ca trend observed in the literature data (Fig.20). Both Ca and Al in olivine are temperature dependent, meaning that as temperature increases, their concentrations increase as well, explaining the positive correlation exhibited in Figure 20.

4.2 Geothermometry

As discussed in section 1.5.2, five geothermometers (T_{Al}, T_{Ca}, T_{FeMg}, T_{BKN}, and T_{REE}) are used to calculate the equilibrium temperatures for the xenoliths (Table. 3) and compared with petrographic textures and lithology (Fig. 21, 22). T_{Al} which is based on Al exchange between olivine and spinel, yield the narrowest range of temperatures between 829 ºC and 941 ºC with an uncertainty of ± 20 ºC based on calibration uncertainty, except for sample MH-02-109 which reached 1022 ºC. T_{Ca} which is based on Ca exchange between olivine and cpx, also have a narrow temperature range between 837 ºC and 969 ºC with an uncertainty of ± 20 ºC. In comparison the other olivine major element thermometer T_{FeMg}, based on Fe and Mg exchange between olivine and spinel, records the highest and widest range of temperatures, from 982 ºC to 1272 ºC. For this study, I have recalculated T_{BKN} at an assumed pressure of 15 kbar,

Table 3. Geothermobarometry results for all samples. All the temperatures are reported in °C. Both T_{Al} and T_{Ca} habe inherent uncertainty ± 20 °C, and T_{BKN} has inherent uncertainty ± 15 °C. The P_{Sc} is reported in kbar and depth is reported in km. P_{Sc} mean are calculated by using average Ca. P_{Sc} preferred are calculated using average Ca for non-sieved samples, MH-02-04, and MH-02-109, and minimum Ca for sieved samples.

Sample Names	Rock Type	texture	TAl	TFeMg	TCa	TBKN	TREE	uncertainty (±1σ)	PSC (mean)	depth(mean)	PSC (preferred)	Depth (preferred)
MH-02-121	lherzolite	no sieve	860	1063	875	853	897	34	13	39	13	39
MH-02-10B	lherzolite	no sieve	867	1025	865	811			17	54	17	54
MH-02-10	lherzolite	no sieve	842	1098	857	904	847	27	14	43	14	43
MH-02-108	lherzolite	no sieve	868	1016	876	906	890	45	14	44	14	44
MH-02-100	harzburgite	no sieve	932	1078	931	939			13	40	13	40
MH-02-117-1	lherzolite	weakly sieve	925	1125	951	956			-2	-10	7	20
MH-02-116	lherzolite	weakly sieve	914	1134	933	971			4	10	9	27
MH-02-111	lherzolite	weakly sieve	858	1211	875	948			3	8	12	36
MH-02-04	lherzolite	weakly sieve	846	982	837	859			21	65	21	65
MH-02-9B	harzburgite	weakly sieve	888	1120	928	913			2	5	5	14
MH-02-10C	harzburgite	weakly sieve	936	1122	928	948	1039	29	-3	-10	15	46
MH-02-125	harzburgite	weakly sieve	914	1114	942	952			3	6	7	20
MH-02-115	harzburgite	weakly sieve	924	1144	948	930			-6	-22	7	22
MH-02-117-2	harzburgite	weakly sieve	908	1112	921	958	1084	94	7	22	11	33
95LM1	harzburgite	weakly sieve	941	1162	938	909			5	13	13	41
MH-02-100B		weakly sieve	882	1073	901				-1	-4	11	32
MH-02-20	lherzolite	strongly sieve	860	1272	870	918			-20	-65	14	43
MH-02-102	lherzolite	strongly sieve	840	1158	872	892			-5	-16	9	28
MH-02-15	lherzolite	strongly sieve	857	1154	916	912	933	13	-15	-51	1	2
MH-02-18B	lherzolite	strongly sieve	923	1105	945	1004			-11	-37	8	23
MH-02-12-1	lherzolite	strongly sieve				953						
MP-02-10D	lherzolite	strongly sieve				931						
MH-02-19	harzburgite	strongly sieve	894	1145	925	946			-3	-10	7	21
MH-02-114	harzburgite	strongly sieve	898	1195	947	952			-14	-47	2	6
MH-02-112	harzburgite	strongly sieve	884	1155	910	997	949	33	-1	-7	9	27
MH-02-115B	harzburgite	strongly sieve	923	1136	938	938			-3	-13	10	30
MH-02-14		strongly sieve	829	1233	887				-15	-51	2	5
MH-02-109	lherzolite		1022	1127	969	1064			20	63	20	63

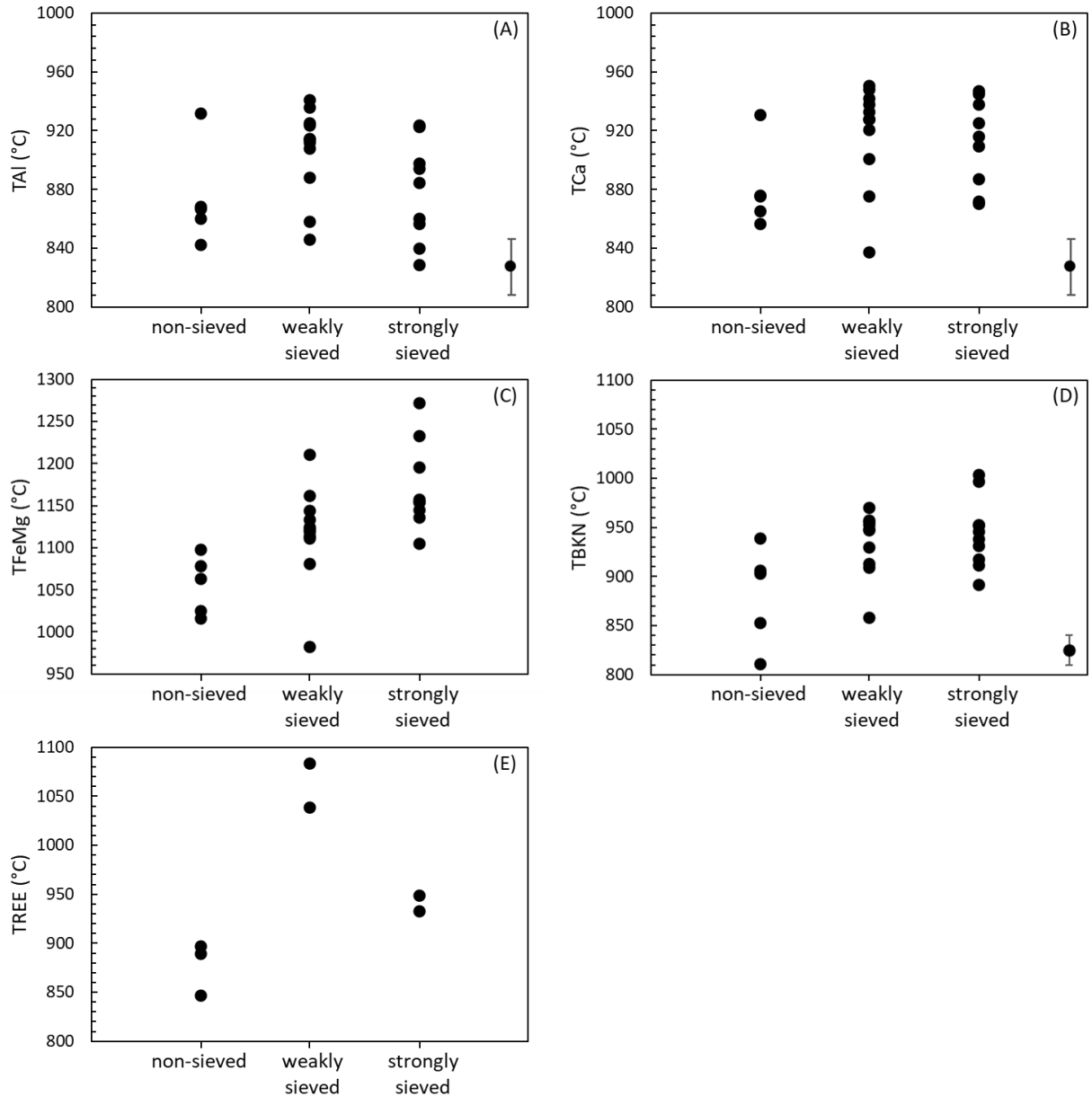

Fig. 21. Plot comparing various temperatures with the petrographic textures in samples. (A) T_{Al}. (B) T_{Ca}. (C) T_{FeMg}. (D) T_{BKN} at 15 kbar. (E) T_{REE} at 15 kbar.

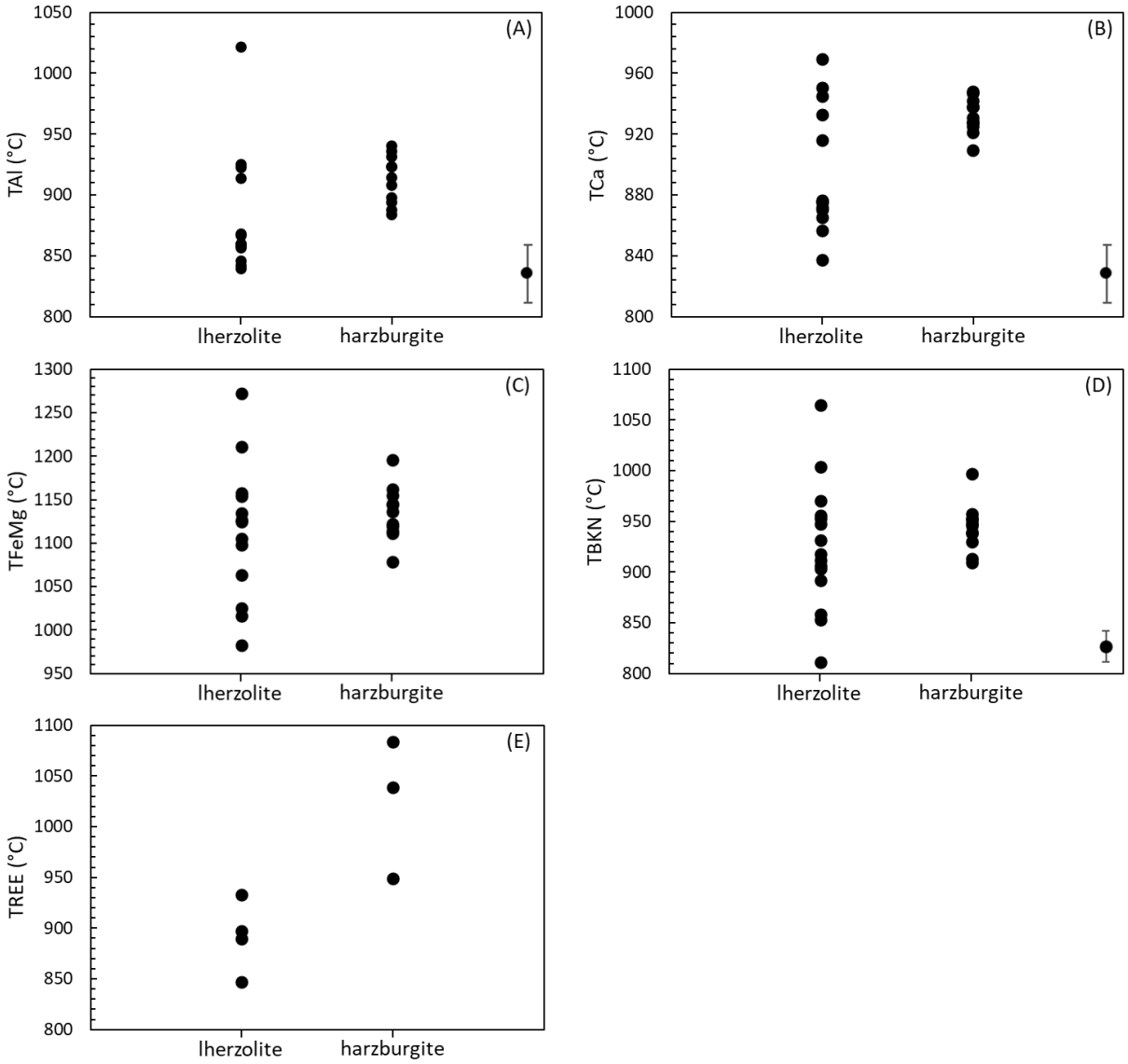

Fig. 22. Plot comparing calculated temperatures with lithology. (A) T_{Al}. (B) T_{Ca}. (B) T_{FeMg}. (C) T_{BKN} result at 15 kbar. (D) T_{REE} at 15 kbar.

corresponding to the median depth of Cordilleran mantle lithosphere (Harder and Russell 2006), resulting in temperatures between 811 ºC and 1004 ºC, with the exception of MH-02-109 which is 1064 ºC. The T_{BKN} thermometer has an inherent uncertainty of ± 15 ºC. These values are generally consistent with Harder and Russell (2006) who calculated the T_{BKN} at 12 kbar. The average REE concentrations in coexisting cpx and opx from seven samples are used to calculate the T_{REE} temperature based on REE exchange between cpx and opx, which range from 847 ºC to 1084 ºC. Most results obtained from T_{REE} thermometer have uncertainties ranging between 13 ºC and 45 ºC; however the sample with the highest TREE value of 1084 ºC has a large standard error at ± 94 ºC.

Among the five thermometers, T_{FeMg} consistently yields the highest temperatures for each sample, 100 to 200 ºC higher than the other thermometers (Fig.23D). This discrepancy exceeds the normal uncertainty expected from geothermometers. T_{Al}, T_{Ca}, and T_{REE} are positively correlated with the T_{BKN} (Fig.23). In most samples, T_{BKN} is 10 to 60 degrees higher than both T_{Al} and T_{Ca} (Fig.23A, 23B). For five samples, T_{REE} and T_{BKN} temperatures are similar, while in the remaining two samples, T_{REE} estimates are significantly higher than those from T_{BKN} (Fig.23C). In general, Al has lower diffusivity in olivine compared to Ca and higher closure temperatures, so T_{Al} is expected to record a higher temperature than T_{Ca}, but this is not observed in Llangorse xenoliths. In fact, T_{Ca} is tens of degrees higher than T_{Al}. This discrepancy might suggest that T_{Ca} is recording a heating (not cooling) temperature.

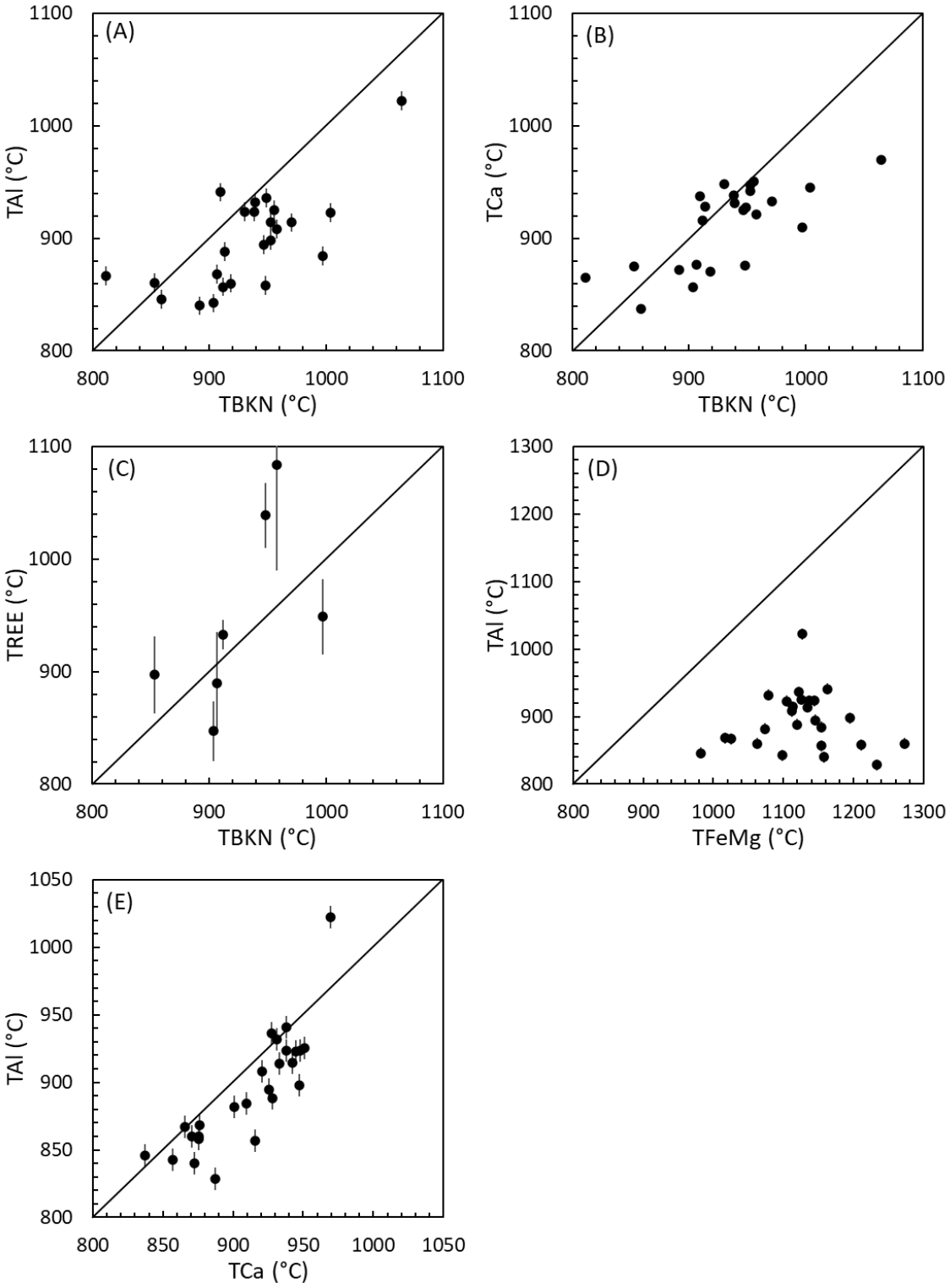

Fig. 23. Plot of difference between temperature estimates among all five geothermometers. (A) T_{Al} vs T_{BKN}. (B) T_{Ca} vs T_{BKN}. (C) T_{REE} vs T_{BKN}. (D) T_{Al} vs T_{FeMg}. (D) T_{Al} vs T_{Ca}. Error bars for T_{Al} are calculated using 1 standard deviation of Al and Ca concentration. Error bars for T_{REE} are derived from the REE inversions (Liang et al. 2013).

Figure 21 shows that temperatures from three of the thermometers (T_{FeMg}, T_{BKN}, and T_{REE}) are strongly correlated with the degree of sieved texture, whereas the T_{Al} and T_{Ca} show no correlation with textures. For both T_{FeMg} and T_{BKN}, the non-sieved samples consistently record the lowest temperatures, while strongly sieved samples have the highest (Fig.21C, 21D). Specifically, T_{FeMg} varies from 1016 ºC to 1098 ºC for non-sieved samples, 1082 ºC to 1211 ºC for weakly sieved samples, and 1105 ºC to 1272 ºC for strongly sieved samples (Fig.21C). However, there is one outlier, MH-02-04, with the lowest temperature of 982 ºC. Texturally, MH-02-04 is in the transition state between non-sieved and sieved samples. Unlike other weakly sieved samples, MH-02-04 has uniform Ca across olivine, and most of the sample is texturally non-sieved at the thin section scale. However, a portion of the sample has weakly sieved rims less than ten micron thick, so it has been grouped with the weakly sieved samples.

The T_{REE} results present an unusual pattern (Fig.21E). Weakly sieved samples show the highest temperature estimates at 1039 ºC and 1084 ºC, significantly higher than both the non-sieved and strongly sieved groups. In comparison, the non-sieved samples are coldest and vary from 847 ºC to 897 ºC and the two strongly sieved samples are at 933 ºC and 949 ºC. Note however only one third of the samples have been examined for T_{REE}, and so its trend with texture is less defined than the other thermometers.

Figure 22 suggests a correlation between temperature and lithology. Temperatures from four of the thermometers (T_{Al}, T_{Ca}, T_{FeMg}, and T_{BKN}) show a wider range for lherzolites, than for harzburgites. Additionally, the lower temperature results are only observed in lherzolite samples. This variation is likely due to the sample size, as 15 lherzolite samples and 11 harzburgite samples were used in thermometry calculations. Alternatively, it is possible that the harzburgite samples originate from a lower part of the mantle lithosphere, whereas lherzolite

samples are distributed throughout the entire mantle lithosphere. However, the harzburgites record much higher T_{REE} temperatures than lherzolites (Fig.22E), but this is based on a small sample size of only 7 of the 26 rocks studied.

4.3 Geobarometry

The equilibrium pressures of the Llangorse samples are directly calculated using the P_{SC} barometer based on Ca exchange between olivine and cpx. As discussed in section 1.5.2, the P_{Sc} is best paired with T_{Al} to achieve a more precise estimate because Al has relatively slow diffusivity in olivine and thus T_{Al} is least affected by heating and development of sieved textures. The results are reported in Table 3 and plotted in Figure 24 and 25 which show two ways in which Ca in olivine was used to calculate P_{Sc}. The 'preferred' P_{SC} values are calculated using the average Ca for non-sieved samples, MH-02-04, and MH-02-109, and minimum Ca for any samples with sieved textures. The 'mean' P_{SC} values are calculated using average Ca in olivine for all the samples.

In what follows the calculated P_{SC} was converted to depth using the equation 1.

$$\text{Depth} = \text{Depth}_{\text{Moho}} + ((P/10 - P_{\text{Moho}}) * 1000000) / \rho g. \qquad \text{Equation 1}$$

Where depth of Moho is assumed to be 33 km, P_{Moho} is 1.1 GPa, and ρ (mantle density) is 3200 kg/m³. When using the average Ca for the sieved samples, the results produce some geologically unrealistic outcomes. All the strongly sieved samples yielded negative pressures, and most weakly sieved xenoliths record depths shallower than 33 km, above the Moho of the Llangorse region (Table 3) (Audet et al. 2020). In contrast, by using the average Ca, non-sieved samples produce more realistic depths from 39 km to 54 km, which are below the Moho (Fig.24). The non-sieved samples, MH-02-04 and MH-02-109 also produce reasonable depths at 65 km and 63 km.

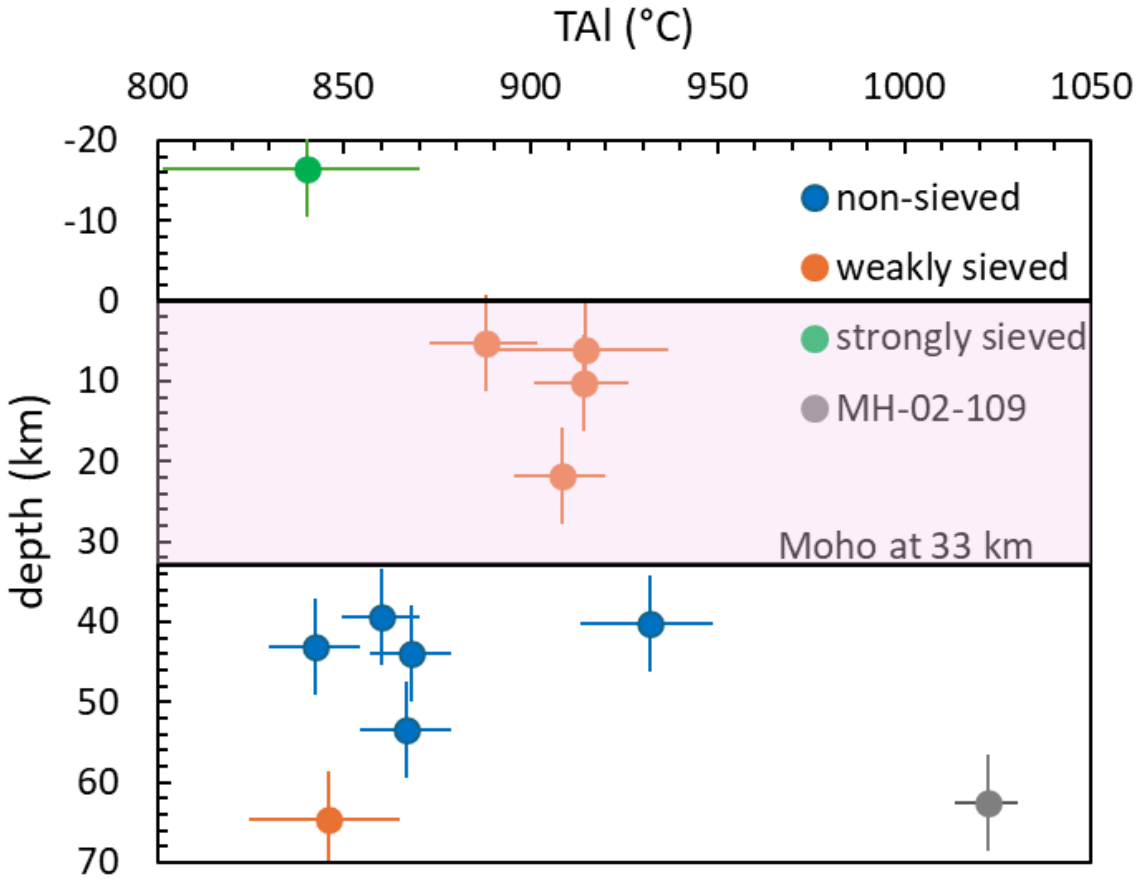

Fig. 24. Plot of filtered 'mean' depth in km vs T_{Al} in degrees. The Moho depth is at 33 km (Audet et al. 2019). Samples with Ca standard deviation above 80 ppm are filtered out. Horizontal error bars are calculated T_{Al} uncertainties using Al 1 standard deviation. Error bars are uncertainty in experimental calibration (± 1.5 kbar) for the P_{SC} barometer.

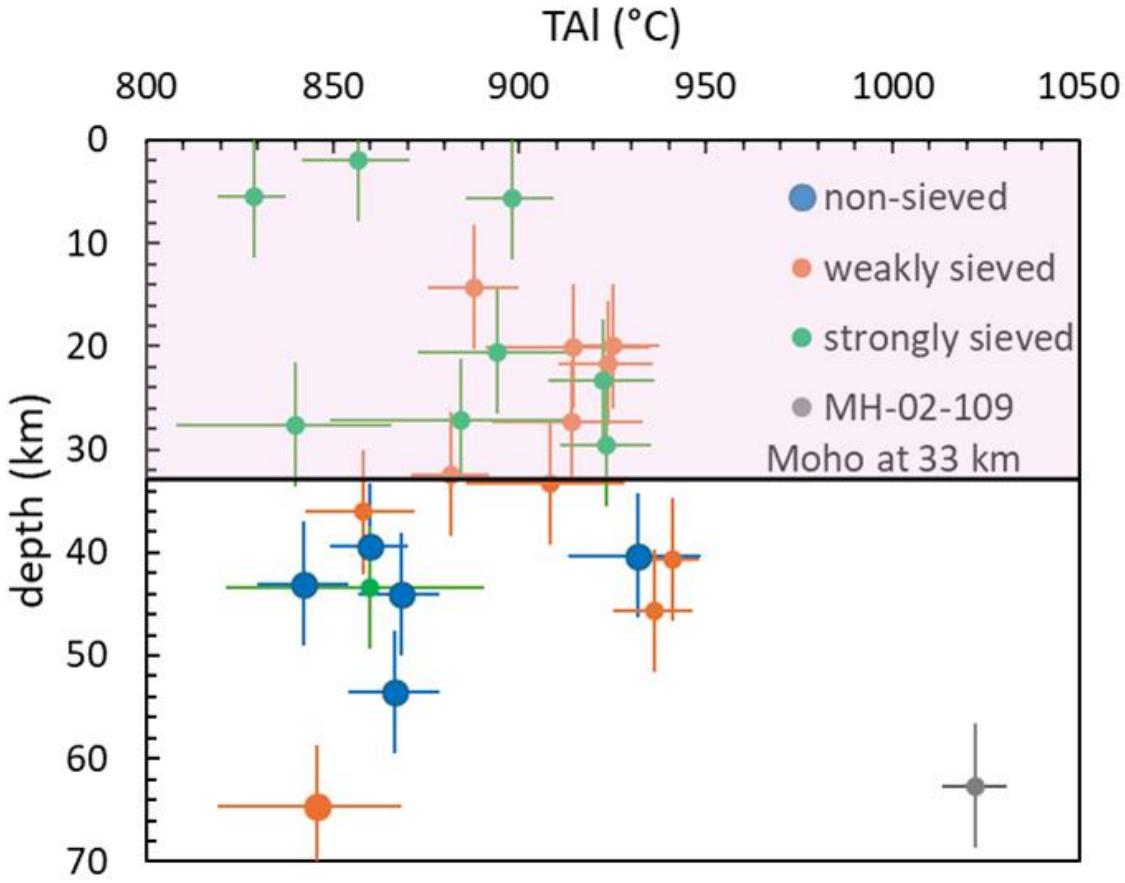

Fig. 25. Plot of preferred depth in km vs T_{Al} in degrees. The Moho depth is at 33 km (Audet et al. 2019). Horizontal error bars are calculated T_{Al} uncertainties using 1 standard deviation for Al in olivine. Error bars are uncertainty in experimental calibration (± 1.5 kbar) for the P_{SC} barometer.

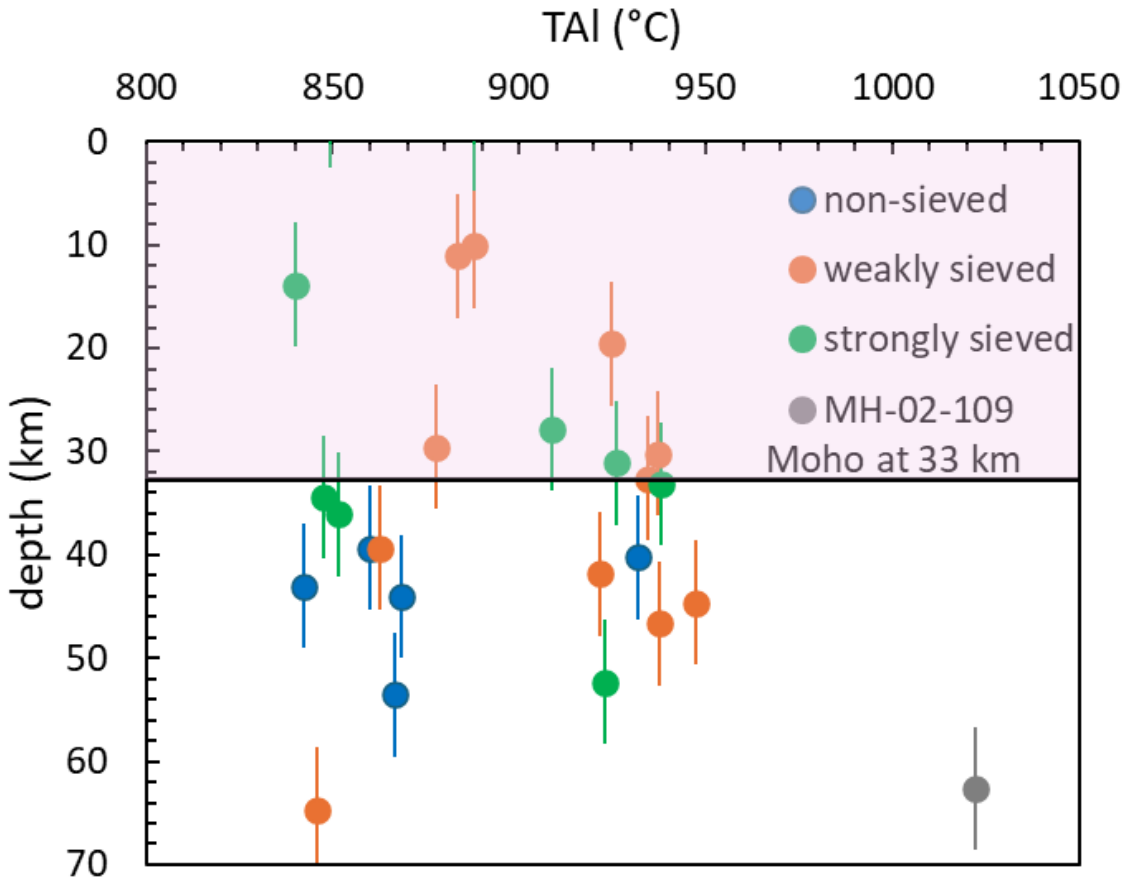

Fig. 26. Plot of depth (km) vs T_{Al} in °C for xenolith samples. The T_{Al} temperature and depth are calculated using minimum Ca and selected Al in olivine. The Moho depth is at 33 km (Audet et al. 2019). Error bars are uncertainty in experimental calibration (± 1.5 kbar) for the P_{SC} barometer. Only samples giving positive depths are plotted (two strongly sieved samples are excluded from this plot).

Figure 25 shows that by using the minimum Ca in olivine (instead of the average) for the sieved samples, more than half of the weakly sieved samples yield realistic results from 33 km to 54 km, and the remaining samples are near the Moho depth, between 14 km and 27 km. Additionally, all strongly sieved samples now have positive pressures. However, most strong sieved samples still record depths above the Moho with depths ranging from 2 km to 30 km, except one at 43 km.

Figure 25 also shows that some of the sieved samples exhibit large uncertainties in T_{Al} which was calculated based on 1 standard deviation. These uncertainties could be inherent to the P_{SC} calculation and may cause huge differences in pressure estimates due to the strong temperature dependence of P_{SC}. To minimize this impact, the temperatures and pressure are recalculated using the Al measurement from the grain with the lowest Ca (instead of the average Al). The results are presented in Figure.26. With this adjustment, and accounting for the uncertainties, all but six of the Llangorse samples have realistic depth estimates below the Moho.

4.4 Host Lava Temperature

The host lava temperatures are calculated using the olivine-melt thermometers T_{Mg}, based on Mg partitioning $D_{Mg}^{Ol/liq}$ (Putirka 2008), and T_{Ni}, based on Ni partitioning $D_{Ni}^{Ol/liq}$ (Pu et al. 2017). Individual olivine phenocryst core and rim analyses from this study, along with whole rock chemistry data from Harder et al. (2003) and Abraham et al. (2001) are used in the T_{Mg} and T_{Ni} calculations, respectively. According to Roeder and Emslie (1970), only the olivine phenocrysts with Fe-Mg partitioning distribution coefficient (K_D) values of 0.30 ± 0.03 are in equilibrium with the melt. K_D is calculated using Equation 2.

$$K_D = \frac{(X_{FeO}^{Ol})(X_{MgO}^{melt})}{(X_{FeO}^{melt})(X_{MgO}^{Ol})} \qquad \text{Equation 2}$$

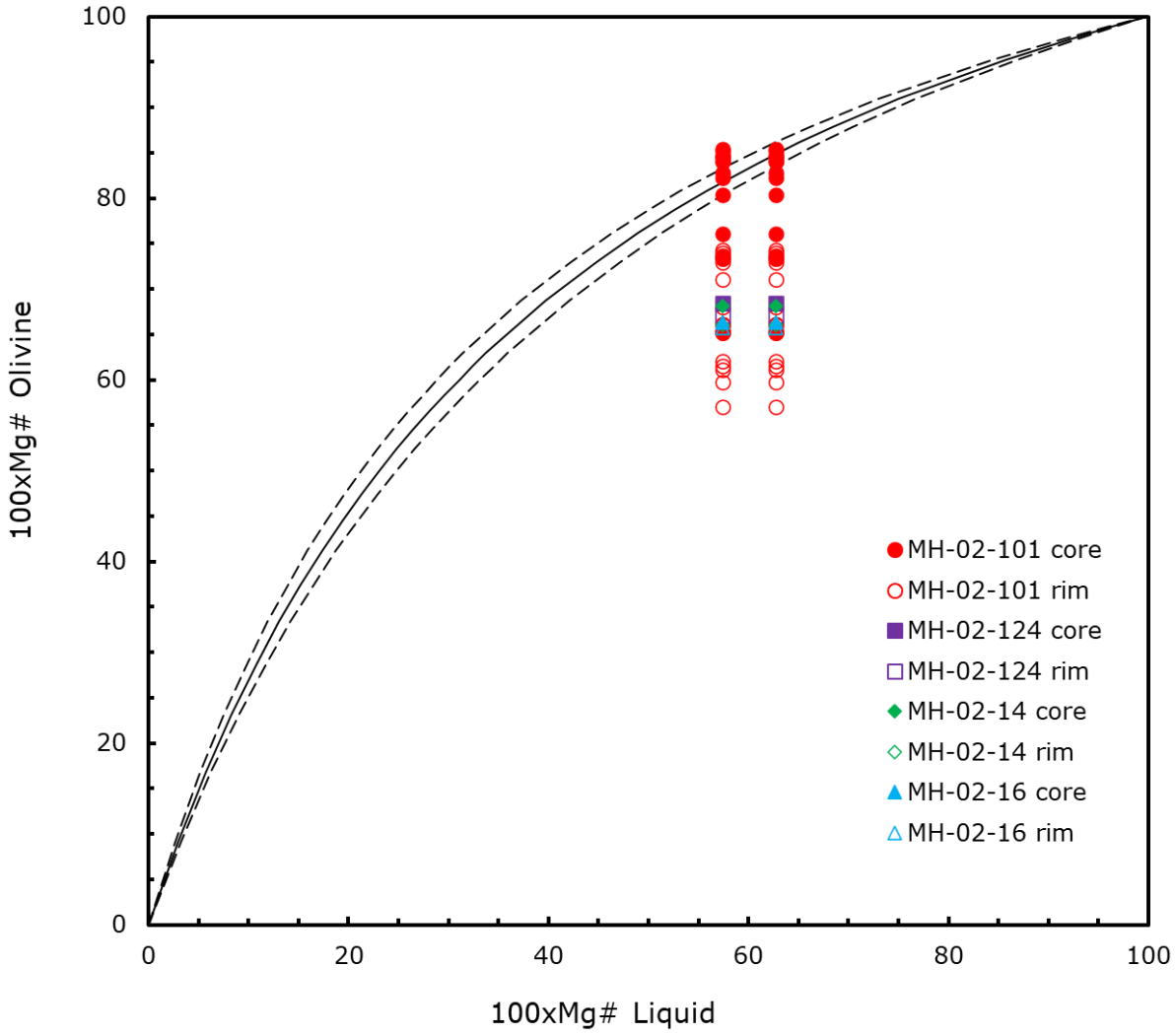

Fig. 27. Rhodes diagram (Dungan et al. 1978; Rhodes et al. 1979) showing the Mg# of olivine phenocryst cores and rims vs Mg# of liquid from melt (Abraham et al. 2001; Harder et al. 2003). Only the sample compositions within the dashed lines are in equilibrium with the melt.

Phenocrysts that are not in equilibrium with the melt (bulk rock) are filtered out using the Rhodes diagram, which compares the Mg# in liquid from melt and Mg# in olivine phenocryst to check if they achieve the equilibrium K_D value (Dungan et al. 1978; Rhodes et al. 1979). The Rhodes diagram shows that only some of the phenocryst core compositions from sample MH-02-101 are in equilibrium with the melts (Fig.27).

For T_{Mg}, temperatures are calculated assuming 0 wt % H_2O in the melt at surface pressure, yielding results between 1278 and 1302 °C (Table.4). With 1 wt % H_2O, the temperatures decrease by approximately 24 °C, ranging from 1254 to 1278 °C (Table.4). A further increase in H_2O concentration to 2 wt % lowers the temperatures to 1232 to 1255 °C (Table.4). If the pressure increases to 15 kbar with no H_2O present, resulting temperatures will rise by 80 °C, ranging from 1358 to 1383 °C (Table.4).

Temperatures calculated using the T_{Ni} thermometer range between 1275 and 1293 °C (Table.4). A recent study by Pu et al. (2017) suggests that T_{Mg} is more sensitive to H_2O concentration in the melt; if H_2O is present, T_{Mg} tends to overestimate the temperatures. In contrast, T_{Ni} is less sensitive to H_2O contents, meaning that the difference between T_{Ni} and T_{Mg} can be used to determine whether the melt is anhydrous (Pu et al. 2017). Specifically, if T_{Ni} - T_{Mg} is positive or zero, the melt is considered anhydrous, if negative, then it indicates the presence of water (Pu et al. 2017). These T_{Ni} temperatures are very close to the T_{Mg} temperatures which are 4 and 13 °C higher or 3 °C lower than T_{Mg} (Table.4), suggesting that the melt is anhydrous or very trace amounts of H_2O (<1 wt%) are present (Pu et al. 2017).

The host lava temperatures are also calculated using the olivine-spinel major element thermometer T_{FeMg}. Individual spinel inclusion compositions, coupled with the core and rim compositions of the host olivine phenocrysts are used for these calculations. When using

phenocryst core compositions, T_{FeMg} yields lava temperatures ranging from 453 to 959 °C. In contrast, when phenocryst rim compositions are used, the temperatures rise to 503 to 1531 °C. Clearly these temperature results are unrealistic as they are even lower than the peridotite solidus temperature. Considering that most spinel inclusions are magnetite (Fig.12), they are very likely not in equilibrium with the host olivine phenocrysts.

Table 4. Calculated host lava temperatures in °C.

Sample	TMg (anhydrous)	TMg (1% H2O)	TMg (2% H2O)	TMg (anhydrous) at 15 kbar	TNi	TNi - TMg
MH-02-101-O1	1287	1263	1241	1367	1291	4
MH-02-101-O3	1297	1273	1250	1378		
MH-02-101-O4	1298	1274	1251	1378		
MH-02-101-O5	1280	1256	1234	1360	1293	13
MH-02-101-O6	1300	1275	1252	1380		
MH-02-101-O7	1278	1254	1232	1358	1275	-3
MH-02-101-O8	1299	1275	1252	1380		
MH-02-101-O9	1301	1277	1254	1382		
MH-02-101-O10	1302	1278	1255	1383		
MH-02-101-O15	1299	1275	1252	1380		

CHAPTER 5: Discussion

5.1 Lithosphere Mantle Origin

The whole-rock concentrations of incompatible elements (Sr, Y, Zr, Nb, Ba, and LREE) in four Llangorse samples were reconstructed for comparison with their measured concentrations from Harder and Russell (2006). These are reconstructed by multiplying the average incompatible element compositions of cpx and opx by their modal fractions, and assuming olivine and spinel contain little of these trace elements. The percentage differences between measured and reconstructed compositions are calculated and plotted in Figure 28. The plot reveals some degree of inflated concentrations for highly incompatible elements measured in the bulk rock analysis of all four samples. This inflation could be explained by contamination of 0.3 and 2.0 % of host basanite lavas. This inflation phenomenon is commonly observed in other peridotite xenoliths (Schmidberger and Francis 2001; Harvey et al. 2021).

Previous studies (Carlson et al. 2005; Pearson et al. 2005) suggest that most subcontinental mantle xenoliths originated as depleted residues of partial melting. The nonmodal fractional melting model of Warren (2016) is applied to examine the degree of partial melting recorded by the Llangorse xenoliths, assuming they are simple residues. This model uses a depleted MORB mantle composition (Workman and Hart 2005) as the source, with melting occurring based on the reaction 0.56 opx + 0.72 cpx + 0.04 spinel = 0.34 olivine + 1 melt (Wasylenki et al. 2003) at 1300 ºC and 1.0 GPa. The result shows that the REE patterns of two Llangorse lherzolites samples (MH-02-10 and MH-02-108) along with most of the Cordilleran lherzolites from the literature (fig.17B) (Shi et al. 1998) can be reproduced by one percent partial melting of depleted MORB mantle. In contrast, the LREE depletion trends in sample MH-02-15, MH-02-125 and a few other Cordilleran lherzolites (fig.17B) (Shi et al. 1998) suggest they

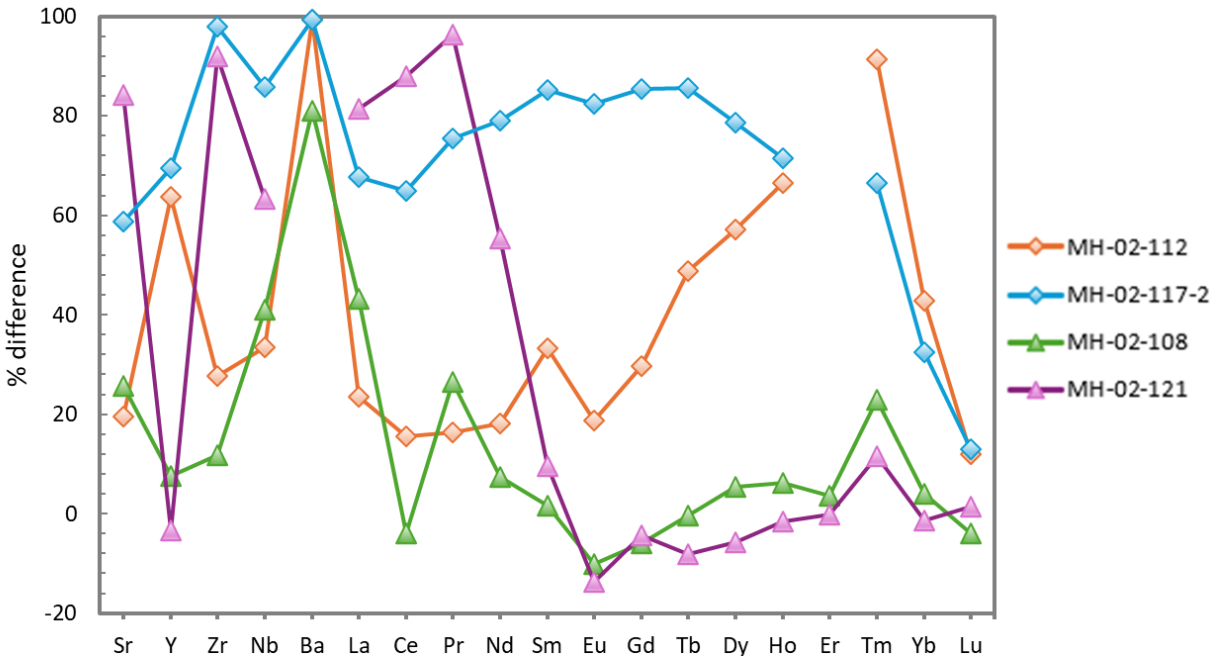

Fig. 28. The % difference in highly incompatible elements concentrations between measured whole rock powders (Harder and Russell 2006) and reconstructed samples of Llangorse xenoliths.

experienced approximately five percent partial melting. However, their HREE concentrations are well above the one-percent partial melting line. This potentially indicates that Cordilleran mantle is less depleted than the typical depleted MORB mantle. In comparison, none of the Llangorse harzburgites, nor the harzburgites from literature (Shi et al. 1998), align with the partial melting model of Warren (2016) (Fig.17A), because they are strongly enriched in LREE, far exceeding the source cpx composition. This LREE enrichment is likely due to melt invasions and metasomatisms that happened when xenoliths were entrained in the host magma.

5.2 Geotherm and Lithosphere Thickness

A previous study (Harder and Russell 2006) used average surface heat flow and heat production measurements for the northern Cordillera (Lewis et al. 2003) to construct the regional geotherm model for the Llangorse locality. They projected the T_{BKN} temperatures of xenolith samples to this model geotherm, to estimate the thickness of mantle lithosphere beneath the Llangorse region is 18 km to 39 km thick. However, this method is not direct and there are several issues with geotherm projection. According to Lewis et al. (2003), the average surface heat flow and heat production for the regions between 57 to 59 ºN are 73 ± 11 mWm^{-2} and 1.6 ± 0.8 μWm^{-3}, respectively. In contrast, regions above 59 °N exhibit significantly higher values, with a surface heat flow of 105 ± 22 mWm^{-2} and heat production of 4.6 ± 2.4 μWm^{-3} (Lewis et al. 2003). The Llangorse locality, situated between 59°19'N and 59°25'N, lies at this boundary, making it difficult to determine whether the values for regions between 57 to 59 ºN or those above 59 ºN are more appropriate for a model geotherm calculation. In addition, when calculating the lithospheric mantle thickness, Harder and Russell (2006) assume the maximum T_{BKN} temperatures (1065 – 1100 °C) represent the deepest samples from Llangorse locality. However, this assumption is problematic, as these maximum T_{BKN} temperatures are derived from

the rim compositions of strongly sieved samples and MH-02-109, which shows heavily melt invasions. Clearly, by showing strongly sieved texture, such samples are influenced by later thermal events, hence they do not reflect equilibrium mantle conditions.

In this study, I used the P_{SC} geobarometer (Table 3) to directly calculate the pressure conditions and sampled depth of Llangorse xenoliths instead. However, the P_{SC} barometer is based on the Ca exchange between olivine and cpx which is both temperature and pressure dependent. Additionally, because Ca has relatively high diffusivity in olivine (Coogan et al. 2005), depth estimates from the P_{SC} barometer can be influenced by later thermal events.

The results (Fig.26) show that about half of the sieved samples have depth estimates above the average Cordilleran Moho depth of 33 km depth (Audet et al. 2020). This discrepancy is likely due to the high Ca concentration and pronounced Ca zoning observed in the olivine from all sieved samples (Fig.16), which also exhibit higher T_{FeMg} temperature. Because Fe-Mg exchange between olivine and spinel occurs rapidly (Ozawa 1984), the T_{FeMg} thermometer is highly sensitive to heating, suggesting that these sieved samples have been significantly heated. Although minimum Ca concentrations are used to calculate the depth, it remains possible that the true equilibrium Ca concentrations in each sieved sample is not preserved, or that the olivine core Ca concentrations reequilibrated during heating, resulting in anomalous depth estimates that plot above the Moho using P_{SC}. Therefore, the depth estimates from the sieved samples are not robust and likely do not represent the real depth of the mantle lithosphere beneath Llangorse locality.

All non-sieved samples have depth estimates ranging from 38 to 54 km (Fig. 26). These estimates are considered robust, as there is no evidence of chemical zoning or textural disequilibrium in these samples. While most sieved samples by either minimum Ca with average

Al or minimum Ca with selected Al methods (Fig. 25, 26) have depth estimates below the Moho, these results remain questionable. Given the fast diffusivity of Ca in olivine, it is possible that the Ca concentrations re-equilibrated during heating in the sieved samples, and for these samples it's possible the true equilibrium Ca concentrations were not captured during measurement, leading to potential underestimates of depth.

Logically, the depth estimates should be positively correlated with temperature estimates, as temperature increases with depth in the mantle. However, this relationship is not clearly observed in the Llangorse samples unless they are divided into two sets. Figure 26 shows that most non-sieved samples, along with a few sieved samples, follow one trend, while the remaining samples form a separate trend which is more scattered toward higher temperatures. Most sieved samples exhibit temperature estimates (by T_{Al}) about 50 °C higher than the non-sieved samples, yet they appear at the same or even shallower depths. The hotter temperature of the sieved samples should be robust, as no Al zoning is observed in these samples. This discrepancy further indicates that the sieved samples have been heated, resulting in underestimates of their sampled pressures because of the T effect on the Ca-in-olivine barometer. For this reason, I conclude that only the non-sieved samples and any sieved samples that follow their same trend are representative of the true depth of the mantle lithosphere beneath the Llangorse locality.

A recent study by Russell and Jones (2023) shows that, due to the size and density differences between ascending low viscosity magmas and mantle xenoliths, a lag time can develop between the eruption of initial sampling magma and the arrival of xenoliths. This can result in xenoliths sampled from greater depth having longer entrainment times in the magma, leading to extended lag times (Russell and Jones 2023). The two distinct trends for sieved and

non-sieved samples, as well as the strong zoning and disequilibrium texture in the sieved samples observed for the Llangorse xenoliths, could be explained by the lag time effect. Most sieved samples likely originated from greater depths, as indicated by their consistently higher temperature estimates from all geothermometers when compared to non-sieved samples (Fig.21). These deeper xenoliths, having been derived from greater depth, were entrained in the ascending magma for longer periods. During this prolonged entrainment in the hot magma, elements with high diffusivity such as Fe, Mg and Ca in olivine began to equilibrate with the elevated temperature condition, resulting in the strong Ca zoning patterns and high T_{FeMg} temperatures observed in sieved samples (Fig.21C). At same time, pyroxene in these sieved samples started to break down, forming the characteristic sieve texture. In contrast, shallower xenoliths were entrained for shorter times, limiting the extent of heating by the host magma and preventing the development of chemical zoning and sieved texture.

Alternatively, the sieved samples may have been picked up by the ascending magma at an earlier stage than non-sieved. If the magma paused during its ascent and was stored in the crust or upper mantle for a period before erupting, these early-entrained xenoliths could have been significantly heated during this storage phase, leading to the decomposition of the pyroxenes and the re-equilibration of Ca in olivine. A third possibility is that the deeper and hotter samples which show sieved texture have been significantly heated in the mantle lithosphere before they were sampled by ascending host magma. The source of the heating could be thinning of lithosphere, bringing hotter asthenosphere mantle in contact with overlying lithosphere.

Based on the non-sieved samples and sieved samples following the same trend, I conclude that the mantle lithosphere under Llangorse locality is 31 km thick with the Moho

depth at 34 km and lithosphere-asthenosphere boundary (LAB) at 65 km. This is consistent with both recent geophysical measurements using seismic tomography, which measured the Moho depth to be between 33 and 36 km near Llangorse (Audet et al. 2020), and geochemical interpretations based on SiO_2 barometry which calculated origin depth of Neogene to Quaternary lavas in British Columbia and Yukon and concluded that the LAB is at a depth of 65 ± 10 km (Hyndman and Canil 2021).

The geothermometry results of the Llangorse xenoliths help constrain the temperature conditions of the mantle lithosphere. Several thermometers are used to recover these conditions. As discussed in the geothermobarometry section, all the thermometers are recording the cooling temperatures. The REE in pyroxenes has the slowest diffusivity, hence the T_{REE} has the highest closure temperature which is more likely to record the highest formation temperature, hence they cannot represent current Moho temperature as the mantle lithosphere has undergone subsequent cooling. The minimum temperatures recovered by T_{BKN} and T_{Al} from the Llangorse locality are 811 °C and 829 °C. Therefore, the temperature at the Moho is estimated to be between 811 and 829 °C. It remains possible that shallower samples were either not collected in the field, not examined in the geochemical analyses, or were thermally disturbed leading to sieved texture, which prevented accurate depth recovery through barometry calculation.

To obtain more accurate depth estimates for thermally disrupted sieved samples, a model geotherm for the Llangorse region can be constructed by using the T-depth array of the most robust samples as T-depth constraints. The T_{BKN} values for sieved samples can then be projected onto this model geotherm to estimate their true depths. The model geotherm follows the approach of Harder and Russell (2006) and assumes a simple two-layer lithosphere composed of crust and mantle. The crustal layer is assumed to have constant heat production (A_0), surface heat

flow (q_0), and thermal conductivity (K_1), while the mantle layer has constant thermal conductivity (K_2). The crustal thickness (Z_m) is set at 33 km based on recent seismic observations which are only 100 km away from Llangorse locality (Audet et al.2020). The steady-state conductive temperature distribution for the one-dimensional crustal lithosphere is governed by Equation 3.

$$T(z) = T_O + \frac{q_0}{K_1} Z - \frac{A_0 Z^2}{2K_1} \qquad 0 < Z < Z_m \qquad \text{Equation 3}$$

where Z is the depth. T(z) is the temperature at depth Z.

$$T(z) = T(Z_m) + \frac{q_m}{K_2}(Z - Z_m) \qquad Z_m < Z \qquad \text{Equation 4}$$

Where

$$q_m = q_0 - Z_M A_0 \qquad \text{Equation 5}$$

T_0 is the surface temperature which is assumed to be 10 °C. q_0 is surface heat flow. K_1 is the thermal conductivity of the crust which is 2.5 W/mK. A_0 is constant crustal heat production. For the mantle layer the temperature profile is linear and can be described by equation 4, Where q_m is the heat flow at the base of the crust. K_2 is the thermal conductivity of the mantle which is at 3.2 W/mk. The heat flow at the base of the crust can be calculated using equation 5. All the physical parameters used in modelling are listed in Table 5.

Table. 5. Parameters used in modelling geotherms

Property	Layer 1 Crust	Layer 2 Mantle
T_0 (°C)	10	
q_0 (mW/m²)	73 - 95	
Z_{moho} (km)	33	
A_0 (µM/m³)	0.8 – 1.6	0
K (W/mK)	2.5	3.2
P (kg/m³)	2700	3200

Several attempts are made for fitting a model geotherm to the robust samples. Unfortunately, due to the limited number of robust samples and the steep gradient of the T-depth array, none of the model geotherms are unique or fit well (Fig.29). To match the steep T-depth gradient for the samples derived from thermobarometry, the geotherm would need to be quite steep. However, a geotherm that steep would intersect the mantle peridotite solidus at much greater depth, resulting in an unrealistic LAB depth which contradicts previous observations (Audet et al. 2019; Hyndman and Canil 2021).

Considering the scatter in the T-depth array of robust samples, only one model geotherm (A_0 = 1.1 μW/m³ q_0 = 76 mW/m²) provides a good fit (Figure.30). This geotherm fits most of the robust samples except two. It intersects with wet peridotite solidus (300 ppm) (Hirschmann et al. 2009) and yields a LAB condition at 1284 °C and 74 km with an inherent uncertainty of ± 6 km from the P_{SC}. This result is within the uncertainty compared to the previous interpretation (Hyndman and Canil 2021). Additionally, this depth is consistent with the Llangorse lava origin depth (68 ± 4 km) calculated from Si barometry (Canil and Hyndman 2023). However, this geotherm will create a slightly lower Moho temperature at 774 ± 15 °C. The T_{BKN} temperatures of the remaining sieved samples are projected to this model geotherm, which create reasonable depths range between 44 and 52 km.

The model geotherms from Harder and Russell (2006) are reconstructed and compared with the T-depth result from thermobarometry (Fig.31). In their model, they assumed a Moho depth of 36 km, slightly deeper than the 33 km used in this study. As anticipated, none of the model geotherms of Harder and Russell (2006) perfectly align with the T-depth array derived from thermobarometry. However, taking into account the uncertainty of the P_{SC}, one of their geotherms which has surface heat flow of 69.3 mW/m² and crustal heat production of 0.8 μW/m³

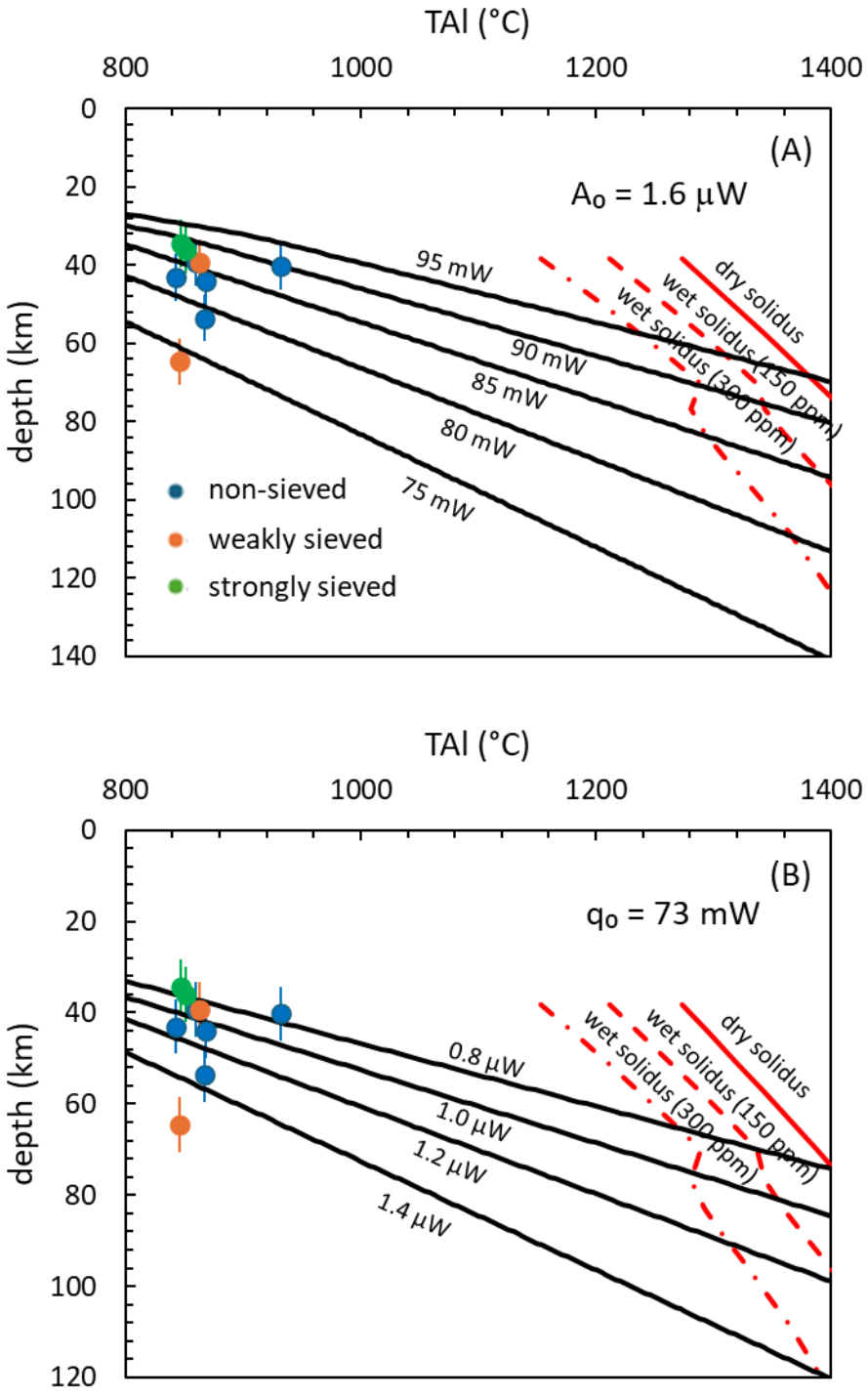

Fig. 29. Model geotherms calculated at various surface heat flow and crustal heat production compared with T-depth of Llangorse samples. Uncertainties of (± 6 km) are in experimental calibration. Dry and wet (with 150 and 300 ppm H_2O) mantle peridotite solidus (ppm is parts per million) are from Hirschmann et al. (2009). (A) Model geotherms calculated using average Cordilleran crustal heat production (A_0 = 1.6 µW/m³) (Lewis et al. 2013) and various surface

heat flow. (B) Model geotherms calculated using average Cordilleran surface heat flow (q_0 = 73 mW/m²) (Lewis et al. 2013) and various crustal heat production.

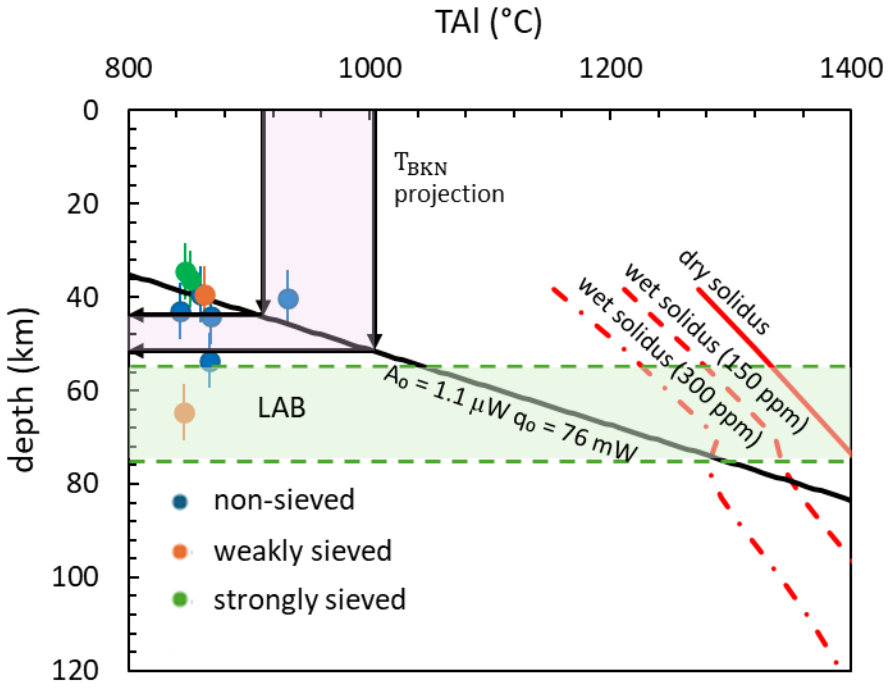

Fig. 30. Model geotherms calculated assuming surface heat flow (q_0 = 76 mW/m^2) and crustal heat production (A_0 = 1.1 µW/m³). Dry and wet (with 150 and 300 ppm H_2O) mantle peridotite solidus lines are from Hirschmann et al. 2009. Uncertainties are in experimental calibration of the barometer (± 6 km). The average LAB depth of Canadian Cordillera is 65 ± 10 km (Hyndman and Canil 2021).

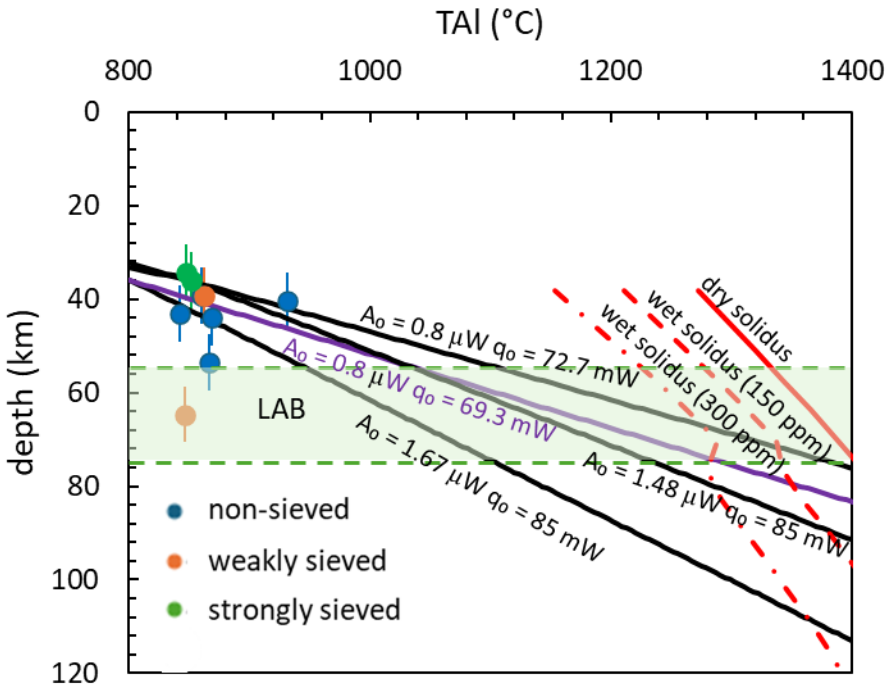

Fig. 31. Reconstructed geotherms following (Harder and Russell 2006). Only the purple geotherm can reasonably align with the T-depth array. A_0 is crustal heat production. q_0 is surface heat flow. Dry and wet (with 150 and 300 ppm H_2O) mantle peridotite solidus are from Hirschmann et al. 2009. Uncertainties are in experimental calibration of the barometer (± 6 km). LAB depth is from Hyndman and Canil (2021).

fits reasonably well with the thermobarometry results and is quite similar to the model geotherm chosen in this study (Fig.31). This geotherm intersects the wet peridotite solidus line (300 ppm Hirschmann et al. 2009) at 1283 °C and 75 km depth. If the T_{BKN} temperatures from remaining sieved samples are projected to this geotherm, their sample depths will range between 45 and 52 km.

Compared to other Cordilleran xenolith localities (Canil and Russell 2022), the Llangorse locality appears to sit on a much colder geotherm (Fig.32). This suggests that the surface heat flow at Llangorse may be lower, or that the heat production is higher than at the Mt. Timothy and Summit Lake localities (Fig.32). Additionally, the colder geotherm at Llangorse implies that the LAB beneath this locality could be deeper and hotter compared to the other two sites (Fig.32). Furthermore, the results potentially suggest that the Moho is colder at the Llangorse locality compared to the other two sites, with Summit Lake having the hottest Moho (Fig.32).

Figure 33 shows a compilation of all published spinel peridotite compositions to calculate their sample temperature and pressure conditions using P_{SC} coupled with T_{Al}. In most xenolith suites, the temperature is positively correlated with the depth. The T-depth array for all the xenolith suites exhibit a similar gradient. Most depth estimates are reasonable and fall into the spinel peridotite stability field. However, there are some samples from Kerguelen Island and Jiaohe that have depth estimates exceeding 80 km, falling into the garnet peridotite stability field. Interestingly all these samples from Kerguelen and Jiaohe are spinel harzburgites which are more depleted compared to lherzolite.

The spinel-garnet peridotite transition is governed by the reaction: spinel + opx = garnet + olivine. The depth of this transition is controlled by the Cr-Al ratio in spinel. Recent studies by Ziberna et al. (2013) and Ziberna and Klemme (2016) indicate that the density change

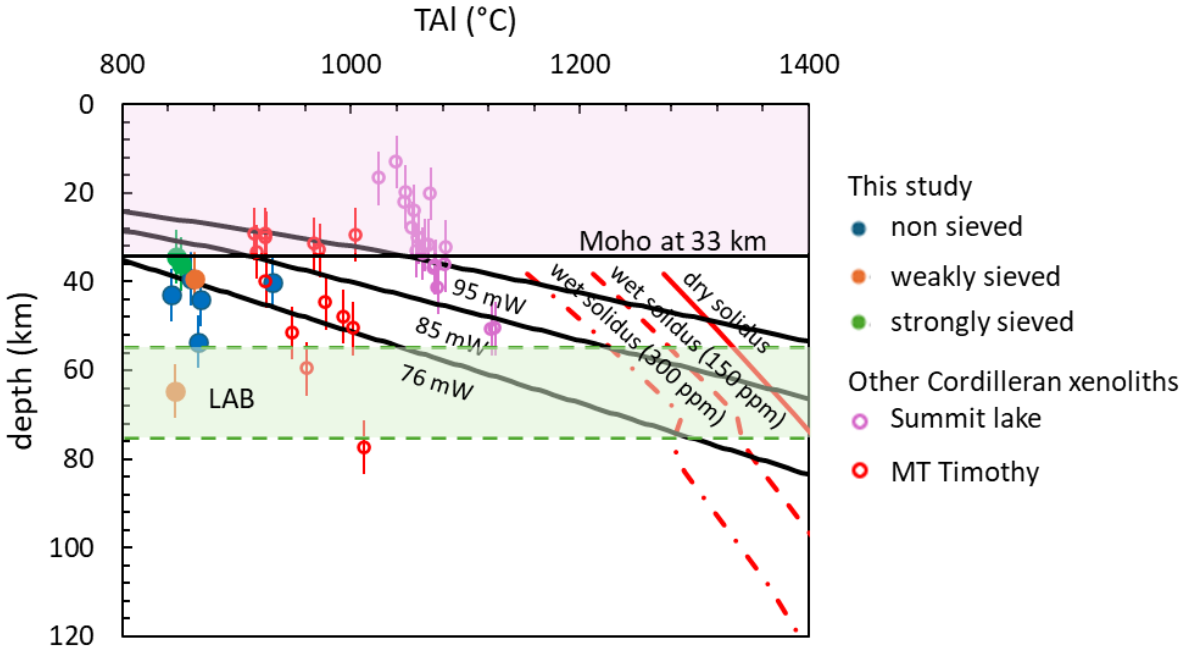

Fig. 32. Model geotherms calculated using surface heat production where A_0 = 1.1 µW/m³ and various surface heat flow. Uncertainties are in experimental calibration of the barometer (± 6 km). Dry and wet (with 150 and 300 ppm H_2O) mantle peridotite solidus are from Hirschmann et al. (2009). Other Cordilleran xenoliths are from (Canil and Russell 2022). The average Moho depth is from Audet et al. (2020). LAB depth is from Hyndman and Canil (2021).

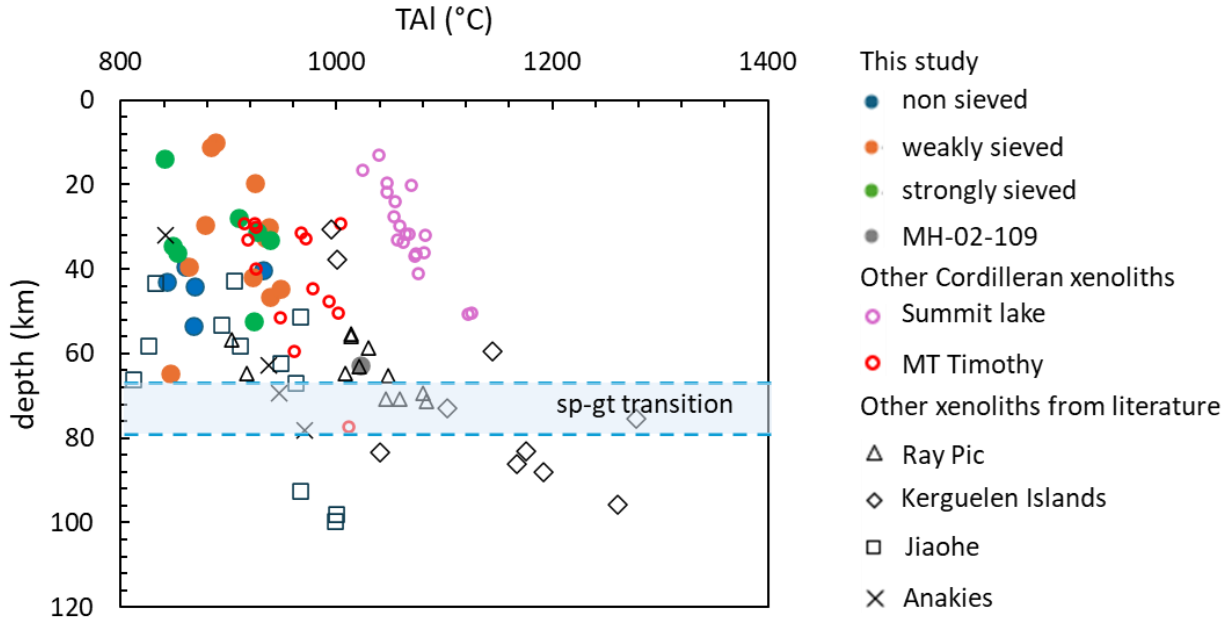

Fig. 33. Plot of depth in km vs T_{Al} in °C. Hollow symbols are published data for xenoliths from elsewhere in the Cordillera (Canil and Russell 2022) and worldwide (Gregoire et al. 2000; Mallmann et al. 2009; De Hoog et al. 2010; Lin et al. 2023). The average spinel-garnet peridotite transition depth for continental off-craton mantle lithosphere is at 73 ± 6 km (Canil et al. 2021a).

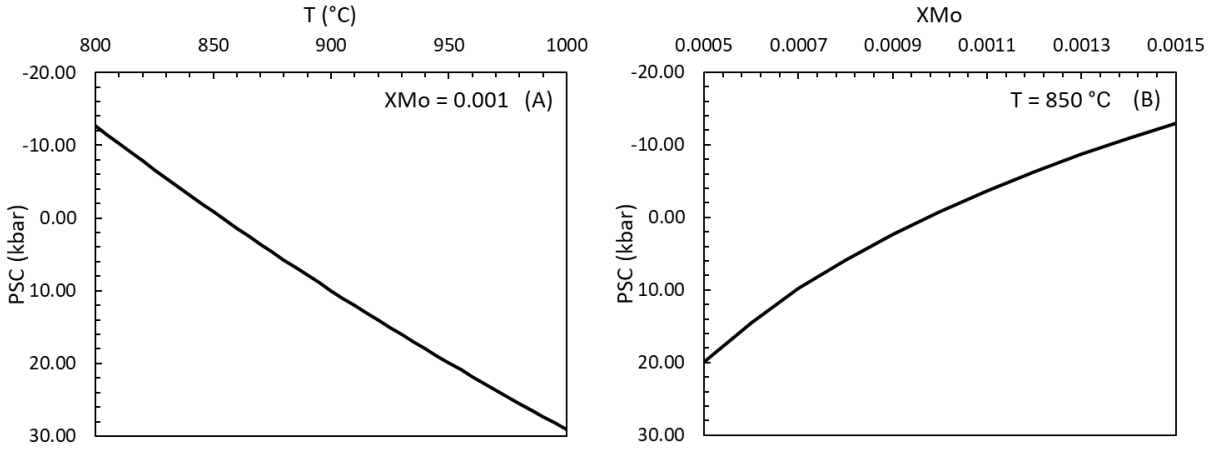

Fig. 34. Plot of temperature and Ca dependence of P_{SC} barometry. (A) temperature vs P_{SC} when X_{Mo} fixed at 0.001. (B) X_{Mo} vs P_{SC} when temperature is fixed at 850 °C.

associated with the spinel-garnet peridotite transition is smooth and highly dependent on bulk compositions. In more depleted mantle compositions, this transition is not reflected in the mantle density profile (Ziberna and Klemme 2016). Furthermore, Canil et al. (2021a) demonstrate that more depleted compositions have a higher Cr/Al ratio which stabilizes spinel peridotite to higher pressure, pushing the spinel-garnet peridotite transition to greater depth. This might explain why those harzburgite samples have estimated depths exceeding 80 km.

In view of the scatter in the Llangorse samples, and their potential use to constrain a geotherm it is important to consider the uncertainties in T and P from compositional data alone, as well as the effects of the strong T dependence of the P_{SC} barometer. The temperature and Ca concentration dependence of the P_{SC} barometer is presented in Figure 34. The results indicate that for fixed Ca in olivine for every 10 °C increase in temperature, the calculated pressure estimates rise by approximately 2 kbar, equivalent to about 6 km in depth (Fig.34A). In contrast, when temperature is fixed, for every 0.0001 increase in X_{Mo} (Ca in apfu in Ol) which is about 28 ppm Ca depending on olivine composition, the pressure decreased by approximately 2 to 6 kbar, depending on the specific conditions (Fig.34B.). This trend potentially suggests that P_{SC} cannot be paired with T_{BKN} and T_{REE} thermometers, as they generally record temperatures about 50 °C higher than T_{Al}, which could lead to pressure overestimation and result pressures falling within the garnet stability field. For instance, using sample MH-02-108 as example, it has T_{Al}, T_{BKN}, and T_{REE} temperature at 868, 906, and 890 °C, respectively. When P_{SC} is coupled with T_{Al}, it yields a depth estimates of 44 km; in contrast, coupling P_{SC} with T_{BKN} or T_{REE} increases the depth estimates to 70 and 59 km respectively.

As noted above, Ca can be mobile in olivine by late heating of xenoliths, affecting the calculated P_{SC}. To address this problem, a recent study by Lin et al. (2023) proposed adjusting

the Ca concentration in olivine by incorporating the temperature recorded by T_{Al} into a Ca thermometer which accounts for both pressure and temperature effects to derive a 'fixed' Ca concentration. However, there are several problems with this method. By applying this method, all mantle xenolith suites align along a universal geotherm with surface heat production of 97 mW/m^2 and heat production of 2.2 $\mu W/m^3$ (Fig.35), which fit best with all the results. Consequently, using the Lin et al (2023) method, it would seem unnecessary to measure the Ca concentration in olivine, as temperature estimates from any reliable thermometers could be used to adjust Ca or even be projected on this universal geotherm. For the Llangorse samples, the P_{Lin} results seem reasonable, with depth estimates ranging from 36 to 56 km, aligning well with recent seismic measurements (Audet et al. 2019; Audet et al. 2020). However, the depth estimates for Kerguelen Island xenolith suite range from 52 to 129 km which is highly questionable. Based on P_{Lin}, these samples lie far beyond the spinel peridotite stability field, even considering their depleted composition. Moreover, the assumption of a universal geotherm for all spinel peridotites is very unlikely, especially considering the diverse tectonic settings from which these xenoliths were collected. If this geotherm is accurate, the depth of the Cordilleran LAB where the geotherm crosses the peridotite solidus, will exceed 140 km (Fig.35.), as the universal geotherm intersects the dry peridotite solidus at about 200 km depth and the wet peridotite solidus (300 ppm water) at about 147 km depth. This outcome contradicts all the seismic observations and geochemical interpretations of the Cordilleran lithosphere (Audet et al. 2019; Canil et al. 2021a).

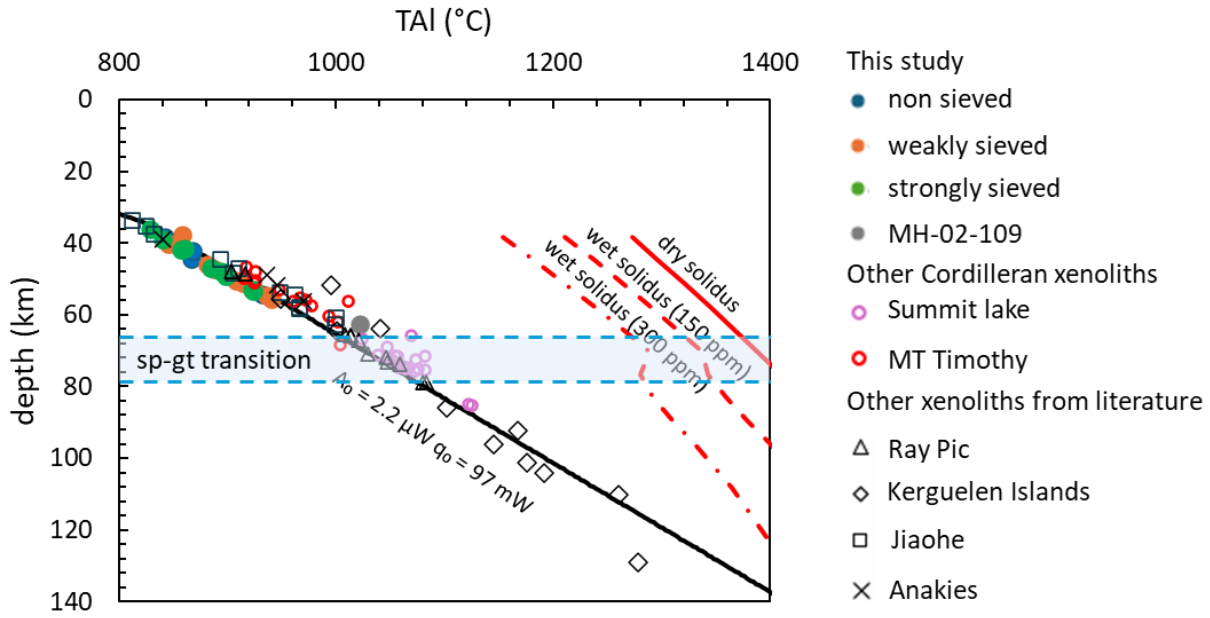

Fig. 35. Plot of depth in km vs T_{Al} in °C. The depths are converted from P_{Lin}. Hollow symbols are published data for xenoliths from elsewhere in the Cordillera (Canil and Russell 2022) and worldwide (Gregoire et al. 2000; Mallmann et al. 2009; De Hoog et al. 2010; Lin et al. 2023). Superimposed on the array of xenoliths is a best fit geotherm calculated using surface heat flow (q_0) of 97 mW/m² and heat production (A_0) of 2.2 µW/m³. Also shown is the mantle solidus for dry (solid) and 150, 300 ppm water (dashed) after Hirschmann et al. (2009). The spinel-garnet peridotite transition field is from Canil et al. (2021a).

5.3 Heating and Residence Time of the Xenoliths in Magma

As discussed in the results section, all the sieved samples exhibit pronounced Ca zoning in olivine with cores of grains consistently having lower Ca concentrations than the rims. The Ca concentration in olivine increases with rising temperature or decreasing pressure, and vice versa (Shejwalkar and Coogan 2013). Given the exceptionally high Ca concentrations in the rims and the observed normal zoning patterns, the sieved samples likely experienced significant heating. To estimate the timescale of this heating event, diffusion chronometry (Costa et al. 2020) is applied.

Fick's second law can be used to determine the time a crystal spends at a given temperature. In single dimension, the Fick's second law is expressed as equation 5.

$$\frac{dC}{dt} = D\frac{d^2C}{dx} \qquad \text{Equation 5}$$

where *D* is the diffusion coefficient at given temperature, *x* is the distance from the rim, and *C* is the concentration. To solve this equation, the error function is used. The error function solution to Fick's second law can be written as equation 6

$$C = C_1 + (C_2 - C_1) * Erf\left(\frac{x}{2\sqrt{D*t}}\right) \qquad \text{Equation 6}$$

where *D* is the diffusion coefficient at given temperature, *x* is the distance from the rim, C is the concentration at given distance *x*, C_1 is the initial concentration at the grain boundary (where $x = 0$), C_2 is the original concentration at the core and *t* is the time in seconds. By fitting the error function to the observed zoning profile, the time duration of heating can be obtained (Fig.36).

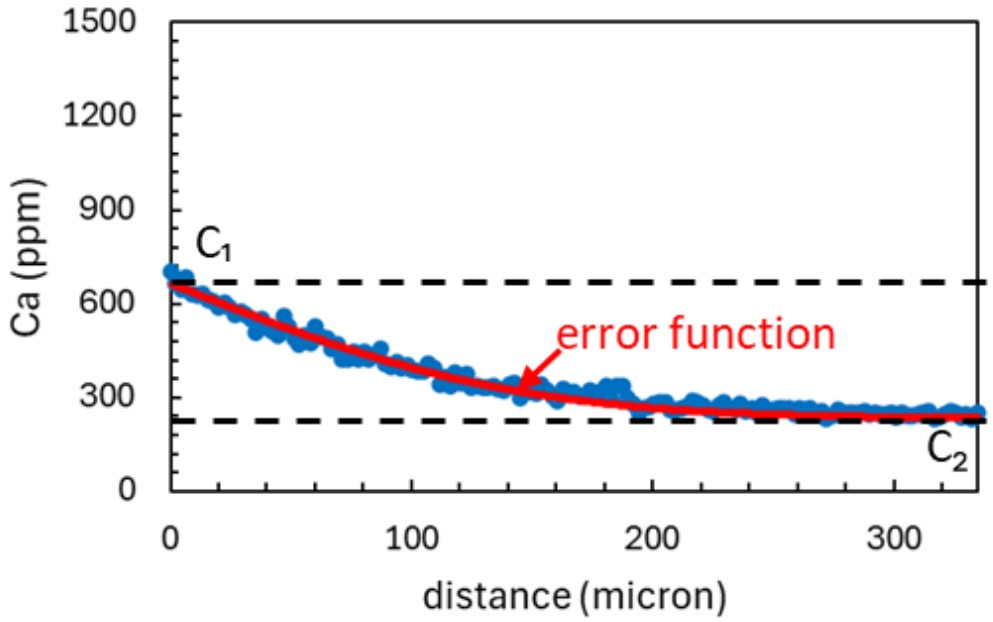

Fig. 36. Fit of Equation 6 to the measured zoning profile from sample MH-02-100B. C_1 is the initial concentration at the grain boundary (where $x = 0$). C_2 is the original concentration at the core.

Table. 6. Diffusion coefficients (Coogan et al. 2005) used in fitting olivine zoning profile.

Temperature (°C)	crystal axis	diffusion coefficient (m^2/s)
1100	100	2.6E-18
1100	001	4.9E-18
1200	100	7.7E-18
1300	100	2.8E-17
1300	001	6.01E-17

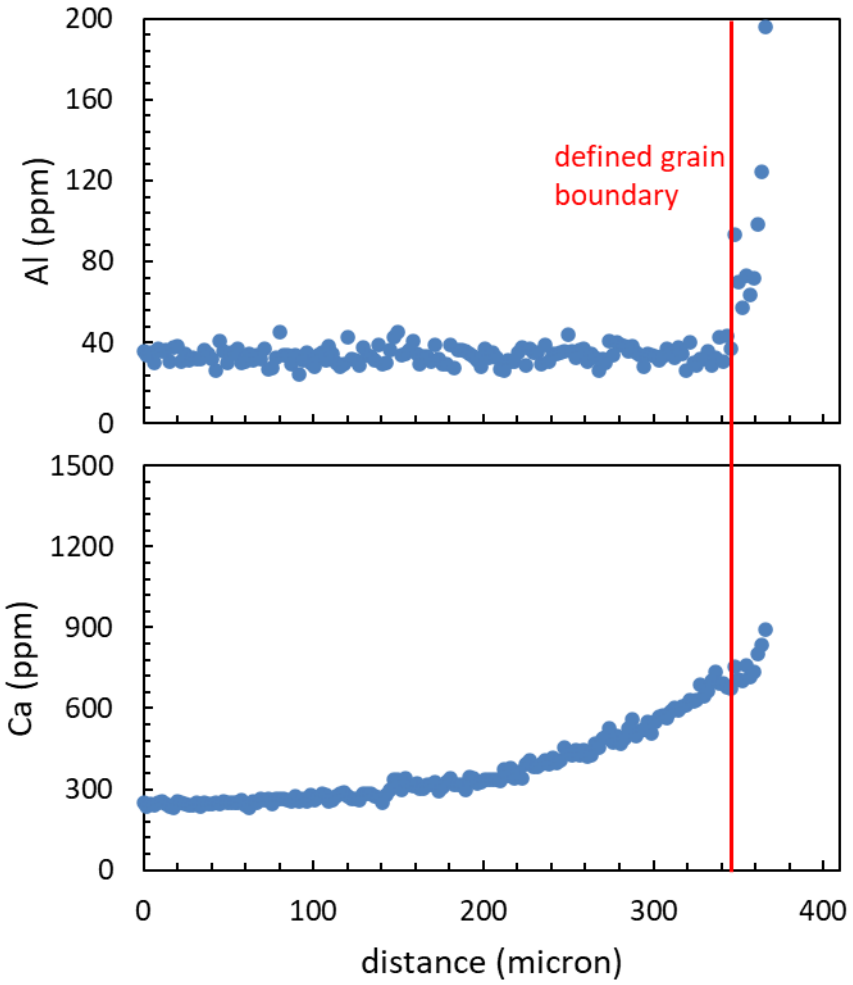

Fig. 37. Measured zoning profile for sample MH-02-100B. The olivine grain boundary is defined by the beginning of abrupt increase of Al concentration.

The highly precise experimentally determined diffusion coefficients for Ca in olivine from Coogan et al. (2005) are used in this study to calculate the timescales of heating. The diffusion coefficients at different temperatures (1100, 1200, and 1300 °C) and along different axes (001, 100) are considered (Table.6). Only the best zoning profiles that extend from the grain boundary directly to the core are selected for fitting. The grain boundary (where $x = 0$) is defined by the point where the Al concentration begins to increase abruptly (Fig.37). The calculated timescales are presented in Table 7, and each individual fitted zoning profile is provided in Appendix F. The uncertainties of the timescale are ± 15 %, which is inherited from experimental determined diffusion coefficients. However, if the initial boundary Ca concentrations are changed by 10 %, the calculated timescale may change by up to 50 %, while still yielding a reasonable fit to zoning profiles. Despite this potential variation, the resulting timescales remain within the range of several to hundreds of years.

Based on the simple zoning patterns observed in each sample, there is no evidence of a complex thermal history involving multiple heating and cooling cycles. No correlation between the heating timescales and the degree of sieve texture is observed. The results indicate that the sieved samples experienced heating for a duration ranging from a few years to hundreds of years, depending on the temperature of the heat source (Table.7). One potential source of this heating event could be the entrainment of xenoliths in the host lava itself during ascent to surface. If the heat source is the host lava, which has an estimated temperature of approximately 1300 °C based on olivine-melt thermometry (see section 4.4), the sieved samples would need to have been entrained in the host lava for several to tens of years, with the timescale varying depending on the crystal axis along which diffusion occurred.

Table. 7. Calculated heating timescales for six sieved samples using olivine Ca zoning profiles. Distances are from the boundary of the grain, which is defined by the point where the Al concentration begins to change, to the core of the grain. C_1 is the initial concentration at the grain boundary (where $x = 0$). C_2 is the original concentration at the core.

		t (years)							
sample	texture	1100 °C [100]	1100 °C [001]	1200°C [100]	1300 °C [100]	1300 °C [001]	distance (micron)	C_1 (ppm)	C_2 (ppm)
MH-02-9B-1	weakly sieved	50	27	17	4.5	2	762	540	310
MH-02-9B-3		150	85	55	15	7	269	615	315
MH-02-9B-5		63	34	21	5	2.5	543	670	320
MH-02-10C-2	weakly sieved	90	48	30	8.5	4	477	635	340
MH-02-10C-3		220	120	72	21	10	460	850	440
MH-02-10C-4		1000	530	330	90	42	629	920	420
MH-02-10C-5		900	480	300	85	40	773	825	445
MH-02-10C-8		155	83	53	14.5	7	812	765	360
MH-02-100B-3	weakly sieved	160	90	55	16	7	203	930	550
MH-02-100B-4		35	18	10	3	1.5	193	885	670
MH-02-100B-5		115	60	38	10.5	5	381	770	250
MH-02-100B-7		79	40	26	8	3.5	335	665	235
MH-02-18B-1	strongly sieved	340	180	115	31	15	662	850	320
MH-02-18B-2		135	70	45	12	6	321	800	490
MH-02-18B-4		110	55	36	10	4.5	484	750	360
MH-02-18B-5		280	150	93	27	11	445	930	620
MH-02-18B-6		33	18	11	3.5	1.5	756	533	330
MH-02-12-1-1	strongly sieved	140	68	45	12	6	617	880	410
MH-02-12-1-2		150	85	50	14	7	365	1060	770
MH-02-12-1-3		185	100	65	17	8	392	1120	780
MH-02-114-1	strongly sieved	1000	520	330	90	43	669	995	430
MH-02-114-2		750	410	260	73	35	671	1000	320
MH-02-114-3		400	200	130	35	17	772	980	405
MH-02-114-4		350	180	113	31	15	600	940	550
MH-02-114-6		1400	710	450	130	60	716	960	360

A timescale of tens of years for xenolith entrainment is significantly longer than the typical timescales of the xenolith lagging process (Russell and Jones 2023) described in Section.5.2, which occurs over a matter of days. This lagging process is driven by the size and density differences between ascending low viscosity magmas carrying the mantle xenoliths, leading to a delay between the eruption of original sampling magma and the arrival of xenoliths. For the zoning timescales to align with this shorter duration, the lava would need to be hotter than 1400 °C, a temperature that contradicts all thermometry results and is not observed in nature in alkalic basalt lavas (Putirka 2008). This suggests that the mantle xenoliths may have resided in the host magma for several to tens of years before being transported to the surface. Consequently, the host lava was likely stored at crustal or upper mantle depths for at least 60 years prior to eruption. This duration aligns with typical magma storage timescales observed in modern volcanic systems (e.g., Pyle 1992; Cooper et al. 2001; Cooper and Kent 2014; Mutch et al. 2019). Additionally, a recent study by Mutch et al. (2019) suggests that xenoliths could be stored in magma for thousands of years before eruption. Some of the timescales calculated for some samples in this study also fall within that range.

Alternatively, the sieved samples might have been heated in the lithosphere, prior to magma sampling. To melt the pyroxenes observed in the sieved samples, the heating source would need to exceed the peridotite solidus temperature. The deepest sieved sample from the P_{SC} calculation has a pressure estimate of 65 km depth. At this depth, the wet solidus temperature (with 300 ppm water) is approximately 1265 °C. Therefore, if the heating source had a temperature above 1265 °C, the sieved samples may have experienced heating on the order of years to hundreds of years before being sampled by the ascending magma.

5.4 Cooling History of Cordilleran Lithosphere

The origin and extent of the hot and thin Cordilleran mantle lithosphere remains a debated topic. Previous studies by Bao et al. (2014) and Audet et al. (2019) suggest that the Cordilleran lithospheric mantle has been completely removed or replaced in the past 50 million years, based on seismic tomography, mantle seismic velocity, and crustal rock cooling ages. These 'delamination' models would require a mantle cooling rate between 2 and 20 °C/Myr assuming linear cooling (Canil et al. 2021b). In this study, I use xenolith data to test this model and provide further constraints on the cooling history of the Cordilleran mantle lithosphere.

The difference between T_{BKN} and T_{REE} results have been widely used to interpret the thermal history of mantle peridotites in various tectonic settings (Dygert and Liang 2015; Dygert et al. 2017; Smye et al. 2017; McGoldrick et al. 2018; Canil et al. 2019; Canil et al. 2021b). As discussed in previous sections, both T_{BKN} and T_{REE} thermometers are based on chemical exchange between coexisting cpx and opx. The T_{BKN} thermometer relies on major element Ca-Mg-Fe exchange, while the T_{REE} thermometer is based on REE diffusion exchange (Cherniak and Liang 2007; Cherniak and Dimanov 2010). For the T_{REE} thermometer, the opx phase which has the lowest REE concentration is the main control of the equilibrium timescale following the 'minor rule' principle (Liang 2014). In subcontinental mantle setting, the difference between T_{BKN} and T_{REE} is generally small, often within 80 degrees, which is consistent with the long cooling durations of the lithospheres beneath thicker continental crusts (Liang et al. 2013; Dygert and Liang 2015). In contrast, ophiolites which cool rapidly by seafloor spreading typically show larger differences between T_{BKN} and T_{REE}, ranging from 100 to 400 °C.

As mentioned in the thermometry section (Section.4.2) five of the Llangorse xenolith samples exhibit a temperature difference between T_{REE} and T_{BKN} of less than 80 °C (Fig.23C),

indicate cooling rate less than 10^{-5} °C/Myr (Canil et al. 2021b). This suggests slow cooling of the mantle lithosphere. The remaining two samples have $\Delta T_{REE} - T_{BKN}$ greater than 80 °C potentially indicating faster cooling of the Cordilleran mantle lithosphere. However, one of the sample MH-02-117-2 has a huge uncertainty of ± 94 °C (Table.3) from REE inversion calculations (Liang et al. 2013). This uncertainty exceeds typical uncertainty of ± 30 °C for thermometry of such samples (e.g. Canil et al. 2021b) indicating that this value is not reliable. The other 'fast cooling' sample has $\Delta T_{REE} - T_{BKN}$ at 91 °C (Fig.23C) which is slightly over the 80 °C. Additionally, the T_{BKN} temperatures are calculated based on selected cpx and opx composition instead of an average (Harder and Russell 2006). I recalculate T_{BKN} temperature for a few sieved samples using the average pyroxene core compositions and average pyroxene compositions (without rim analysis) from Harder and Russell (unpublished); the T_{BKN} temperatures have increased about 10 and 30 °C, respectively. Considering this uncertainty, is questionable if these two samples are really 'rapid cooled'. Even if the 91 °C difference is accepted as accurate, the corresponding cooling rate would range between 10^{-4} and 10^{-3} °C/Myr, which is still much slower than the rapid cooling rate required by the 'delamination' model. Therefore, the Cordilleran mantle lithosphere beneath Llangorse, at least that represented by the 5 xenoliths in this study, cooled slowly and is not likely to been recently 'replaced'. More xenoliths from more localities could fortify this conclusion.

CHAPTER 6: Conclusions

1. Based on equilibrium textures, the Llangorse peridotite xenoliths can be divided into three groups: non-sieved, weakly sieved, and strongly sieved samples. Despite textural differences, all the xenoliths show uniform olivine major element chemistry, with restricted Mg# values ranging from 0.887 to 0.917. However, significant Ca zoning is observed in the sieved samples, indicating late heating, while no Al zoning is detected in any of the sample types.
2. Clinopyroxene in harzburgite samples is strongly enriched in LREE, likely due to melt infiltration and metasomatism. In contrast, cpx in lherzolites display normal REE patterns (with LREE depletion). When comparing the REE compositions of cpx with a partial melting model, it suggests that the Cordilleran mantle lithosphere has experienced 0 to 5% partial melting. The original composition of the Cordilleran mantle lithosphere is likely less depleted compared to depleted MORB. However, the REE compositions of cpx from harzburgites cannot be fit with a simple partial melting model.
3. Whole rock trace element compositions are reconstructed using pyroxene compositions and modal mineralogy. When compared to measured whole rock compositions, the measured highly incompatible elements concentrations are highly inflated. This discrepancy is likely due to melt invasion along grain boundaries and metasomatism processes.
4. Temperature estimates for the Llangorse xenoliths vary across different thermometers. T_{Al} ranges from 829 to 941 °C, T_{Ca} from 837 to 969 °C, T_{BKN} from 811 to 1004 °C, T_{REE} from 847 to 1084 °C, and T_{FeMg} from 982 to 1272 °C. In general, the sieved samples exhibit higher temperatures for any thermometer compared to the non-sieved samples. Harzburgites tend to display consistently high temperatures, while lherzolites show a broader range of temperatures. This trend may indicate that harzburgites are either located in deeper parts of the mantle lithosphere or have experienced significant heating. Due to the high diffusivity of Fe-Mg and Ca in olivine, it is likely that the T_{Ca} and T_{FeMg} thermometers record the heating temperatures.

5. The temperatures of lavas hosting the xenoliths are calculated using olivine-melt thermometers, with T_{Ni} yielding a temperature range between 1275 and 1293 °C. Under surface pressure and dry conditions, the T_{Mg} temperature ranging from 1278 to 1302 °C. A 1 % increase in water concentration will cause the T_{Mg} temperature to drop by about 24 °C. With a pressure increase to 15 kbar, T_{Mg} will increase by about 80 °C, reaching 1358 to 1383 °C. The positive and slightly negative $\Delta T_{Ni} - T_{Mg}$ differences indicate that the melt contains only trace amounts of H_2O.

6. Geobarometers based on Ca in olivine can be used to estimate the depth of origin of the xenoliths. The non-sieved samples and a single weakly sieved sample (MH-02-04) yield robust depth estimates between 39 to 54 km and 65 km by using average Ca and Al concentrations in olivine. In contrast by using average Ca, all the strongly sieved samples have negative pressure estimates, and most weakly sieved samples have depth estimates above Moho at approximately 33 km depth. When using the minimum Ca concentrations and corresponding Al concentrations from the same olivine grain, most of the sieved samples provide depth estimates below the Moho, with an uncertainty of ±6 km.

7. The sampled depths of all published spinel peridotites which have high precision olivine Ca and Al concentrations are calculated using P_{SC} coupled with T_{Al}. Most samples yield reasonable depth estimates within the spinel stability field. Samples in the garnet stability field are mostly depleted harzburgites. Due to their higher Cr / Al ratio, spinel harzburgites can be stable up to 100 km depth. These results suggest that P_{SC} coupled with T_{Al} can provide reliable pressures estimates for spinel peridotites.

8. The P_{SC} barometer is sensitive to both temperature and pressure. For every 10°C increase in temperature, the pressure estimate rises by approximately 2 kbar. Conversely, an increase of 0.0001 Ca apfu will cause the pressure estimate to decrease by about 2 to 6 kbar. The high temperature dependency of the P_{SC} potentially indicates that it cannot be coupled with T_{BKN} or T_{REE}, which will overestimate the sampled depth.

9. Based on the non-sieved samples and robust sieved samples, the mantle lithosphere beneath Llangorse in northern BC is 31 km thick, with the Moho at 34 km depth and having a temperature of 811 – 829 °C. The LAB is located at 65 ± 6 km depth. None of the model geotherms can perfectly align with the T-depth array derived from thermobarometry due to scatter in the samples due to the strong temperature dependency of the P_{SC}. Considering the high uncertainty of the depth estimates, the best-fit geotherm has surface heat flow of 76 mW/m² and heat production of 1.1 mW/m³. This geotherm intersects the wet solidus (with 300 ppm water) at 1284 °C and 74 km (± 6 km). However, it produces a Moho temperature of 774 °C (±15 °C).

10. Compared to other Cordilleran xenolith suites, the Llangorse samples are situated on a colder geotherm, which suggests either lower surface heat flow or higher heat production. Additionally, these geotherms indicate that the Moho at Llangorse is colder, while the LAB may be deeper and hotter compared to other localities.

11. A recent study by Lin et al. (2023) suggests fixing the Ca concentration using the T_{Al} temperature. However, applying this method results in all spinel peridotite samples aligning perfectly with a universal geotherm characterized by a surface heat flow of 97 mW/m² and heat production of 2.2 mW/m³. This outcome is highly unlikely to be accurate, as spinel peridotites originate from diverse tectonic settings. Additionally, several samples have depth estimates exceeding 100 km, reaching up to 130 km, which places them in the garnet stability field. Even considering the depleted composition of these samples, it is very unlikely that spinel will be stable over 100 km depth. Furthermore, this universal geotherm intersects the wet solidus line at depths greater than 140 km, contradicting both geophysical and geochemical evidence observed in the Canadian Cordillera.

12. The zoning profiles for Ca in olivine of the sieved samples indicate that they have experienced heating over a timescale ranging from several years to hundreds of years, depending on the assumed heat source temperature. If the heating source is host lava, the sieved samples likely

were heated for duration of several to tens of years. This suggests that the sieved samples may have been entrained by ascending magma at an early stage, with the magma subsequently stored in the upper mantle or crustal level for at least 40 years before the eruption. Alternatively, it is possible that these sieved samples underwent heating prior to being sampled by the ascending magma.

13. The observed differences between T_{REE} and T_{BKN} in five of the Llangorse samples could suggest a slow cooling history of Cordilleran lithosphere, which contradicts to the 'delamination' model. The slow cooling rate indicates that Cordilleran lithosphere is likely ancient

References

Abraham, A. C., Francis, D., and Polvé, M. 2001. Recent alkaline basalts as probes of the lithospheric mantle roots of the northern Canadian Cordillera. Chemical Geology, **175**: 361-386.

Abraham, A. C., Francis, D., and Polvé, M. 2005. Origin of recent alkaline lavas by lithospheric thinning beneath the northern Canadian Cordillera. Canadian Journal of Earth Sciences, **42**(6): 1073–1095.

Aitken, J. D. 1959. Atlin, British Columbia. Geological Survey of Canada, Memoir, **307**: 89

Audet, P., Currie, C. A., Schaeffer, A. J., and Hill, A. M. 2019. Seismic evidence for lithospheric thinning and heat in the northern Canadian Cordillera. Geophysical Research Letters, **46**(8): 4249–4257.

Audet, P., Schutt, D. L., Schaeffer, A. J., Estève, C., Aster, R. C., and Cubley, J. F. 2020. Moho Variations across the Northern Canadian Cordillera. Seismological Research Letters, **91**(6): 3076–3085.

Bao, X., Eaton, D. W., and Guest, B. 2014. Plateau uplift in western Canada caused by lithospheric delamination along a craton edge. Nature Geoscience, **7**(11): 830–833.

Batanova, V.G., Thompson, J.M., Danyushevsky, L.V., Portnyagin, M.V., Garbe-Schönberg, D., Hauri, E., Kimura, J.-I., Chang, Q., Senda, R., Goemann, K., Chauvel, C., Campillo, S., Ionov, D.A. and Sobolev, A.V. 2019. New Olivine Reference Material for In Situ Microanalysis. Geostandards and Geoanalytical Research, **43**(3): 453-473.

Brearley, M., Scarfe, C., and Fujii, T. 1984. The petrology of ultramafic xenoliths from Summit Lake, near Prince George, British Columbia. Contributions to Mineralogy and Petrology, **88**: 53-63.

Brey, G., and Köhler, T. 1990. Geothermobarometry in four-phase lherzolites II. New thermobarometers, and practical assessment of existing thermobarometers. Journal of Petrology, **31**(6): 1353-1378.

Canil, D. and Hyndman, R. D. 2023. Equilibration depth and temperature of Neogene alkaline lavas in the Cordillera of Alaska and Canada as a constraint on the lithosphere-asthenosphere boundary. Canadian Journal of Earth Sciences, **60**(8): 1206-1222.

Canil, D., and Russell, J. K. 2022. Xenoliths reveal a hot Moho and thin lithosphere at the Cordillera–craton boundary of western Canada. Geology, **50**(10): 1135–1139.

Canil, D., Grundy, R., and Johnston, S.T. 2019. Thermal history of the Donjek harzburgite massif in ophiolite from Yukon, Canada with implications for the cooling of oceanic mantle lithosphere. Lithos, **328-329**: 33–42.

Canil, D., Hyndman, R. D., and Fode, D. 2021a. Hygrometric control on the lithosphere–asthenosphere boundary: a 28 million year record from the Canadian Cordillera. Geophysical Research Letters, **48**(9): e2020GL091957.

Canil, D., Russell, J. K., and Fode, D. 2021b. A test of models for recent lithosphere foundering or replacement in the Canadian Cordillera using peridotite xenolith geothermometry. Lithos, **398– 399**(10): 106329.

Carignan, J., Ludden, J., and Francis, D., 1994. Isotopic characteristics of mantle sources for Quaternary continental alkaline magmas in the northern Canadian Cordillera. Earth and Planetary Science Letters, **128**: 271–286.

Carlson, R.W., Pearson, D.G., and James, D.E. 2005. Physical, chemical, and chronological characteristics of continental mantle. Reviews of Geophysics, **43**(1).

Chapman, D. S., and Pollack, H. N. 1975. Global heat flow: a new look. Earth and Planetary Science Letters, **28**: 23-32.

Chen, Y., Gu, Y. J., Currie, C. A., Johnston, S. T., Hung, S.-H., Schaeffer, A. J., and Audet, P. 2019. Seismic evidence for a mantle suture and implications for the origin of the Canadian Cordillera. Nature Communications, **10**: 2249.

Cherniak, D. J., and Dimanov, A. 2010. Diffusion in pyroxene, mica and amphibole. Reviews in Mineralogy and Geochemistry, **72**: 641–690.

Cherniak, D. J., and Liang, Y. 2007. Rare earth element diffusion in natural enstatite. Geochimica et Cosmochimica Acta, **71**: 1324–1340.

Clowes, R. M., Zelt, C. A., Amor, J. R., and Ellis, R. M. 1995. Lithospheric structure in the southern Canadian Cordillera from a network of seismic refraction lines. Canadian Journal of Earth Sciences, **32**(10): 1485–1513.

Coogan, L. A., Hain, A., Stahl, S., and Chakraborty, S. 2005. Experimental determination of the diffusion coefficient for calcium in olivine between 900°C and 1500°C. Geochimica et Cosmochimica Acta, **69**(14): 3683-3694.

Coogan, L. A., Saunders, A. D., and Wilson, R. N. 2014. Aluminum-in-olivine thermometry of primitive basalts: Evidence of an anomalously hot mantle source for large igneous provinces. Chemical Geology, **368**: 1–10.

Cook, F. A., and Erdmer, P. 2005. An 1800 km cross section of the lithosphere through the northwestern North American plate: lessons from 4.0 billion years of Earth's history. Canadian Journal of Earth Sciences, **42**(6): 1295–1311.

Cooper, K. M., and Kent, A. J. R. 2014. Rapid remobilization of magmatic crystals kept in cold storage. Nature, **506**: 480-483.

Cooper, K. M., Reid, M. R., Murrell, M. T., and Clague, D. A. 2001. Crystal and magma residence at Kilauea Volcano, Hawaii: ^{230}Th-^{226}Ra dating of the 1955 east rift eruption. Earth and Planetary Science Letters, **184**: 703–718.

Costa, F., Shea, T., and Ubide, T. Diffusion chronometry and the timescales of magmatic processes. Nature Reviews Earth & Environment, **1**: 201–214.

Currie, C. A., and Hyndman, R. D. 2006. The thermal structure of subduction zone back arcs. Journal of Geophysical Research, **111**(B8): B08404.

Currie, C. A., and Yu, T.-C. 2023. Geodynamic studies of southwestern Canada: subduction zone processes and backarc mantle dynamics. Canadian Journal of Earth Sciences, **60**(9): 1283-1306.

Currie, C. A., Huismans, R. S., and Beaumont, C. 2008. Thinning of continental backarc lithosphere by flow-induced gravitational instability. Earth and Planetary Science Letters, **269**(3–4): 436–447.

De Hoog, J. C., Gall, L., and Cornell, D. H. 2010. Trace-element geochemistry of mantle olivine and application to mantle petrogenesis and geothermobarometry. Chemical Geology, **270**(1–4): 196–215.

Dickinson, W. R. 2004. Evolution of the North American Cordillera. Annual Review of Earth and Planetary Sciences, **32**(5): 13–45.

Dickinson, W. R., and Snyder, W. S. 1979. Geometry of subducted slabs related to San Andreas Transform. Journal of Geology, **87**: 609–627.

Dixon, J. E., Dixon, T. H., Bell, D. R., and Malservisi, R. 2004. Lateral variation in upper mantle viscosity: Role of water. Earth and Planetary Science Letters, **222**(2): 451–467.

Dodson M.H., 1973. Closure temperature in cooling geochronological and petrological systems. Contributions to Mineralogy and Petrology, **40**: 259–274.

Donovan, J. J., Moy, A., von der Handt, A., Gainsforth, Z., Maner, J. L., Nachlas, W., and Fournelle, J. 2023. A New Method for Dead Time Calibration and a New Expression for Correction of WDS Intensities for Microanalysis. Microscopy and Microanalysis, **29**(3): 1096-1110.

D'Souza, R.J., Canil, D., and Coogan, L.A. 2020. Geobarometry for spinel peridotites using Ca and Al in olivine. Contributions to Mineralogy and Petrology, **175**:5.

Dungan, M. A., Long, P. E., Rhodes, J. M. 1978. Magma mixing at mid-ocean ridges: evidence from legs 45 and 45-DSDP. Geophysical Research Letters, **5**:423-425.

Dygert, N., and Liang, Y. 2015. Temperatures and cooling rates recorded in REE in coexisting pyroxenes in ophiolitic and abyssal peridotites. Earth and Planetary Science Letters, **420**: 151-161.

Dygert, N., Kelemen, P.B., and Liang, Y. 2017. Spatial variations in cooling rate in the mantle section of the Samail ophiolite in Oman: Implications for formation of lithosphere at mid-ocean ridges. Earth and Planetary Science Letters, **465**: 134–144.

Edwards, B. R., and Russell, J. K. 2000. Distribution, nature, and origin of Neogene-Quaternary magmatism in the northern Cordilleran volcanic province, Canada. The Geological Society of America Bulletin, **112**(8): 1280–1295.

Francis, D., and Ludden, J. 1995. The Signature of Amphibole in Mafic Alkaline Lavas, a Study in the Northern Canadian Cordillera. Journal of Petrology, **36**(5): 1171–1191.

Francis, D., Minarik, W., Proenza, Y., and Shi, L. 2010. An overview of the Canadian Cordilleran lithospheric mantle. Canadian Journal of Earth Sciences, **47**(4): 353–368.

Frey, F., and Prinz, M. 1978. Ultramafic inclusions from San Carlos, Arizona: petrologic and geochemical data bearing on their petrogenesis. Earth and Planetary Science Letters, **38**(1): 129–176.

Fujii, T., and Scarfe, C. M. 1982. Petrology of ultramafic nodules from West Kettle River, near Kelowna, Southern British Columbia. Contribution to Mineralogy and Petrology, **80**: 297-306.

Gregoire, M., Moine, B. N., O'Reilly, S. Y., Cottin, J. Y., and Giret, A. 2000. Trace element residence and partitioning in mantle xenoliths metasomatized by highly alkaline, silicate- and carbonate-rich melts (Kerguelen Islands, Indian Ocean). Journal of Petrology, **41**(4): 477–509.

Hardebol, N. J., Pysklywec, R. N., and Stephenson, R. 2012. Small-scale convection at a continental back-arc to craton transition: application to the southern Canadian Cordillera. Journal of Geophysical Research, **117**(B1): n/a.

Harder, M. 2004. The Llangorse volcanic field: volcanology and mantle petrology. M.Sc. thesis, University of British Columbia.

Harder, M. and Russell, J. K. 2006. Thermal state of the upper mantle beneath the Northern Cordillera Volcanic Province (NCVP), British Columbia, Canada. Lithos, **87**(1-2): 1-22.

Harder, M., Russell, J. K., Anderson, R. G. and Edwards, B. R. 2003. Llangorse volcanic field, British Columbia. Natural Resources Canada, Geological Survey of Canada.

Harvey, J., Yoshikawa, Y., Hammond, S.J., and Burton, K.W. 2012. Deciphering the trace element characteristics in Kilbourne Hole peridotite xenoliths: Melt–rock interaction and metasomatism beneath the Rio Grande Rift, SW USA. Journal of Petrology, **53**: 1709–1742.

Hirschmann, M. M., Tenner, T., Aubaud, C., and Withers, A. C. 2009. Dehydration melting of nominally anhydrous mantle: The primacy of partitioning. Physics of the Earth and Planetary Interiors, **176**: 54-68.

Hole, M. J., Rogers, G., Saunders, A. D., and Storey, M. 1991. Relation between alkalic volcanism and slab-window formation. Geology, **19**: 657–660.

Honda, S., and Saito, M. 2003. Small-scale convection under the backarc occurring in the low viscosity wedge. Earth and Planetary Science Letters, **216**(4): 703–715.

Hyndman, R. D. 2010. The consequences of Canadian Cordillera thermal regime in recent tectonics and elevation: a review. Canadian Journal of Earth Sciences, **47**(5): 621–632.

Hyndman, R. D., and Canil, D. 2021. Geophysical and geochemical constraints on Neogene–recent volcanism in the North American Cordillera. Geochemistry, Geophysics, Geosystems, **22**(5): e2021GC009637.

Hyndman, R. D., and Currie, C. A. 2011. Why is the North American Cordillera high? Hot backarcs, thermal isostasy, and mountain belts. Geology, **39**(8): 783–786.

Hyndman, R. D., and Lewis, T. J. 1999. Geophysical consequences of the Cordillera–craton thermal transition in southwestern Canada. Tectonophysics, **306**(3–4): 397–422.

Jean, M. M., and Shervais, J. W. 2017. The distribution of fluid mobile and other incompatible trace elements in orthopyroxene from mantle wedge peridotites. Chemical Geology, **457**: 118-130.

Jochum, K. P., et al. 2006. MPI-DING reference glasses for in situ microanalysis: New reference values for element concentrations and isotope ratios. Geochemistry, Geophysics, Geosystems, **7**(2).

Johnston, S. T. 2008. The Cordilleran ribbon continent of North America. Annual Review of Earth and Planetary Sciences, **36**(5): 495–530.

Lewis, T.J., Hyndman, R.D., and Flück, P. 2003. Heat flow, heat generation, and crustal temperatures in the northern Canadian Cordillera: thermal control of tectonics. Journal of Geophysical Research 108 (B6), 2316.

Li, J., Kornprobst, J., Vielzeuf, D., and Fabriès, J. 1995. An improved experimental calibration of the olivine-spinel geothermometer. Chinese Journal of Geochemistry, **14**: 68–77.

Liang, Y. 2014. Time scales of diffusive re-equilibration in bi-mineralic systems with and without a fluid phase. Geochimica et Cosmochimica Acta, **132**: 274–287.

Liang, Y., Sun, C., and Yao, L. 2013. A REE-in-two-pyroxene thermometer for mafic and ultramafic rocks. Geochimica et Cosmochimica Acta, **102**: 246-260.

Lin, A-B., Aulbach, S., Zheng, J.-P., Uenver-Thiele, L., Woodland, A. B., and Zhang, H.-F. 2023. Petrogenesis, sampling depth, thermal and redox evolution of spinel peridotite xenoliths from Jiaohe, NE China: Insights from trace elements in all rock-forming silicate minerals. Journal of Geophysical Research: Solid Earth, **128**(10).

Littlejohn, A. L., and Greenwood, H. J. 1974. Lherzolite nodules in basalts from British Columbia, Canada. Canadian Journal of Earth Sciences, **11**: 1288-1308.

Mallmann, G., O'Neill, H.S.C., and Klemme, S. 2009. Heterogeneous distribution of phosphorus in olivine from otherwise well-equilibrated spinel peridotite xenoliths and its implications for the mantle geochemistry of lithium. Contributions to Mineralogy and Petrology, **158**: 485–504.

McGoldrick, S., Canil, D., and Zagorevski, A. 2018. Contrasting thermal and melting histories for segments of mantle lithosphere in the Nahlin ophiolite, British Columbia, Canada. Contributions to Mineralogy and Petrology, **173**:25.

Monger, J. W. H., and Price, R. A. 2002. The Canadian Cordillera: geology and tectonic evolution. Canadian Society of Exploration Geophysicists Recorder, **27**(2): 17–36.

Mutch, E. J. F., Maclennan, J., Holland, T. J. B., and Buisman, I. 2019. Millennial storage of near-Moho magma. Science, **365**(6450): 260-264.

Ozawa, K. 1984. Olivine-spinel geospeedometry: Analysis of diffusion-controlled Mg-Fe^{2+} exchange. Geochimica et Cosmochimica Acta, **48**(12): 2597-2611.

Pearson, D. G., Canil, D., and Shirey, S. B. 2005. Mantle samples included in volcanic rocks: xenoliths and diamonds. In: Holland, H.D., Turekian, K.K., Carlson, R.W. (Eds.), Treatise on Geochemistry: The Mantle and the Core. Elsevier Pergamon Amsterdam, pp. 175–275.

Peslier, A. H., Francis, D., and Ludden, J. 2002. The lithospheric mantle beneath continental margins: melting and melt-rock reaction in Canadian Cordillera xenoliths. Journal of Petrology, **43**(11): 2013–2048.

Postlethwaite, B., Bostock, M.G., Christensen, N.I., Snyder, D.B. 2014. Seismic velocities and composition of the Canadian crust. Tectonophysics, **633**: 256-267.

Pu, X., Lange, R. A., and Moore, G. 2017. A comparison of olivine-melt thermometers based on D_{Mg} and D_{Ni}: The effects of melt composition, temperature, and pressure with applications to MORBs and hydrous arc basalts. American Mineralogist, **102**(4): 750–765.

Putirka, K. D. 2008. Thermometers and Barometers for Volcanic Systems. Reviews in Mineralogy and Geochemistry, **69**(1): 61–120.

Pyle, D. M. 1992. The volume and residence time of magma beneath active volcanoes determined by decay-series disequilibria methods. Earth and Planetary Science Letters, **112**(1-4): 61-73.

Ranalli, G. 1980. Rheological properties of the upper mantle in Canada from olivine microrheology. Canadian Journal of Earth Sciences, **17**: 1499–1505.

Rhodes, J. M., Dungan, M. A., Blanchard, D. P., and Long, P. E. 1979. Magma mixing at mid-ocean ridges: Evidence from basalts drilled near 22° N on the Mid-Atlantic Ridge. Tectonophysics, **55**(1-2): 35–61.

Rippe, D., Unsworth, M. J., and Currie, C. A. 2013. Magnetotelluric constraints on the fluid content in the upper mantle beneath the southern Canadian Cordillera: implications for rheology. Journal of Geophysical Research: Solid Earth, **118**(10): 5601–5624.

Roeder, P. L., and Emslie, R. F. 1970. Olivine-liquid equilibrium. Contributions to Mineralogy and Petrology, **29**(4): 275–289.

Ross, J.V. 1983. The nature and rheology of the Cordilleran upper mantle of British Columbia: inferences from peridotite xenoliths. Tectonophysics, **100**: 321–357.

Russell, J. K., and Jones, T. J. 2023. Transport and eruption of mantle xenoliths creates a lagging problem. Communications Earth & Environment, **4**: 177.

Russell, J. K., Edwards, B. R., Williams-Jones, G., and Hickson, C. J. 2023. Pleistocene to Holocene volcanism in the Canadian Cordillera. Canadian Journal of Earth Sciences, **60**: 1443–1466.

Ryan, W. B. F., Carbotte, S. M., Coplan, J. O., O'Hara, S., Melkonian, A., Arko, R., Weissel, R. A., Ferrini, V., Goodwillie, A., Nitsche, F., Bonczkowski, J., and Zemsky, R. 2009. Global Multi-Resolution Topography synthesis. Geochemistry, Geophysics, Geosystems, **10**(3).

Schaeffer, A. J., and Lebedev, S. 2014. Imaging the North American continent using waveform inversion of global and USArray data. Earth and Planetary Science Letters, **402**(9): 26–41.

Schmidberger, S.S., and Francis, D. 2001. Constraints on the trace element composition of the Archean mantle root beneath Somerset Island, Arctic Canada. Journal of Petrology, **42**: 1095–1117.

Shejwalkar, A., and Coogan, L. A. 2013. Experimental calibration of the roles of temperature and composition in the Ca-in-olivine geothermometer at 0.1 MPa. Lithos, **177**: 54-60.

Shi, L., Francis, D., Ludden, J., Frederiksen, A., and Bostock, M. 1998. Xenolith evidence for lithospheric melting above anomalously hot mantle under the northern Canadian Cordillera. Contributions to Mineralogy and Petrology, **131**(1): 39–53.

Sigloch, K., and Mihalynuk, M. G. 2013. Intra-oceanic subduction shaped the assembly of Cordilleran North America. Nature, **496**(7443): 50–56.

Smye, A., Seman, S., Hudak, M., and Crispin, K. 2017. Rates of mantle cooling and exhumation during rifting constrained by REE-in-pyroxene speedometry. Geochemistry, Geophysics, Geosystems, **18**: 2510–2525.

Soregaroli, A. 1968. Geology of Boss Mountain Mine, British Columbia. Ph.D. Thesis, University of British Columbia, Vancouver, B.C.

Stevens, R. E. 1944. Composition of some chromites of the western Hemisphere. American Mineralogist, **29**: 1-34.

Sun, S. S., and McDonough, W. F. 1989. Chemical Isotope systematics of the oceanic basalts: implications for mantle composition and processes. In Magmatism in the oceans basins, Edited by A.D. Saunders and M.J. Norry. Geological Society, London, 313-345.

Thorkelson, D. J. 1996. Subduction of diverging plates and the principles of slab window formation. Tectonophysics, **255**: 47–63.

Thorkelson, D. J., and Breitsprecher, K. 2005. Partial melting of slab window margins: Genesis of adakitic and non-adakitic magmas. Lithos, **79**: 25-41.

Thorkelson, D. J., and Taylor, R. P. 1989. Cordilleran slab windows. Geology, **17**: 833–836.

Thorkelson, D. J., Madsen, J. K., and Sluggett, C. L. 2011. Mantle flow through the Northern Cordilleran slab window revealed by volcanic geochemistry. Geology, **39**(3): 267–270.

Valentine, G. A., and Perry, F. V. 2007. Tectonically controlled, time-predictable basaltic volcanism from a lithospheric mantle source (central Basin and Range Province), USA. Earth and Planetary Science Letters, **261**: 201-216.

Warren, J. M. 2016. Global variations in abyssal peridotite compositions. Lithos, **248-251**: 193-219.

Wasylenki, L. E., Baker, M. B., Kent. A. J. R., and Stolper, E. M. 2003. Near-solidus melting of the shallow upper mantle: Partial melting experiments on depleted peridotite. Journal of Petrology, **44**(7):1163–1191.

Workman, R. K., and Hart, S. R. 2005. Major and trace element composition of the depleted MORB mantle (DMM). Earth and Planetary Science Letters, **231**:53–72.

Ziberna, L., and Klemme, S. 2016. Application of thermodynamic modelling to natural mantle xenoliths: examples of density variations and pressure– temperature evolution of the lithospheric mantle. Contributions to Mineralogy and Petrology, **171**: 16.

Ziberna, L., Klemme, S., and Nimis, P. 2013. Garnet and spinel in fertile and depleted mantle: Insights from thermodynamic modeling. Contributions to Mineralogy and Petrology, **166**: 411-421.

Appendix A: Mineral analyses by electron microprobe in weight %.

Appendix A (Table A1): Mineral chemistry for olivine in xenoliths

Sample	Analysis	Next to	SiO_2	Al_2O_3	Cr_2O_3	FeO	NiO	MnO	MgO	CaO	Total
MH-02-115	rim	spinel	41.09	0.01	0.03	8.06	0.37	0.15	50.39	0.10	100.20
MH-02-115	core	spinel	40.99	0.01	0.02	8.10	0.39	0.10	50.42	0.05	100.07
MH-02-115	rim	spinel	40.92	0.01	0.12	8.01	0.39	0.14	50.40	0.11	100.10
MH-02-115	core	spinel	40.70	0.01	0.03	8.15	0.38	0.11	50.33	0.12	99.83
MH-02-115	rim	cpx	40.75	0.00	0.02	8.18	0.37	0.11	50.04	0.10	99.59
MH-02-115	core	cpx	40.66	0.02	0.02	8.06	0.40	0.13	50.33	0.06	99.67
MH-02-115	rim	spinel	41.19	0.01	0.15	8.14	0.39	0.12	50.52	0.05	100.55
MH-02-115	core	spinel	40.81	0.01	0.00	8.09	0.39	0.12	50.33	0.05	99.81
MH-02-115	rim	cpx	41.05	0.02	0.03	8.11	0.38	0.11	50.46	0.14	100.29
MH-02-115	core	cpx	40.82	0.01	0.02	8.11	0.37	0.12	50.32	0.08	99.85
MH-02-115	rim	cpx	40.86	0.00	0.02	8.10	0.38	0.13	50.22	0.14	99.86
MH-02-115	core	cpx	40.82	0.01	0.03	8.04	0.38	0.11	50.33	0.15	99.87
Average			40.89	0.01	0.02	8.10	0.38	0.12	50.34	0.10	99.98
1 STD			0.16	0.01	0.01	0.05	0.01	0.01	0.12	0.04	0.28
MH-02-116	rim	cpx	40.87	0.01	0.03	8.21	0.36	0.13	50.12	0.15	99.88
MH-02-116	core	cpx	41.00	0.02	0.02	8.34	0.43	0.13	50.29	0.05	100.27
MH-02-116	rim	spinel	40.99	0.01	0.16	8.05	0.39	0.13	50.32	0.06	100.11
MH-02-116	core	spinel	40.85	0.02	0.00	8.35	0.38	0.13	50.00	0.06	99.81
MH-02-116	rim	cpx	40.74	0.01	0.01	8.35	0.40	0.12	50.25	0.12	100.00
MH-02-116	core	cpx	40.82	0.01	0.00	8.33	0.39	0.12	50.27	0.07	100.00
MH-02-116	rim	spinel	40.84	0.00	0.16	8.35	0.37	0.11	50.38	0.12	100.33
MH-02-116	core	spinel	40.74	0.02	0.01	8.39	0.41	0.14	50.38	0.05	100.13
MH-02-116	rim	spinel	41.06	0.02	0.21	8.26	0.40	0.13	50.19	0.11	100.38
MH-02-116	core	spinel	41.02	0.00	0.01	8.27	0.41	0.10	50.24	0.06	100.11
MH-02-116	rim	cpx	40.60	0.01	0.01	8.37	0.38	0.13	49.89	0.13	99.52
MH-02-116	core	cpx	40.81	0.01	0.02	8.35	0.40	0.12	50.10	0.07	99.88
Average			40.86	0.01	0.01	8.30	0.39	0.12	50.20	0.09	100.03
1 STD			0.14	0.01	0.01	0.09	0.02	0.01	0.15	0.04	0.24

Appendix A (Table A1): Mineral chemistry for olivine in xenoliths (continued)

Sample	Analysis	Next to	SiO_2	Al_2O_3	Cr_2O_3	FeO	NiO	MnO	MgO	CaO	Total
MH-02-19	rim	cpx	40.65	0.00	0.04	8.37	0.38	0.13	50.22	0.12	99.91
MH-02-19	core	cpx	40.52	0.00	0.02	8.38	0.39	0.11	50.08	0.06	99.56
MH-02-19	rim	cpx	40.78	0.01	0.02	8.39	0.36	0.16	49.86	0.13	99.72
MH-02-19	core	cpx	40.76	0.01	0.03	8.38	0.36	0.13	50.06	0.06	99.79
MH-02-19	rim	cpx	40.71	0.01	0.03	8.44	0.38	0.12	50.20	0.06	99.95
MH-02-19	core	cpx	40.59	0.01	0.02	8.46	0.40	0.12	50.17	0.06	99.84
MH-02-19	rim	spinel	40.85	0.01	0.04	8.49	0.37	0.14	50.16	0.07	100.12
MH-02-19	core	spinel	40.77	0.01	0.01	8.48	0.36	0.12	49.74	0.06	99.56
MH-02-19	rim	spinel	40.82	0.01	0.11	8.43	0.34	0.14	50.18	0.11	100.14
MH-02-19	core	spinel	41.01	0.01	0.05	8.45	0.37	0.14	50.22	0.06	100.32
MH-02-19	rim	spinel	41.06	0.01	0.05	8.31	0.33	0.10	50.28	0.13	100.27
MH-02-19	core	spinel	40.72	0.00	0.04	8.28	0.38	0.11	49.90	0.11	99.52
Average			40.77	0.01	0.03	8.41	0.37	0.13	50.09	0.09	99.89
1 STD			0.15	0.01	0.01	0.07	0.02	0.01	0.17	0.03	0.28
MH-02-125	rim	spinel	41.22	0.02	0.16	8.45	0.38	0.10	50.20	0.13	100.65
MH-02-125	core	spinel	40.92	0.01	0.02	8.70	0.36	0.13	50.12	0.06	100.32
MH-02-125	rim	spinel	40.67	0.01	0.15	8.52	0.38	0.14	49.83	0.13	99.83
MH-02-125	core	spinel	40.82	0.03	0.02	8.67	0.38	0.12	49.86	0.06	99.96
MH-02-125	rim	cpx	41.04	0.00	0.03	8.46	0.37	0.13	49.99	0.15	100.19
MH-02-125	core	cpx	40.65	0.01	0.01	8.43	0.40	0.15	49.67	0.12	99.43
MH-02-125	rim	cpx	41.19	0.01	0.02	8.37	0.37	0.12	49.93	0.11	100.13
MH-02-125	core	cpx	40.79	0.00	0.02	8.43	0.37	0.12	49.78	0.06	99.57
MH-02-125	rim	cpx	41.00	0.02	0.02	8.35	0.37	0.12	49.95	0.15	99.98
MH-02-125	core	cpx	40.85	0.01	0.03	8.42	0.41	0.13	49.83	0.07	99.75
MH-02-125	rim	spinel	41.17	0.01	0.11	8.48	0.39	0.13	50.19	0.12	100.60
MH-02-125	core	spinel	40.86	0.01	0.02	8.51	0.38	0.11	49.83	0.07	99.81
Average			40.93	0.01	0.02	8.48	0.38	0.13	49.93	0.10	100.02
1 STD			0.20	0.01	0.01	0.11	0.01	0.01	0.16	0.03	0.38

Appendix A (Table A1): Mineral chemistry for olivine in xenoliths (continued)

Sample	Analysis	Next to	SiO_2	Al_2O_3	Cr_2O_3	FeO	NiO	MnO	MgO	CaO	Total
MH-02-121	rim	spinel	40.38	0.01	0.18	9.18	0.39	0.15	48.88	0.06	99.23
MH-02-121	core	spinel	40.74	0.01	0.01	9.19	0.42	0.13	49.61	0.04	100.15
MH-02-121	rim	spinel	40.52	0.03	0.11	9.19	0.39	0.16	49.18	0.04	99.62
MH-02-121	core	spinel	40.57	0.01	0.00	9.19	0.39	0.11	49.38	0.04	99.68
MH-02-121	rim	cpx	40.63	0.01	0.01	9.09	0.38	0.14	49.46	0.05	99.77
MH-02-121	core	cpx	40.64	0.02	0.00	9.20	0.41	0.14	49.45	0.05	99.90
MH-02-121	rim	spinel	40.56	0.02	0.12	9.10	0.40	0.15	49.60	0.03	99.98
MH-02-121	core	spinel	40.67	0.01	0.01	9.23	0.43	0.12	49.65	0.04	100.16
MH-02-121	rim	cpx	40.63	0.04	0.00	9.07	0.39	0.13	49.33	0.05	99.62
MH-02-121	core	cpx	40.84	0.01	0.02	9.16	0.39	0.16	49.46	0.03	100.08
MH-02-121	rim	cpx	40.66	0.01	0.00	9.17	0.36	0.11	49.48	0.05	99.85
MH-02-121	core	cpx	40.62	0.00	0.01	9.10	0.40	0.13	49.02	0.04	99.32
MH-02-121	rim	spinel	40.59	0.03	0.02	9.20	0.39	0.10	49.39	0.04	99.76
MH-02-121	core	spinel	40.95	0.01	0.01	9.19	0.41	0.11	49.48	0.03	100.19
MH-02-121	rim	cpx	40.65	0.02	0.02	9.20	0.38	0.13	49.61	0.03	100.05
MH-02-121	core	cpx	40.62	0.06	0.01	9.21	0.40	0.13	49.69	0.05	100.16
MH-02-121	rim	cpx	40.57	0.01	0.01	9.14	0.41	0.14	49.47	0.06	99.81
MH-02-121	core	cpx	40.57	0.03	0.00	9.09	0.41	0.10	49.31	0.05	99.56
MH-02-121	rim	spinel	40.53	0.01	0.07	9.11	0.40	0.13	49.40	0.03	99.68
MH-02-121	core	spinel	40.39	0.00	0.00	9.18	0.42	0.13	49.51	0.04	99.67
Average			40.62	0.02	0.01	9.16	0.40	0.13	49.42	0.04	99.81
1 STD			0.13	0.01	0.01	0.05	0.02	0.02	0.20	0.01	0.27

Appendix A (Table A1): Mineral chemistry for olivine in xenoliths (continued)

Sample	Analysis	Next to	SiO_2	Al_2O_3	Cr_2O_3	FeO	NiO	MnO	MgO	CaO	Total
MH-02-112	rim	cpx	40.81	0.01	0.05	8.24	0.37	0.13	50.45	0.13	100.20
MH-02-112	core	cpx	40.74	0.02	0.03	8.17	0.41	0.14	50.39	0.08	99.99
MH-02-112	rim	spinel	40.82	0.02	0.13	8.06	0.35	0.10	49.99	0.12	99.61
MH-02-112	core	spinel	40.69	0.00	0.02	8.24	0.38	0.14	50.34	0.04	99.84
MH-02-112	rim	cpx	40.75	0.01	0.04	8.11	0.40	0.11	50.17	0.10	99.68
MH-02-112	core	cpx	40.52	0.00	0.03	8.24	0.39	0.15	50.32	0.04	99.68
MH-02-112	rim	cpx	40.85	0.01	0.06	8.14	0.36	0.11	50.54	0.13	100.19
MH-02-112	core	cpx	40.70	0.00	0.03	8.26	0.41	0.11	50.29	0.06	99.87
MH-02-112	rim	cpx	40.62	0.01	0.03	8.14	0.38	0.12	50.11	0.13	99.53
MH-02-112	core	cpx	40.72	0.00	0.03	8.23	0.38	0.12	50.21	0.07	99.76
MH-02-112	rim	spinel	40.80	0.02	0.08	8.08	0.34	0.14	50.35	0.11	99.90
MH-02-112	core	spinel	40.79	0.01	0.02	8.22	0.40	0.11	50.20	0.05	99.80
MH-02-112	rim	spinel	40.82	0.01	0.06	8.08	0.38	0.10	50.15	0.12	99.71
MH-02-112	core	spinel	40.70	0.02	0.04	8.19	0.37	0.13	49.93	0.08	99.47
MH-02-112	rim	cpx	40.85	0.00	0.02	8.44	0.38	0.14	50.12	0.12	100.07
MH-02-112	core	cpx	41.01	0.01	0.04	8.25	0.39	0.12	50.31	0.06	100.18
MH-02-112	rim	spinel	40.82	0.02	0.16	7.83	0.33	0.11	50.08	0.12	99.47
MH-02-112	core	spinel	40.69	0.01	0.04	8.25	0.36	0.14	50.03	0.07	99.58
MH-02-112	rim	spinel	40.78	0.01	0.03	8.19	0.36	0.15	49.90	0.06	99.47
MH-02-112	core	spinel	40.63	0.01	0.00	8.14	0.38	0.10	50.10	0.06	99.41
Average			40.76	0.01	0.03	8.17	0.38	0.12	50.20	0.09	99.77
1 STD			0.10	0.01	0.01	0.12	0.02	0.02	0.17	0.03	0.26

Appendix A (Table A1): Mineral chemistry for olivine in xenoliths (continued)

Sample	Analysis	Next to	SiO_2	Al_2O_3	Cr_2O_3	FeO	NiO	MnO	MgO	CaO	Total
MH-02-117-2	rim	cpx	40.87	0.01	0.04	8.51	0.39	0.14	49.85	0.11	99.92
MH-02-117-2	core	cpx	40.71	0.01	0.01	8.42	0.37	0.13	49.72	0.05	99.42
MH-02-117-2	rim	cpx	40.57	0.00	0.03	8.45	0.39	0.11	49.90	0.11	99.57
MH-02-117-2	core	cpx	40.48	0.01	0.00	8.40	0.38	0.12	49.70	0.06	99.14
MH-02-117-2	rim	spinel	40.48	0.01	0.06	8.69	0.34	0.13	49.61	0.12	99.44
MH-02-117-2	core	spinel	40.52	0.01	0.05	8.61	0.39	0.12	49.74	0.07	99.49
MH-02-117-2	rim	spinel	40.58	0.00	0.09	8.55	0.37	0.13	49.79	0.12	99.64
MH-02-117-2	core	spinel	40.32	0.01	0.04	8.56	0.40	0.11	49.85	0.06	99.35
MH-02-117-2	rim	spinel	40.49	0.00	0.08	8.53	0.39	0.12	49.73	0.11	99.45
MH-02-117-2	core	spinel	40.44	0.01	0.03	8.59	0.38	0.12	49.84	0.06	99.47
MH-02-117-2	rim	spinel	40.66	0.01	0.11	8.47	0.37	0.14	49.89	0.07	99.71
MH-02-117-2	core	spinel	40.57	0.02	0.02	8.50	0.40	0.12	49.74	0.06	99.43
MH-02-117-2	rim	cpx	40.60	0.01	0.02	8.57	0.39	0.13	50.02	0.13	99.87
MH-02-117-2	core	cpx	40.41	0.01	0.03	8.54	0.40	0.13	49.89	0.06	99.46
MH-02-117-2	rim	spinel	40.54	0.01	0.01	8.46	0.39	0.11	49.76	0.09	99.35
MH-02-117-2	core	spinel	40.41	0.02	0.03	8.52	0.38	0.13	49.69	0.06	99.23
MH-02-117-2	rim	cpx	40.84	0.01	0.04	8.42	0.43	0.13	50.10	0.13	100.10
MH-02-117-2	core	cpx	40.60	0.01	0.03	8.50	0.40	0.11	50.00	0.07	99.72
MH-02-117-2	rim	cpx	40.62	0.00	0.04	8.49	0.38	0.12	49.77	0.12	99.55
MH-02-117-2	core	cpx	40.92	0.01	0.02	8.53	0.36	0.11	50.17	0.06	100.19
Average			40.58	0.01	0.03	8.52	0.38	0.12	49.84	0.09	99.58
1 STD			0.16	0.01	0.02	0.07	0.02	0.01	0.15	0.03	0.27

Appendix A (Table A1): Mineral chemistry for olivine in xenoliths (continued)

Sample	Analysis	Next to	SiO_2	Al_2O_3	Cr_2O_3	FeO	NiO	MnO	MgO	CaO	Total
MH-02-15	rim	spinel	40.52	0.01	0.01	8.95	0.35	0.12	49.27	0.07	99.30
MH-02-15	core	spinel	40.78	0.00	0.01	9.17	0.36	0.14	49.42	0.04	99.92
MH-02-15	rim	spinel	40.39	0.01	0.05	9.07	0.36	0.14	49.02	0.12	99.16
MH-02-15	core	spinel	40.67	0.02	0.00	8.98	0.38	0.10	49.14	0.04	99.33
MH-02-15	rim	spinel	40.70	0.01	0.04	9.25	0.37	0.15	49.26	0.10	99.87
MH-02-15	core	spinel	40.83	0.00	0.01	9.26	0.37	0.14	49.29	0.09	100.01
MH-02-15	rim	cpx	40.70	0.01	0.04	8.92	0.39	0.12	49.44	0.12	99.74
MH-02-15	core	cpx	40.58	0.00	0.04	8.87	0.38	0.14	49.25	0.12	99.37
MH-02-15	rim	cpx	40.45	0.01	0.01	8.98	0.36	0.12	48.95	0.15	99.04
MH-02-15	core	cpx	40.61	0.01	0.02	9.15	0.37	0.12	49.45	0.09	99.82
MH-02-15	rim	cpx	41.04	0.01	0.03	9.06	0.36	0.15	49.32	0.15	100.12
MH-02-15	core	cpx	40.71	0.01	0.05	9.09	0.37	0.14	49.29	0.10	99.76
Average			40.67	0.01	0.03	9.06	0.37	0.13	49.26	0.10	99.62
1 STD			0.18	0.01	0.02	0.13	0.01	0.01	0.16	0.04	0.36
MH-02-100	rim	spinel	40.80	0.00	0.02	8.27	0.38	0.13	50.10	0.05	99.76
MH-02-100	core	spinel	40.91	0.01	0.01	8.20	0.39	0.13	50.07	0.05	99.77
MH-02-100	rim	spinel	40.84	0.01	0.29	8.27	0.38	0.14	49.87	0.10	99.90
MH-02-100	core	spinel	40.95	0.01	0.00	8.20	0.38	0.11	50.08	0.06	99.78
MH-02-100	rim	spinel	41.00	0.01	0.28	8.20	0.39	0.10	50.35	0.05	100.39
MH-02-100	core	spinel	40.77	0.01	0.02	8.21	0.40	0.11	50.07	0.05	99.64
MH-02-100	rim	cpx	41.07	0.01	0.03	8.17	0.39	0.11	50.08	0.14	100.01
MH-02-100	core	cpx	40.93	0.01	0.03	8.20	0.39	0.13	50.17	0.05	99.90
MH-02-100	rim	cpx	40.93	0.02	0.01	8.27	0.39	0.13	50.26	0.05	100.06
MH-02-100	core	cpx	41.00	0.01	0.00	8.21	0.39	0.12	50.12	0.05	99.89
MH-02-100	rim	cpx	40.87	0.01	0.01	8.01	0.37	0.13	49.69	0.13	99.22
MH-02-100	core	cpx	40.78	0.01	0.03	8.28	0.41	0.11	49.96	0.05	99.64
MH-02-100	rim	spinel	40.98	0.01	0.01	8.36	0.39	0.10	50.03	0.05	99.93
MH-02-100	core	spinel	40.92	0.01	0.00	8.32	0.41	0.12	50.22	0.05	100.05
Average			40.91	0.01	0.01	8.23	0.39	0.12	50.08	0.07	99.85
1 STD			0.09	0.00	0.01	0.08	0.01	0.01	0.16	0.03	0.27

Appendix A (Table A1): Mineral chemistry for olivine in xenoliths (continued)

Sample	Analysis	Next to	SiO_2	Al_2O_3	Cr_2O_3	FeO	NiO	MnO	MgO	CaO	Total
95LM1	rim	spinel	40.81	0.02	0.17	8.03	0.40	0.10	50.08	0.16	99.76
95LM1	core	spinel	40.85	0.02	0.01	8.00	0.38	0.14	50.25	0.06	99.70
95LM1	rim	spinel	40.94	0.01	0.09	7.96	0.36	0.10	50.25	0.11	99.82
95LM1	core	spinel	41.07	0.01	0.01	8.05	0.38	0.12	50.35	0.07	100.06
95LM1	rim	spinel	40.89	0.02	0.20	8.32	0.33	0.15	50.09	0.15	100.16
95LM1	core	spinel	41.10	0.01	0.00	8.10	0.38	0.11	50.11	0.07	99.89
95LM1	rim	spinel	41.12	0.01	0.14	8.03	0.38	0.12	50.51	0.06	100.38
95LM1	core	spinel	41.10	0.00	0.01	8.02	0.37	0.12	50.29	0.04	99.97
95LM1	rim	cpx	41.00	0.01	0.01	8.21	0.40	0.12	50.17	0.15	100.07
95LM1	core	cpx	41.12	0.01	0.02	8.06	0.37	0.14	50.42	0.07	100.21
95LM1	rim	cpx	40.97	0.02	0.02	8.10	0.38	0.12	50.17	0.17	99.95
95LM1	core	cpx	41.10	0.01	0.03	8.14	0.40	0.12	50.42	0.05	100.27
95LM1	rim	opx	41.16	0.01	0.02	8.04	0.38	0.15	50.47	0.07	100.29
95LM1	core	opx	41.01	0.01	0.01	8.10	0.37	0.11	50.43	0.06	100.11
95LM1	rim	cpx	41.04	0.02	0.01	8.03	0.38	0.12	50.19	0.20	99.98
95LM1	core	cpx	40.89	0.02	0.02	8.00	0.39	0.12	50.28	0.06	99.77
95LM1	rim	cpx	41.06	0.01	0.04	7.99	0.40	0.11	50.09	0.13	99.83
95LM1	core	cpx	40.89	0.01	0.03	7.94	0.38	0.10	50.30	0.11	99.77
95LM1	rim	opx	41.18	0.00	0.01	8.21	0.41	0.11	50.31	0.10	100.35
95LM1	core	opx	41.01	0.03	0.04	8.27	0.36	0.13	50.57	0.08	100.50
Average			41.02	0.01	0.02	8.08	0.38	0.12	50.29	0.10	100.04
1 STD			0.11	0.01	0.01	0.10	0.02	0.02	0.15	0.05	0.24

Appendix A (Table A1): Mineral chemistry for olivine in xenoliths (continued)

Sample	Analysis	Next to	SiO_2	Al_2O_3	Cr_2O_3	FeO	NiO	MnO	MgO	CaO	Total
MH-02-10C	rim	cpx	41.05	0.01	0.01	8.16	0.37	0.13	50.22	0.08	100.03
MH-02-10C	core	cpx	40.79	0.01	0.00	8.14	0.39	0.11	49.91	0.07	99.42
MH-02-10C	rim	cpx	41.03	0.01	0.02	8.43	0.39	0.11	49.99	0.14	100.12
MH-02-10C	core	cpx	40.69	0.01	0.03	8.22	0.41	0.12	50.02	0.07	99.58
MH-02-10C	rim	cpx	41.09	0.01	0.03	8.26	0.40	0.13	50.06	0.13	100.10
MH-02-10C	core	cpx	40.97	0.02	0.00	8.30	0.38	0.13	50.14	0.06	99.99
MH-02-10C	rim	spinel	41.16	0.01	0.05	8.45	0.36	0.10	50.11	0.13	100.38
MH-02-10C	core	spinel	41.11	0.01	0.02	8.28	0.37	0.15	50.15	0.11	100.20
MH-02-10C	rim	spinel	40.96	0.00	0.14	8.36	0.37	0.12	50.01	0.15	100.11
MH-02-10C	core	spinel	40.86	0.01	0.04	8.33	0.36	0.13	49.86	0.12	99.71
MH-02-10C	rim	spinel	40.89	0.01	0.09	8.46	0.37	0.11	49.99	0.10	100.01
MH-02-10C	core	spinel	40.89	0.01	0.00	8.32	0.38	0.12	50.02	0.06	99.81
MH-02-10C	rim	spinel	40.87	0.01	0.16	8.22	0.37	0.13	50.13	0.14	100.04
MH-02-10C	core	spinel	41.14	0.01	0.03	8.32	0.37	0.12	50.12	0.12	100.22
MH-02-10C	rim	spinel	40.97	0.00	0.13	8.22	0.38	0.11	50.10	0.13	100.04
MH-02-10C	core	spinel	41.03	0.00	0.02	8.38	0.39	0.13	50.31	0.07	100.33
MH-02-10C	rim	cpx	40.99	0.01	0.03	8.19	0.38	0.13	49.87	0.15	99.74
MH-02-10C	core	cpx	40.94	0.00	0.01	8.21	0.36	0.12	50.20	0.07	99.91
MH-02-10C	rim	opx	41.01	0.01	0.02	8.24	0.38	0.13	50.08	0.13	100.01
MH-02-10C	core	opx	41.23	0.00	0.01	8.31	0.39	0.15	50.41	0.07	100.56
Average			40.98	0.01	0.02	8.29	0.38	0.12	50.09	0.11	100.02
1 STD			0.13	0.01	0.02	0.09	0.01	0.01	0.14	0.03	0.27

Appendix A (Table A1): Mineral chemistry for olivine in xenoliths (continued)

Sample	Analysis	Next to	SiO_2	Al_2O_3	Cr_2O_3	FeO	NiO	MnO	MgO	CaO	Total
MH-02-04	rim	cpx	40.79	0.01	0.00	8.78	0.39	0.14	49.89	0.05	100.03
MH-02-04	core	cpx	40.86	0.00	0.00	8.72	0.39	0.14	49.69	0.03	99.84
MH-02-04	rim	cpx	40.97	0.01	0.00	8.59	0.39	0.14	49.78	0.05	99.93
MH-02-04	core	cpx	40.87	0.00	0.02	8.70	0.37	0.12	49.90	0.02	99.99
MH-02-04	rim	cpx	40.90	0.01	0.00	8.65	0.41	0.13	49.83	0.07	100.00
MH-02-04	core	cpx	40.78	0.00	0.00	8.84	0.40	0.09	50.00	0.02	100.14
MH-02-04	rim	cpx	40.86	0.01	0.02	8.79	0.40	0.13	49.74	0.02	99.97
MH-02-04	core	cpx	40.77	0.01	0.01	8.66	0.37	0.14	49.67	0.02	99.66
MH-02-04	rim	olivine	40.95	0.00	0.00	8.73	0.41	0.13	49.78	0.02	100.03
MH-02-04	core	olivine	41.01	0.00	0.01	8.81	0.42	0.12	49.93	0.03	100.33
MH-02-04	rim	spinel	40.81	0.01	0.02	8.67	0.39	0.12	49.82	0.02	99.84
MH-02-04	core	spinel	40.94	0.01	0.00	8.57	0.41	0.14	49.93	0.02	100.03
MH-02-04	rim	spinel	41.17	0.01	0.06	8.68	0.41	0.13	50.04	0.02	100.51
MH-02-04	core	spinel	40.84	0.01	0.01	8.73	0.43	0.12	50.08	0.02	100.25
MH-02-04	rim	spinel	40.77	0.01	0.02	8.76	0.41	0.13	49.76	0.02	99.88
MH-02-04	core	spinel	40.89	0.00	0.00	8.60	0.39	0.13	49.55	0.03	99.59
MH-02-04	rim	spinel	40.77	0.01	0.02	8.68	0.40	0.10	49.91	0.03	99.92
MH-02-04	core	spinel	40.98	0.01	0.00	8.74	0.40	0.13	49.92	0.03	100.20
MH-02-04	rim	cpx	40.85	0.01	0.02	8.82	0.38	0.13	49.90	0.03	100.14
MH-02-04	core	cpx	40.76	0.01	0.00	8.69	0.44	0.12	49.88	0.02	99.93
Average			40.88	0.01	0.01	8.71	0.40	0.13	49.85	0.03	100.01
1 STD			0.10	0.00	0.01	0.08	0.02	0.01	0.13	0.01	0.21

Appendix A (Table A1): Mineral chemistry for olivine in xenoliths (continued)

Sample	Analysis	Next to	SiO_2	Al_2O_3	Cr_2O_3	FeO	NiO	MnO	MgO	CaO	Total
MH-02-102	rim	spinel	40.49	0.01	0.06	9.40	0.38	0.13	49.23	0.14	99.83
MH-02-102	core	spinel	40.52	0.01	0.01	9.28	0.38	0.16	49.46	0.07	99.89
MH-02-102	rim	cpx	40.66	0.01	0.03	9.23	0.40	0.11	49.50	0.10	100.04
MH-02-102	core	cpx	40.62	0.01	0.01	9.35	0.41	0.14	49.62	0.04	100.19
MH-02-102	rim	spinel	40.64	0.01	0.03	9.22	0.42	0.13	49.59	0.09	100.12
MH-02-102	core	spinel	40.44	0.00	0.00	9.27	0.40	0.13	49.57	0.04	99.86
MH-02-102	rim	cpx	40.65	0.00	0.04	9.21	0.42	0.13	49.48	0.13	100.06
MH-02-102	core	cpx	40.57	0.01	0.03	9.26	0.41	0.14	49.66	0.12	100.20
MH-02-102	rim	spinel	40.50	0.00	0.10	9.04	0.37	0.17	49.65	0.09	99.92
MH-02-102	core	spinel	40.58	0.00	0.02	9.33	0.40	0.14	49.65	0.06	100.17
MH-02-102	rim	cpx	40.41	0.00	0.02	9.23	0.39	0.15	49.47	0.11	99.77
MH-02-102	core	cpx	40.60	0.00	0.02	9.33	0.43	0.15	49.68	0.05	100.26
Average			40.56	0.01	0.02	9.26	0.40	0.14	49.55	0.09	100.02
1 STD			0.08	0.00	0.01	0.09	0.02	0.02	0.13	0.04	0.17
MH-02-117-1	rim	spinel	40.71	0.00	0.34	8.76	0.35	0.13	49.96	0.11	100.36
MH-02-117-1	core	spinel	40.80	0.01	0.02	8.89	0.38	0.14	49.90	0.08	100.21
MH-02-117-1	rim	cpx	40.74	0.00	0.03	8.53	0.38	0.13	49.99	0.11	99.90
MH-02-117-1	core	cpx	40.86	0.00	0.03	8.52	0.40	0.13	49.99	0.05	99.98
MH-02-117-1	rim	cpx	40.79	0.01	0.04	8.55	0.39	0.13	50.07	0.12	100.09
MH-02-117-1	core	cpx	40.74	0.00	0.01	8.54	0.37	0.10	50.28	0.05	100.09
MH-02-117-1	rim	spinel	40.16	0.01	0.25	8.43	0.39	0.13	49.71	0.13	99.21
MH-02-117-1	core	spinel	40.40	0.00	0.02	8.48	0.39	0.11	49.64	0.05	99.09
MH-02-117-1	rim	spinel	40.72	0.01	0.11	8.34	0.39	0.11	50.00	0.11	99.80
MH-02-117-1	core	spinel	40.72	0.00	0.04	8.33	0.37	0.13	49.97	0.06	99.62
MH-02-117-1	rim	cpx	40.44	0.00	0.01	8.46	0.40	0.11	49.90	0.12	99.46
MH-02-117-1	core	cpx	40.42	0.01	0.01	8.61	0.39	0.12	49.99	0.07	99.62
Average			40.62	0.01	0.02	8.54	0.38	0.12	49.95	0.09	99.73
1 STD			0.22	0.00	0.01	0.16	0.02	0.01	0.16	0.03	0.40

Appendix A (Table A1): Mineral chemistry for olivine in xenoliths (continued)

Sample	Analysis	Next to	SiO_2	Al_2O_3	Cr_2O_3	FeO	NiO	MnO	MgO	CaO	Total
MH-02-114	rim	cpx	40.99	0.01	0.03	7.94	0.39	0.12	50.19	0.16	99.83
MH-02-114	core	cpx	41.11	0.01	0.00	8.10	0.40	0.10	50.50	0.06	100.28
MH-02-114	rim	spinel	40.83	0.01	0.10	7.92	0.38	0.13	50.59	0.08	100.05
MH-02-114	core	spinel	40.74	0.00	0.00	8.00	0.40	0.13	50.52	0.06	99.86
MH-02-114	rim	spinel	40.89	0.01	0.18	7.96	0.40	0.12	50.61	0.13	100.31
MH-02-114	core	spinel	40.98	0.01	0.03	8.04	0.39	0.12	50.32	0.06	99.96
MH-02-114	rim	cpx	40.64	0.01	0.04	8.12	0.37	0.11	49.98	0.16	99.43
MH-02-114	core	cpx	40.72	0.00	0.02	8.01	0.37	0.12	50.22	0.15	99.62
MH-02-114	rim	cpx	40.35	0.01	0.02	8.10	0.36	0.14	49.96	0.19	99.12
MH-02-114	core	cpx	41.04	0.00	0.02	8.11	0.37	0.12	50.39	0.06	100.10
MH-02-114	rim	spinel	40.80	0.02	0.15	8.01	0.39	0.11	50.53	0.17	100.18
MH-02-114	core	spinel	40.64	0.01	0.02	8.07	0.41	0.11	50.17	0.12	99.54
Average			40.81	0.01	0.02	8.03	0.39	0.12	50.33	0.12	99.82
1 STD			0.21	0.00	0.01	0.07	0.01	0.01	0.23	0.05	0.37
MH-02-20	rim	cpx	40.22	0.00	0.02	9.61	0.34	0.14	48.98	0.16	99.46
MH-02-20	core	cpx	40.67	0.01	0.01	9.42	0.38	0.15	49.38	0.07	100.10
MH-02-20	rim	cpx	40.38	0.00	0.01	9.39	0.37	0.13	49.04	0.16	99.49
MH-02-20	core	cpx	40.46	0.00	0.01	9.46	0.37	0.13	49.21	0.05	99.69
MH-02-20	rim	spinel	40.04	0.00	0.06	9.49	0.35	0.14	49.33	0.18	99.58
MH-02-20	core	spinel	40.01	0.00	0.04	9.47	0.35	0.12	49.21	0.13	99.33
MH-02-20	rim	spinel	40.52	0.02	0.03	9.57	0.35	0.15	49.36	0.15	100.15
MH-02-20	core	spinel	40.25	0.01	0.00	9.56	0.35	0.15	49.25	0.04	99.62
MH-02-20	rim	spinel	40.29	0.02	0.07	9.89	0.36	0.14	48.66	0.11	99.54
MH-02-20	core	spinel	40.30	0.01	0.01	9.45	0.39	0.12	48.93	0.04	99.25
MH-02-20	rim	cpx	40.43	0.00	0.03	9.63	0.38	0.13	49.51	0.15	100.24
MH-02-20	core	cpx	40.54	0.00	0.01	9.45	0.41	0.13	49.60	0.06	100.21
Average			40.34	0.01	0.02	9.53	0.37	0.14	49.21	0.11	99.72
1 STD			0.20	0.01	0.02	0.14	0.02	0.01	0.27	0.05	0.36

Appendix A (Table A1): Mineral chemistry for olivine in xenoliths (continued)

Sample	Analysis	Next to	SiO_2	Al_2O_3	Cr_2O_3	FeO	NiO	MnO	MgO	CaO	Total
MH-02-100B	rim	spinel	40.89	0.00	0.06	8.23	0.33	0.12	50.20	0.13	99.97
MH-02-100B	core	spinel	40.54	0.00	0.03	8.53	0.37	0.08	50.14	0.05	99.75
MH-02-100B	rim	cpx	40.60	0.00	0.02	8.83	0.35	0.14	50.12	0.14	100.19
MH-02-100B	core	cpx	40.51	0.01	0.03	8.76	0.36	0.12	50.18	0.07	100.03
MH-02-100B	rim	spinel	40.72	0.01	0.10	8.65	0.36	0.11	50.35	0.13	100.42
MH-02-100B	core	spinel	40.51	0.00	0.02	8.76	0.37	0.11	50.08	0.12	99.96
MH-02-100B	rim	spinel	40.49	0.01	0.12	8.67	0.37	0.13	50.17	0.12	100.09
MH-02-100B	core	spinel	40.67	0.00	0.01	8.72	0.42	0.13	50.27	0.04	100.26
MH-02-100B	rim	cpx	40.31	0.00	0.03	8.68	0.39	0.14	50.02	0.16	99.74
MH-02-100B	core	cpx	40.86	0.01	0.02	8.70	0.38	0.12	50.36	0.08	100.52
MH-02-100B	rim	cpx	40.79	0.00	0.02	8.66	0.39	0.11	50.37	0.13	100.47
MH-02-100B	core	cpx	40.69	0.00	0.02	8.66	0.40	0.16	50.54	0.03	100.50
Average			40.63	0.00	0.02	8.65	0.37	0.12	50.23	0.10	100.14
1 STD			0.17	0.01	0.01	0.15	0.02	0.02	0.15	0.04	0.28
MH-02-115B	rim	spinel	41.01	0.01	0.17	8.38	0.37	0.10	50.28	0.13	100.45
MH-02-115B	core	spinel	40.92	0.01	0.02	8.14	0.40	0.10	50.61	0.06	100.25
MH-02-115B	rim	cpx	40.93	0.01	0.00	8.13	0.41	0.14	50.35	0.16	100.13
MH-02-115B	core	cpx	40.82	0.00	0.03	8.09	0.38	0.11	50.55	0.06	100.03
MH-02-115B	rim	cpx	40.67	0.01	0.03	8.09	0.39	0.12	50.45	0.15	99.91
MH-02-115B	core	cpx	40.83	0.01	0.00	8.16	0.40	0.12	50.55	0.06	100.13
MH-02-115B	rim	cpx	40.63	0.00	0.01	8.08	0.36	0.12	49.81	0.16	99.16
MH-02-115B	core	cpx	40.77	0.00	0.01	8.13	0.40	0.11	50.40	0.10	99.92
MH-02-115B	rim	spinel	40.98	0.02	0.25	8.04	0.36	0.12	50.50	0.12	100.39
MH-02-115B	core	spinel	40.97	0.00	0.01	8.16	0.40	0.11	50.49	0.06	100.20
MH-02-115B	rim	spinel	40.63	0.01	0.23	8.06	0.38	0.11	50.33	0.11	99.87
MH-02-115B	core	spinel	40.89	0.00	0.00	8.15	0.43	0.10	50.71	0.06	100.34
Average			40.84	0.01	0.01	8.13	0.39	0.11	50.42	0.10	100.02
1 STD			0.14	0.01	0.01	0.09	0.02	0.01	0.23	0.04	0.34

Appendix A (Table A1): Mineral chemistry for olivine in xenoliths (continued)

Sample	Analysis	Next to	SiO_2	Al_2O_3	Cr_2O_3	FeO	NiO	MnO	MgO	CaO	Total
MH-02-109	rim	cpx	40.77	0.02	0.02	8.27	0.40	0.13	49.97	0.11	99.69
MH-02-109	core	cpx	40.75	0.02	0.01	8.18	0.39	0.11	50.19	0.07	99.71
MH-02-109	rim	spinel	40.56	0.03	0.16	8.43	0.41	0.14	50.30	0.10	100.13
MH-02-109	core	spinel	40.80	0.03	0.01	8.23	0.38	0.14	50.56	0.08	100.22
MH-02-109	rim	cpx	40.83	0.03	0.02	8.29	0.38	0.12	50.53	0.09	100.29
MH-02-109	core	cpx	40.62	0.02	0.02	8.26	0.35	0.13	50.50	0.07	99.96
MH-02-109	rim	cpx	40.90	0.03	0.03	8.20	0.38	0.11	50.27	0.12	100.04
MH-02-109	core	cpx	40.80	0.02	0.02	8.17	0.40	0.13	50.36	0.07	99.97
MH-02-109	rim	spinel	40.79	0.01	0.19	8.28	0.38	0.14	50.55	0.09	100.44
MH-02-109	core	spinel	40.86	0.02	0.03	8.12	0.42	0.14	50.45	0.08	100.12
MH-02-109	rim	cpx	40.65	0.03	0.05	8.22	0.40	0.12	50.46	0.12	100.05
MH-02-109	core	cpx	40.79	0.02	0.02	8.27	0.39	0.11	50.50	0.07	100.18
MH-02-109	rim	spinel	40.70	0.03	0.12	8.25	0.34	0.11	50.31	0.08	99.94
MH-02-109	core	spinel	41.05	0.02	0.00	8.22	0.39	0.11	50.37	0.07	100.23
MH-02-109	rim	spinel	40.74	0.02	0.31	8.26	0.37	0.12	50.19	0.10	100.11
MH-02-109	core	spinel	40.59	0.02	0.01	8.14	0.38	0.13	50.40	0.07	99.75
Average			40.76	0.02	0.02	8.24	0.38	0.12	50.37	0.09	100.01
1 STD			0.12	0.00	0.01	0.07	0.02	0.01	0.16	0.02	0.21
MH-02-14	rim	spinel	40.43	0.00	0.05	10.54	0.34	0.17	48.78	0.18	100.48
MH-02-14	core	spinel	40.60	0.00	0.03	10.22	0.36	0.16	48.91	0.15	100.43
MH-02-14	rim	spinel	40.87	0.00	0.17	9.18	0.37	0.15	49.59	0.13	100.46
MH-02-14	core	spinel	40.69	0.02	0.02	9.42	0.36	0.14	49.53	0.07	100.24
MH-02-14	rim	spinel	40.76	0.01	0.08	9.83	0.36	0.14	49.16	0.15	100.48
MH-02-14	core	spinel	40.53	0.01	0.00	9.77	0.38	0.14	49.16	0.04	100.04
Average			40.65	0.01	0.02	9.83	0.36	0.15	49.19	0.12	100.31
1 STD			0.16	0.01	0.02	0.50	0.01	0.01	0.32	0.05	0.18

Appendix A (Table A1): Mineral chemistry for olivine in xenoliths (Harder and Russell unpublished) (continued)

Sample	Analysis	SiO_2	Al_2O_3	Cr_2O_3	FeO	NiO	MnO	MgO	CaO	Na_2O	TiO_2	Total
MH-02-111		40.77	0.00	0.00	10.89	0.32	0.14	47.97	0.07	0.02	0.00	100.18
MH-02-111		40.52	0.02	0.00	11.16	0.36	0.14	48.26	0.13	0.00	0.00	100.59
MH-02-111		40.54	0.00	0.00	10.81	0.31	0.16	48.18	0.14	0.01	0.00	100.16
MH-02-111		40.72	0.01	0.07	11.04	0.31	0.20	48.42	0.13	0.02	0.00	100.92
MH-02-111		40.92	0.00	0.06	10.91	0.36	0.14	48.40	0.13	0.00	0.00	100.92
MH-02-111		40.91	0.02	0.04	11.05	0.33	0.16	48.40	0.01	0.00	0.01	100.93
Average		40.73	0.01	0.03	10.98	0.33	0.16	48.27	0.10	0.01	0.00	100.62
1 STD		0.17	0.01	0.03	0.13	0.02	0.02	0.18	0.05	0.01	0.00	0.37
MH-02-10		40.90	0.02	0.00	9.60	0.37	0.13	49.26	0.03	0.01	0.00	100.32
MH-02-10		40.94	0.00	0.03	9.54	0.44	0.13	49.61	0.03	0.01	0.00	100.73
MH-02-10		40.39	0.00	0.00	9.58	0.38	0.14	49.23	0.04	0.00	0.00	99.77
MH-02-10		40.86	0.00	0.00	9.72	0.42	0.15	49.60	0.04	0.00	0.00	100.79
MH-02-10		40.72	0.02	0.00	9.67	0.34	0.15	49.44	0.03	0.02	0.00	100.39
MH-02-10		40.73	0.00	0.05	9.56	0.42	0.11	49.33	0.00	0.01	0.03	100.23
MH-02-10	rim	40.75	0.01	0.00	9.80	0.40	0.13	49.59	0.02	0.02	0.01	100.72
MH-02-10	core	41.02	0.00	0.00	9.72	0.04	0.13	49.63	0.03	0.00	0.00	100.56
Average		40.79	0.01	0.01	9.65	0.35	0.13	49.46	0.03	0.01	0.00	100.44
1 STD		0.19	0.01	0.02	0.09	0.13	0.01	0.17	0.01	0.01	0.01	0.34
MH-02-9B		41.02	0.00	0.02	8.34	0.38	0.14	50.09	0.11	0.02	0.02	100.14
MH-02-9B		40.72	0.00	0.02	8.24	0.37	0.15	50.24	0.11	0.00	0.02	99.88
MH-02-9B		41.04	0.02	0.04	8.38	0.38	0.13	50.07	0.15	0.01	0.01	100.24
MH-02-9B		40.89	0.02	0.00	8.37	0.26	0.12	50.27	0.13	0.01	0.00	100.06
MH-02-9B		40.85	0.00	0.00	8.24	0.41	0.15	50.14	0.14	0.01	0.00	99.95
Average		40.91	0.01	0.02	8.31	0.36	0.14	50.16	0.13	0.01	0.01	100.05
1 STD		0.13	0.01	0.02	0.07	0.06	0.01	0.09	0.02	0.01	0.01	0.14

Appendix A (Table A1): Mineral chemistry for olivine in xenoliths (Harder and Russell unpublished) (continued)

Sample	Analysis	SiO_2	Al_2O_3	Cr_2O_3	FeO	NiO	MnO	MgO	CaO	Na_2O	TiO_2	Total
MH-02-108		40.34	0.00	0.03	9.30	0.36	0.14	49.57	0.03	0.01	0.00	99.78
MH-02-108		41.09	0.01	0.00	9.48	0.41	0.09	49.62	0.04	0.00	0.01	100.76
MH-02-108	rim	40.75	0.01	0.03	9.36	0.36	0.10	49.81	0.03	0.00	0.01	100.46
MH-02-108	core	41.02	0.00	0.04	9.28	0.42	0.12	49.83	0.03	0.00	0.02	100.76
MH-02-108		40.45	0.00	0.02	9.24	0.39	0.12	49.70	0.03	0.01	0.00	99.95
MH-02-108		40.77	0.01	0.00	9.27	0.36	0.12	49.54	0.03	0.01	0.00	100.12
MH-02-108		40.72	0.00	0.02	9.15	0.37	0.08	49.66	0.03	0.01	0.00	100.04
Average		40.73	0.00	0.02	9.30	0.38	0.11	49.68	0.03	0.01	0.01	100.27
1 STD		0.27	0.00	0.02	0.10	0.03	0.02	0.11	0.01	0.01	0.01	0.39
MH-02-10B		40.01	0.01	0.04	8.74	0.35	0.16	50.18	0.05	0.01	0.01	99.55
MH-02-10B		40.76	0.02	0.04	8.47	0.40	0.12	50.07	0.04	0.00	0.01	99.93
MH-02-10B		40.18	0.00	0.03	8.67	0.33	0.13	49.69	0.06	0.00	0.00	99.10
MH-02-10B		40.36	0.00	0.00	8.41	0.37	0.15	49.88	0.06	0.00	0.01	99.25
MH-02-10B		39.99	0.01	0.01	8.39	0.39	0.10	49.84	0.03	0.00	0.00	98.77
MH-02-10B		40.40	0.02	0.00	8.52	0.41	0.11	49.96	0.03	0.00	0.00	99.45
MH-02-10B		40.18	0.02	0.00	8.58	0.35	0.14	49.99	0.05	0.01	0.00	99.31
Average		40.27	0.01	0.02	8.54	0.37	0.13	49.94	0.04	0.00	0.00	99.34
1 STD		0.27	0.01	0.02	0.13	0.03	0.02	0.16	0.01	0.00	0.01	0.37

Appendix A (Table A1): Mineral chemistry for olivine in xenoliths (Harder and Russell unpublished) (continued)

Sample	Analysis	SiO_2	Al_2O_3	Cr_2O_3	FeO	NiO	MnO	MgO	CaO	Na_2O	TiO_2	Total
MH-02-18B		40.36	0.01	0.01	8.04	0.41	0.13	50.16	0.12	0.09	0.01	99.34
MH-02-18B	rim	40.43	0.01	0.00	8.39	0.38	0.10	50.26	0.17	0.00	0.00	99.74
MH-02-18B	core	40.28	0.02	0.00	8.16	0.39	0.12	49.96	0.12	0.00	0.00	99.06
MH-02-18B		39.89	0.01	0.04	8.47	0.34	0.12	49.71	0.06	0.03	0.01	98.70
MH-02-18B		39.89	0.00	0.06	8.77	0.26	0.17	49.47	0.13	0.00	0.05	98.80
MH-02-18B	rim	40.56	0.00	0.05	8.02	0.38	0.10	49.84	0.13	0.00	0.01	99.09
MH-02-18B	core	40.13	0.01	0.02	8.30	0.38	0.14	50.12	0.05	0.02	0.00	99.18
MH-02-18B		40.54	0.01	0.08	8.12	0.39	0.11	49.98	0.16	0.00	0.02	99.41
MH-02-18B		40.05	0.02	0.04	8.29	0.30	0.14	49.82	0.10	0.03	0.02	98.80
MH-02-18B	rim	40.62	0.03	0.09	8.54	0.39	0.16	50.32	0.16	0.03	0.00	100.34
MH-02-18B	core	40.45	0.02	0.07	7.99	0.38	0.09	50.19	0.13	0.02	0.00	99.34
Average		40.29	0.01	0.04	8.28	0.36	0.13	49.98	0.12	0.02	0.01	99.25
1 STD		0.26	0.01	0.03	0.25	0.04	0.03	0.26	0.04	0.03	0.01	0.47

Appendix A (Table A2): Mineral chemistry for olivine phenocrysts

Sample	Analysis	SiO_2	Al_2O_3	Cr_2O_3	FeO	NiO	MnO	MgO	CaO	Total
MH-02-16	rim	36.48	0.03	0.00	30.77	0.09	0.59	31.43	0.28	99.67
MH-02-16	core	36.61	0.02	0.01	30.70	0.07	0.60	31.51	0.25	99.77
MH-02-16	rim	36.36	0.03	0.01	30.10	0.08	0.59	31.93	0.30	99.38
MH-02-16	core	36.54	0.03	0.00	30.08	0.10	0.55	32.21	0.33	99.84
MH-02-16	rim	36.66	0.01	0.01	29.14	0.09	0.53	32.77	0.26	99.47
MH-02-16	core	36.77	0.03	0.02	29.42	0.07	0.54	32.58	0.35	99.78
MH-02-16	rim	36.66	0.04	0.01	30.07	0.07	0.58	32.34	0.28	100.05
MH-02-16	core	36.61	0.03	0.00	29.67	0.10	0.53	32.36	0.34	99.64
MH-02-16	rim	36.88	0.03	0.02	28.66	0.08	0.51	33.31	0.27	99.76
MH-02-16	core	37.07	0.03	0.00	27.43	0.12	0.47	34.11	0.34	99.57
MH-02-16	rim	36.35	0.03	0.00	31.38	0.09	0.56	31.05	0.32	99.78
MH-02-16	core	36.76	0.05	0.00	30.82	0.09	0.57	31.92	0.39	100.61
MH-02-16	rim	36.63	0.03	0.00	29.42	0.07	0.56	32.26	0.31	99.27
MH-02-16	core	36.74	0.03	0.00	28.99	0.08	0.52	32.86	0.35	99.58
MH-02-16	rim	36.34	0.03	0.00	30.37	0.09	0.55	31.51	0.27	99.17
MH-02-16	core	36.51	0.02	0.01	30.52	0.08	0.55	31.83	0.26	99.78
MH-02-16	rim	36.85	0.04	0.00	29.48	0.09	0.54	32.41	0.29	99.70
MH-02-16	core	36.94	0.02	0.01	28.41	0.11	0.54	33.43	0.34	99.80
MH-02-16	rim	36.31	0.03	0.00	31.39	0.08	0.56	30.99	0.33	99.70
MH-02-16	core	36.32	0.02	0.00	31.53	0.10	0.56	30.70	0.24	99.46
MH-02-16	rim	36.61	0.04	0.01	30.35	0.09	0.56	31.94	0.30	99.90
MH-02-16	core	36.84	0.04	0.00	29.89	0.12	0.52	32.60	0.33	100.33
MH-02-16	rim	36.74	0.03	0.00	29.70	0.09	0.56	32.43	0.28	99.82
MH-02-16	core	36.86	0.01	0.00	29.46	0.11	0.53	32.86	0.39	100.23
MH-02-16	rim	36.95	0.03	0.00	29.13	0.09	0.54	33.06	0.26	100.05
MH-02-16	core	37.24	0.04	0.00	27.97	0.09	0.56	34.22	0.34	100.47
MH-02-16	rim	36.86	0.03	0.00	29.32	0.09	0.53	32.76	0.32	99.91
MH-02-16	core	36.78	0.03	0.00	29.04	0.07	0.56	33.16	0.36	100.00
MH-02-16	rim	36.69	0.03	0.00	29.85	0.09	0.55	32.60	0.25	100.04

Appendix A (Table A2): Mineral chemistry for olivine phenocrysts (continued)

Sample	Analysis	SiO_2	Al_2O_3	Cr_2O_3	FeO	NiO	MnO	MgO	CaO	Total
MH-02-16	core	36.88	0.02	0.00	28.86	0.08	0.53	33.44	0.25	100.07
Rim average		36.62	0.03	0.00	29.94	0.09	0.55	32.18	0.29	99.71
1 STD		0.21	0.01	0.01	0.81	0.01	0.02	0.70	0.03	0.28
Core average		36.77	0.03	0.00	29.52	0.09	0.54	32.65	0.32	99.93
1 STD		0.23	0.01	0.01	1.12	0.02	0.03	0.96	0.05	0.35
MH-02-14	rim	37.11	0.02	0.00	29.41	0.10	0.49	33.01	0.44	100.59
MH-02-14	core	37.02	0.03	0.00	27.25	0.14	0.44	34.40	0.49	99.76
MH-02-14	rim	36.63	0.02	0.00	30.41	0.11	0.51	31.93	0.44	100.05
MH-02-14	core	37.43	0.03	0.00	27.52	0.14	0.42	34.63	0.44	100.61
MH-02-14	rim	36.59	0.02	0.00	30.31	0.10	0.50	31.87	0.43	99.82
MH-02-14	core	36.78	0.04	0.00	28.86	0.11	0.47	33.20	0.46	99.92
MH-02-14	rim	37.09	0.03	0.00	28.60	0.12	0.47	33.50	0.47	100.27
MH-02-14	core	37.37	0.03	0.00	27.36	0.12	0.44	34.40	0.48	100.19
MH-02-14	rim	36.55	0.02	0.00	31.39	0.06	0.52	30.93	0.45	99.92
MH-02-14	core	36.86	0.03	0.00	29.39	0.10	0.50	32.72	0.46	100.05
MH-02-14	rim	36.91	0.04	0.00	28.17	0.11	0.44	33.48	0.46	99.62
MH-02-14	core	36.88	0.03	0.00	27.95	0.13	0.42	33.91	0.46	99.78
MH-02-14	rim	36.96	0.02	0.00	30.32	0.10	0.48	31.91	0.47	100.26
MH-02-14	core	37.23	0.05	0.00	28.19	0.11	0.44	33.82	0.45	100.29
MH-02-14	rim	36.28	0.02	0.00	32.25	0.07	0.57	30.10	0.44	99.73
MH-02-14	core	36.99	0.02	0.00	28.61	0.11	0.45	33.23	0.44	99.85
MH-02-14	rim	37.02	0.03	0.00	29.52	0.12	0.53	32.48	0.43	100.14
MH-02-14	core	37.15	0.03	0.00	27.96	0.14	0.49	33.60	0.44	99.81
MH-02-14	rim	36.86	0.02	0.00	28.81	0.12	0.47	33.11	0.46	99.86
MH-02-14	core	37.13	0.02	0.00	27.61	0.15	0.46	34.24	0.44	100.05
MH-02-14	rim	36.41	0.01	0.01	30.17	0.12	0.52	31.75	0.46	99.45
MH-02-14	core	36.95	0.02	0.01	28.97	0.10	0.44	32.96	0.44	99.90
MH-02-14	rim	37.40	0.02	0.00	27.53	0.11	0.45	34.50	0.45	100.46
MH-02-14	core	37.20	0.05	0.00	27.47	0.13	0.44	34.33	0.52	100.14

Appendix A (Table A2): Mineral chemistry for olivine phenocrysts (continued)

Sample	Analysis	SiO_2	Al_2O_3	Cr_2O_3	FeO	NiO	MnO	MgO	CaO	Total
MH-02-14	rim	36.58	0.01	0.00	31.01	0.09	0.53	31.28	0.44	99.95
MH-02-14	core	36.87	0.03	0.00	29.72	0.12	0.48	32.38	0.44	100.04
MH-02-14	rim	36.54	0.01	0.00	28.89	0.12	0.52	32.38	0.45	98.91
MH-02-14	core	36.87	0.02	0.00	27.62	0.13	0.42	34.05	0.46	99.58
MH-02-14	rim	36.92	0.03	0.00	28.74	0.12	0.48	33.09	0.46	99.84
MH-02-14	core	37.03	0.03	0.00	26.97	0.12	0.41	34.36	0.46	99.39
Rim average		36.79	0.02	0.00	29.70	0.10	0.50	32.36	0.45	99.92
1 STD		0.31	0.01	0.00	1.29	0.02	0.03	1.13	0.01	0.42
Core average		37.05	0.03	0.00	28.10	0.12	0.45	33.75	0.46	99.96
1 STD		0.20	0.01	0.00	0.83	0.02	0.03	0.70	0.02	0.29
MH-02-124A	rim	36.58	0.03	0.00	28.04	0.13	0.44	32.87	0.46	98.55
MH-02-124A	core	37.23	0.03	0.00	26.70	0.15	0.44	34.67	0.47	99.70
MH-02-124A	rim	36.90	0.03	0.01	28.40	0.13	0.48	33.36	0.47	99.78
MH-02-124A	core	37.27	0.01	0.00	28.08	0.14	0.45	33.88	0.45	100.29
MH-02-124A	rim	36.71	0.02	0.00	28.33	0.13	0.47	33.16	0.47	99.30
MH-02-124A	core	37.14	0.01	0.01	27.70	0.14	0.43	34.14	0.46	100.04
MH-02-124A	rim	36.33	0.01	0.00	29.88	0.10	0.51	31.62	0.42	98.88
MH-02-124A	core	36.55	0.03	0.00	28.27	0.10	0.45	32.91	0.47	98.79
MH-02-124A	rim	36.89	0.02	0.00	29.33	0.11	0.49	32.69	0.44	99.97
MH-02-124A	core	37.09	0.01	0.00	28.09	0.12	0.44	34.04	0.46	100.25
MH-02-124A	rim	36.83	0.01	0.00	29.72	0.10	0.47	32.25	0.47	99.85
MH-02-124A	core	37.29	0.03	0.00	27.06	0.12	0.44	34.47	0.48	99.90
MH-02-124A	rim	36.86	0.02	0.01	27.97	0.14	0.40	33.16	0.49	99.04
MH-02-124A	core	37.27	0.03	0.00	27.24	0.15	0.42	34.20	0.44	99.76
MH-02-124A	rim	36.73	0.02	0.00	28.66	0.10	0.48	32.82	0.48	99.30
MH-02-124A	core	34.97	0.41	0.00	29.77	0.13	0.41	29.68	0.63	96.00
MH-02-124A	rim	37.09	0.04	0.00	28.63	0.12	0.48	33.36	0.46	100.16
MH-02-124A	core	37.41	0.02	0.00	26.95	0.15	0.43	34.87	0.45	100.29
MH-02-124A	rim	37.40	0.02	0.00	27.58	0.10	0.45	34.25	0.46	100.25

Appendix A (Table A2): Mineral chemistry for olivine phenocrysts (continued)

Sample	Analysis	SiO_2	Al_2O_3	Cr_2O_3	FeO	NiO	MnO	MgO	CaO	Total
MH-02-124A	core	36.94	0.00	0.00	27.24	0.13	0.40	34.43	0.49	99.63
MH-02-124A	rim	36.84	0.02	0.00	29.12	0.12	0.47	33.06	0.47	100.12
MH-02-124A	core	37.08	0.04	0.01	27.94	0.13	0.44	34.06	0.47	100.16
MH-02-124A	rim	37.10	0.02	0.01	28.85	0.12	0.48	33.22	0.46	100.26
MH-02-124A	core	37.22	0.04	0.01	27.42	0.13	0.42	34.54	0.46	100.23
MH-02-124A	rim	36.64	0.02	0.00	29.20	0.14	0.50	33.02	0.48	100.00
MH-02-124A	core	36.98	0.02	0.00	28.51	0.13	0.46	33.30	0.43	99.84
MH-02-124A	rim	37.22	0.03	0.01	28.62	0.13	0.47	33.67	0.49	100.64
MH-02-124A	core	37.31	0.03	0.00	27.63	0.13	0.44	34.44	0.51	100.48
MH-02-124A	rim	36.40	0.03	0.00	30.16	0.11	0.53	32.10	0.46	99.79
MH-02-124A	core	36.95	0.02	0.00	28.58	0.13	0.48	33.27	0.48	99.92
Rim average		36.84	0.02	0.00	28.83	0.12	0.47	32.97	0.46	99.73
1 STD		0.29	0.01	0.00	0.74	0.01	0.03	0.64	0.02	0.59
Core average		36.98	0.05	0.00	27.81	0.13	0.44	33.79	0.48	99.69
1 STD		0.60	0.10	0.00	0.79	0.01	0.02	1.27	0.05	1.10
MH-02-101	rim	35.66	0.02	0.00	33.89	0.05	0.63	28.19	0.53	98.97
MH-02-101	core	38.71	0.06	0.05	18.18	0.20	0.24	41.67	0.33	99.44
MH-02-101	rim	36.60	0.02	0.00	30.14	0.11	0.52	31.64	0.52	99.55
MH-02-101	core	37.76	0.01	0.00	23.92	0.14	0.36	36.98	0.45	99.61
MH-02-101	rim	36.55	0.05	0.00	29.31	0.10	0.51	32.13	0.51	99.14
MH-02-101	core	39.67	0.05	0.02	13.83	0.31	0.15	45.35	0.22	99.59
MH-02-101	rim	37.80	0.05	0.03	23.72	0.18	0.37	37.02	0.42	99.59
MH-02-101	core	39.87	0.06	0.02	14.09	0.27	0.18	45.57	0.24	100.30
MH-02-101	rim	36.62	0.05	0.01	29.38	0.11	0.49	32.03	0.53	99.23
MH-02-101	core	39.19	0.05	0.02	16.60	0.20	0.22	43.14	0.26	99.69
MH-02-101	rim	37.80	0.05	0.02	23.38	0.14	0.34	37.34	0.39	99.46
MH-02-101	core	39.28	0.07	0.04	14.63	0.26	0.18	44.88	0.24	99.58
MH-02-101	rim	35.53	0.02	0.01	35.94	0.07	0.63	26.75	0.54	99.49
MH-02-101	core	39.35	0.05	0.01	16.20	0.22	0.21	43.62	0.26	99.93

Appendix A (Table A2): Mineral chemistry for olivine phenocrysts (continued)

Sample	Analysis	SiO_2	Al_2O_3	Cr_2O_3	FeO	NiO	MnO	MgO	CaO	Total
MH-02-101	rim	36.10	0.04	0.01	32.87	0.08	0.54	29.48	0.48	99.60
MH-02-101	core	39.38	0.05	0.04	14.52	0.28	0.15	44.92	0.22	99.57
MH-02-101	rim	35.89	0.03	0.02	32.49	0.08	0.52	29.83	0.54	99.39
MH-02-101	core	39.22	0.06	0.02	15.09	0.25	0.19	44.70	0.27	99.79
MH-02-101	rim	37.36	0.05	0.01	25.71	0.10	0.40	35.47	0.50	99.60
MH-02-101	core	39.53	0.06	0.02	15.06	0.22	0.19	44.56	0.23	99.87
MH-02-101	rim	36.53	0.04	0.01	29.91	0.07	0.49	31.77	0.54	99.36
MH-02-101	core	37.82	0.03	0.02	23.84	0.14	0.40	37.37	0.50	100.12
MH-02-101	rim	37.10	0.04	0.00	28.11	0.11	0.43	33.47	0.54	99.78
MH-02-101	core	37.60	0.03	0.00	23.79	0.11	0.34	36.79	0.48	99.13
MH-02-101	rim	35.83	0.03	0.00	32.94	0.10	0.58	29.08	0.56	99.12
MH-02-101	core	35.79	0.42	0.06	30.07	0.10	0.48	31.63	0.54	99.09
MH-02-101	rim	37.79	0.04	0.02	23.19	0.11	0.36	37.51	0.48	99.49
MH-02-101	core	38.08	0.06	0.00	21.79	0.12	0.28	38.94	0.39	99.66
MH-02-101	rim	37.63	0.05	0.04	24.25	0.10	0.34	36.73	0.53	99.67
MH-02-101	core	39.43	0.06	0.04	14.65	0.22	0.17	45.08	0.23	99.87
Rim average		36.72	0.04	0.01	29.01	0.10	0.48	32.56	0.51	99.43
1 STD		0.82	0.01	0.01	4.18	0.03	0.10	3.56	0.05	0.23
Core average		38.71	0.07	0.02	18.42	0.20	0.25	41.68	0.32	99.68
1 STD		1.10	0.10	0.02	5.00	0.07	0.10	4.29	0.11	0.32

Appendix A (Table A3): Mineral chemistry for spinel in xenoliths

Sample	Analysis	SiO_2	TiO_2	Al_2O_3	V_2O_5	Cr_2O_3	FeO	NiO	MnO	MgO	CaO	O	Total
MH-02-100B	rim	0.06	0.04	33.69	0.20	35.28	11.09	0.18	0.19	17.10	0.03	0.06	97.92
MH-02-100B	core	0.00	0.05	33.53	0.21	35.52	11.27	0.18	0.19	17.33	0.02	0.11	98.41
MH-02-100B	rim	0.02	0.06	34.11	0.26	35.54	11.09	0.15	0.20	17.24	0.01	0.03	98.72
MH-02-100B	core	0.02	0.04	34.02	0.25	36.27	11.20	0.15	0.18	17.27	0.00	0.03	99.44
MH-02-100B	rim	0.10	0.03	33.47	0.21	34.93	10.72	0.17	0.15	17.10	0.01	0.04	96.91
MH-02-100B	core	0.02	0.05	33.75	0.22	36.39	10.97	0.15	0.16	17.11	0.01	0.01	98.84
MH-02-100B	rim	0.01	0.04	34.07	0.24	36.56	11.09	0.16	0.16	17.20	0.01	0.00	99.53
MH-02-100B	core	0.02	0.05	33.71	0.22	36.65	11.14	0.20	0.17	17.28	0.00	0.03	99.48
MH-02-100B	rim	0.00	0.04	33.91	0.21	36.69	11.08	0.14	0.19	17.15	0.00	0.01	99.42
MH-02-100B	core	0.02	0.04	33.58	0.25	36.39	11.18	0.15	0.19	17.11	0.00	0.03	98.94
Average		0.03	0.04	33.78	0.23	36.02	11.08	0.16	0.18	17.19	0.01	0.03	98.76
1 STD		0.03	0.01	0.23	0.02	0.64	0.15	0.02	0.02	0.09	0.01	0.03	0.84
MH-02-14	rim	0.01	0.24	51.52	0.12	15.63	11.08	0.31	0.11	19.71	0.00	0.16	98.88
MH-02-14	core	0.01	0.08	51.06	0.10	15.50	11.15	0.33	0.12	19.83	0.00	0.23	98.43
MH-02-14	rim	0.06	0.07	51.93	0.10	15.46	9.74	0.33	0.13	20.59	0.01	0.18	98.61
MH-02-14	core	0.02	0.06	52.25	0.09	15.49	9.52	0.33	0.11	20.55	0.00	0.15	98.57
MH-02-14	rim	0.05	0.11	51.43	0.15	15.38	10.54	0.38	0.13	19.88	0.01	0.17	98.22
MH-02-14	core	0.02	0.09	51.17	0.11	15.49	10.30	0.33	0.11	20.05	0.00	0.19	97.85
Average		0.03	0.11	51.56	0.11	15.49	10.39	0.33	0.12	20.10	0.00	0.18	98.42
1 STD		0.02	0.07	0.45	0.02	0.08	0.67	0.02	0.01	0.38	0.01	0.03	0.36

Appendix A (Table A4): Mineral chemistry for spinel inclusions in olivine phenocrysts

Sample	SiO_2	TiO_2	Al_2O_3	V_2O_5	Cr_2O_3	FeO	NiO	MnO	MgO	CaO	O	Total
MH-02-124A	0.10	12.19	9.42	0.96	2.85	65.76	0.13	0.41	3.18	0.05	2.91	97.96
MH-02-124A	0.07	10.58	11.29	0.92	8.48	60.69	0.15	0.39	3.96	0.09	2.58	99.20
MH-02-124A	0.03	22.34	3.40	0.66	2.48	63.85	0.10	0.48	4.28	0.06	1.97	99.65
MH-02-124A	0.04	21.07	2.25	0.50	0.08	68.49	0.08	0.54	3.23	0.09	2.52	98.90
MH-02-124A	0.07	18.50	5.02	0.74	0.58	67.63	0.13	0.44	3.10	0.10	2.57	98.88
MH-02-101	0.2	14.7	11.5	0.8	13.9	49.3	0.1	0.5	4.7	0.0	1.1	96.9
MH-02-101	0.1	2.2	19.7	0.3	27.2	38.5	0.1	0.4	6.5	0.0	1.4	96.4
MH-02-101	0.1	5.9	19.1	0.4	18.9	41.7	0.2	0.3	9.2	0.0	1.8	97.6
MH-02-101	0.2	3.2	23.8	0.3	21.1	37.8	0.1	0.3	8.6	0.0	1.5	97.0
MH-02-101	0.3	3.0	23.1	0.3	21.4	38.7	0.1	0.3	8.2	0.0	1.5	96.9
MH-02-101	0.1	8.1	19.6	0.6	17.8	40.9	0.1	0.4	8.6	0.1	1.4	97.6
MH-02-16	0.35	7.23	9.72	0.43	11.55	61.04	0.10	0.52	2.84	0.07	2.93	96.77
MH-02-16	0.10	2.82	16.88	0.34	16.43	53.31	0.06	0.43	3.73	0.05	2.57	96.72
MH-02-16	0.08	4.97	13.15	0.46	15.38	56.00	0.05	0.40	3.39	0.02	2.64	96.55
MH-02-16	0.44	2.20	14.53	0.35	19.03	53.41	0.08	0.49	3.61	0.04	2.62	96.79
MH-02-16	0.10	2.11	15.11	0.37	20.19	52.19	0.11	0.45	3.42	0.05	2.50	96.60
MH-02-16	0.11	6.26	11.43	0.45	17.49	54.14	0.10	0.50	3.43	0.13	2.37	96.40
MH-02-14	0.42	7.34	15.26	1.02	7.37	58.52	0.14	0.39	4.21	0.03	2.62	97.32
MH-02-14	0.05	14.38	7.34	0.91	2.71	65.77	0.12	0.45	3.05	0.09	2.74	97.62
MH-02-14	0.09	15.82	6.63	0.89	1.89	66.16	0.17	0.44	3.30	0.05	2.67	98.11
MH-02-14	0.10	15.95	5.14	0.97	1.04	68.87	0.10	0.51	2.41	0.05	2.83	97.98
MH-02-14	0.11	10.71	10.22	0.90	6.82	61.92	0.09	0.41	3.57	0.06	2.71	97.51
MH-02-14	0.06	22.89	2.17	0.58	0.22	66.47	0.11	0.57	2.87	0.05	2.06	98.05
MH-02-14	0.08	16.79	5.25	0.86	0.61	67.65	0.11	0.50	2.75	0.05	2.71	97.36

Appendix B: Mineral analyses by LA-ICP-MS in ppm.

Appendix B (Table B1): Trace element data for olivine in xenoliths

Sample	Next to	Al	Ca	Sc	Ti	V	Cr	Mn	Co	Ni	Cu	Zn	Y
MH-02-121	spinel	30.0	171.3	2.8	4.0	2.2	39.91	1158.4	156.9	3667.2	0.8	59.4	0.0
MH-02-121	spinel	32.7	189.3	2.9	4.2	2.0	38.29	1128.4	150.6	3553.4	0.5	56.4	0.0
MH-02-121	cpx	38.5	184.8	3.1	5.7	2.3	40.25	1165.2	160.7	3772.6	0.9	55.0	0.0
MH-02-121	cpx	34.7	208.1	3.2	4.9	2.3	40.03	1162.3	155.7	3542.7	1.2	54.7	0.0
MH-02-121	cpx	29.6	171.5	2.8	4.8	1.9	42.01	1190.4	166.1	3821.7	0.7	59.6	0.0
MH-02-121	spinel	34.3	180.4	3.1	4.7	2.0	38.22	1145.8	159.3	3601.7	0.6	58.7	0.0
MH-02-121	spinel	33.7	174.2	3.0	4.7	2.1	39.77	1153.4	159.9	3606.0	1.0	57.9	0.0
MH-02-10B	cpx	33.5	163.7	3.1	1.6	1.9	59.12	1157.0	158.2	3557.9	BLOD	50.7	0.0
MH-02-10B	spinel	39.4	166.6	3.2	2.0	2.2	70.50	1149.0	161.4	3602.1	0.6	52.4	0.0
MH-02-10B	spinel	28.8	168.7	2.9	2.1	1.8	54.21	1065.7	149.8	3354.3	BLOD	45.9	0.0
MH-02-10B	spinel	31.4	156.2	3.3	1.4	2.3	61.80	1121.0	156.8	3445.3	BLOD	46.6	0.0
MH-02-10B	spinel	34.1	168.1	3.4	1.2	2.0	60.37	1108.5	154.8	3441.4	1.2	45.7	0.0
MH-02-10B	spinel	37.7	172.0	3.1	2.6	1.9	58.78	1105.8	150.3	3334.1	3.4	50.0	0.0
MH-02-10B	cpx	32.4	160.2	3.3	1.1	2.0	64.40	1115.3	156.6	3565.9	BLOD	47.0	0.0
MH-02-10B	cpx	32.2	154.0	3.3	1.3	1.8	60.95	1114.9	154.2	3458.8	BLOD	46.8	0.0
MH-02-10B	cpx	28.5	158.9	2.9	1.7	1.7	57.23	1073.7	148.1	3270.3	BLOD	46.3	0.0
MH-02-10B	cpx	34.7	158.6	3.3	2.1	1.9	60.89	1118.4	154.5	3376.1	0.7	46.2	0.0
MH-02-10D	spinel	27.6	576.1	4.6	4.4	9.6	225.76	1241.9	154.1	3278.3	2.2	65.6	0.1
MH-02-10D	cpx	26.1	744.8	7.9	4.9	13.6	389.60	1342.7	146.4	2752.5	1.8	57.2	0.1
MH-02-10D	cpx	36.3	840.6	7.2	5.6	11.2	291.51	1268.4	142.4	2984.2	2.1	56.8	0.1
MH-02-10D	cpx	30.2	758.6	5.5	3.5	11.6	413.45	1239.3	140.0	2924.5	2.3	54.2	0.1
MH-02-10D	spinel	24.5	752.6	6.6	5.8	10.6	288.34	1308.6	148.0	3050.7	2.8	67.8	0.1
MH-02-10D	spinel	25.3	811.2	7.2	3.6	10.5	315.04	1270.6	140.0	2899.7	1.9	64.0	0.1
MH-02-10D	spinel	26.1	823.1	7.4	4.2	11.1	322.39	1292.6	146.7	2807.0	2.3	68.4	0.1
MH-02-10D	spinel	27.8	791.5	9.9	6.3	12.5	349.44	1361.7	138.2	2544.5	2.1	68.5	0.1

Appendix B (Table B1): Trace element data for olivine in xenoliths (continued)

Sample	Next to	Al	Ca	Sc	Ti	V	Cr	Mn	Co	Ni	Cu	Zn	Y
MH-02-10	spinel	24.8	156.8	1.6	8.0	1.0	19.7	979.0	135.6	2787.9	BLOD	35.9	0.0
MH-02-10	cpx	29.7	162.3	1.7	8.9	1.1	22.3	997.7	134.4	2828.9	1.1	37.4	0.0
MH-02-10	cpx	26.6	151.7	1.5	8.4	1.1	22.2	994.3	136.7	2831.4	BLOD	38.0	BLOD
MH-02-10	spinel	31.6	166.0	1.5	10.9	1.1	22.7	995.1	132.0	2707.0	1.8	37.7	0.0
MH-02-10	cpx	31.5	150.3	1.6	9.2	1.2	24.9	996.6	134.2	2862.5	BLOD	39.7	0.0
MH-02-10	cpx	32.5	165.4	1.6	8.3	1.0	22.7	986.7	132.0	2757.7	2.5	38.5	0.0
MH-02-10	cpx	26.7	154.9	1.5	6.7	1.2	22.4	974.5	132.2	2722.1	4.7	36.6	0.0
MH-02-10	spinel	24.0	144.4	1.4	6.9	1.1	20.7	1008.8	132.6	2803.8	BLOD	39.0	0.0
MH-02-10	spinel	28.4	154.1	1.5	8.9	1.1	21.6	990.6	132.5	2746.4	1.6	39.0	0.0
MH-02-108	cpx + spinel	38.8	199.8	1.6	9.6	1.5	44.4	957.2	132.2	2784.6	1.9	48.6	0.0
MH-02-108	cpx	33.5	181.1	1.6	8.9	1.5	40.8	947.7	129.7	2835.7	1.4	46.9	0.0
MH-02-108	cpx	34.9	187.2	1.7	8.7	1.4	42.5	953.0	130.8	2785.8	4.1	54.3	0.0
MH-02-108	cpx + spinel	31.6	186.1	1.6	7.2	1.5	42.0	949.4	131.8	2852.1	BLOD	45.1	0.0
MH-02-108	olivine	31.4	175.4	1.6	8.8	1.5	43.8	951.6	133.3	2850.0	BLOD	45.0	0.0
MH-02-108	olivine	37.4	191.2	1.5	8.7	1.5	43.0	942.5	129.6	2797.1	1.8	49.8	0.0
MH-02-108	cpx	30.7	180.0	1.6	7.6	1.4	40.7	908.2	125.3	2754.4	BLOD	43.5	0.0
MH-02-18B	cpx	42.5	783.3	3.2	4.1	4.5	258.1	908.3	130.9	2943.8	0.8	48.9	0.0
MH-02-18B	cpx	40.7	481.8	2.9	3.6	5.2	274.7	917.4	130.8	2982.0	2.8	50.4	0.0
MH-02-18B	spinel	49.2	745.6	3.1	4.5	4.2	197.2	902.6	130.4	2938.4	1.6	51.1	0.0
MH-02-18B	spinel	50.6	541.3	3.3	3.6	5.0	210.0	952.6	131.8	3032.3	2.8	51.0	0.0
MH-02-18B	cpx	40.6	737.0	3.0	3.8	7.0	385.9	949.0	123.1	2802.1	4.1	49.0	0.0
MH-02-18B	cpx	41.7	667.8	3.0	7.2	4.9	229.4	909.7	130.2	2947.2	1.6	49.5	0.0
MH-02-18B	spinel	45.8	507.9	3.7	1.6	4.5	234.4	942.9	131.1	3014.2	1.9	55.5	0.0
MH-02-18B	spinel	35.2	640.0	3.6	20.6	7.3	222.5	929.6	135.9	3054.2	2.1	57.7	0.1
MH-02-18B	spinel	49.8	325.0	2.6	2.1	5.0	204.5	917.3	128.6	3004.5	5.9	58.3	BLOD
MH-02-18B	spinel	45.3	683.6	3.7	1.2	3.7	237.0	920.3	127.9	2897.0=	1.2	53.9	0.0

Appendix B (Table B1): Trace element data for olivine in xenoliths (continued)

Sample	Next to	Al	Ca	Sc	Ti	V	Cr	Mn	Co	Ni	Cu	Zn	Y
MH-02-112	cpx	19.3	393.5	2.7	9.4	2.9	263.4	895.2	122.5	2839.1	1.2	49.5	0.0
MH-02-112	cpx	33.3	273.7	3.2	2.6	3.5	208.4	887.8	123.9	2734.3	1.0	45.5	0.0
MH-02-112	cpx	20.6	536.7	3.0	8.8	3.5	264.8	862.6	119.3	2700.6	1.0	43.2	0.0
MH-02-112	spinel	30.5	255.9	2.4	2.3	2.8	173.3	876.5	126.7	2838.9	1.3	49.9	0.0
MH-02-112	cpx	21.7	477.0	3.3	7.9	4.1	322.0	908.6	121.0	2627.1	1.4	47.7	0.0
MH-02-112	spinel	41.4	259.4	3.5	0.8	2.9	181.5	929.7	123.3	2714.1	1.2	58.8	0.0
MH-02-112	spinel	26.1	285.4	2.4	6.0	2.6	160.7	904.4	133.0	2859.6	1.0	54.4	0.1
MH-02-112	cpx	28.3	328.1	2.7	7.2	3.8	259.0	879.3	122.0	2619.6	1.1	45.5	0.0
MH-02-112	spinel	39.7	242.6	2.4	1.4	2.9	119.8	891.5	128.6	2785.7	0.9	54.4	0.0
MH-02-112	spinel	30.7	406.2	3.3	3.2	2.6	220.8	944.9	132.3	2726.8	1.0	61.9	0.0
MH-02-117-2	spinel	49.3	303.2	2.5	5.7	3.5	127.1	887.3	122.0	2706.0	1.0	47.2	0.0
MH-02-117-2	cpx	35.7	290.5	2.7	9.5	5.1	185.7	949.9	127.3	2817.0	BLOD	50.8	0.0
MH-02-117-2	cpx	34.1	317.5	2.3	13.9	3.0	139.3	840.8	124.4	2712.7	BLOD	45.2	0.0
MH-02-117-2	spinel	29.1	377.8	2.6	11.0	4.8	306.2	928.6	127.2	2970.0	1.2	53.3	0.0
MH-02-117-2	spinel	39.5	286.3	3.2	4.1	4.5	174.1	924.5	133.2	2844.6	BLOD	55.9	0.0
MH-02-117-2	spinel	31.8	326.4	2.6	14.7	4.5	185.6	912.2	127.0	2945.1	0.6	49.4	0.0
MH-02-117-2	cpx	35.3	274.9	2.5	11.3	3.2	139.6	898.6	125.8	2805.1	BLOD	46.1	0.0
MH-02-117-2	cpx	37.1	307.9	2.8	5.3	3.8	158.5	898.5	129.6	2899.1	BLOD	51.8	0.0
MH-02-117-2	cpx	43.1	270.0	2.3	3.3	3.0	115.2	860.3	121.2	2792.5	1.2	45.7	0.0
MH-02-117-2	spinel	43.4	285.5	2.4	3.1	4.2	161.1	895.8	128.1	2820.5	1.1	47.4	0.0
MH-02-117-2	spinel	48.2	310.1	2.6	4.0	3.3	118.4	863.5	124.3	2830.4	0.9	46.1	0.0
MH-02-111	cpx	31.3	440.9	1.8	28.1	3.7	68.2	1123.7	137.4	2709.1	3.0	46.6	0.1
MH-02-111	cpx	34.9	219.0	1.7	19.4	3.1	35.4	1073.7	130.9	2586.3	1.2	45.5	0.0
MH-02-111	spinel	26.8	362.3	1.7	20.9	4.3	70.5	1107.7	140.7	2452.7	BLOD	50.4	0.1
MH-02-111	cpx	34.7	194.5	1.4	13.9	2.3	26.9	1093.9	138.0	2548.7	BLOD	41.6	0.0
MH-02-111	spinel	34.9	213.9	1.5	18.6	2.9	36.9	1152.5	142.0	2776.2	BLOD	56.9	0.0
MH-02-111	spinel	27.6	206.6	1.4	18.1	3.1	36.8	1086.7	135.6	2676.2	BLOD	50.4	0.0
MH-02-111	cpx	33.3	221.6	1.5	19.9	2.8	40.4	1148.0	134.6	2588.5	BLOD	50.0	0.0
MH-02-111	spinel	35.9	268.6	1.6	19.1	2.8	42.0	1117.9	137.4	2654.1	1.1	50.7	0.1
MH-02-111	spinel	40.2	218.6	1.5	19.9	2.5	30.3	1139.1	140.1	2709.2	1.7	49.2	0.0

Appendix B (Table B1): Trace element data for olivine in xenoliths (continued)

Sample	Next to	Al	Ca	Sc	Ti	V	Cr	Mn	Co	Ni	Cu	Zn	Y
MH-02-100	spinel	52.6	288.2	2.3	0.4	1.7	89.1	891.4	123.9	2854.8	BLOD	46.7	BLOD
MH-02-100	spinel	45.2	290.0	2.2	0.6	1.2	88.4	864.4	121.6	2752.7	3.4	52.3	BLOD
MH-02-100	cpx	40.3	347.8	2.2	BLOD	1.8	141.0	874.3	125.3	2809.1	0.5	48.1	BLOD
MH-02-100	cpx	46.3	304.9	2.1	0.3	1.4	80.7	858.2	125.2	2836.6	0.5	46.4	BLOD
MH-02-100	cpx	38.1	261.0	1.8	0.2	1.4	82.5	861.1	128.6	2952.5	0.7	44.3	BLOD
MH-02-100	cpx	52.0	294.8	2.1	1.6	1.5	84.8	888.5	124.0	2918.0	4.3	54.0	BLOD
MH-02-100	cpx	42.8	276.7	2.1	0.4	1.5	84.0	895.7	133.5	3104.5	1.2	46.5	BLOD
MH-02-100	spinel	57.3	289.1	2.6	0.3	1.5	97.9	858.9	125.1	2852.8	BLOD	47.5	BLOD
MH-02-100	spinel	41.0	279.8	2.1	BLOD	1.7	114.4	889.1	125.9	2865.1	0.6	50.5	BLOD
MH-02-100	spinel	43.1	294.3	2.3	0.1	1.4	81.8	878.8	128.8	2946.2	BLOD	45.1	BLOD
MH-02-12	spinel	32.0	367.9	4.0	5.8	6.8	188.9	1019.9	129.6	2707.4	3.0	53.8	0.1
MH-02-12	spinel	51.8	799.5	5.1	13.2	8.8	281.8	1071.8	135.1	2827.5	2.8	57.8	0.1
MH-02-12	spinel	29.9	798.5	5.2	8.5	8.5	273.1	1061.7	129.4	2805.7	2.8	55.1	0.1
MH-02-12	cpx	29.4	917.9	4.0	7.4	7.9	250.0	1044.8	130.3	2713.7	3.7	59.8	0.1
MH-02-12	cpx	34.2	1027.3	4.6	8.7	8.1	289.2	1066.7	129.6	2727.9	4.2	63.1	0.1
MH-02-12	cpx + spinel	30.2	1037.5	4.7	6.9	7.1	255.3	1042.2	128.2	2667.2	2.3	60.2	0.1
MH-02-12	spinel	41.3	1011.5	7.7	8.6	8.9	258.4	1107.6	126.7	2578.5	1.6	67.6	0.1
MH-02-12	spinel	33.0	1105.9	5.5	7.3	8.6	250.3	1061.6	125.5	2725.8	1.7	53.4	0.1
MH-02-12	spinel	30.7	663.7	4.8	5.7	8.1	226.8	1009.1	128.4	2749.1	2.2	57.5	0.1
MH-02-12	olivine	33.0	1003.9	7.2	5.4	9.5	271.4	1086.4	131.6	2711.4	2.8	61.6	0.1
MH-02-04	spinel	20.4	118.4	1.4	0.9	0.9	48.3	863.6	120.1	2668.2	2.8	38.1	BLOD
MH-02-04	spinel	26.1	125.1	1.5	2.4	0.9	43.5	875.3	123.6	2706.9	1.4	37.5	0.0
MH-02-04	spinel	22.3	122.9	1.6	1.6	0.9	43.9	877.9	124.3	2810.5	3.0	36.9	0.0
MH-02-04	cpx	23.9	129.9	1.7	2.1	1.0	42.6	905.6	126.4	2826.7	BLOD	40.4	BLOD
MH-02-04	spinel	38.1	121.7	1.6	3.8	1.2	61.1	906.6	127.0	2772.2	2.3	39.7	0.0
MH-02-04	cpx	31.0	132.5	1.8	3.0	0.9	45.7	921.4	129.3	2903.8	0.5	40.6	BLOD
MH-02-04	cpx	21.5	117.2	1.4	1.6	0.9	39.7	886.6	125.2	2778.2	BLOD	41.9	0.0
MH-02-04	cpx	28.8	133.1	1.8	2.5	1.0	42.1	908.7	125.9	2800.9	BLOD	40.0	0.0
MH-02-04	spinel	23.7	124.8	1.7	2.2	0.9	38.7	894.6	126.6	2830.5	0.4	40.2	0.0

Appendix B (Table B1): Trace element data for olivine in xenoliths (continued)

Sample	Next to	Al	Ca	Sc	Ti	V	Cr	Mn	Co	Ni	Cu	Zn	Y
MH-02-9B	spinel + cpx	29.1	326.9	2.1	6.9	1.7	98.0	857.3	122.9	2700.5	0.8	47.0	0.0
MH-02-9B	spinel + cpx	25.8	360.6	2.1	12.0	1.7	135.6	861.1	122.2	2697.1	0.9	48.1	0.0
MH-02-9B	spinel	29.3	341.4	2.3	9.3	1.9	129.6	882.3	122.9	2722.1	1.2	46.3	0.0
MH-02-9B	spinel	30.6	291.1	2.1	5.9	1.7	84.0	887.6	128.8	2830.2	1.3	46.6	0.0
MH-02-9B	spinel	27.1	286.3	2.0	4.9	1.7	100.3	870.5	122.7	2630.5	0.9	49.1	0.0
MH-02-9B	cpx	23.0	303.8	2.0	12.4	2.0	107.0	864.4	123.6	2730.8	0.9	46.4	0.0
MH-02-9B	cpx	27.96	315.4	2.3	6.0	1.8	96.0	894.7	124.8	2809.8	1.0	44.3	0.0
MH-02-9B	cpx	25.8	322.3	2.3	15.6	2.2	95.0	890.4	128.9	2864.1	0.7	49.5	0.0
MH-02-9B	spinel	30.6	303.3	2.1	5.4	2.0	142.9	895.1	126.1	2781.3	2.3	48.9	0.0
MH-02-9B	spinel	32.3	291.9	2.5	3.0	2.1	83.0	905.6	128.3	2876.3	0.9	48.9	0.0
MH-02-10C	cpx	50.4	285.3	2.3	1.8	2.7	109.2	925.4	126.4	2805.8	0.5	44.9	0.0
MH-02-10C	cpx	54.4	428.2	2.6	3.5	3.2	157.8	940.9	130.0	2910.3	1.1	48.1	0.0
MH-02-10C	cpx	51.3	462.7	2.6	5.5	3.4	173.2	885.8	127.3	2880.8	0.8	46.9	0.0
MH-02-10C	cpx + spinel	50.0	448.6	2.6	6.2	4.1	186.2	931.6	129.2	2932.6	1.6	47.1	0.0
MH-02-10C	cpx	57.6	326.4	2.6	4.7	3.4	118.3	938.3	129.0	2904.2	2.0	46.6	0.0
MH-02-10C	spinel	44.1	529.0	2.3	5.9	3.3	232.7	918.3	128.2	2918.6	1.4	43.5	0.0
MH-02-10C	spinel	46.7	653.1	2.4	8.1	4.3	287.1	910.4	129.0	2889.8	2.6	47.3	0.0
MH-02-10C	spinel	47.9	527.0	3.0	8.3	4.0	228.6	975.4	135.5	2948.6	3.4	54.7	0.0
MH-02-10C	spinel	46.7	904.6	3.3	12.5	4.2	293.4	953.4	130.5	2786.0	2.1	49.1	0.0
MH-02-10C	spinel	49.0	551.5	2.5	7.4	3.8	207.0	923.5	132.6	3020.0	0.7	45.3	0.0
MH-02-15	cpx	36.1	565.6	2.7	3.6	6.9	204.3	968.7	127.6	2681.7	1.7	42.0	0.1
MH-02-15	spinel	30.8	421.9	2.0	2.8	4.6	135.6	921.4	127.0	2704.4	0.6	48.5	0.0
MH-02-15	cpx	39.0	561.0	2.5	7.7	5.6	167.2	956.9	131.5	2822.8	1.0	43.8	0.1
MH-02-15	spinel	30.3	263.0	2.1	1.7	3.6	126.4	951.8	131.3	2787.3	0.7	52.2	0.0
MH-02-15	cpx + spinel	31.1	430.5	2.2	1.9	4.3	153.5	930.0	133.2	2704.0	0.9	55.4	0.0
MH-02-15	spinel	31.3	723.0	4.4	4.5	7.5	288.8	979.0	118.1	2403.2	2.6	45.6	0.1
MH-02-15	cpx + spinel	37.6	496.1	3.3	4.2	4.4	132.3	988.5	126.4	2702.1	2.7	52.3	0.0
MH-02-15	cpx	25.1	466.5	3.1	3.5	6.7	195.9	939.0	126.9	2784.2	0.7	41.5	0.0
MH-02-15	spinel	30.6	345.0	2.2	3.2	4.5	178.7	1036.2	133.0	2735.9	2.1	65.4	0.0
MH-02-15	spinel	31.9	312.3	1.9	3.3	3.8	110.2	981.5	128.0	2841.5	0.6	46.3	0.0

Appendix B (Table B1): Trace element data for olivine in xenoliths (continued)

Sample	Next to	Al	Ca	Sc	Ti	V	Cr	Mn	Co	Ni	Cu	Zn	Y
MH-02-125	spinel	49.1	324.5	2.6	1.3	2.0	93.2	900.8	123.9	2803.3	0.9	45.1	0.0
MH-02-125	spinel	49.0	339.4	2.5	1.7	2.1	90.7	892.7	124.4	2818.8	0.7	44.8	0.0
MH-02-125	cpx	31.9	400.2	2.7	18.3	3.2	111.2	926.8	122.6	3074.5	0.6	47.0	0.0
MH-02-125	cpx	33.4	435.3	2.7	19.5	3.4	128.7	888.2	122.2	2777.0	0.5	44.3	0.1
MH-02-125	spinel	46.1	344.6	2.7	5.5	3.6	173.6	905.0	124.7	2850.9	1.7	54.7	0.0
MH-02-125	cpx	45.9	348.3	2.6	4.0	2.4	97.0	908.3	124.4	2836.1	0.8	46.9	0.0
MH-02-125	cpx	45.9	363.3	2.5	10.7	3.0	125.8	925.1	125.2	2866.8	2.2	50.2	0.0
MH-02-125	cpx	32.3	513.4	2.8	20.3	3.8	178.7	912.4	123.5	2810.5	0.8	47.5	0.0
MH-02-125	spinel	48.6	349.3	2.8	1.0	2.6	103.7	921.2	127.3	2919.8	0.9	48.9	0.0
MH-02-125	spinel	38.8	338.6	2.2	5.5	2.9	162.0	900.6	129.2	2909.8	1.2	48.8	0.0
MH-02-116	cpx	29.8	298.5	2.3	11.7	2.2	96.9	950.9	133.2	3048.6	0.8	50.6	0.0
MH-02-116	cpx	36.3	471.7	2.3	13.3	2.1	124.3	899.7	129.0	2900.3	1.7	51.8	0.0
MH-02-116	cpx	47.2	319.2	2.4	1.9	1.9	90.8	922.8	133.1	3066.7	2.9	56.2	0.0
MH-02-116	spinel	30.8	397.3	2.5	4.2	2.5	169.7	936.9	132.0	2924.8	1.3	64.7	0.0
MH-02-116	spinel	43.1	369.0	2.2	6.9	2.6	102.0	925.4	130.8	3019.2	2.3	56.0	0.0
MH-02-116	spinel	42.4	332.8	2.3	5.3	2.0	106.8	890.5	131.8	3035.7	1.7	56.5	0.0
MH-02-116	cpx	38.3	359.5	2.7	17.2	3.4	114.6	883.5	129.7	2933.3	1.7	50.0	0.1
MH-02-116	spinel	35.8	338.2	2.2	0.4	2.5	96.7	894.5	131.1	2990.0	1.1	51.6	0.0
MH-02-116	cpx	32.8	301.6	2.0	3.6	2.7	103.1	941.1	135.2	2974.0	1.5	55.6	0.0
MH-02-116	spinel	32.0	387.7	2.3	4.4	2.0	169.1	889.1	130.7	2996.8	1.5	56.8	0.0
MH-02-19	cpx	27.6	310.0	2.5	25.4	5.9	202.7	918.4	132.9	2870.0	1.2	47.3	0.1
MH-02-19	cpx	28.0	503.1	3.5	37.8	6.8	297.6	949.3	134.1	2897.3	0.7	50.6	0.1
MH-02-19	cpx	29.1	280.4	3.2	28.2	6.5	156.0	932.2	143.8	3117.7	1.0	47.6	0.0
MH-02-19	cpx	32.4	363.6	3.0	27.3	7.0	239.2	927.1	130.9	2867.1	1.2	49.6	0.1
MH-02-19	cpx	43.9	318.5	3.2	16.8	5.1	113.2	870.2	129.6	2821.4	1.3	45.1	0.0
MH-02-19	spinel	40.2	450.9	3.9	18.6	4.0	192.0	918.9	127.6	2722.5	0.8	50.7	0.1
MH-02-19	spinel	31.2	333.8	3.1	36.0	8.8	257.0	921.6	123.0	2637.9	2.1	47.2	0.1
MH-02-19	spinel	31.4	508.7	3.3	29.8	6.4	354.3	953.4	124.7	2730.4	1.1	46.4	0.0
MH-02-19	spinel	32.6	522.9	3.1	36.7	5.9	209.7	904.6	128.8	2796.7	2.5	47.5	0.1
MH-02-19	olivine	37.5	286.9	2.6	19.0	5.9	142.6	921.5	127.0	2766.1	1.2	50.5	0.0

Appendix B (Table B1): Trace element data for olivine in xenoliths (continued)

Sample	Next to	Al	Ca	Sc	Ti	V	Cr	Mn	Co	Ni	Cu	Zn	Y
MH-02-115	spinel	40.5	593.2	2.8	10.0	3.1	203.3	855.3	125.3	2786.0	1.6	46.9	0.0
MH-02-115	cpx	41.9	438.1	2.7	6.9	2.4	167.7	886.3	127.8	2843.5	1.2	48.7	0.0
MH-02-115	cpx	37.0	610.9	2.5	5.2	3.1	213.7	898.2	126.3	2903.9	0.7	50.2	0.0
MH-02-115	cpx	47.9	837.8	3.2	6.5	3.1	178.0	887.4	129.5	2886.8	1.6	46.6	0.0
MH-02-115	cpx	48.5	440.7	2.4	2.9	2.5	103.4	913.7	130.6	2993.5	1.7	45.0	0.0
MH-02-115	cpx + spinel	45.4	371.3	2.5	3.8	2.1	107.3	877.8	126.6	2858.2	2.2	51.7	0.0
MH-02-115	spinel	43.3	621.6	2.9	10.3	2.9	198.8	901.8	130.4	2975.3	4.7	53.5	0.0
MH-02-115	spinel	39.0	517.4	2.3	12.3	2.7	139.6	880.5	126.5	2889.2	0.8	47.5	0.0
MH-02-115	spinel	48.3	336.4	2.5	2.1	1.6	111.2	870.3	128.2	2920.6	3.4	48.9	0.0
95LM1	cpx	42.3	314.5	2.2	0.2	1.7	108.5	862.6	121.8	2823.8	1.1	45.6	BLOD
95LM1	cpx	48.9	378.8	2.3	BLOD	1.8	102.3	882.4	127.0	2893.8	0.7	46.1	0.0
95LM1	spinel	49.3	477.0	2.8	0.4	2.5	161.5	933.0	131.2	2855.5	2.2	61.1	0.0
95LM1	spinel	47.8	324.0	2.1	0.7	1.6	109.9	888.1	128.6	2900.4	1.8	62.8	BLOD
95LM1	cpx	49.1	308.9	2.3	0.2	1.9	120.8	938.3	134.8	3097.6	0.9	49.9	0.0
95LM1	cpx	46.5	592.9	2.8	0.6	2.0	139.6	876.5	128.2	2910.3	0.6	48.4	BLOD
95LM1	spinel	44.9	309.6	2.7	0.2	1.8	113.1	898.5	129.9	2946.5	1.1	47.9	0.0
95LM1	spinel	42.8	742.1	2.7	BLOD	2.0	289.4	878.3	122.4	2830.1	1.2	44.1	BLOD
95LM1	spinel	49.0	333.8	2.6	0.4	1.7	107.8	864.5	123.1	2788.0	1.8	57.4	0.0
95LM1	cpx	47.1	343.2	2.3	0.7	1.7	121.7	896.6	129.4	2900.1	1.4	50.0	0.0
MH-02-117-1	spinel	43.2	348.6	2.2	8.3	2.7	167.2	844.2	125.0	2685.7	1.8	42.6	0.0
MH-02-117-1	cpx	50.3	389.7	3.4	10.0	3.7	191.3	875.9	129.3	2793.5	3.3	42.9	0.0
MH-02-117-1	spinel	45.0	423.0	3.5	8.0	3.6	154.8	882.5	130.1	2809.1	BLOD	50.1	0.0
MH-02-117-1	cpx	41.1	501.9	2.9	19.2	3.2	119.1	851.5	127.7	2802.8	BLOD	45.6	0.0
MH-02-117-1	spinel	40.3	617.9	3.0	7.8	4.3	275.2	888.8	125.9	2760.6	1.6	45.0	0.0
MH-02-117-1	spinel	36.0	664.0	2.7	18.8	3.6	260.1	907.0	130.7	2734.1	2.2	46.0	0.0
MH-02-117-1	spinel	49.4	470.1	4.0	5.2	3.6	186.3	946.6	128.5	2765.1	1.5	52.4	0.0
MH-02-117-1	cpx	43.0	511.8	2.9	15.0	3.3	148.4	864.8	128.6	2810.3	1.4	43.3	0.0
MH-02-117-1	cpx	44.6	406.8	2.8	10.2	3.6	146.5	892.1	129.3	2850.3	2.0	45.2	0.0
MH-02-117-1	cpx	41.0	416.2	2.7	16.7	4.1	159.2	862.7	125.9	2746.6	BLOD	47.5	0.1

Appendix B (Table B1): Trace element data for olivine in xenoliths (continued)

Sample	Next to	Al	Ca	Sc	Ti	V	Cr	Mn	Co	Ni	Cu	Zn	Y
MH-02-20	spinel	30.2	223.9	1.9	8.5	4.8	133.8	945.7	123.0	2583.7	0.6	50.1	0.0
MH-02-20	spinel	32.6	678.2	2.9	7.2	5.0	238.1	1084.9	138.6	2379.5	0.8	68.3	0.0
MH-02-20	spinel	25.7	244.6	2.4	9.4	7.1	107.6	992.8	125.9	2608.4	1.0	45.2	0.1
MH-02-20	spinel	26.8	559.9	2.6	7.6	4.9	148.3	1030.2	131.0	2579.9	0.7	60.8	0.1
MH-02-20	cpx	40.4	594.3	2.7	16.1	7.9	216.8	1001.1	130.3	2766.9	1.1	44.1	0.1
MH-02-20	cpx	28.5	176.1	2.1	9.0	6.0	85.2	996.8	135.1	2893.9	BLOD	43.6	0.0
MH-02-20	cpx	27.8	842.7	2.9	7.0	7.5	299.5	994.0	135.6	2676.2	0.9	44.2	0.1
MH-02-20	spinel	27.1	668.0	3.2	5.9	7.5	306.2	1056.8	137.9	2602.1	0.8	61.3	0.1
MH-02-20	spinel	54.8	823.9	2.9	30.6	6.0	152.9	992.5	135.6	2814.3	BLOD	46.6	0.1
MH-02-20	spinel	24.1	661.2	2.7	7.6	6.3	208.1	1003.4	131.6	2662.8	1.2	42.8	0.1
MH-02-115B	spinel	44.1	351.9	2.2	5.1	2.1	116.0	915.6	130.8	2989.9	0.8	55.5	0.0
MH-02-115B	spinel	42.4	643.9	2.3	6.7	2.0	146.9	939.4	134.9	3058.7	BLOD	52.4	0.0
MH-02-115B	cpx	38.9	391.6	2.1	6.6	2.0	143.0	913.8	130.2	2962.8	0.7	46.9	0.0
MH-02-115B	cpx	53.0	390.2	2.3	4.8	1.9	95.9	889.1	126.4	2922.4	1.0	49.8	0.0
MH-02-115B	cpx	47.2	531.1	2.4	6.5	2.4	155.1	873.2	130.1	2866.2	1.6	50.9	0.0
MH-02-115B	cpx	42.6	521.3	2.1	7.5	1.8	132.3	868.5	123.9	2774.4	0.8	49.8	0.0
MH-02-115B	spinel	46.4	607.4	2.4	4.8	2.0	140.1	889.4	126.9	2878.1	0.7	46.7	0.0
MH-02-115B	spinel	40.6	721.8	2.3	7.9	2.1	203.6	875.3	126.4	2909.8	0.9	49.8	0.0
MH-02-115B	spinel	44.8	309.8	2.1	5.5	1.9	112.3	877.1	128.9	2957.0	1.0	49.5	0.0
MH-02-115B	spinel	39.8	359.3	2.2	8.4	2.2	148.0	911.6	125.1	2882.2	1.1	50.4	0.0
MH-02-109	cpx + spinel	95.2	401.2	2.3	2.3	2.1	157.9	888.0	130.9	2980.9	1.6	50.8	0.0
MH-02-109	cpx	92.5	410.3	2.2	2.3	2.1	158.2	913.0	129.1	2962.0	2.4	46.2	0.0
MH-02-109	cpx	90.2	421.1	2.3	2.0	2.2	156.5	891.8	129.2	2937.3	2.1	49.1	0.0
MH-02-109	spinel	80.1	371.0	2.2	1.9	2.1	155.2	902.8	129.6	2859.0	1.6	47.9	0.0
MH-02-109	spinel	85.6	404.9	2.2	1.9	2.0	145.5	847.4	131.9	2937.8	2.2	47.4	0.0
MH-02-109	cpx + spinel	89.9	394.6	2.2	1.7	2.0	151.8	883.9	127.7	2941.1	2.5	45.2	0.0
MH-02-109	cpx	83.0	385.1	2.1	2.5	2.1	150.7	871.7	124.5	2888.4	1.7	49.0	0.0
MH-02-109	cpx	95.3	436.0	2.4	2.7	1.9	151.3	880.8	125.4	2826.8	2.0	45.7	0.0
MH-02-109	spinel	91.0	412.9	2.3	2.8	2.0	155.6	898.1	131.5	2996.6	2.6	48.2	0.0
MH-02-109	cpx	87.2	389.5	2.2	1.6	2.2	151.6	868.6	128.3	2975.1	1.9	49.2	0.0

Appendix B (Table B1): Trace element data for olivine in xenoliths (continued)

Sample	Next to	Al	Ca	Sc	Ti	V	Cr	Mn	Co	Ni	Cu	Zn	Y
MH-02-114	cpx	33.9	702.1	3.0	11.1	3.1	181.5	861.7	118.7	2731.8	3.9	46.4	0.0
MH-02-114	cpx	31.7	797.6	3.3	12.1	3.0	177.1	894.6	126.6	2883.0	1.9	44.7	0.0
MH-02-114	spinel	29.9	493.5	2.3	14.7	2.1	177.7	874.6	125.7	2860.6	2.1	48.6	0.0
MH-02-114	spinel	34.6	509.6	2.6	11.1	1.9	95.6	844.8	123.5	2810.7	1.4	48.3	0.1
MH-02-114	spinel	32.1	824.7	4.1	8.2	2.4	269.1	924.3	125.1	2675.1	2.4	57.1	0.0
MH-02-114	spinel	30.4	375.7	2.2	5.5	2.1	142.8	901.8	124.7	2905.3	1.7	48.2	0.0
MH-02-114	spinel	29.4	333.6	1.9	7.3	1.5	150.1	875.1	127.7	2897.0	1.8	45.0	0.0
MH-02-114	cpx	38.8	625.3	2.9	10.6	2.3	103.9	875.4	122.2	2776.5	13.9	57.0	0.0
MH-02-114	cpx	30.5	719.1	2.7	10.0	2.6	183.5	868.9	122.3	2735.1	1.3	47.4	0.0
MH-02-114	cpx	28.6	394.4	2.2	14.8	2.6	128.9	879.5	123.8	2786.5	1.4	47.8	0.0
MH-02-100B	spinel	30.7	527.2	3.6	1.5	4.1	160.4	957.2	136.6	2937.4	0.7	59.0	0.0
MH-02-100B	cpx	35.0	288.8	2.1	2.1	3.1	93.7	919.0	129.1	2860.4	1.9	41.6	0.0
MH-02-100B	cpx	36.5	257.3	2.1	2.5	2.1	69.8	900.1	129.3	2910.0	2.0	43.1	0.0
MH-02-100B	spinel	31.6	228.1	2.0	1.8	2.9	97.0	918.9	129.9	2887.5	0.4	49.4	0.0
MH-02-100B	cpx	33.9	250.1	1.9	2.0	2.6	74.4	907.6	130.6	2915.7	0.5	44.0	0.0
MH-02-100B	cpx	33.6	261.2	2.1	2.3	2.6	73.4	902.7	128.2	2856.1	1.3	41.2	0.0
MH-02-100B	cpx	34.5	422.0	2.1	3.3	3.9	134.5	865.2	128.3	2983.3	BLOD	42.1	0.0
MH-02-100B	spinel	34.7	289.4	2.7	2.6	3.1	93.7	964.2	135.0	2990.5	1.8	51.7	0.0
MH-02-100B	spinel	28.1	266.3	1.9	5.8	2.8	106.9	909.0	131.7	2903.4	2.4	46.4	0.0
MH-02-100B	spinel	28.8	542.9	3.8	2.0	4.6	198.7	976.6	137.4	2796.1	0.7	62.6	0.0
MH-02-14	spinel	21.7	718.1	5.4	7.6	7.3	210.9	1034.9	122.2	2412.9	0.9	47.3	0.1
MH-02-14	spinel	27.0	353.3	2.6	10.5	4.9	93.9	1002.5	130.0	2703.4	2.0	48.4	0.1
MH-02-14	cpx	24.1	272.2	2.8	11.2	5.6	130.2	998.4	131.4	2751.3	0.4	43.1	0.1
MH-02-14	cpx	26.3	347.8	2.7	9.3	4.6	83.0	1000.6	132.5	2766.4	0.9	39.7	0.1
MH-02-14	cpx	27.3	208.6	2.2	7.1	4.6	117.8	992.8	128.4	2695.0	1.7	46.6	0.0
MH-02-14	cpx	22.1	250.9	2.3	4.0	5.4	213.9	1035.0	132.8	2835.8	1.3	53.2	0.0
MH-02-14	spinel	25.5	291.7	3.7	6.9	4.8	97.4	974.2	128.0	2693.8	0.7	46.5	0.1
MH-02-14	spinel	24.3	265.0	3.7	6.2	6.6	119.9	990.1	136.2	2915.8	0.9	51.5	0.1
MH-02-14	spinel	23.0	695.9	4.5	6.3	7.8	260.0	1062.7	123.3	2495.7	1.4	54.4	0.1

Appendix B (Table B1): Trace element data for olivine in xenoliths (continued)

Sample	Next to	Al	Ca	Sc	Ti	V	Cr	Mn	Co	Ni	Cu	Zn	Y
MH-02-102	spinel	17.5	296.8	5.4	11.4	11.6	191.5	1316.2	168.2	3702.2	1.4	98.4	0.1
MH-02-102	spinel	29.1	300.9	4.7	5.8	6.9	155.5	1198.3	166.8	3631.9	1.4	103.3	0.1
MH-02-102	spinel	26.4	260.0	4.4	8.1	7.6	149.7	1199.1	168.3	3739.8	BLOD	103.8	0.1
MH-02-102	cpx	31.2	178.1	3.3	7.4	4.4	56.5	1137.0	160.4	3679.3	0.5	77.6	0.0
MH-02-102	cpx	19.9	233.1	3.7	8.4	9.1	141.5	1179.8	166.8	3808.0	1.1	76.1	0.1
MH-02-102	cpx	18.0	212.4	3.9	10.4	9.3	152.2	1189.9	158.0	3695.0	1.0	74.9	0.1
MH-02-102	cpx	27.3	395.9	4.1	9.8	6.6	108.5	1113.3	156.1	3597.7	BLOD	77.2	0.1
MH-02-102	cpx	32.0	285.0	4.5	20.4	10.2	192.0	1191.9	157.9	3583.4	BLOD	82.4	0.1
MH-02-102	spinel	39.7	241.8	3.9	13.8	5.1	133.0	1119.8	158.9	3468.6	BLOD	97.9	0.1
MH-02-102	spinel	35.5	324.2	3.4	6.1	3.9	112.4	1111.3	161.7	3441.0	BLOD	102.2	0.02
MH-02-102	spinel	35.7	237.2	4.4	15.1	6.8	126.7	1168.5	158.7	3584.4	1.3	73.6	0.1
MH-02-102	cpx	24.7	426.7	4.3	11.7	8.0	168.5	1157.7	160.2	3692.9	0.7	86.4	0.1

Appendix B (Table B2): Trace element data for cpx in xenoliths

Sample	Ti	V	Ni	Sr	Y	Zr	Nb	Ba
MH-02-10C	91.3	146.3		260.0	0.7	3.9	1.2	0.3
MH-02-10C	84.7	141.3		242.0	0.7	3.9	1.1	0.4
MH-02-10C	85.9	140.7		239.4	0.7	3.8	1.1	0.3
MH-02-10C	95.1	148.2		265.4	0.8	4.1	1.1	0.8
MH-02-10C	89.5	145.5		245.9	0.7	4.1	1.2	0.3
MH-02-10C	89.4	145.3		246.1	0.7	3.9	1.3	0.3
average	89.3	144.5		249.8	0.7	3.9	1.2	0.4
1 std	3.8	3.0		10.4	0.0	0.1	0.1	0.2
MH-02-117-2	195.6	162.7		96.2	1.2	0.7	0.8	0.1
MH-02-117-2	209.7	170.4		82.3	1.4	0.5	0.6	0.2
MH-02-117-2	187.9	163.7		108.3	1.2	0.5	0.6	0.0
MH-02-117-2	203.6	179.7		209.4	1.6	0.8	0.7	0.1
average	199.2	169.1		124.0	1.3	0.6	0.7	0.1
1 std	9.5	7.8		57.9	0.2	0.1	0.1	0.1
MH-02-112	8.1	146.5		240.5	0.7	65.7	6.7	0.1
MH-02-112	7.7	147.6		255.8	0.7	63.2	6.5	0.1
MH-02-112	7.6	145.6		226.6	0.7	65.7	6.7	0.1
MH-02-112	8.3	151.1		248.4	0.8	67.2	6.7	0.1
average	7.9	147.7		242.8	0.7	65.5	6.7	0.1
1 std	0.3	2.4		12.5	0.0	1.6	0.1	0.0
MH-02-108	1647.4	250.3	290.5	33.3	10.3	12.9	0.1	0.0
MH-02-108	1606.9	244.0	280.0	32.2	9.6	11.5	0.1	0.0
MH-02-108	1703.4	246.8	272.6	31.6	10.0	12.3	0.1	0.0
MH-02-108	1628.6	243.8	277.4	34.2	10.1	12.1	0.1	0.0
MH-02-108	1689.9	239.7	278.1	32.8	10.2	12.3	0.1	0.0
MH-02-108	1626.5	231.6	272.3	34.0	9.9	12.2	0.1	0.5
average	1650.5	242.7	278.5	33.0	10.0	12.2	0.1	0.1
1 std	38.2	6.5	6.6	1.0	0.3	0.4	0.0	0.2

Appendix B (Table B2): Trace element data for cpx in xenoliths (continued)

Sample	La	Ce	Pr	Nd	Sm	Eu	Gd	Tb	Dy	Ho	Er	Tm	Yb	Lu
MH-02-10C	13.01	32.36	3.63	12.06	1.01	0.25	0.40	0.03	0.11	0.02		0.02	0.22	0.03
MH-02-10C	11.74	29.03	3.21	11.00	0.87	0.23	0.35	0.03	0.13	0.03		0.02	0.16	0.03
MH-02-10C	11.78	29.15	3.23	10.98	0.90	0.25	0.37	0.03	0.14	0.03		0.02	0.18	0.03
MH-02-10C	13.35	32.79	3.60	11.99	0.91	0.23	0.43	0.03	0.14	0.03		0.02	0.21	0.03
MH-02-10C	11.91	30.37	3.33	10.75	0.88	0.23	0.39	0.03	0.13	0.02		0.02	0.15	0.03
MH-02-10C	11.43	29.37	3.30	11.29	0.89	0.25	0.38	0.03	0.14	0.03		0.02	0.17	0.03
average	12.20	30.51	3.38	11.35	0.91	0.24	0.39	0.03	0.13	0.03		0.02	0.18	0.03
1 std	0.78	1.67	0.19	0.55	0.05	0.01	0.03	0.00	0.01	0.00		0.00	0.03	0.00
MH-02-117-2	4.37	9.51	0.86	2.47	0.28	0.12	0.21	0.03	0.20	0.05		0.02	0.19	0.03
MH-02-117-2	3.70	7.15	0.62	1.75	0.19	0.08	0.17	0.03	0.19	0.05		0.03	0.23	0.03
MH-02-117-2	4.52	9.70	0.86	2.51	0.32	0.10	0.18	0.03	0.16	0.05		0.03	0.21	0.04
MH-02-117-2	6.64	14.85	1.50	5.13	0.56	0.20	0.32	0.04	0.26	0.06		0.03	0.27	0.04
average	4.81	10.30	0.96	2.96	0.34	0.12	0.22	0.03	0.20	0.05		0.03	0.22	0.04
1 std	1.28	3.25	0.38	1.48	0.16	0.05	0.07	0.01	0.04	0.01		0.00	0.03	0.00
MH-02-112	18.85	44.44	5.10	20.33	2.41	0.75	1.31	0.09	0.27	0.03		0.01	0.12	0.02
MH-02-112	19.68	46.28	5.17	19.83	2.42	0.73	1.16	0.10	0.29	0.02		0.02	0.12	0.03
MH-02-112	18.31	43.72	5.00	19.45	2.44	0.70	1.27	0.09	0.30	0.03		0.01	0.12	0.03
MH-02-112	17.67	41.55	4.79	18.55	2.42	0.73	1.23	0.10	0.30	0.03		0.01	0.10	0.03
average	18.63	44.00	5.01	19.54	2.42	0.73	1.24	0.10	0.29	0.03		0.01	0.12	0.03
1 std	0.85	1.95	0.17	0.75	0.01	0.02	0.06	0.00	0.01	0.00		0.00	0.01	0.00
MH-02-108	0.22	1.05	0.24	1.75	0.83	0.39	1.38	0.26	1.94	0.40	1.28	0.18	1.20	0.17
MH-02-108	0.21	1.05	0.25	1.62	0.83	0.37	1.15	0.24	1.82	0.39	1.12	0.16	1.07	0.15
MH-02-108	0.21	1.03	0.25	1.63	0.82	0.37	1.24	0.25	1.80	0.38	1.17	0.17	1.15	0.16
MH-02-108	0.22	1.13	0.26	1.79	0.91	0.38	1.34	0.27	1.77	0.39	1.14	0.17	1.10	0.15
MH-02-108	0.22	1.09	0.25	1.76	0.84	0.40	1.43	0.27	1.83	0.40	1.19	0.16	1.11	0.16
MH-02-108	0.25	1.13	0.24	1.74	0.86	0.38	1.36	0.26	1.84	0.37	1.13	0.16	1.03	0.16
average	0.22	1.08	0.25	1.72	0.85	0.38	1.32	0.26	1.84	0.39	1.17	0.17	1.11	0.16
1 std	0.01	0.04	0.01	0.07	0.03	0.01	0.10	0.01	0.06	0.01	0.06	0.01	0.06	0.01

Appendix B (Table B2): Trace element data for cpx in xenoliths (continued)

Sample	Ti	V	Ni	Sr	Y	Zr	Nb	Ba
MH-02-121	663.2	237.5	312.1	2.0	8.2	0.1	0.1	0.1
MH-02-121	663.9	240.9	300.7	0.4	8.0	0.1	0.0	0.8
MH-02-121	708.2	246.2	301.4	0.6	8.1	0.1	0.1	0.6
MH-02-121	620.1	236.0	313.9	1.2	8.3	0.1	0.1	0.1
MH-02-121	709.7	252.0	318.9	2.5	8.3	0.1	0.1	0.2
average	673.0	242.5	309.4	1.3	8.2	0.1	0.1	0.4
1 std	37.3	6.6	8.0	0.9	0.1	0.0	0.0	0.3
MH-02-10	2358.4	255.0	261.9	42.2	18.6	21.1	0.0	0.0
MH-02-10	2423.	259.8	273.5	43.0	19.3	21.9	0.0	BLOD
MH-02-10	2415.4	257.5	274.6	43.6	19.3	21.6	0.0	BLOD
MH-02-10	2362.7	261.1	282.2	46.4	19.8	22.0	0.0	0.0
MH-02-10	2331.0	257.5	278.2	45.5	20.5	21.3	0.0	BLOD
MH-02-10	2368.8	261.4	276.1	43.4	20.4	20.0	0.0	BLOD
MH-02-10	2110.8	257.2	303.2	43.8	19.0	18.3	0.0	0.0
average	2338.7	258.5	278.5	44.0	19.5	20.9	0.0	0.0
1 std	105.7	2.3	12.5	1.5	0.7	1.3	0.0	0.0
MH-02-15	684.8	228.4	366.0	0.1	8.7	0.1	0.0	0.0
MH-02-15	694.9	225.8	416.5	0.1	8.7	0.1	0.0	BLOD
MH-02-15	664.8	220.9	348.9	0.2	8.4	0.1	0.0	0.0
MH-02-15	695.4	222.8	344.4	0.1	8.7	0.1	0.0	0.0
MH-02-15	650.6	220.2	348.2	0.1	8.5	0.1	0.0	0.0
MH-02-15	671.8	216.1	336.3	0.1	8.6	0.1	0.0	0.0
MH-02-15	674.5	218.4	347.1	0.1	8.6	0.1	0.0	0.0
average	676.7	221.8	358.2	0.1	8.6	0.1	0.0	0.0
1 std	16.3	4.3	27.2	0.0	0.1	0.0	0.0	0.0

Appendix B (Table B2): Trace element data for cpx in xenoliths (continued)

Sample	La	Ce	Pr	Nd	Sm	Eu	Gd	Tb	Dy	Ho	Er	Tm	Yb	Lu
MH-02-121	0.05	0.02	0.00	0.03	0.12	0.08	0.53	0.15	1.19	0.30	1.02	0.15	1.09	0.16
MH-02-121	0.02	0.02	0.00	0.02	0.12	0.08	0.49	0.14	1.19	0.29	0.95	0.15	1.05	0.14
MH-02-121	0.02	0.01	BLOD	0.03	0.13	0.08	0.53	0.15	1.20	0.29	0.99	0.14	1.14	0.15
MH-02-121	0.03	0.01	0.00	0.03	0.13	0.08	0.51	0.14	1.22	0.29	0.96	0.15	1.09	0.16
MH-02-121	0.04	0.03	0.00	0.04	0.12	0.08	0.54	0.16	1.30	0.31	0.99	0.16	1.14	0.16
average	0.03	0.02	0.00	0.03	0.12	0.08	0.52	0.15	1.22	0.30	0.98	0.15	1.10	0.15
1 std	0.01	0.01	0.00	0.01	0.01	0.00	0.02	0.01	0.04	0.01	0.03	0.01	0.04	0.01
MH-02-10	0.27	1.54	0.32	2.26	1.11	0.50	2.15	0.44	3.32	0.70	2.16	0.31	2.19	0.30
MH-02-10	0.28	1.54	0.33	2.31	1.18	0.52	2.15	0.43	3.32	0.75	2.24	0.32	2.28	0.29
MH-02-10	0.29	1.58	0.34	2.31	1.16	0.52	2.16	0.45	3.37	0.73	2.26	0.32	2.22	0.30
MH-02-10	0.30	1.55	0.33	2.34	1.26	0.52	2.29	0.44	3.48	0.78	2.27	0.34	2.23	0.31
MH-02-10	0.29	1.58	0.34	2.32	1.31	0.54	2.27	0.46	3.58	0.78	2.30	0.35	2.38	0.30
MH-02-10	0.30	1.55	0.35	2.35	1.27	0.55	2.45	0.49	3.76	0.82	2.38	0.34	2.38	0.32
MH-02-10	0.30	1.54	0.33	2.20	1.19	0.52	2.21	0.44	3.38	0.74	2.25	0.33	2.23	0.30
average	0.29	1.55	0.33	2.30	1.21	0.52	2.24	0.45	3.46	0.76	2.27	0.33	2.27	0.31
1 std	0.01	0.02	0.01	0.05	0.07	0.02	0.11	0.02	0.16	0.04	0.06	0.01	0.08	0.01
MH-02-15	0.00	0.00	0.00	0.04	0.14	0.08	0.54	0.14	1.34	0.33	1.09	0.17	1.20	0.17
MH-02-15	0.00	0.01	BLOD	0.03	0.10	0.08	0.47	0.13	1.37	0.34	1.01	0.19	1.21	0.17
MH-02-15	0.01	0.01	0.00	0.04	0.13	0.09	0.56	0.14	1.29	0.34	1.06	0.17	1.21	0.17
MH-02-15	0.00	0.00	0.00	0.03	0.12	0.08	0.52	0.15	1.28	0.35	1.05	0.17	1.18	0.16
MH-02-15	0.02	0.02	0.01	0.04	0.13	0.08	0.55	0.15	1.27	0.33	1.03	0.17	1.17	0.17
MH-02-15	0.00	0.00	0.00	0.04	0.13	0.09	0.56	0.14	1.33	0.32	1.05	0.17	1.16	0.17
MH-02-15	BLOD	0.00	0.00	0.03	0.14	0.09	0.53	0.14	1.30	0.33	1.07	0.16	1.16	0.17
average	0.01	0.01	0.00	0.04	0.13	0.08	0.53	0.14	1.31	0.33	1.05	0.17	1.18	0.17
1 std	0.01	0.00	0.00	0.01	0.01	0.00	0.03	0.00	0.04	0.01	0.03	0.01	0.02	0.00

Appendix B (Table B3): Trace element data for opx in xenoliths

Sample	Ti	V	Ni	Sr	Y	Zr	Nb	Ba
MH-02-10C	42.0	74.4		0.42	0.06	0.41	0.117	0.018
MH-02-10C	41.7	74.3		0.32	0.06	0.42	0.106	0.001
MH-02-10C	42.4	74.0		0.31	0.07	0.42	0.106	BLOD
average	42.1	74.2		0.35	0.07	0.42	0.110	0.010
1 std	0.3	0.2		0.06	0.00	0.01	0.006	0.012
MH-02-117-2	97.1	79.3		0.30	0.10	0.05	0.052	BLOD
MH-02-117-2	92.4	75.6		0.37	0.10	0.06	0.054	0.006
MH-02-117-2	97.1	74.3		0.20	0.10	0.05	0.033	0.005
average	95.5	76.4		0.29	0.10	0.05	0.046	0.005
1 std	2.7	2.6		0.09	0.00	0.01	0.012	0.001
MH-02-112	3.2	45.7		0.26	0.07	2.17	0.193	0.003
MH-02-112	3.5	44.6		0.50	0.07	2.01	0.179	0.021
MH-02-112	3.3	48.4		0.37	0.07	2.57	0.242	0.008
MH-02-112	3.2	47.2		0.30	0.06	2.10	0.200	0.002
MH-02-112	3.4	49.1		1.53	0.07	2.73	0.234	0.002
average	3.3	47.0		0.59	0.07	2.32	0.209	0.007
1 std	0.1	1.9		0.53	0.00	0.32	0.027	0.008
MH-02-108	446.7	89.9	674.8	0.06	0.50	0.49	0.016	0.006
MH-02-108	455.8	92.3	679.4	0.09	0.52	0.51	0.016	0.013
MH-02-108	408.3	83.5	671.5	0.06	0.44	0.44	0.013	0.018
average	436.9	88.5	675.2	0.07	0.49	0.48	0.015	0.013
1 std	25.2	4.6	4.0	0.01	0.04	0.04	0.002	0.006
MH-02-121	177.3	90.6	677.8	0.01	0.41	0.01	0.008	BLOD
MH-02-121	191.1	103.3	666.2	0.01	0.44	0.01	0.007	0.003
MH-02-121	196.3	100.8	672.0	0.03	0.49	0.01	0.009	0.004
MH-02-121	187.9	100.2	683.6	0.01	0.46	0.01	0.006	0.012
MH-02-121	198.9	103.0	694.6	0.00	0.50	0.01	0.010	0.004
average	190.3	99.6	678.8	0.01	0.46	0.01	0.008	0.006
1 std	8.5	5.2	10.9	0.01	0.04	0.00	0.002	0.004

Appendix B (Table B3): Trace element data for opx in xenoliths (continued)

Sample	La	Ce	Pr	Nd	Sm	Eu	Gd	Tb	Dy	Ho	Er	Tm	Yb	Lu
MH-02-10C	0.0175	0.0870	0.0133	0.0571	0.0074	0.0029	0.0108	0.0005	0.0085	0.0013		0.0019	0.0383	0.0085
MH-02-10C	0.0168	0.0778	0.0148	0.0483	0.0080	0.0065	0.0102	0.0004	0.0069	0.0017		0.0023	0.0276	0.0085
MH-02-10C	0.0154	0.0716	0.0136	0.0805	0.0176	0.0041	0.0133	0.0003	0.0033	0.0015		0.0034	0.0358	0.0099
average	0.0166	0.0788	0.0139	0.0619	0.0110	0.0045	0.0114	0.0004	0.0063	0.0015		0.0025	0.0339	0.0090
1 std	0.0011	0.0078	0.0008	0.0166	0.0058	0.0018	0.0017	0.0001	0.0027	0.0002		0.0007	0.0056	0.0008
MH-02-117-2	0.0073	0.0309	0.0051	0.0195	BLOD	0.0017	BLOD	0.0004	0.0125	0.0030		0.0052	0.0455	0.0099
MH-02-117-2	0.0098	0.0364	0.0058	0.0335	0.0106	0.0013	BLOD	0.0011	0.0133	0.0021		0.0039	0.0462	0.0084
MH-02-117-2	0.0102	0.0427	0.0052	0.0362	BLOD	BLOD	0.0094	0.0007	BLOD	0.0023		0.0030	0.0275	0.0089
average	0.0091	0.0367	0.0054	0.0297	0.0106	0.0015	0.0094	0.0007	0.0129	0.0025		0.0040	0.0397	0.0091
1 std	0.0016	0.0059	0.0004	0.0090		0.0003		0.0004	0.0006	0.0005		0.0011	0.0106	0.0008
MH-02-112	0.0151	0.0591	0.0086	0.0608	0.0139	0.0084	0.0199	0.0024	0.0150	0.0027		0.0014	0.0127	0.0051
MH-02-112	0.0131	0.0652	0.0127	0.0521	0.0205	0.0075	0.0233	0.0016	0.0156	0.0016		0.0005	0.0116	0.0041
MH-02-112	0.0197	0.0696	0.0102	0.0571	0.0084	0.0047	0.0209	0.0020	0.0182	0.0019		0.0015	0.0243	0.0057
MH-02-112	0.0127	0.0664	0.0115	0.0700	0.0250	0.0102	0.0167	0.0017	0.0174	0.0015		0.0008	0.0151	0.0040
MH-02-112	0.0610	0.2113	0.0312	0.1530	0.0374	0.0117	0.0331	0.0035	0.0135	0.0025		0.0019	0.0115	0.0050
average	0.0243	0.0943	0.0148	0.0786	0.0211	0.0085	0.0228	0.0023	0.0159	0.0020		0.0012	0.0150	0.0048
1 std	0.0207	0.0655	0.0093	0.0421	0.0111	0.0027	0.0062	0.0008	0.0019	0.0005		0.0005	0.0054	0.0007
MH-02-108	BLOD	0.0012	0.0000	0.0038	0.0032	0.0008	0.0130	0.0044	0.0606	0.0203	0.0673	0.0142	0.1621	0.0313
MH-02-108	BLOD	0.0019	BLOD	0.0051	BLOD	0.0012	0.0293	0.0050	0.0611	0.0154	0.0705	0.0191	0.1523	0.0286
MH-02-108	0.0015	0.0025	0.0005	0.0019	BLOD	0.0019	0.0102	0.0036	0.0452	0.0153	0.0712	0.0154	0.1320	0.0270
average	0.0015	0.0018	0.0003	0.0036	0.0032	0.0013	0.0175	0.0043	0.0556	0.0170	0.0697	0.0162	0.1488	0.0290
1 std		0.0006	0.0004	0.0016		0.0006	0.0103	0.0007	0.0091	0.0029	0.0021	0.0025	0.0153	0.0022
MH-02-121	BLOD	0.0000	0.0000	BLOD	BLOD	0.0000	0.0064	0.0023	0.0257	0.0125	0.0629	0.0162	0.1482	0.0294
MH-02-121	0.0000	BLOD	BLOD	BLOD	0.0000	BLOD	0.0058	0.0036	0.0428	0.0162	0.0735	0.0180	0.1541	0.0269
MH-02-121	BLOD	BLOD	0.0000	BLOD	BLOD	BLOD	0.0081	0.0027	0.0416	0.0145	0.0630	0.0179	0.1768	0.0328
MH-02-121	BLOD	0.0000	BLOD	BLOD	BLOD	0.0000	0.0042	0.0033	0.0379	0.0150	0.0769	0.0147	0.1672	0.0291
MH-02-121	BLOD	BLOD	BLOD	BLOD	BLOD	0.0002	BLOD	0.0027	0.0358	0.0173	0.0804	0.0200	0.1695	0.0321
average	0.0000	0.0000	0.0000		0.0000	0.0001	0.0061	0.0029	0.0368	0.0151	0.0713	0.0174	0.1632	0.0301
1 std		0.0000	0.0000			0.0001	0.0016	0.0005	0.0068	0.0018	0.0081	0.0020	0.0117	0.0024

Appendix B (Table B3): Trace element data for opx in xenoliths (continued)

Sample	Ti	V	Ni	Sr	Y	Zr	Nb	Ba
MH-02-10	497.0	85.4	636.2	0.02	0.71	0.644	0.011	0.000
MH-02-10	481.2	80.2	637.9	0.02	0.68	0.579	0.005	BLOD
MH-02-10	545.9	91.0	664.8	0.07	0.83	0.732	0.004	BLOD
MH-02-10	526.3	86.9	634.0	0.04	0.84	0.753	BLOD	BLOD
MH-02-10	496.8	89.9	662.6	0.05	0.84	0.694	0.005	BLOD
MH-02-10	518.6	94.6	649.8	0.05	0.82	0.676	0.007	BLOD
average	511.0	88.0	647.5	0.04	0.79	0.680	0.006	0.000
1 std	23.6	5.0	13.7	0.02	0.07	0.063	0.003	
MH-02-15	199.5	97.2	704.0	0.04	0.49	0.0171	0.0064	0.022
MH-02-15	217.0	105.3	710.4	0.01	0.55	0.0186	0.0045	BLOD
MH-02-15	209.9	102.8	710.3	0.56	0.51	0.0182	0.0073	BLOD
MH-02-15	209.9	97.1	696.1	BLOD	0.53	0.0150	0.0105	BLOD
average	209.1	100.6	705.2	0.20	0.52	0.0172	0.0072	0.022
1 std	7.2	4.1	6.8	0.31	0.02	0.0016	0.0025	

Appendix B (Table B3): Trace element data for opx in xenoliths (continued)

Sample	La	Ce	Pr	Nd	Sm	Eu	Gd	Tb	Dy	Ho	Er	Tm	Yb	Lu
MH-02-10	0.0001	0.0015	0.0009	BLOD	0.0034	0.0037	0.0211	0.0075	0.0789	0.0310	0.1196	0.0292	0.2089	0.0525
MH-02-10	BLOD	BLOD	0.0004	0.0006	0.0020	0.0013	0.0131	0.0054	0.0651	0.0273	0.1041	0.0245	0.2278	0.0445
MH-02-10	0.0003	0.0011	BLOD	0.0017	0.0035	0.0034	0.0228	0.0086	0.0899	0.0298	0.1279	0.0248	0.2822	0.0534
MH-02-10	BLOD	0.0011	BLOD	0.0034	0.0074	0.0038	0.0213	0.0055	0.0836	0.0303	0.1342	0.0293	0.2865	0.0459
MH-02-10	BLOD	0.0016	BLOD	0.0061	0.0027	0.0014	0.0202	0.0081	0.0978	0.0278	0.1371	0.0325	0.2591	0.0518
MH-02-10	0.0006	0.0011	0.0001	0.0056	0.0023	0.0017	0.0221	0.0080	0.0964	0.0294	0.1273	0.0269	0.2544	0.0499
average	0.0003	0.0013	0.0004	0.0035	0.0035	0.0025	0.0201	0.0072	0.0853	0.0293	0.1251	0.0279	0.2531	0.0497
1 std	0.0003	0.0003	0.0004	0.0024	0.0020	0.0012	0.0035	0.0014	0.0123	0.0014	0.0119	0.0031	0.0303	0.0037
MH-02-15	0.0013	0.0016	BLOD	BLOD	BLOD	BLOD	BLOD	0.0024	0.0402	0.0144	0.0909	0.0196	0.1974	0.0368
MH-02-15	0.0003	0.0004	BLOD	BLOD	BLOD	BLOD	0.0079	0.0041	0.0433	0.0217	0.0788	0.0170	0.2027	0.0388
MH-02-15	0.0000	0.0004	BLOD	BLOD	BLOD	0.0000	0.0028	0.0022	0.0639	0.0181	0.0726	0.0230	0.2141	0.0374
MH-02-15	0.0000	BLOD	BLOD	BLOD	BLOD	BLOD	0.0061	0.0050	0.0466	0.0214	0.0928	0.0199	0.2089	0.0383
average	0.0004	0.0008				0.0000	0.0056	0.0034	0.0485	0.0189	0.0838	0.0198	0.2058	0.0378
1 std	0.0006	0.0007					0.0026	0.0013	0.0106	0.0034	0.0097	0.0025	0.0073	0.0009

Appendix B (Table B4): Trace element data for MONG olivine standard

Sample	Al	Ca	Sc	Ti	V	Cr	Mn	Co	Ni	Cu	Zn	Y
MONG OL -1	212.5	528.0	4.5	37.1	5.9	133.1	1240.2	156.5	3086.0	1.2	68.7	0.1
MONG OL -1	217.8	522.9	4.7	38.2	5.9	132.5	1181.6	152.5	2915.3	8.6	65.3	0.1
MONG OL -1	217.6	533.5	4.4	40.9	5.6	127.1	1174.5	154.8	3004.9	1.7	60.5	0.1
MONG OL -2	214.4	609.7	3.2	40.3	5.0	121.0	1074.4	133.0	2683.0	BLOD	62.2	0.0
MONG OL -2	252.5	646.4	3.0	36.9	5.0	124.9	1083.0	139.0	2633.4	2.8	64.2	0.1
MONG OL -2	222.6	584.9	2.6	31.8	5.1	119.7	1055.5	135.0	2555.6	0.9	61.4	0.1
MONG OL -3	248.4	644.3	3.2	39.1	5.2	128.0	1075.1	141.0	2636.2	2.0	66.5	0.1
MONG OL -3	232.0	617.4	2.8	37.5	5.2	121.2	1065.5	137.0	2625.4	1.2	55.3	0.1
MONG OL -3	234.8	628.2	2.8	38.6	5.2	120.1	1080.4	139.5	2694.9	1.0	57.0	0.1
MONG OL -4	244.2	653.3	3.1	40.9	5.4	128.0	1107.4	139.1	2622.4	1.8	60.3	0.1
MONG OL -4	233.4	625.1	3.0	38.0	5.2	123.7	1110.2	145.5	2785.9	1.3	60.3	0.1
MONG OL -4	236.5	629.6	2.8	37.7	5.1	123.7	1093.7	134.9	2611.4	2.2	66.3	0.1
MONG OL -5	235.7	640.6	3.0	36.8	5.3	122.6	1080.0	137.1	2628.3	2.4	62.0	0.1
MONG OL -5	232.9	630.4	3.1	40.3	5.9	125.1	1121.2	140.4	2734.9	2.9	61.7	0.1
MONG OL -5	222.6	582.8	2.8	38.3	5.2	117.4	1064.2	140.4	2690.6	3.1	59.6	0.1
MONG OL -6	226.2	637.5	3.1	35.3	5.5	116.0	1103.9	148.8	2770.3	1.5	62.8	0.1
MONG OL -6	231.7	618.0	3.0	39.2	5.2	113.1	1067.3	135.4	2674.6	1.1	60.0	0.1
MONG OL -6	234.2	655.5	3.0	37.7	5.1	117.7	1081.3	140.8	2637.5	2.4	61.5	0.1
MONG OL -7	240.6	639.0	3.0	39.4	5.1	126.5	1061.4	137.5	2721.6	4.1	77.0	0.1
MONG OL -7	240.1	666.1	2.7	38.7	4.6	118.8	1045.0	137.1	2548.4	2.1	62.7	0.1
MONG OL -7	227.9	615.9	2.7	39.5	5.8	122.0	1123.6	145.5	2776.2	0.9	54.6	0.0

Appendix C: LA-ICP-MS analysis locations.

(All photomicrographs are taken under cross polarized light, except the ones with PPL label which are taking under plane polarized light)

Appendix C (Figure C1): Analysis locations for sample 95ML1

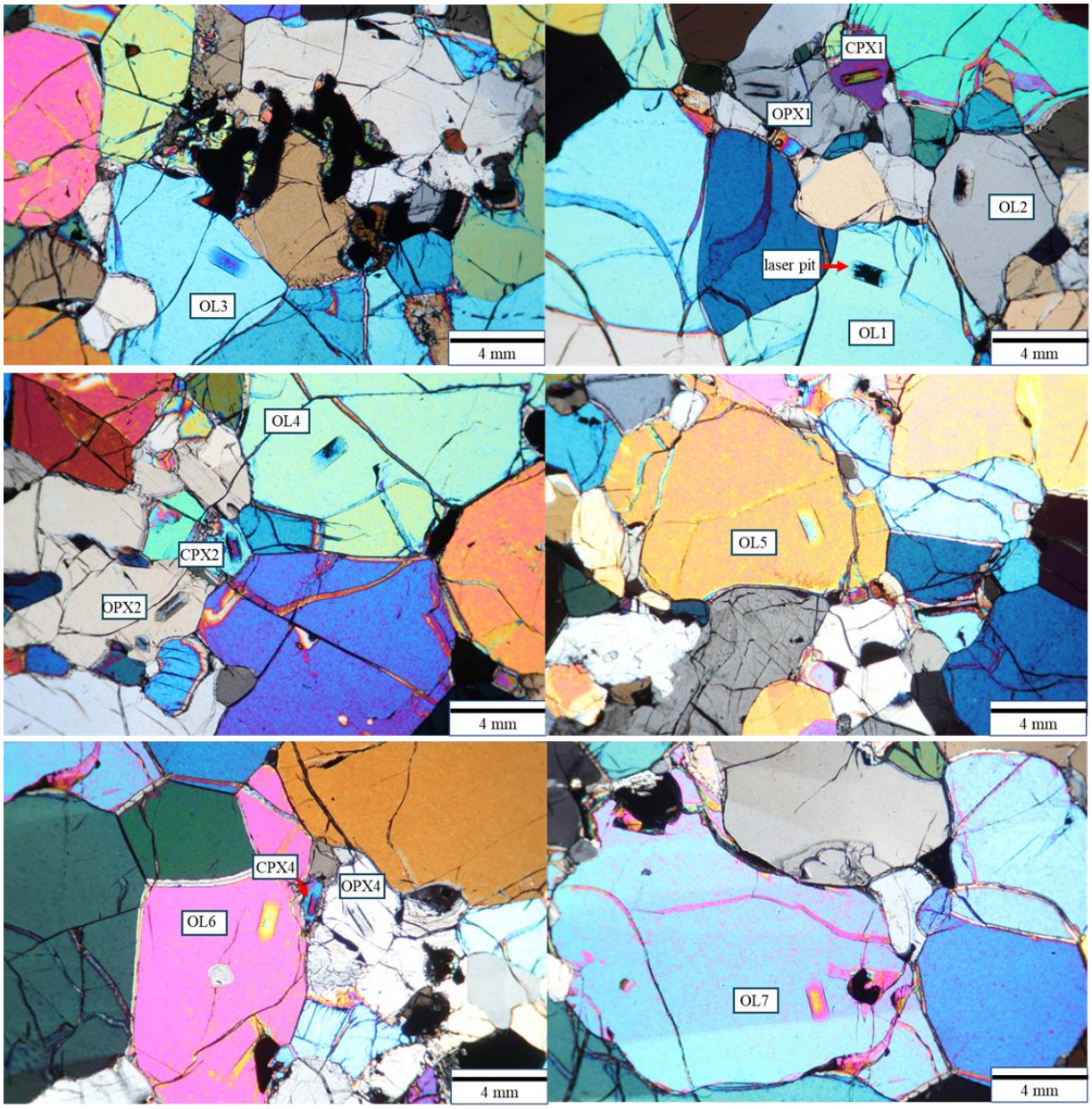

Appendix C (Figure C1): Analysis locations for sample 95ML1 (continued)

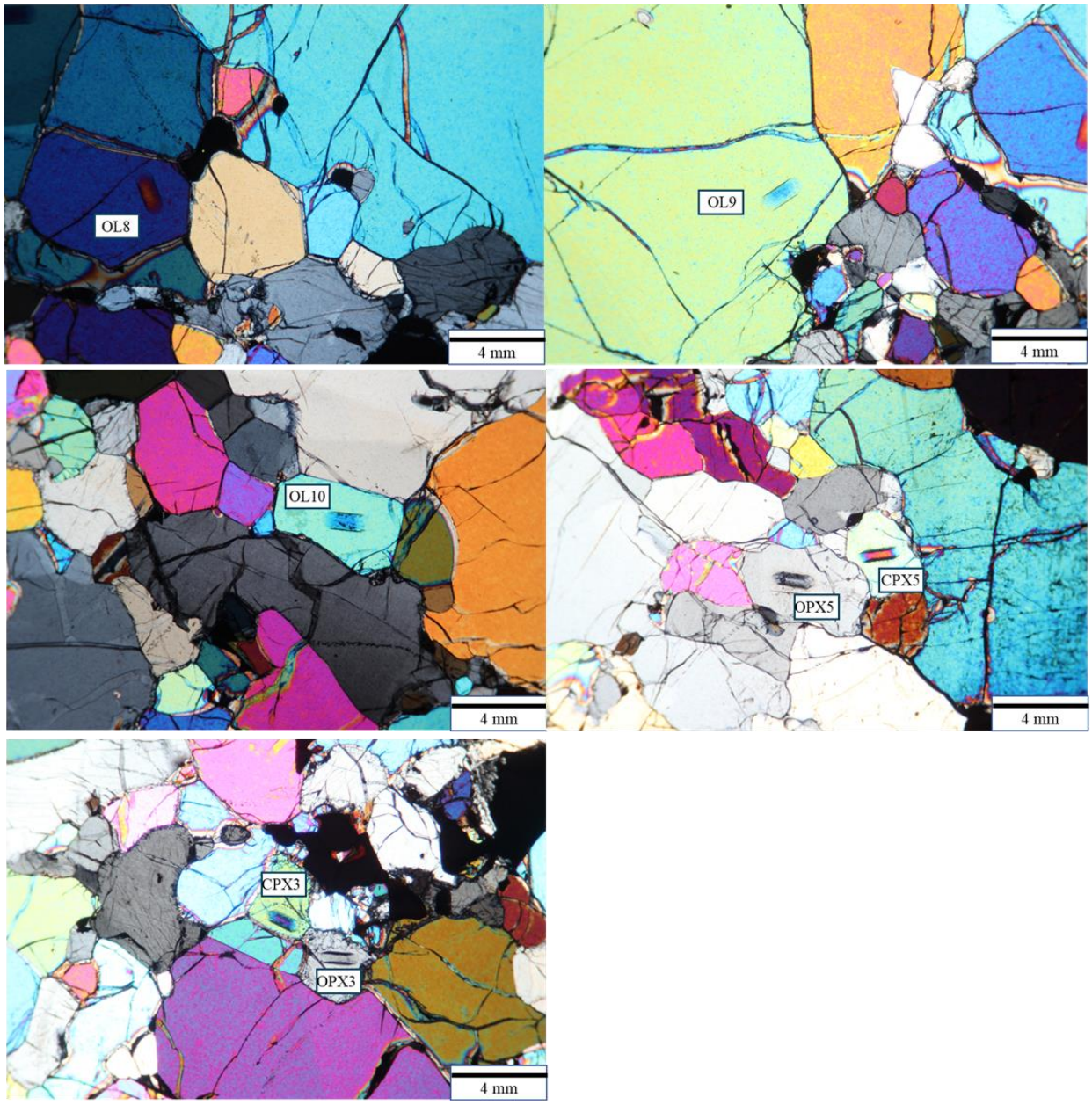

Appendix C (Figure C2): Analysis locations for sample MH-02-04

Appendix C (Figure C2): Analysis locations for sample MH-02-04 (continued)

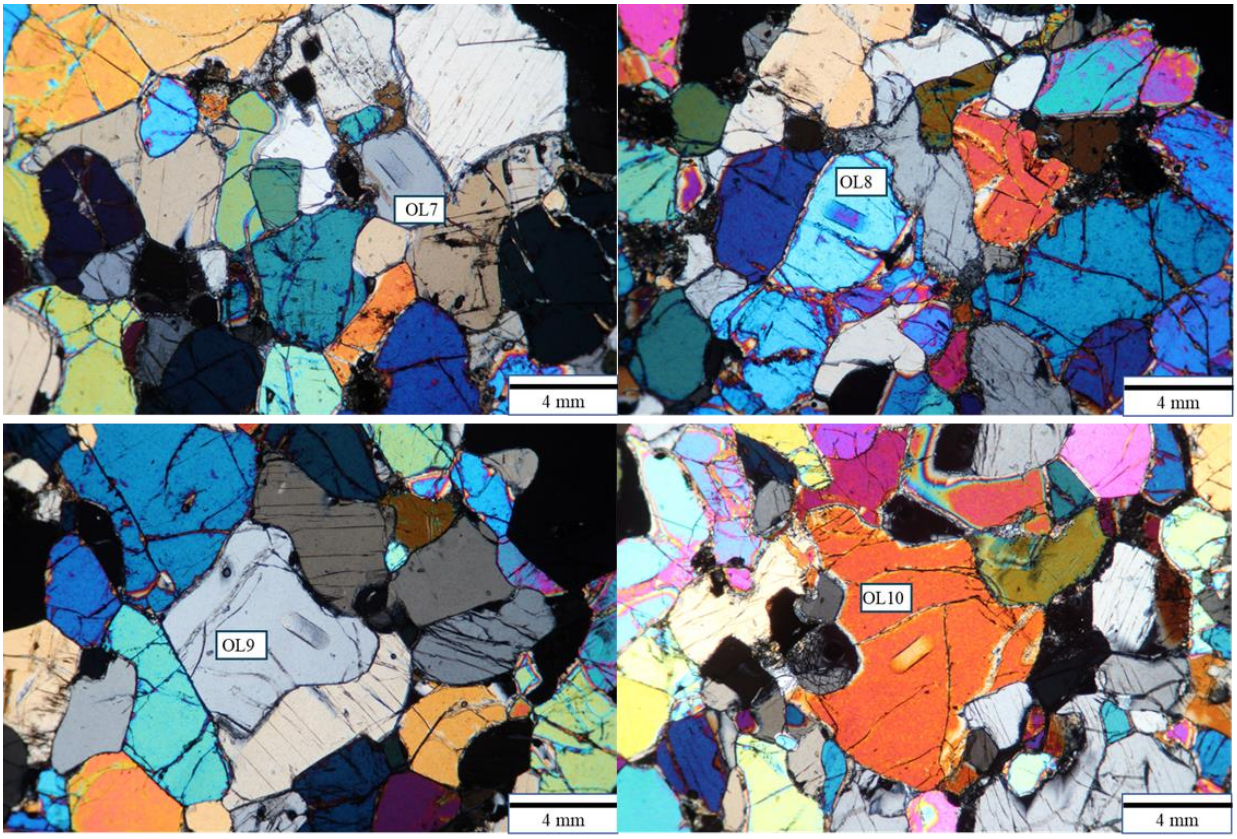

Appendix C (Figure C3): Analysis locations for sample MH-02-9B

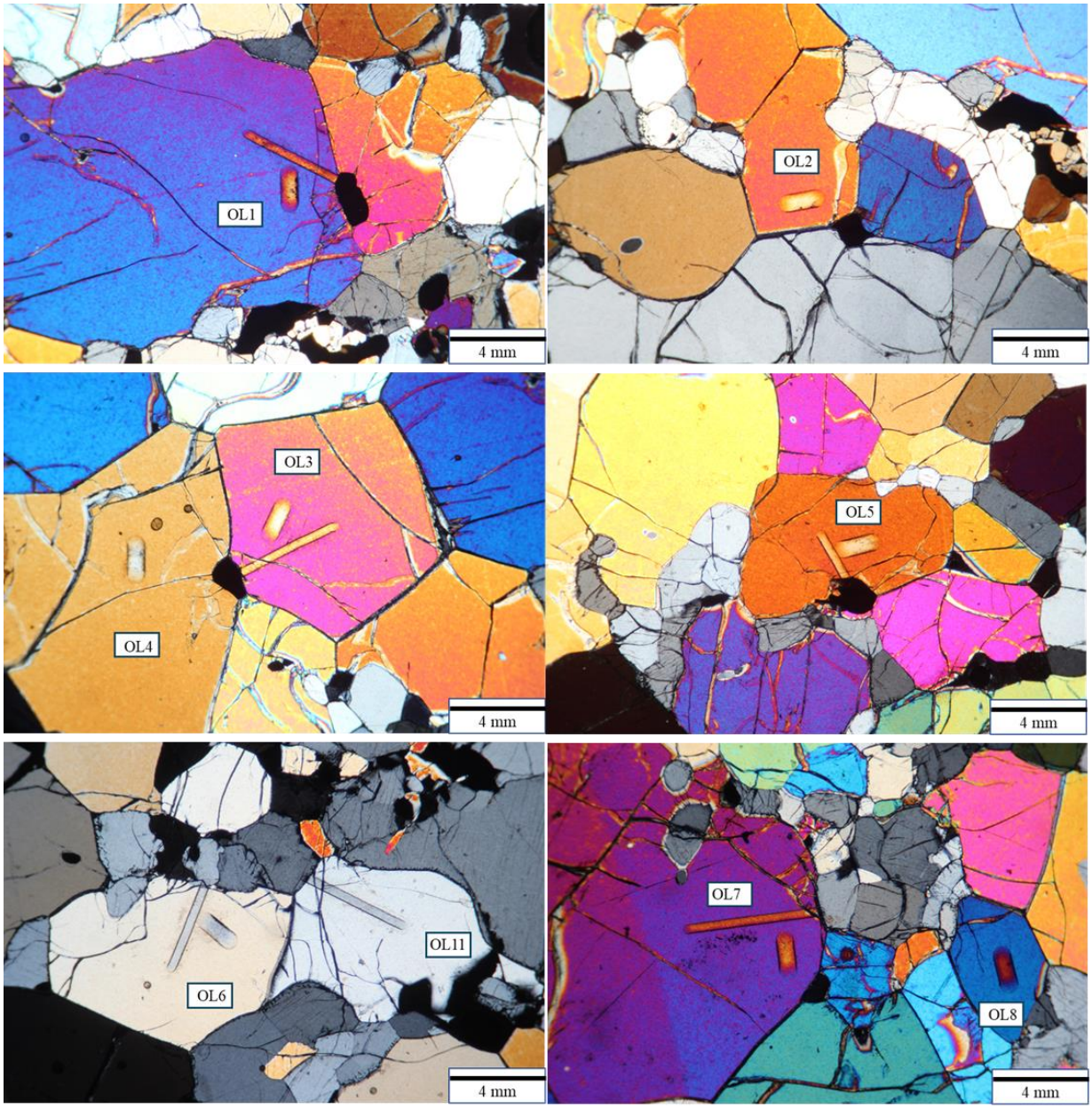

Appendix C (Figure C3): Analysis locations for sample MH-02-9B (continued)

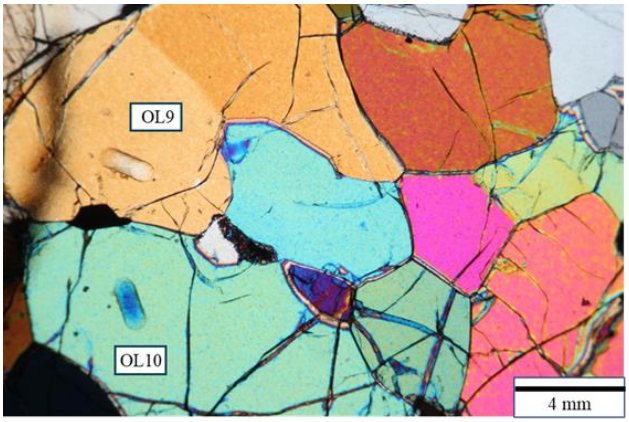

Appendix C (Figure C4): Analysis locations for sample MH-02-10

Appendix C (Figure C4): Analysis locations for sample MH-02-10 (continued)

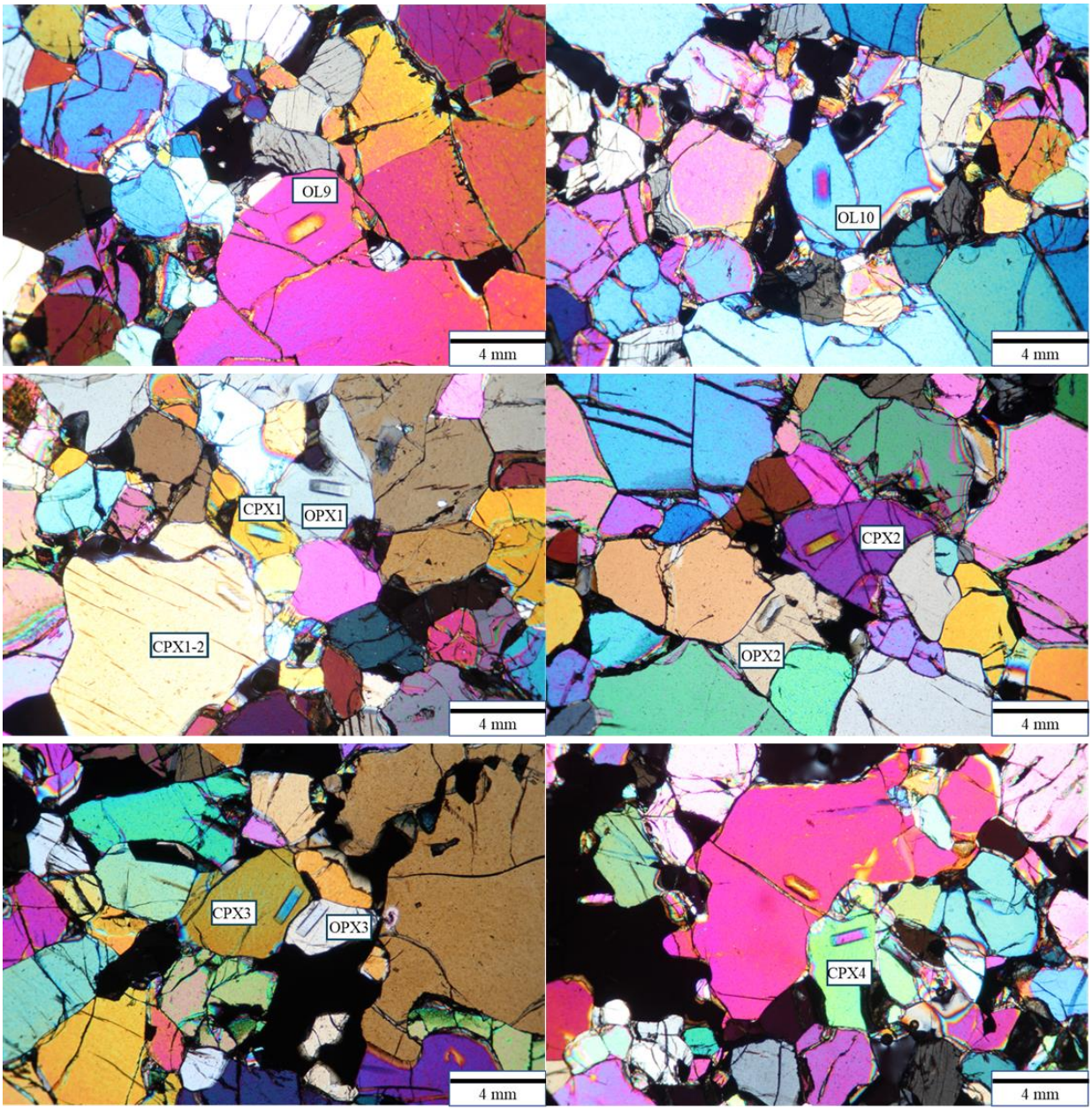
OL9
4 mm
OL10
4 mm
CPX1
OPX1
CPX1-2
4 mm
CPX2
OPX2
4 mm
CPX3
OPX3
4 mm
CPX4
4 mm

Appendix C (Figure C4): Analysis locations for sample MH-02-10 (continued)

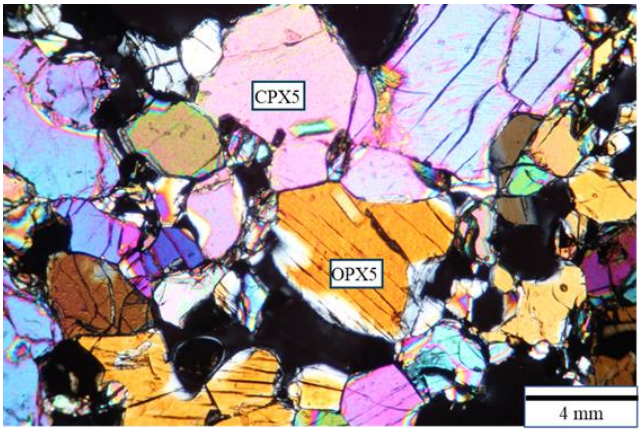

Appendix C (Figure C5): Analysis locations for sample MH-02-10B

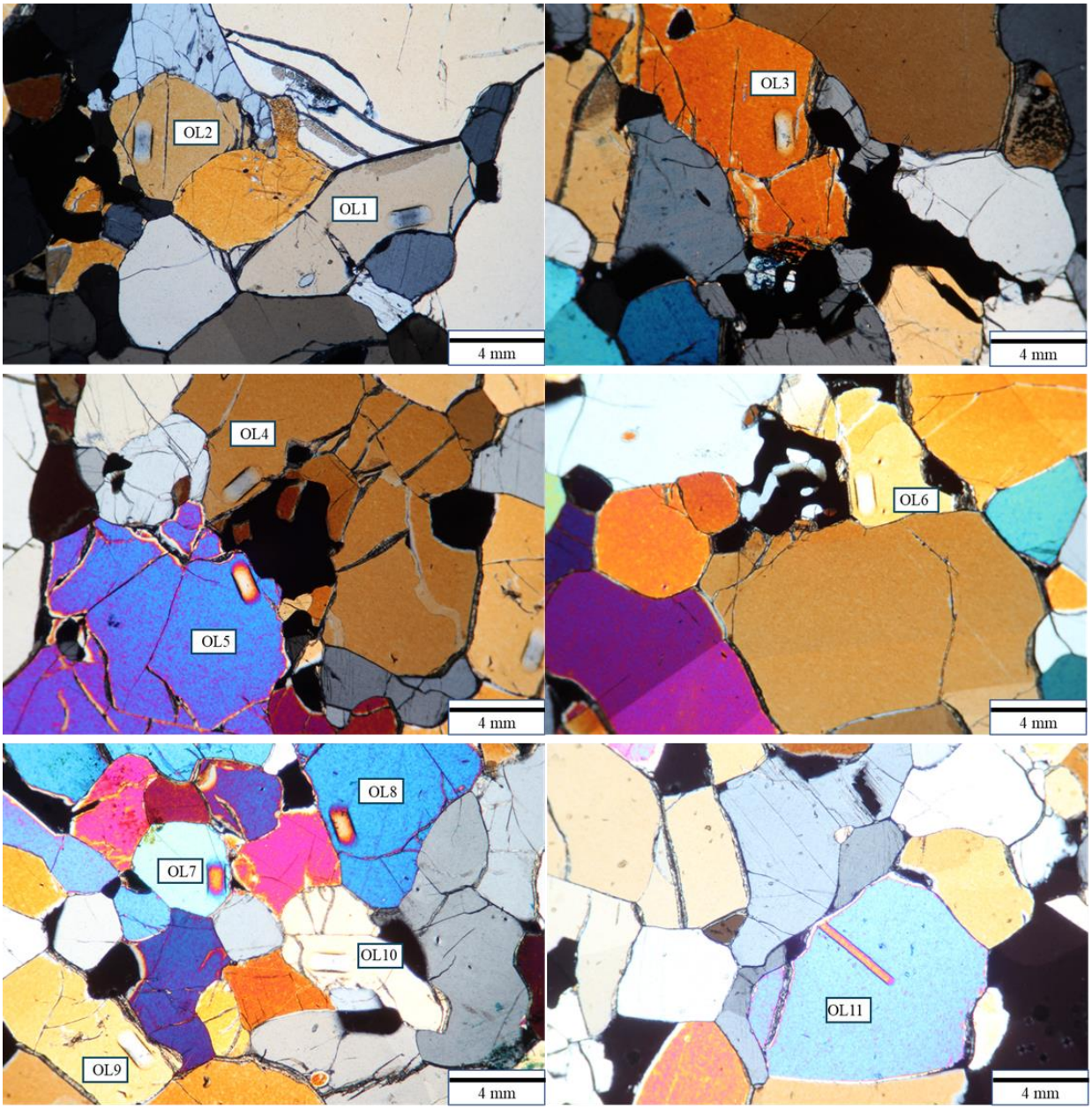

Appendix C (Figure C5): Analysis locations for sample MH-02-10B (continued)

Appendix C (Figure C6): Analysis locations for sample MH-02-10C

Appendix C (Figure C6): Analysis locations for sample MH-02-10C (continued)

Appendix C (Figure C6): Analysis locations for sample MH-02-10C (continued)

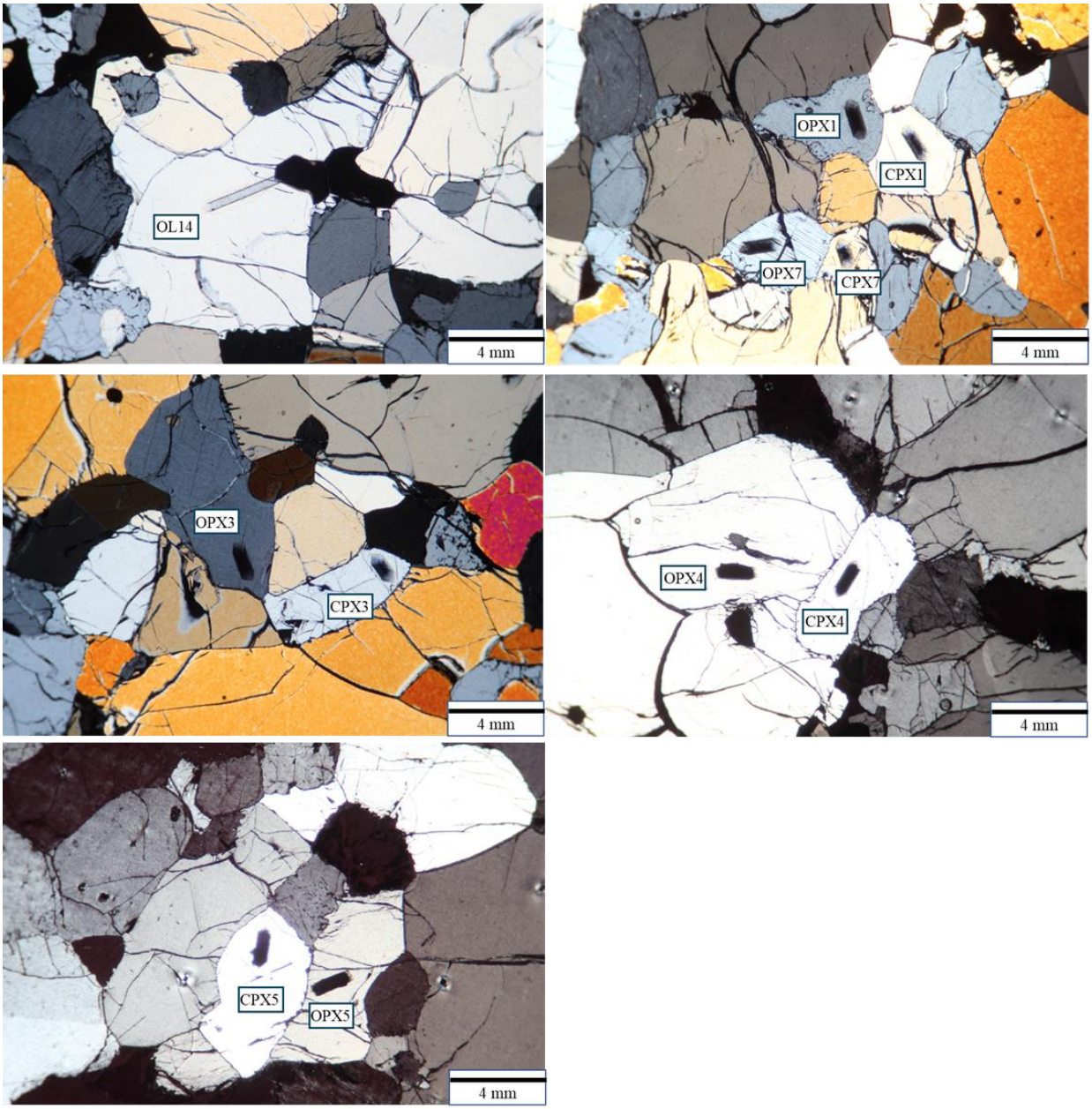

Appendix C (Figure C7): Analysis locations for sample MH-02-121

Appendix C (Figure C7): Analysis locations for sample MH-02-121 (continued)

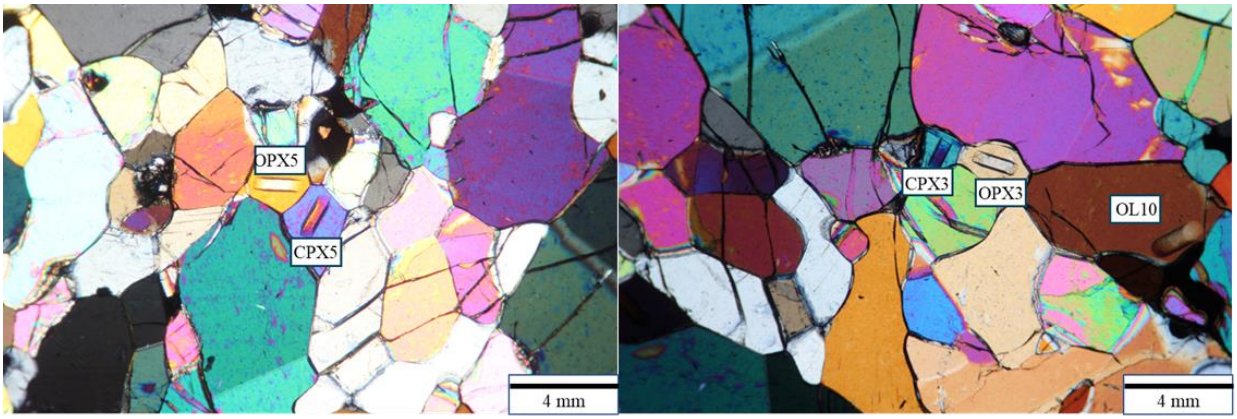

Appendix C (Figure C8): Analysis locations for sample MH-02-14

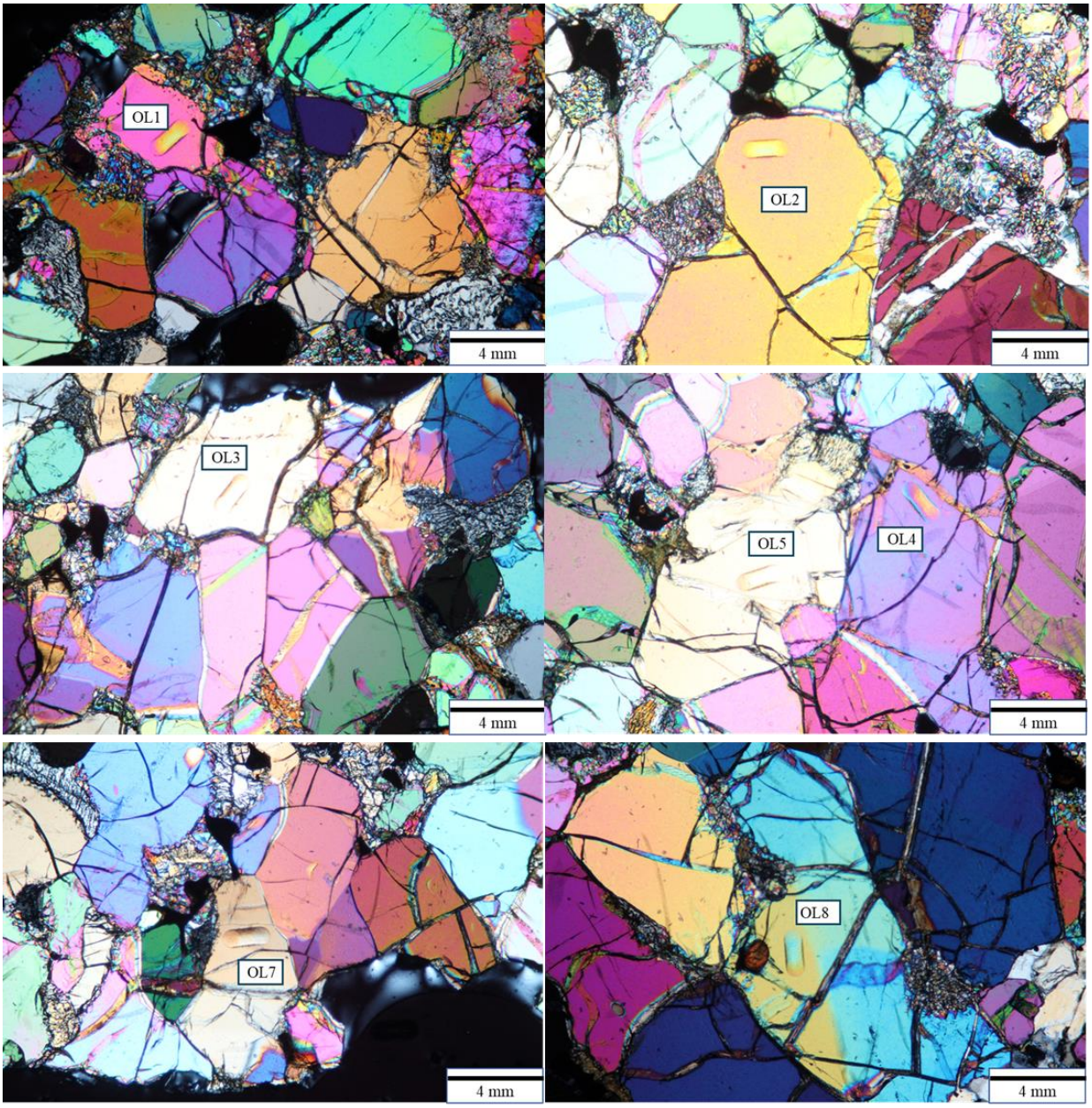

Appendix C (Figure C8): Analysis locations for sample MH-02-14 (continued)

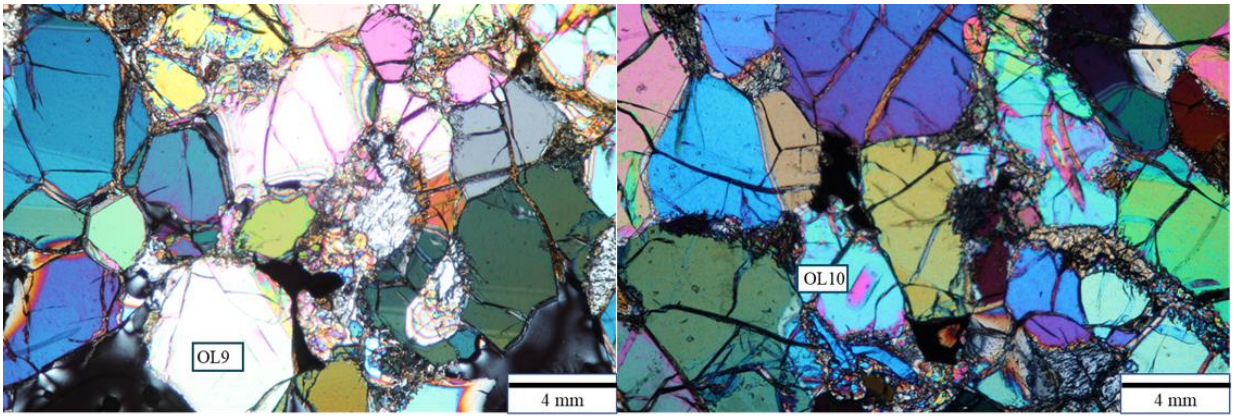

Appendix C (Figure C9): Analysis locations for sample MH-02-15

Appendix C (Figure C9): Analysis locations for sample MH-02-15 (continued)

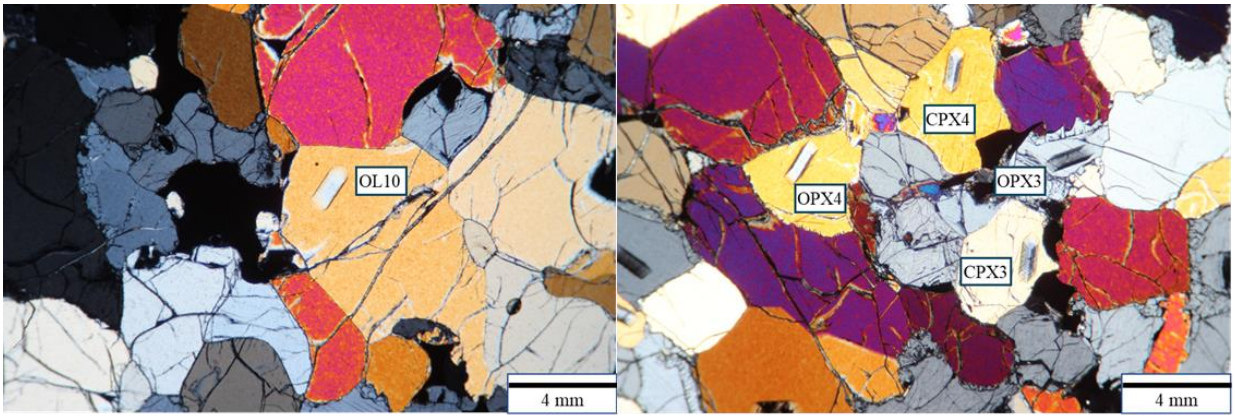

Appendix C (Figure C10): Analysis locations for sample MH-02-18B

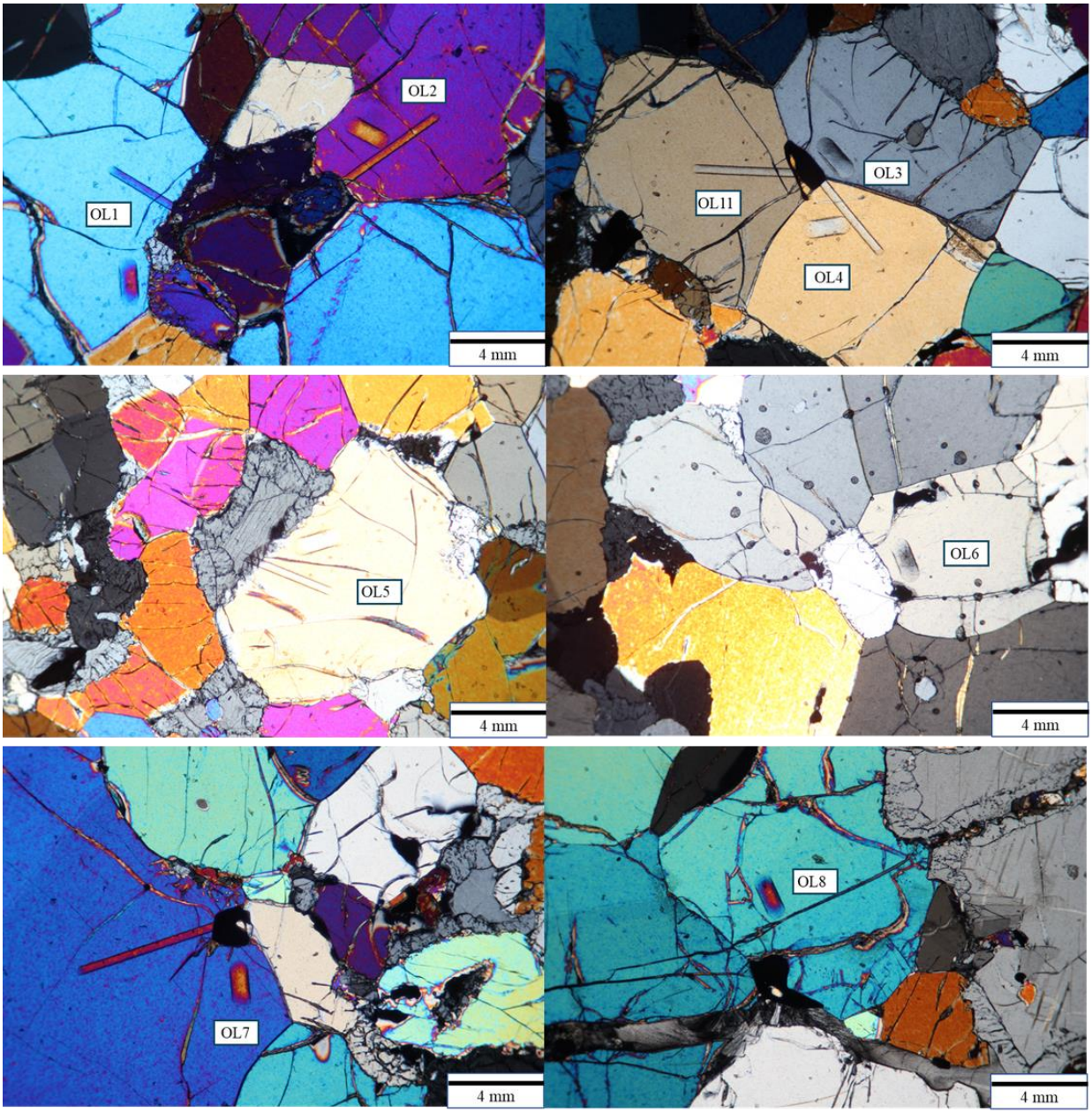

Appendix C (Figure C10): Analysis locations for sample MH-02-18B (continued)

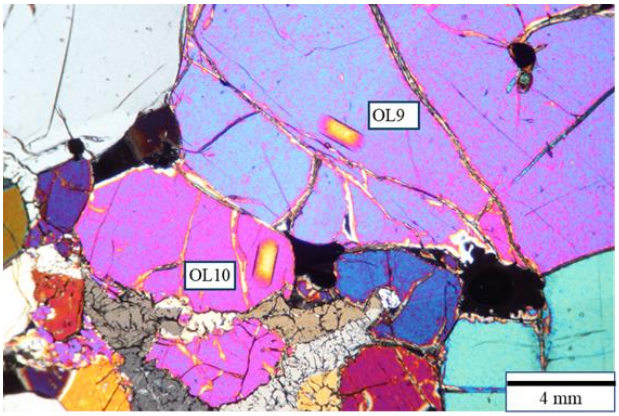

Appendix C (Figure C11): Analysis locations for sample MH-02-19

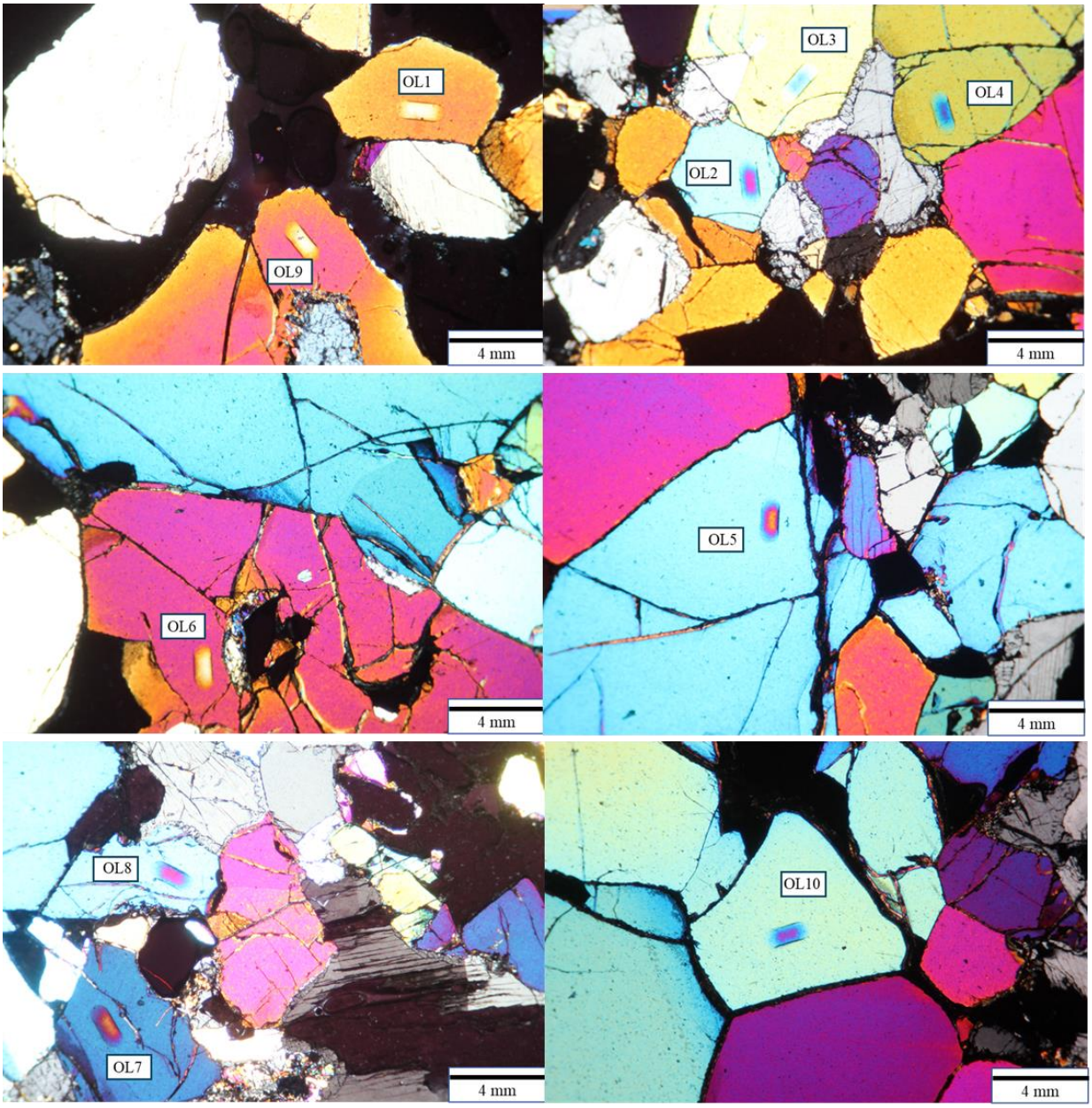

Appendix C (Figure C12): Analysis locations for sample MH-02-20

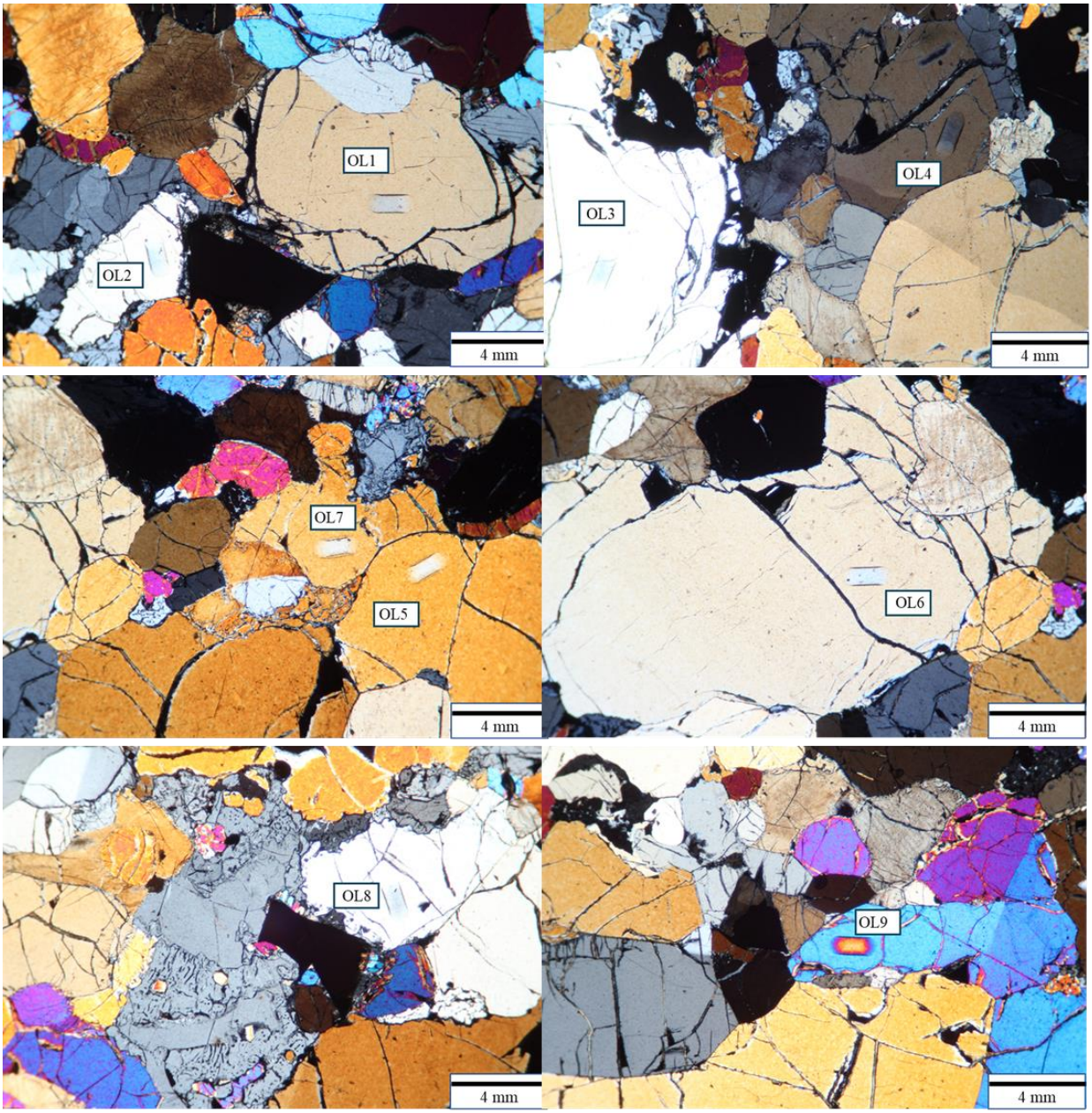

Appendix C (Figure C12): Analysis locations for sample MH-02-20 (continued)

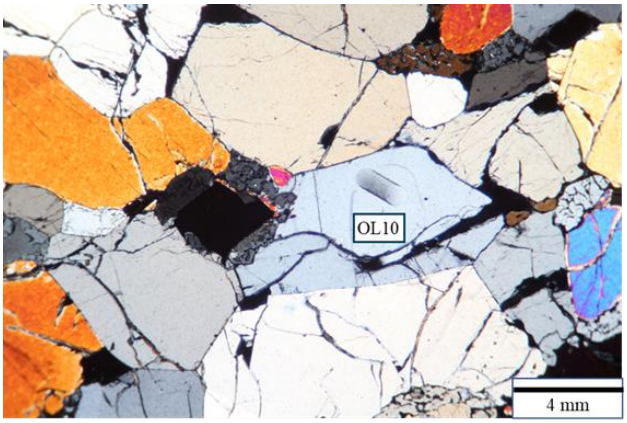

Appendix C (Figure C13): Analysis locations for sample MH-02-100

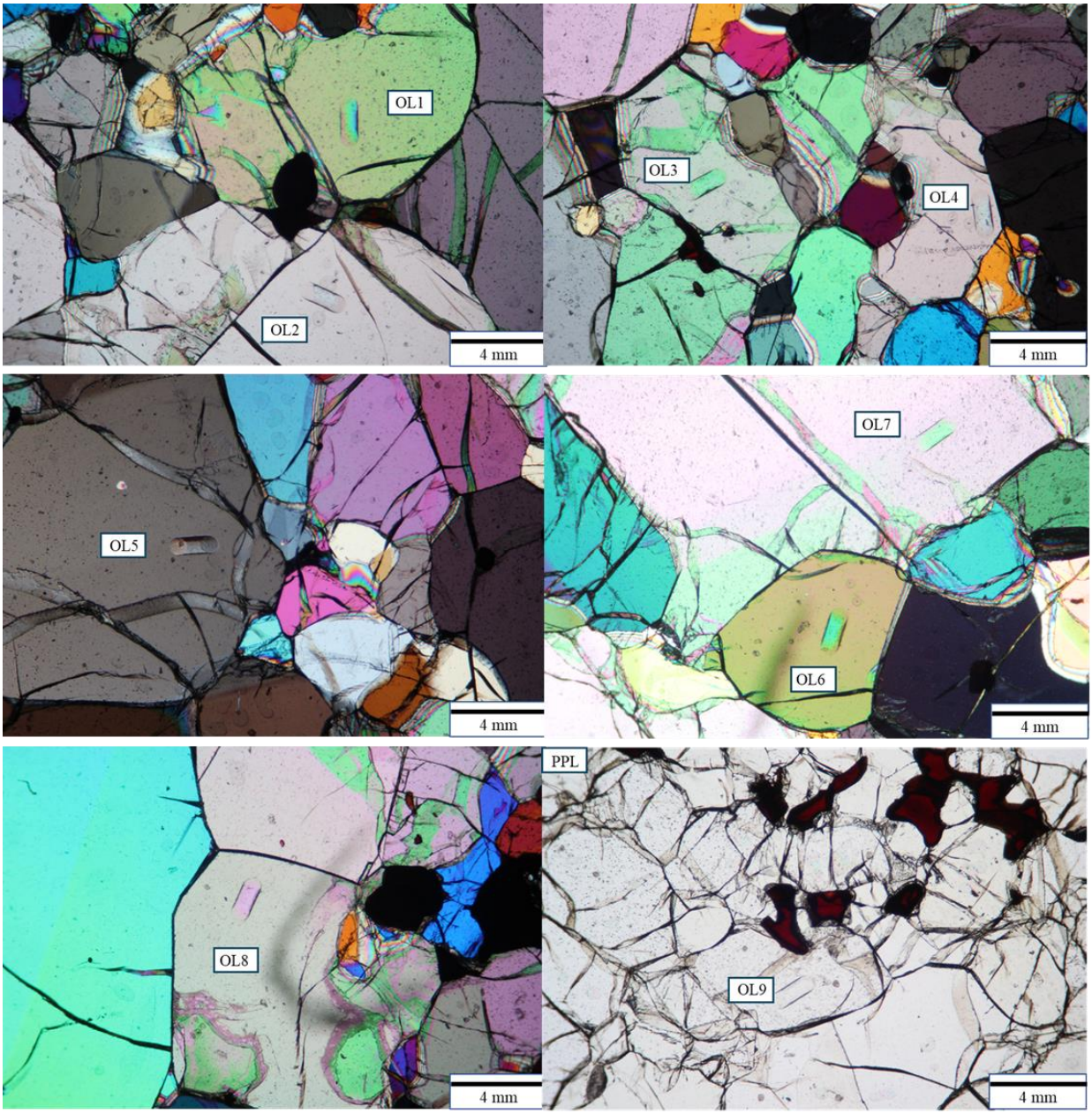

Appendix C (Figure C13): Analysis locations for sample MH-02-100 (continued)

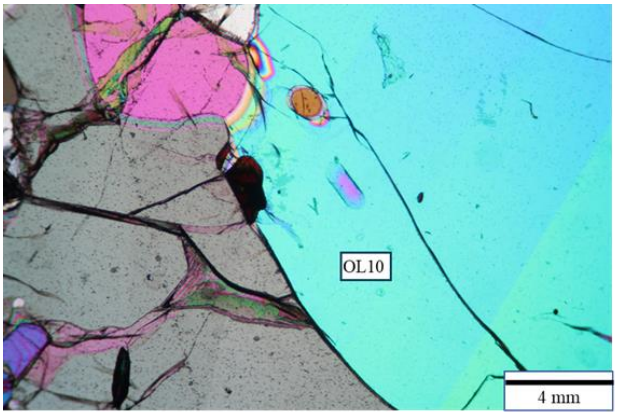

Appendix C (Figure C14): Analysis locations for sample MH-02-100B

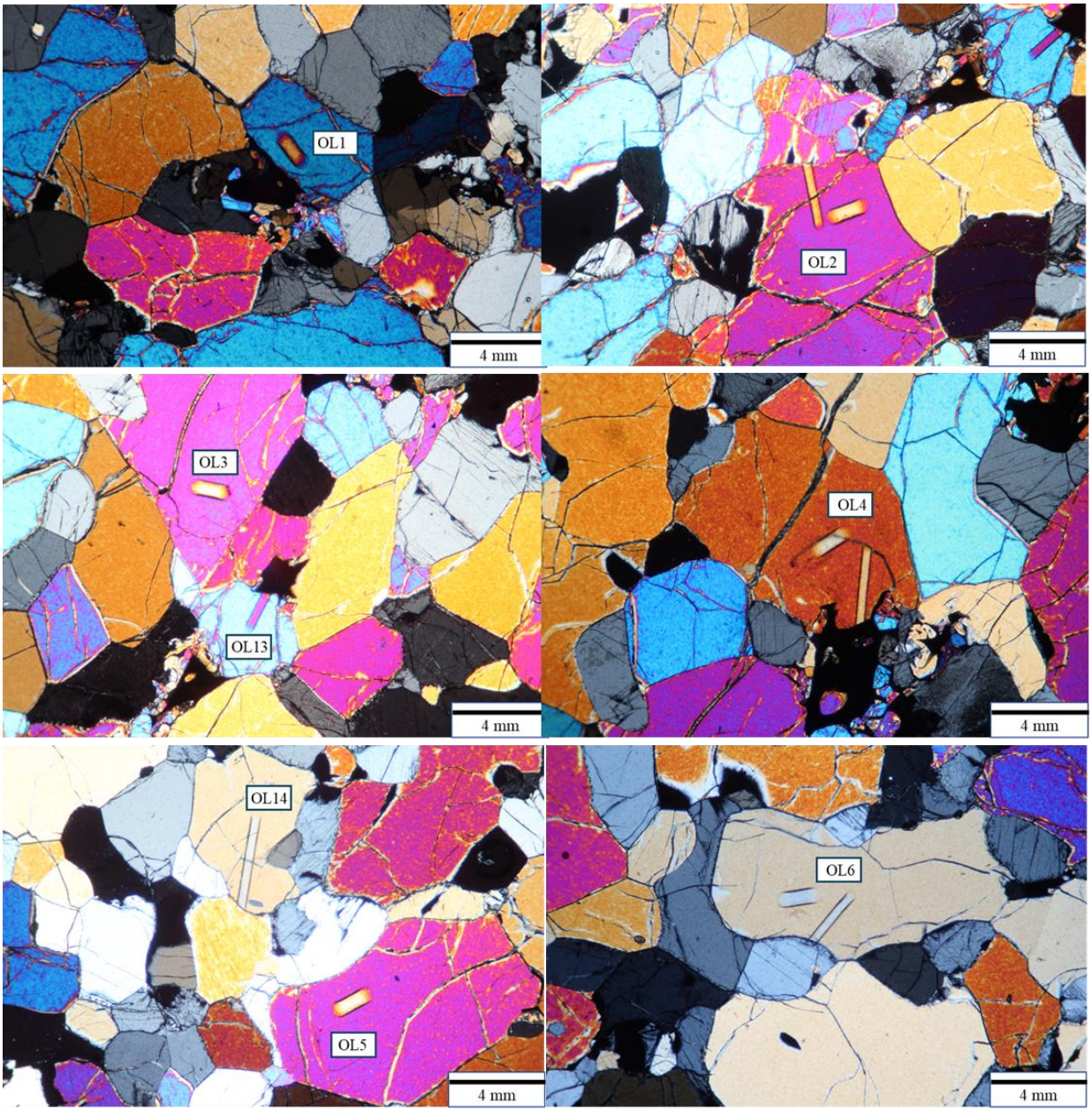

Appendix C (Figure C14): Analysis locations for sample MH-02-100B (continued)

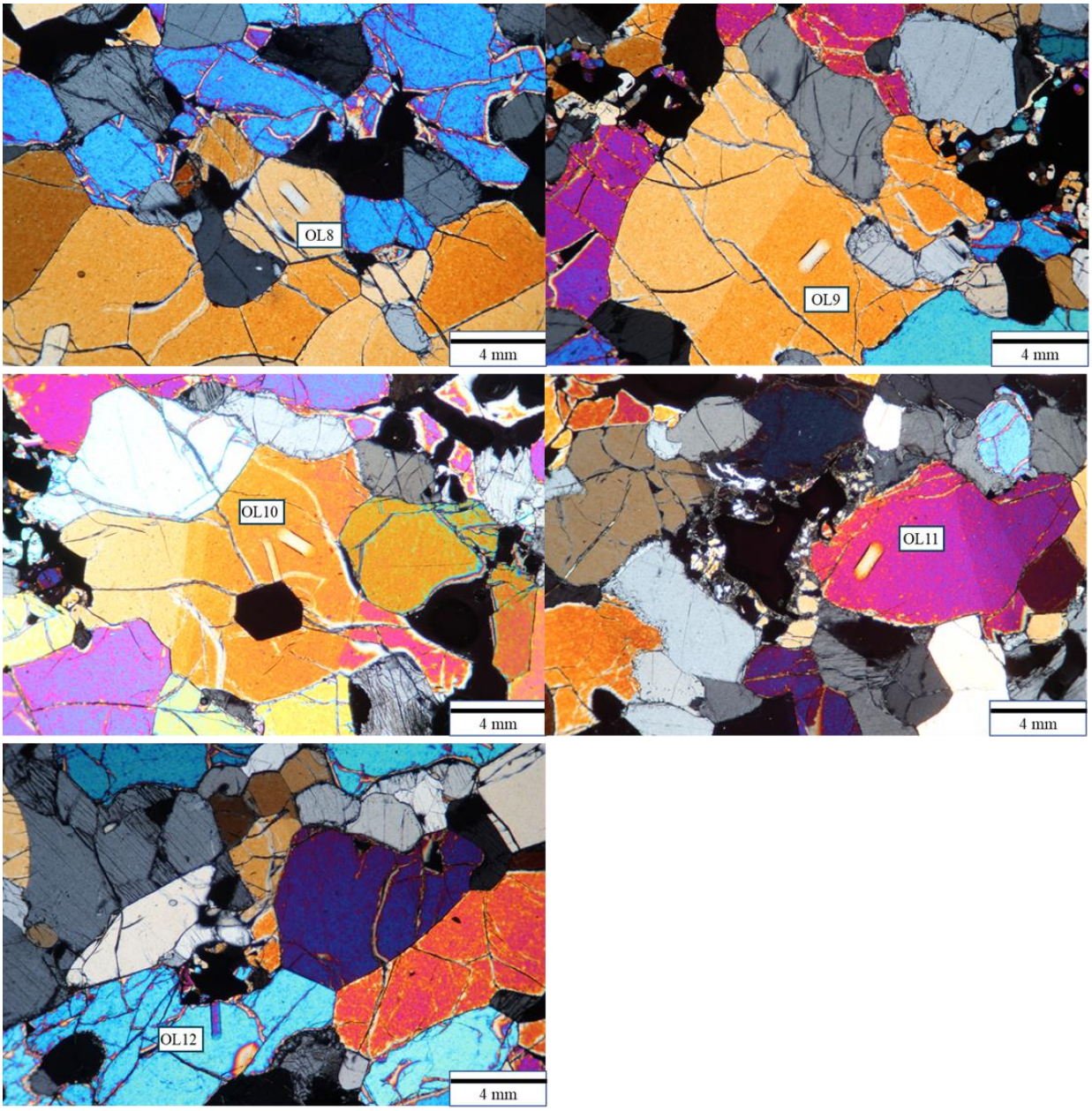

Appendix C (Figure C15): Analysis locations for sample MH-02-102

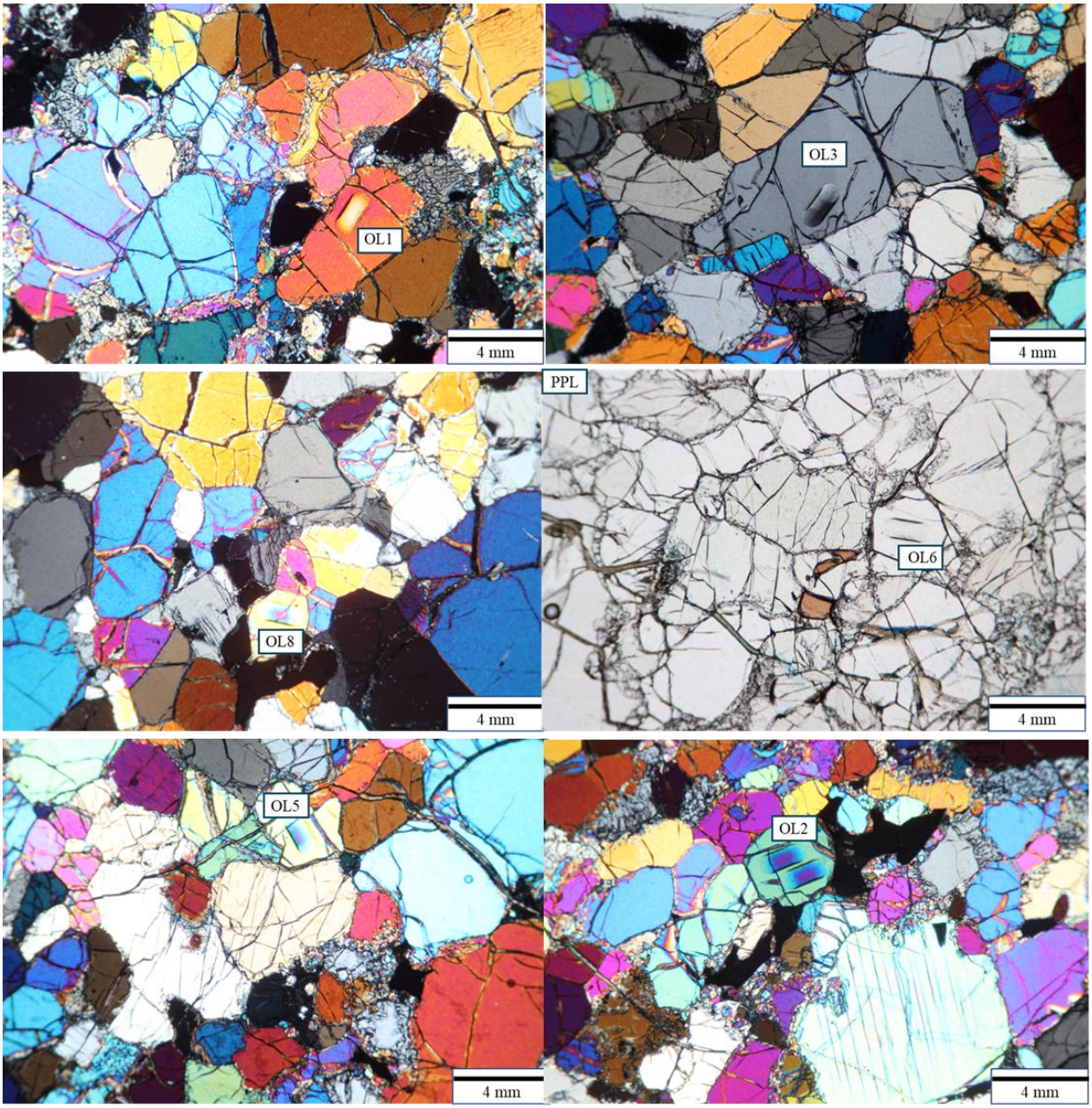

Appendix C (Figure C15): Analysis locations for sample MH-02-102 (continued)

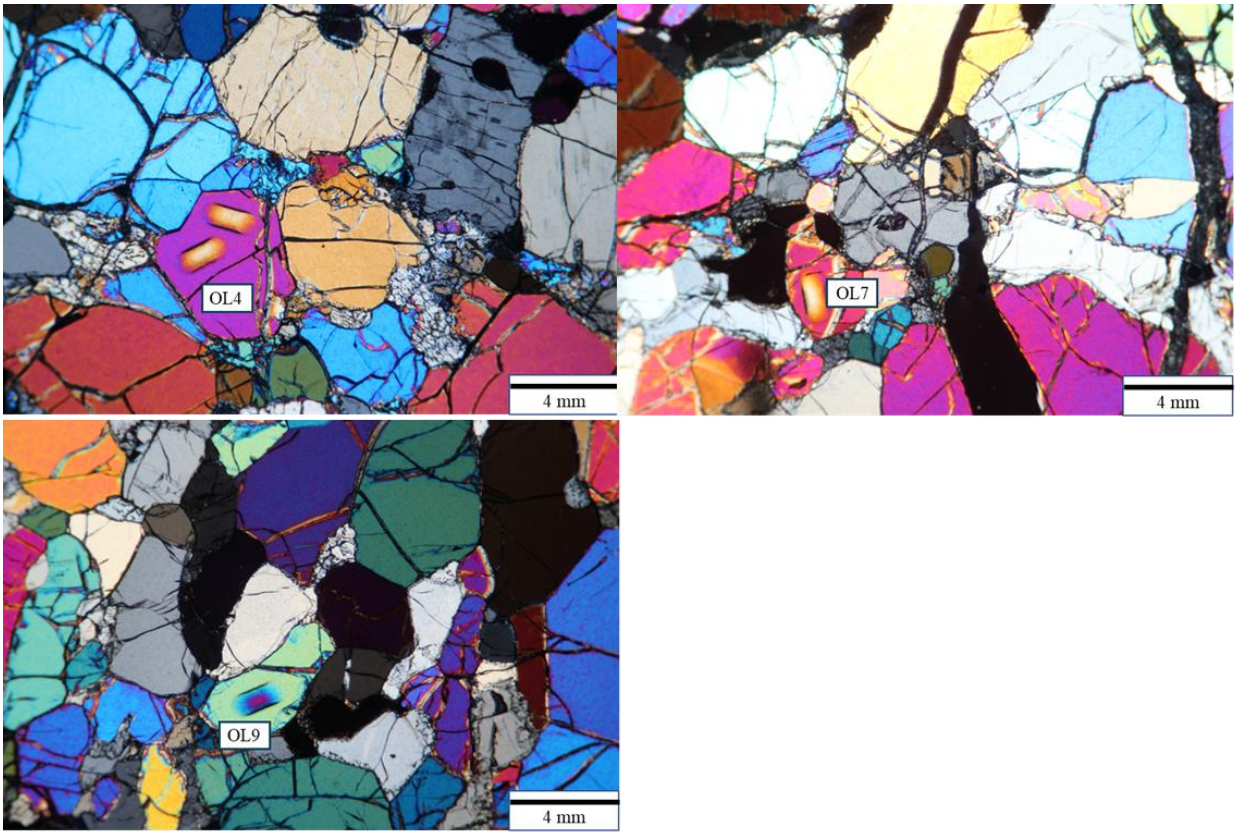

Appendix C (Figure C16): Analysis locations for sample MH-02-108

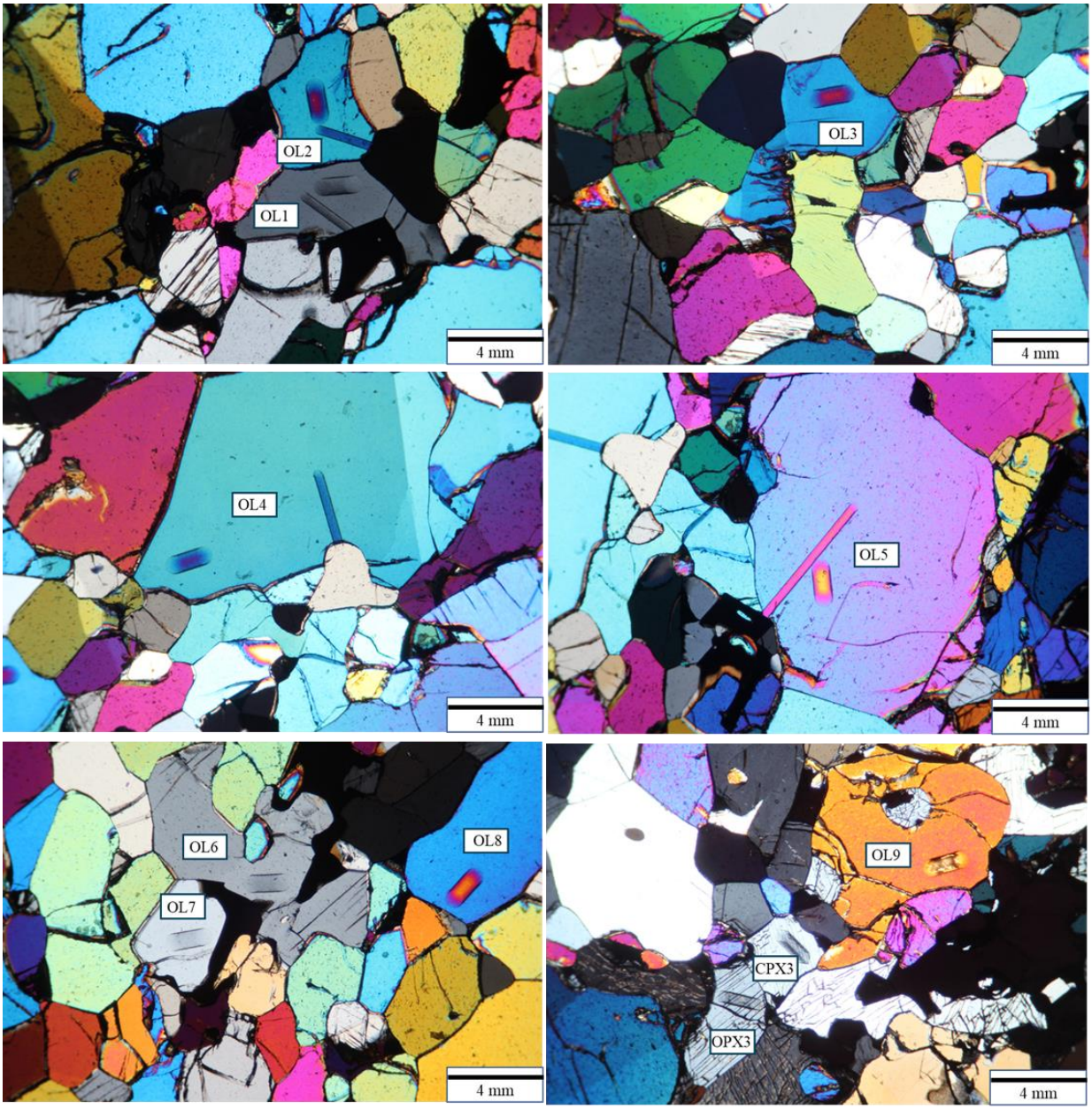

Appendix C (Figure C16): Analysis locations for sample MH-02-108 (continued)

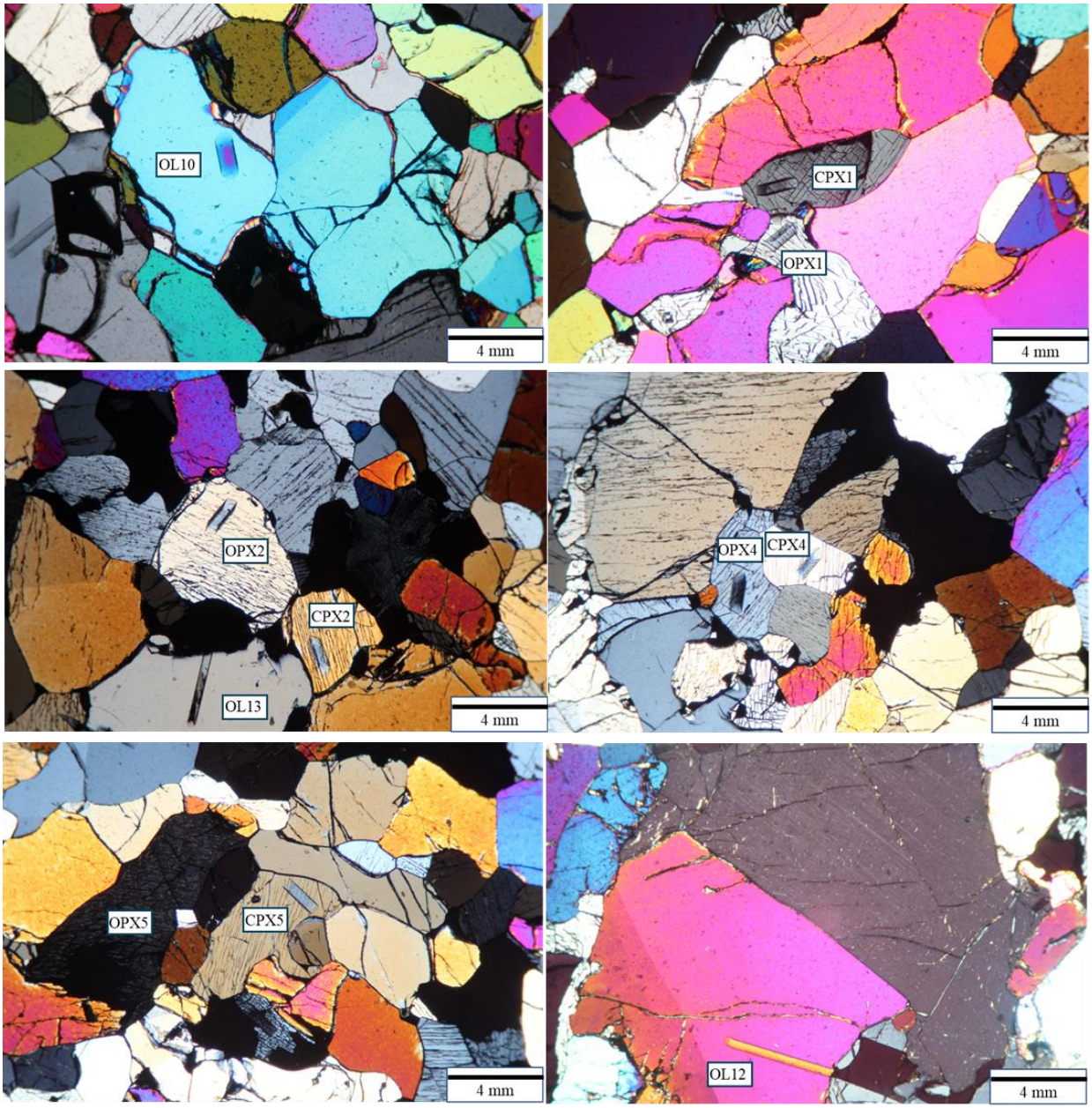

Appendix C (Figure C16): Analysis locations for sample MH-02-108 (continued)

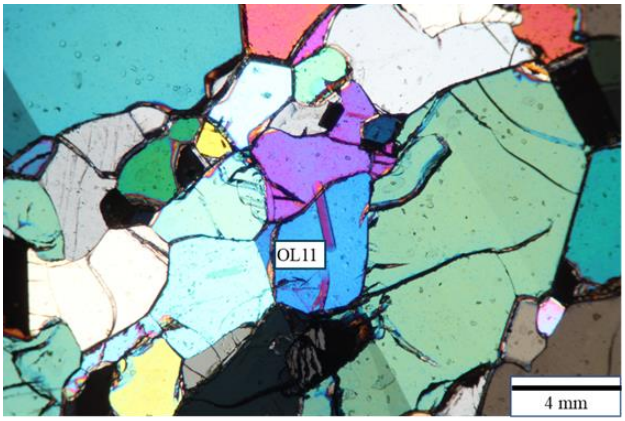

Appendix C (Figure C17): Analysis locations for sample MH-02-109

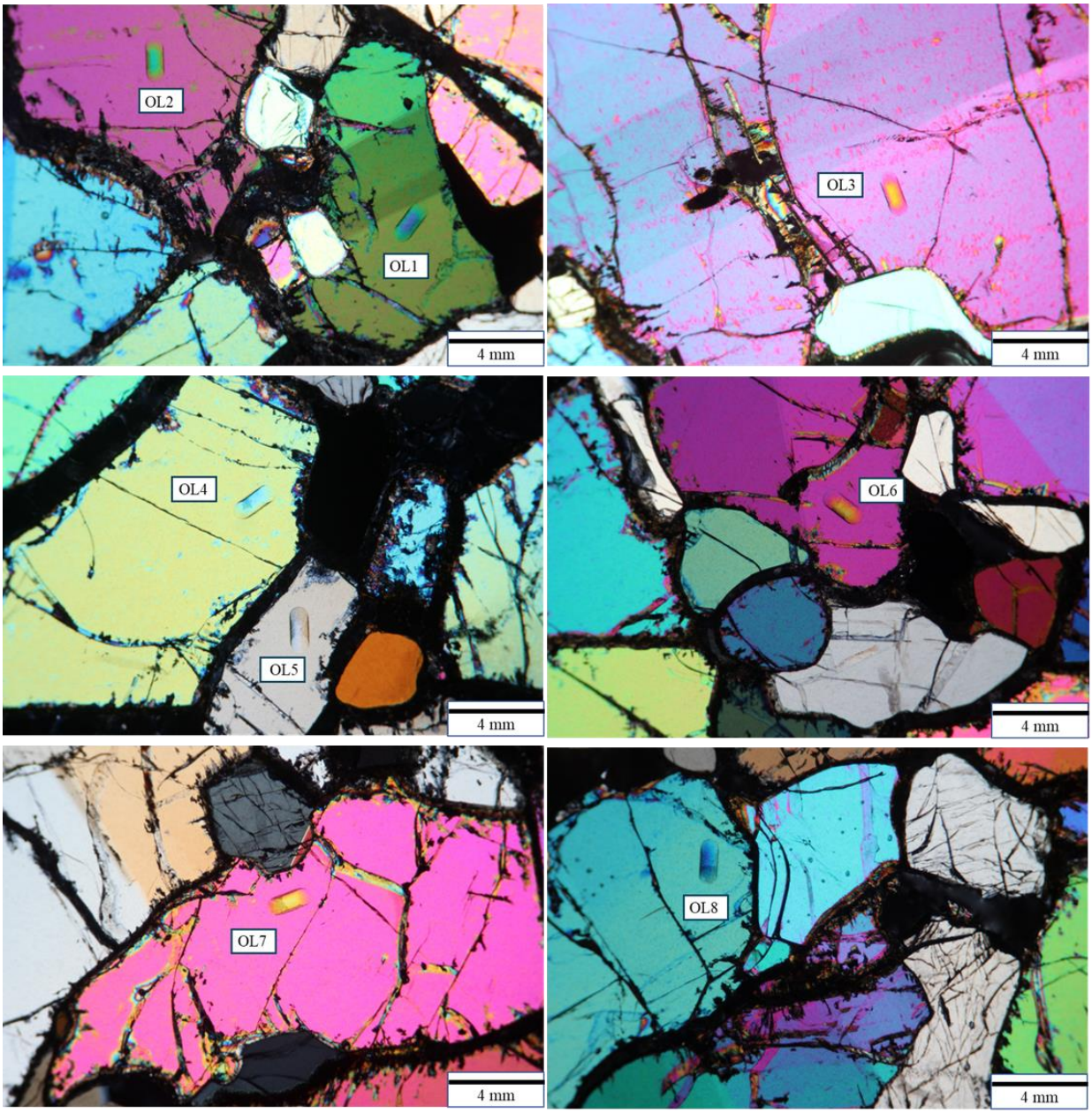

Appendix C (Figure C17): Analysis locations for sample MH-02-109 (continued)

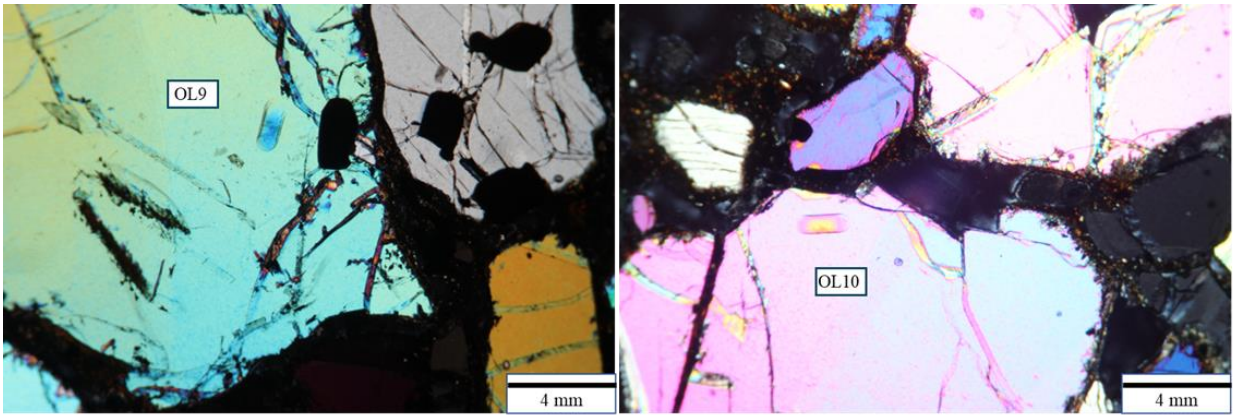

Appendix C (Figure C18): Analysis locations for sample MH-02-111

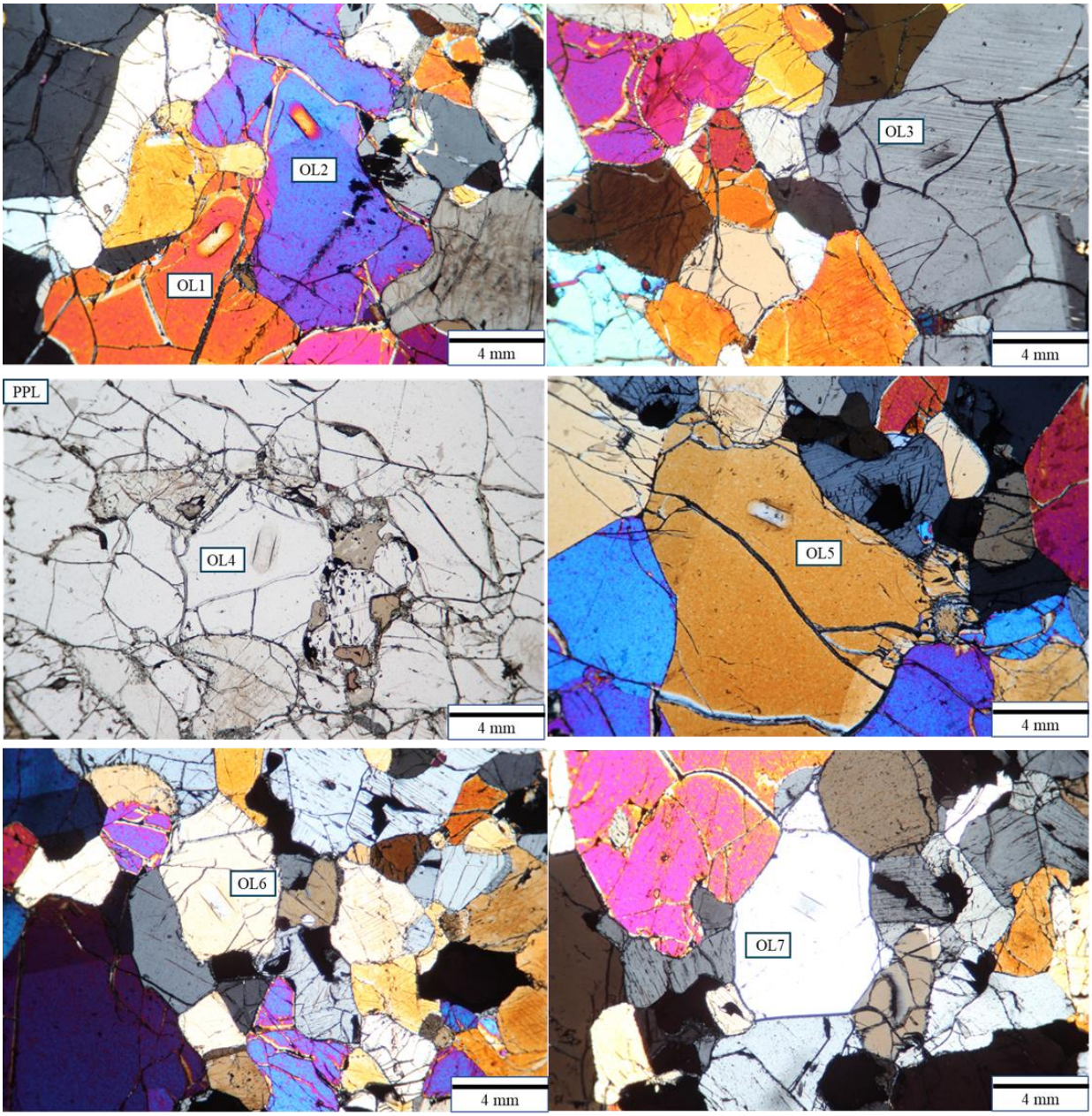

Appendix C (Figure C18): Analysis locations for sample MH-02-111 (continued)

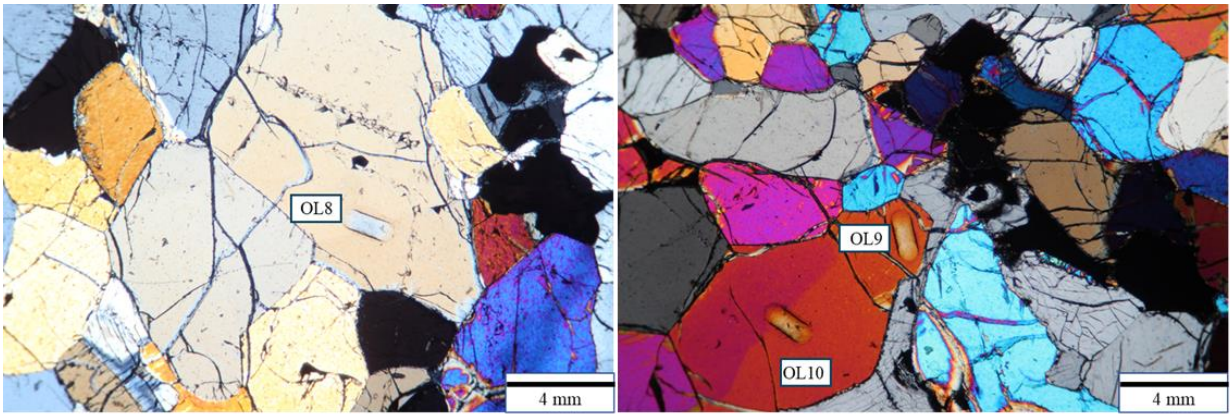

Appendix C (Figure C19): Analysis locations for sample MH-02-112

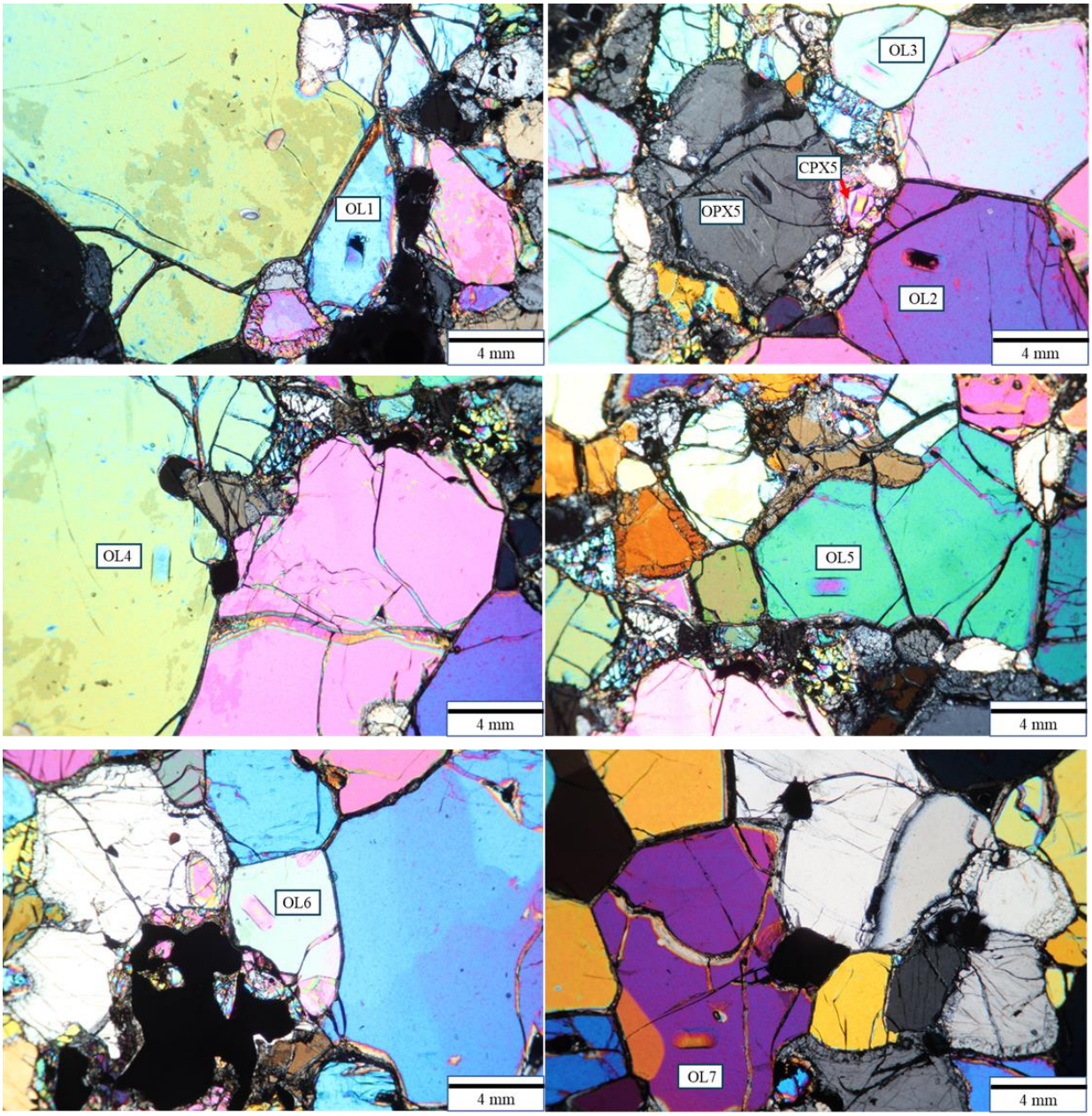

Appendix C (Figure C19): Analysis locations for sample MH-02-112 (continued)

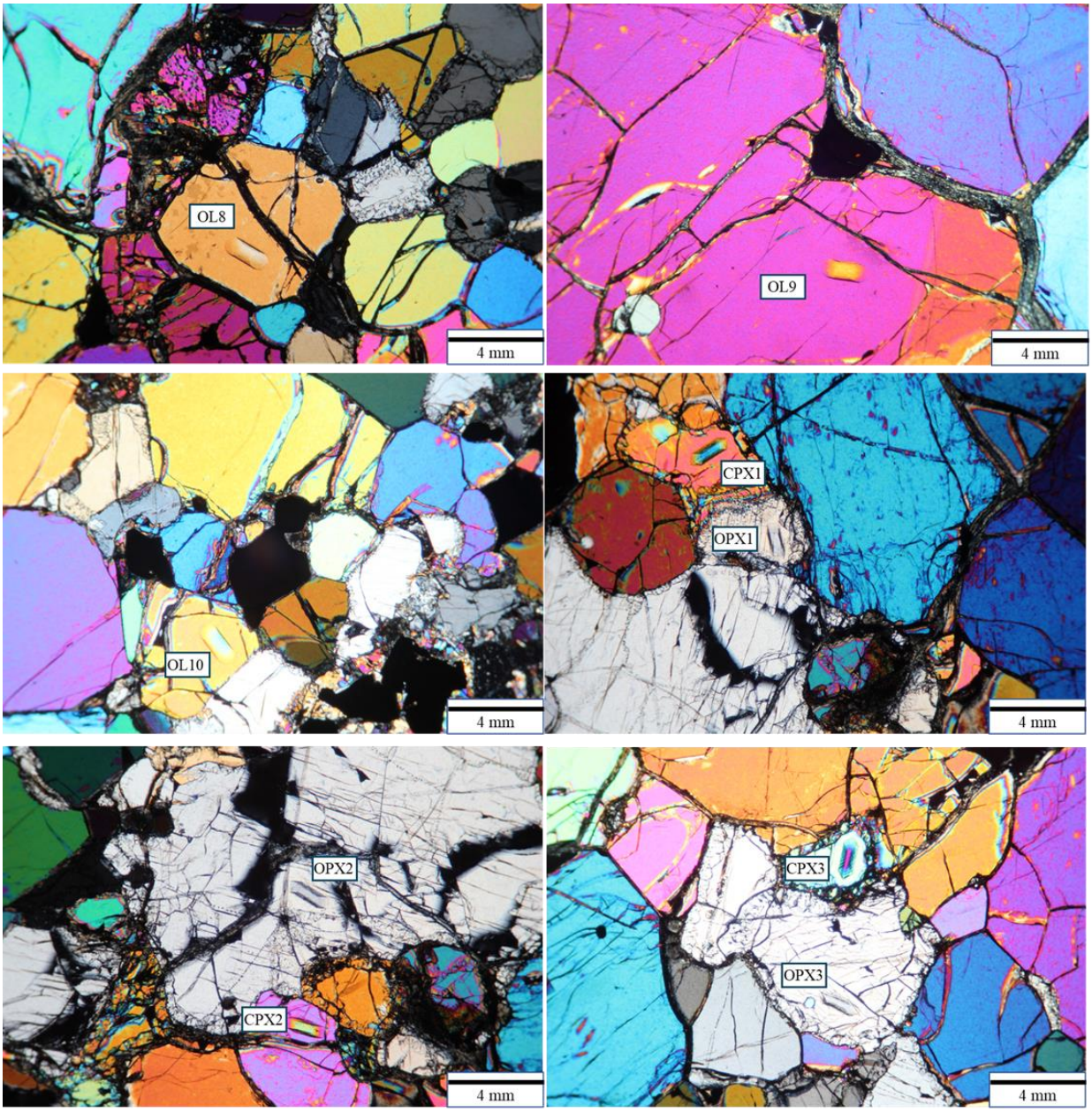

Appendix C (Figure C19): Analysis locations for sample MH-02-112 (continued)

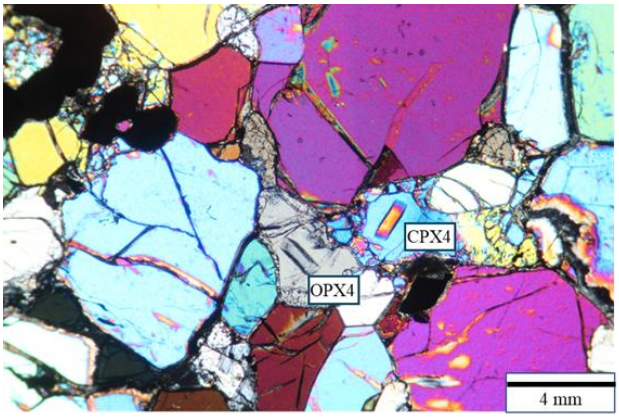

Appendix C (Figure C20): Analysis locations for sample MH-02-115

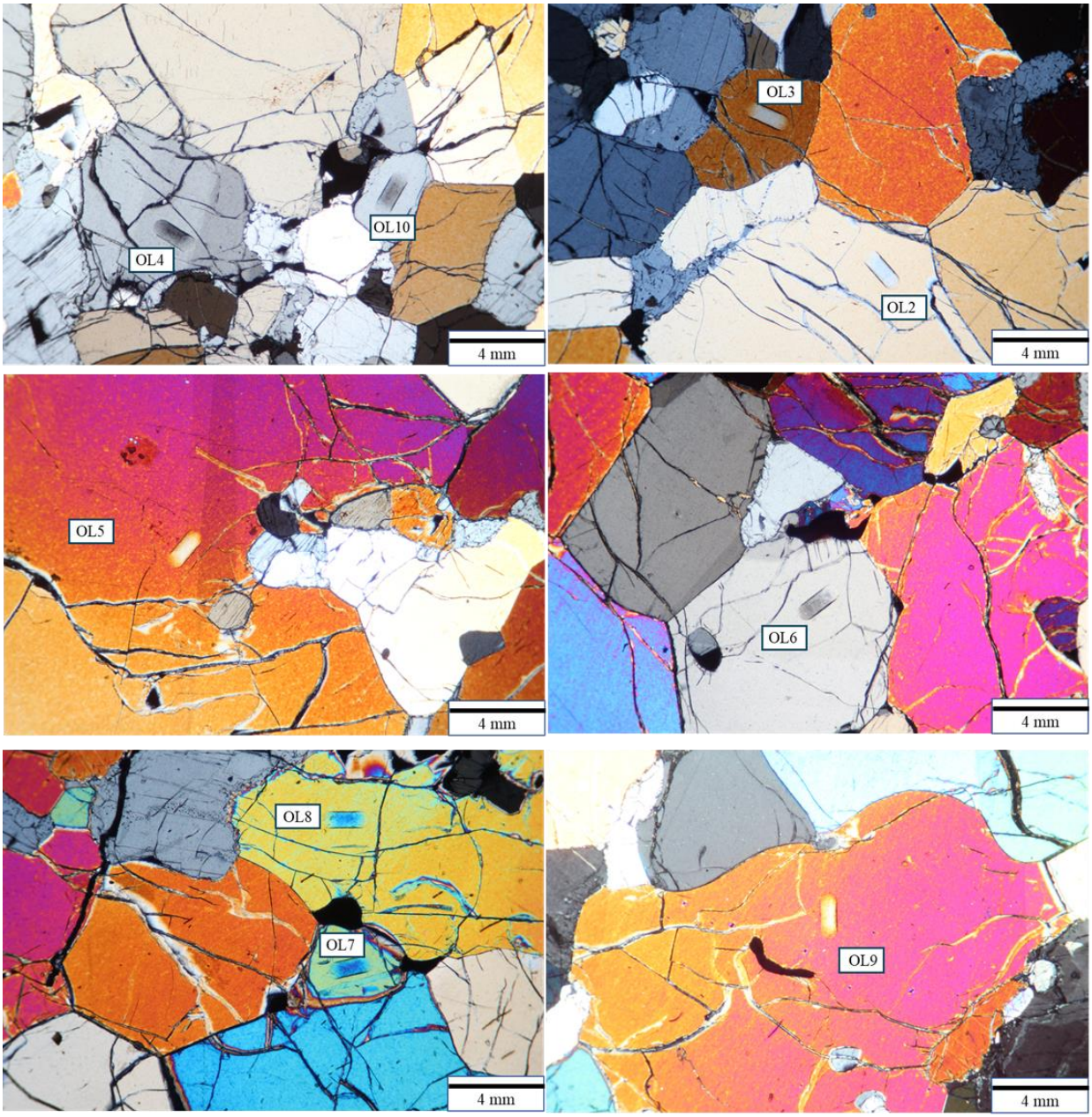

Appendix C (Figure C21): Analysis locations for sample MH-02-115B

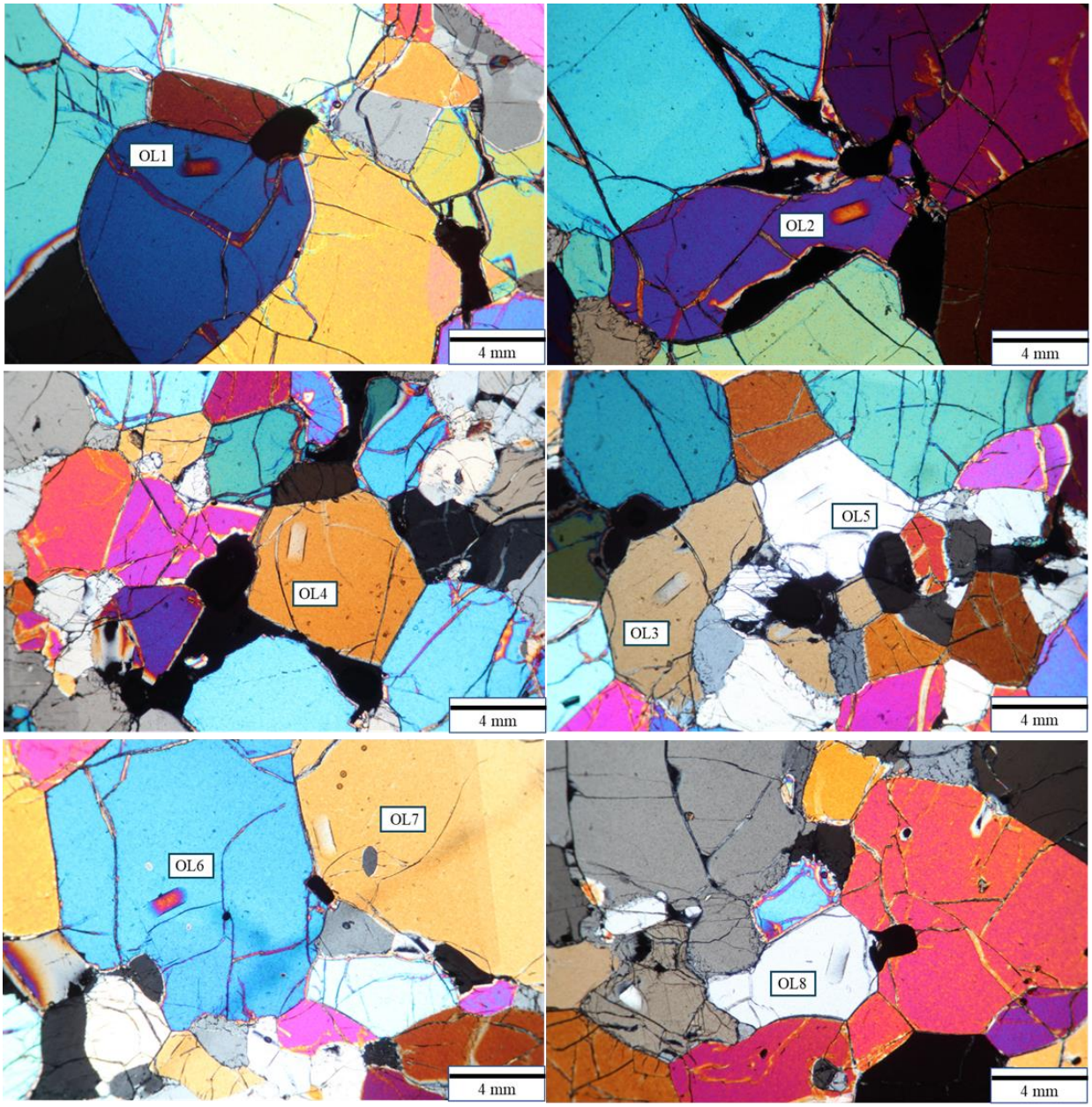

Appendix C (Figure C21): Analysis locations for sample MH-02-115B (continued)

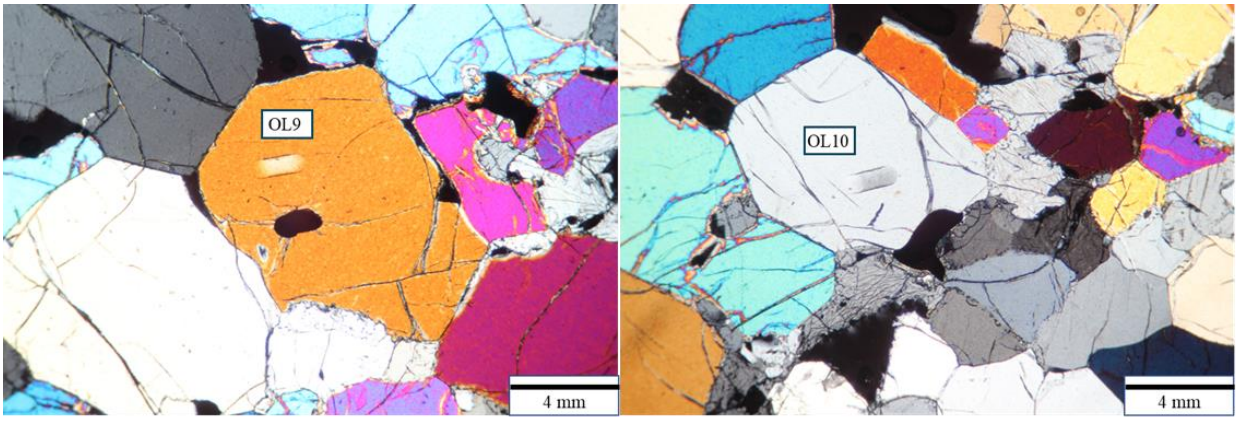

Appendix C (Figure C22): Analysis locations for sample MH-02-116

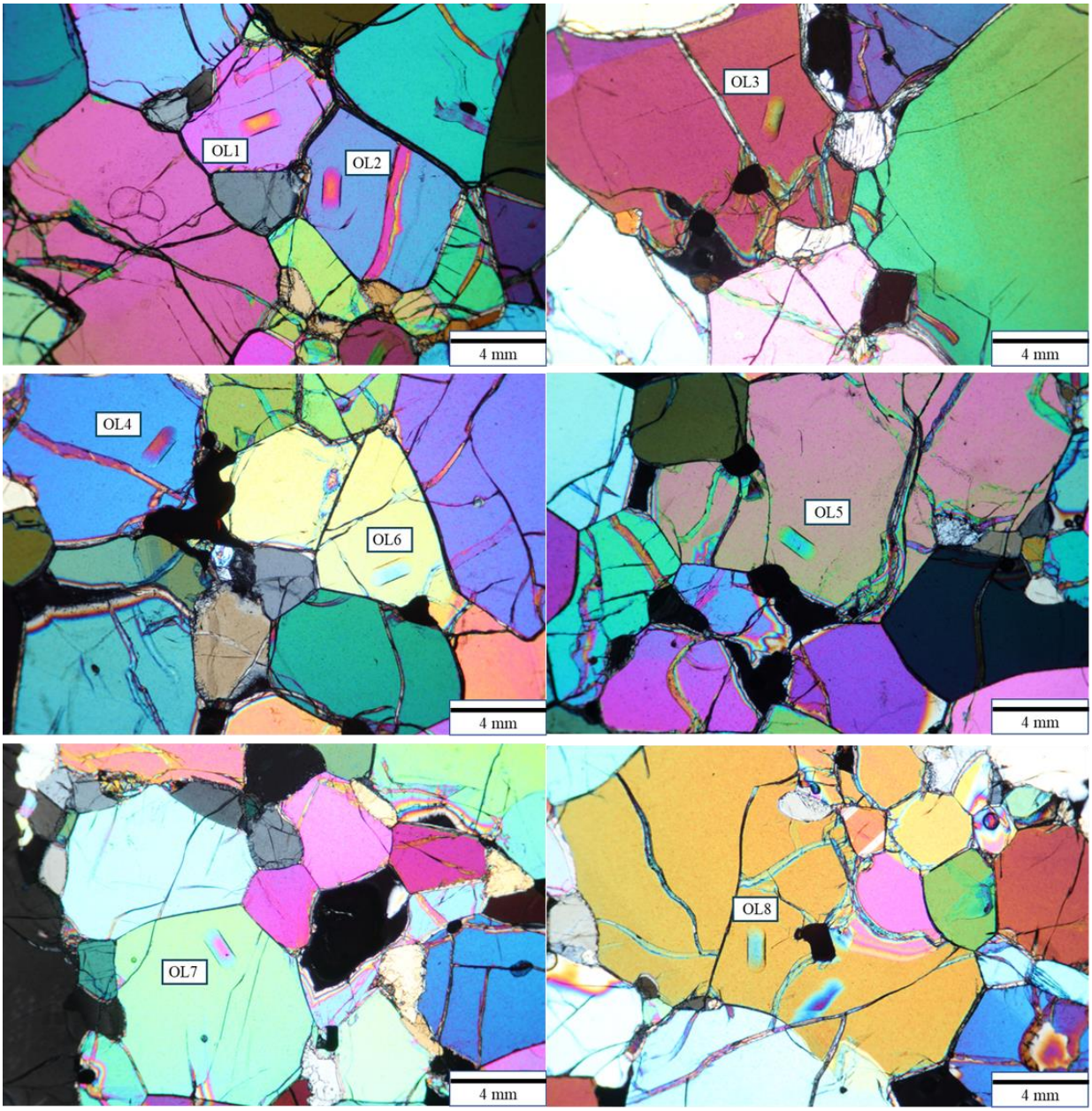

Appendix C (Figure C22): Analysis locations for sample MH-02-116 (continued)

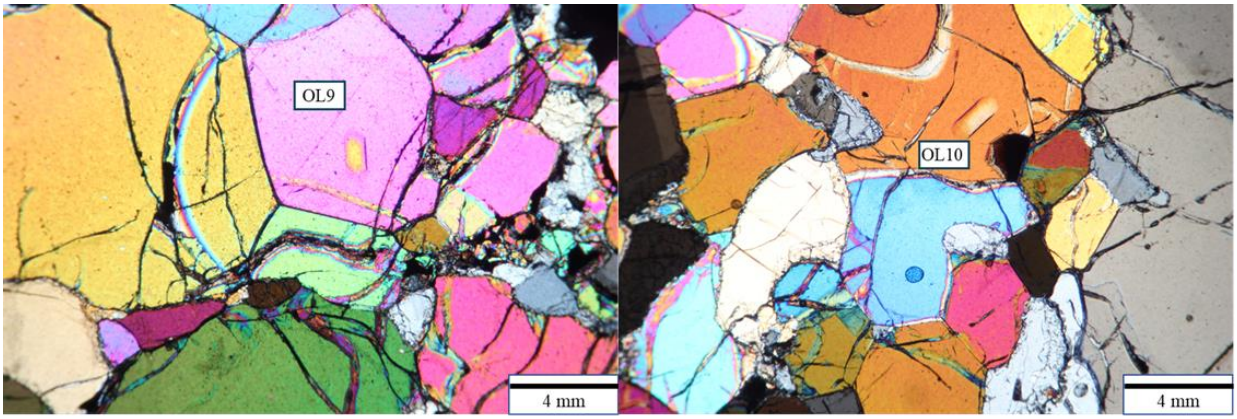

Appendix C (Figure C23): Analysis locations for sample MH-02-117-1

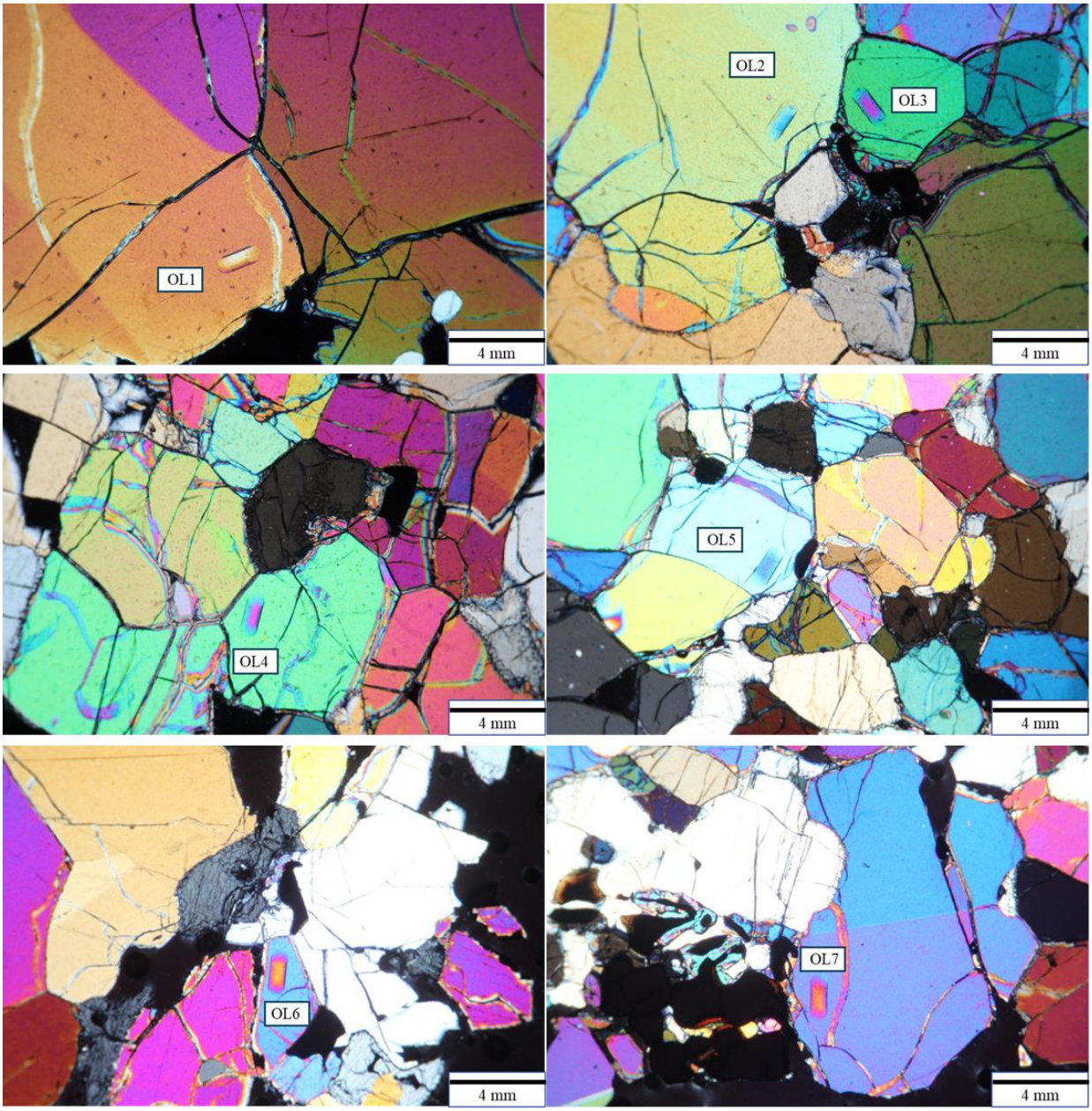

Appendix C (Figure C23): Analysis locations for sample MH-02-117-1 (continued)

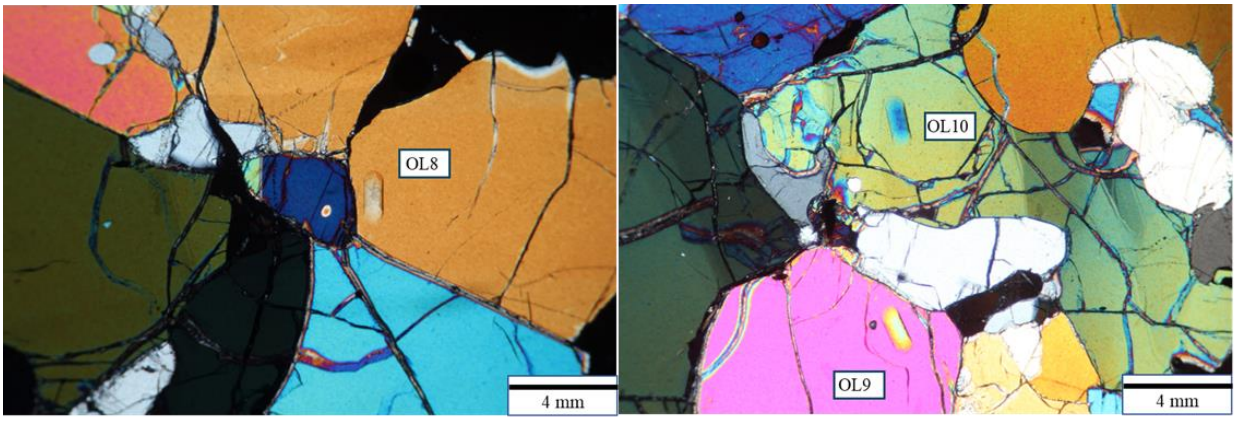

Appendix C (Figure C24): Analysis locations for sample MH-02-117-2

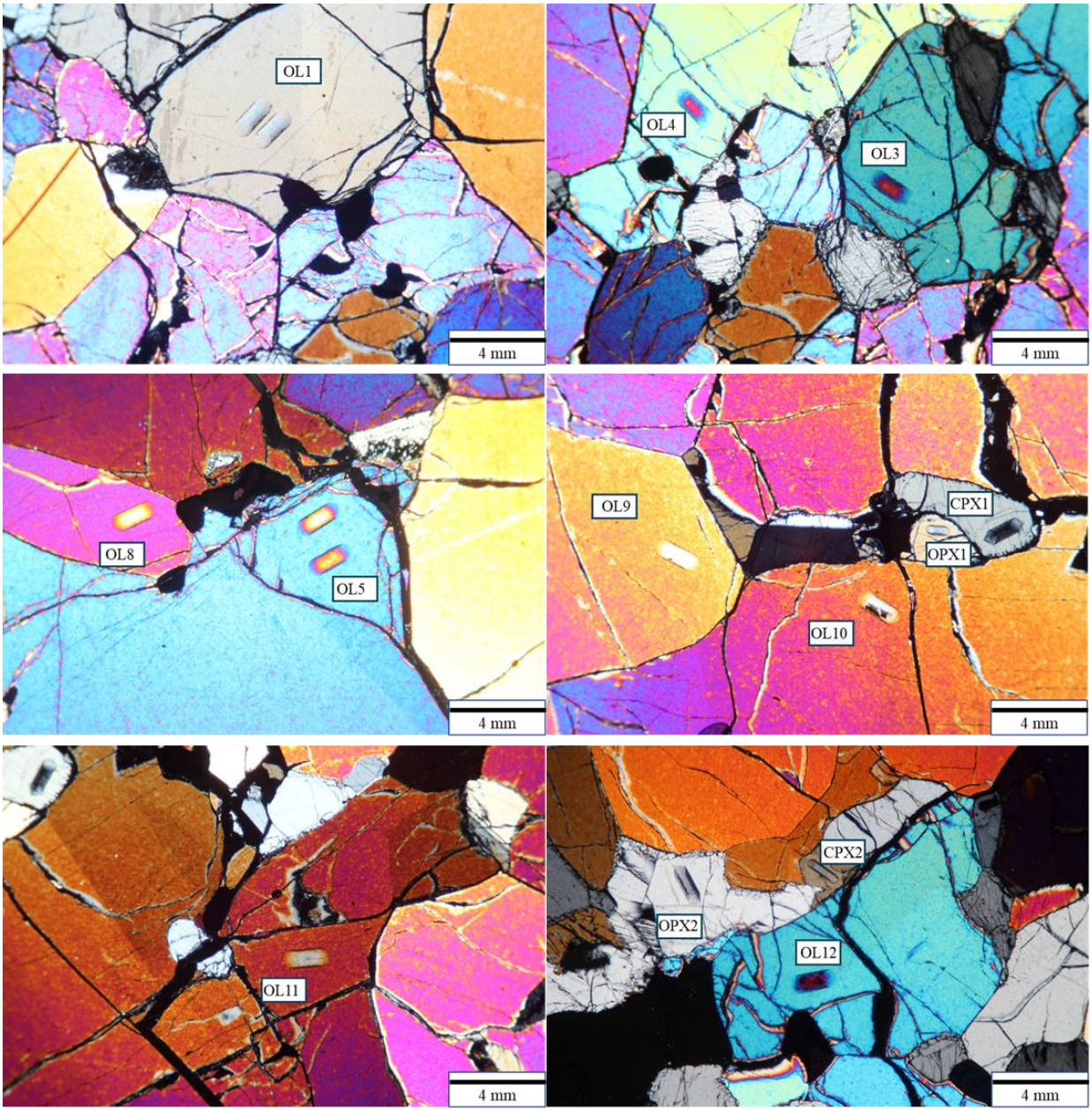

Appendix C (Figure C24): Analysis locations for sample MH-02-117-2 (continued)

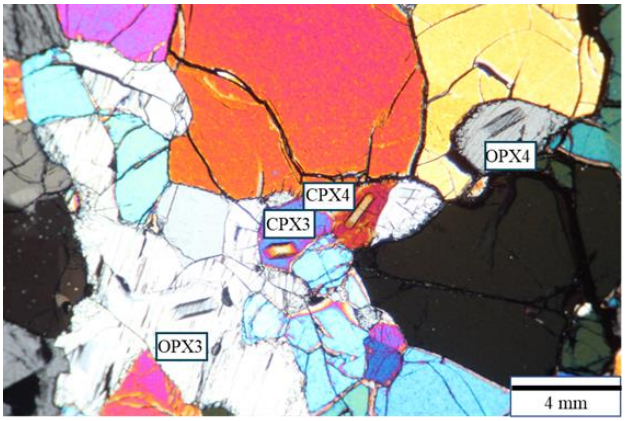

Appendix C (Figure C25): Analysis locations for sample MH-02-125

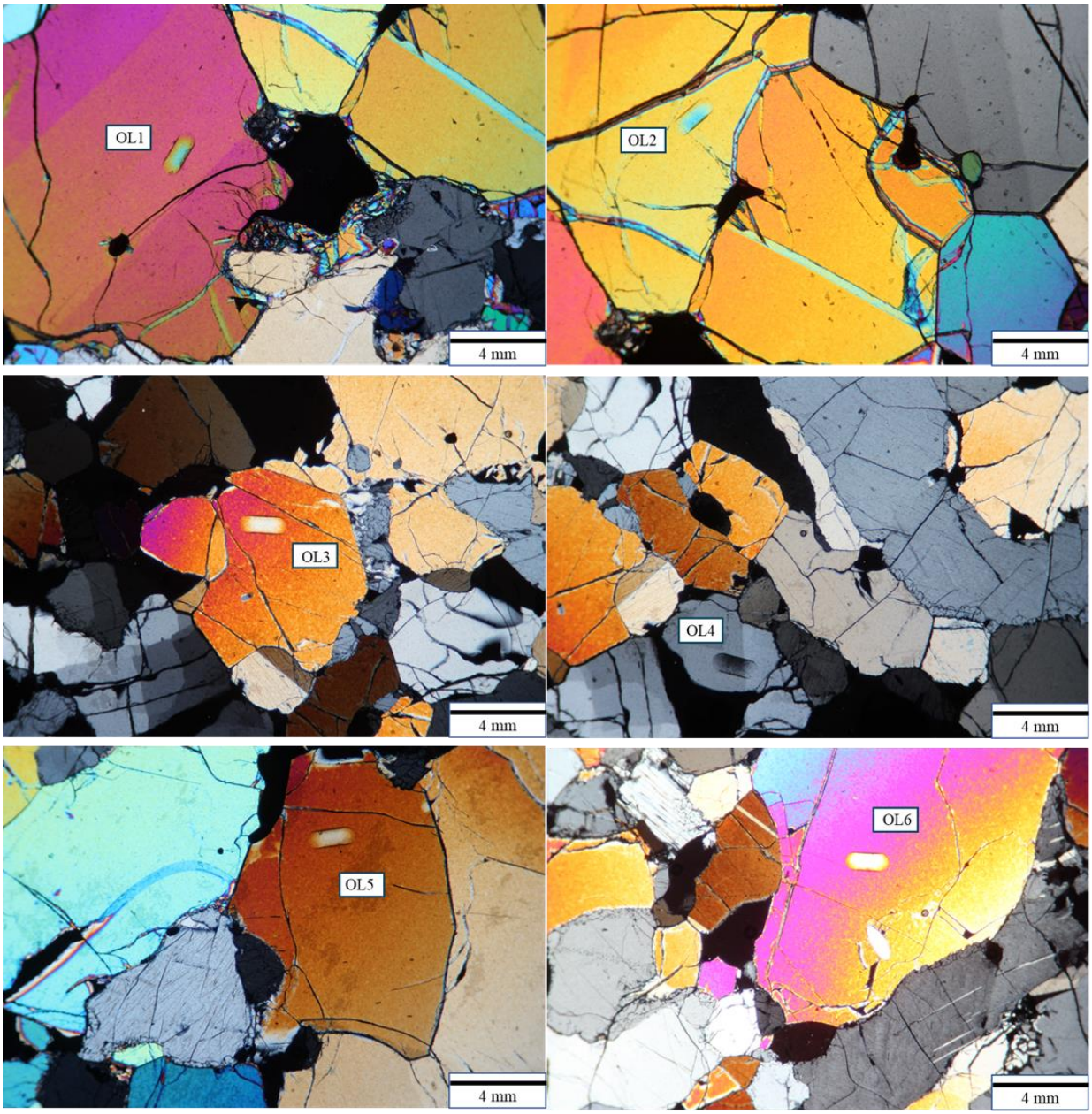

Appendix C (Figure C25): Analysis locations for sample MH-02-125 (continued)

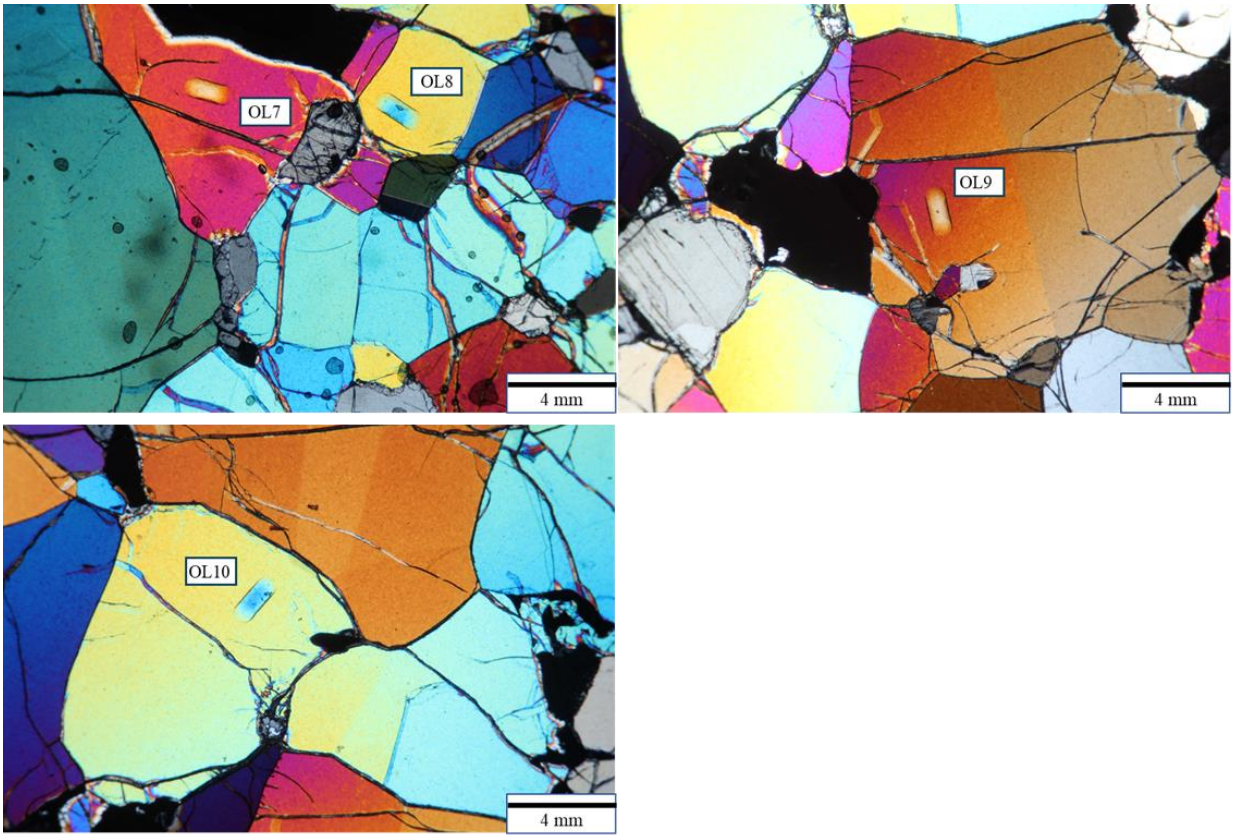

Appendix C (Figure C26): Analysis locations for sample MH-02-114

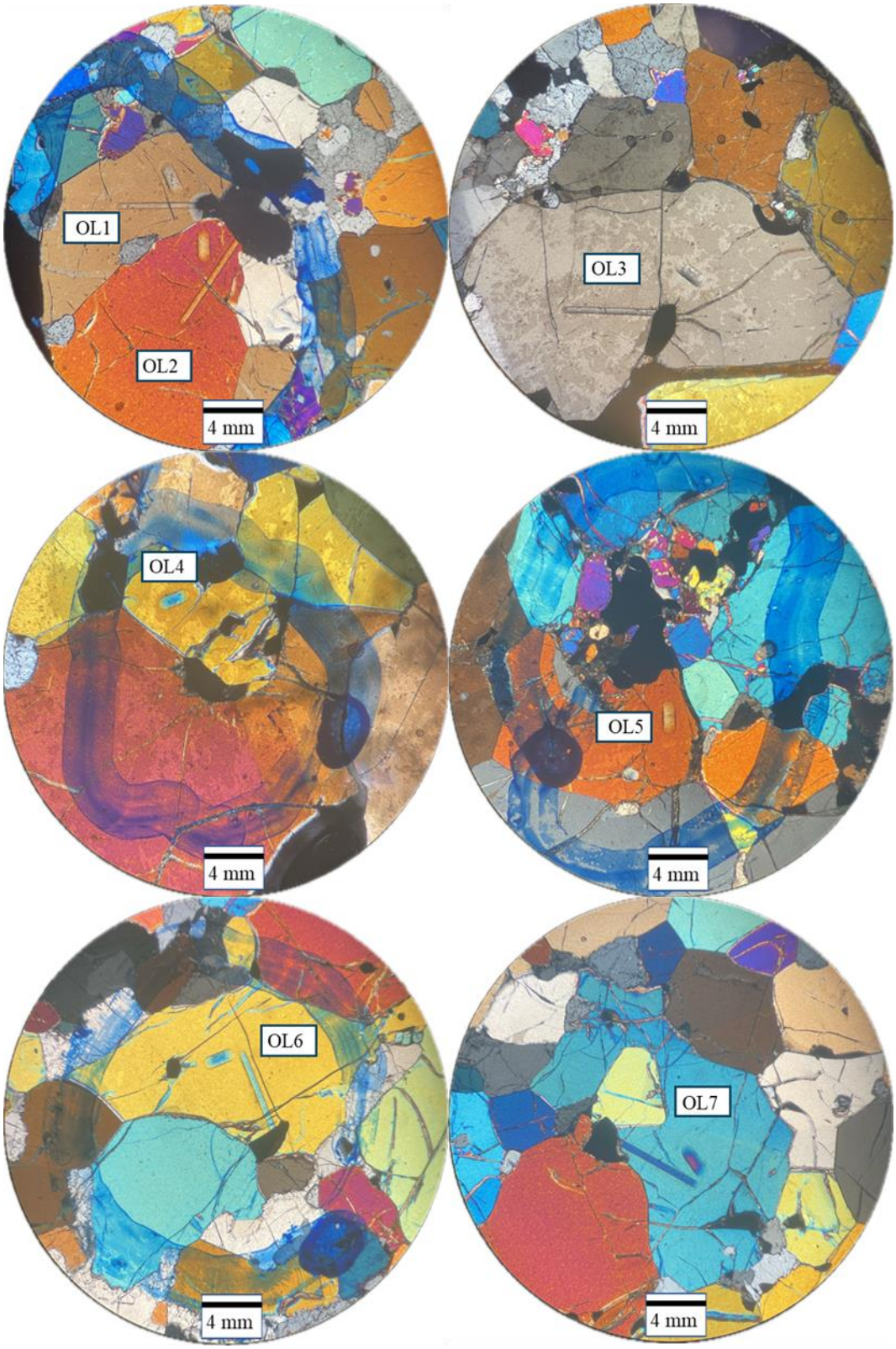

Appendix C (Figure C26): Analysis locations for sample MH-02-114 (continued)

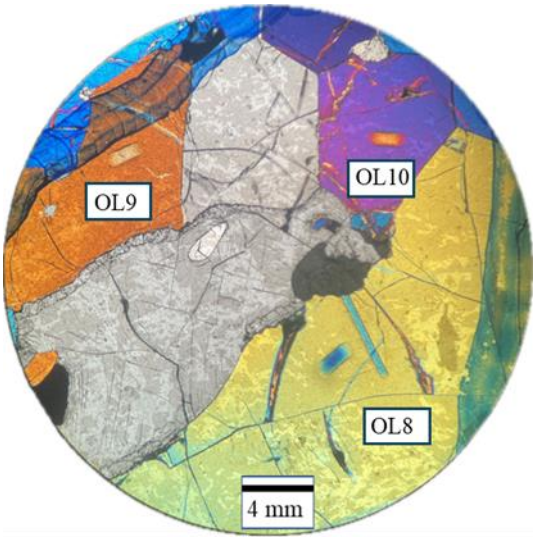

Appendix C (Figure C27): Analysis locations for sample MH-02-10D

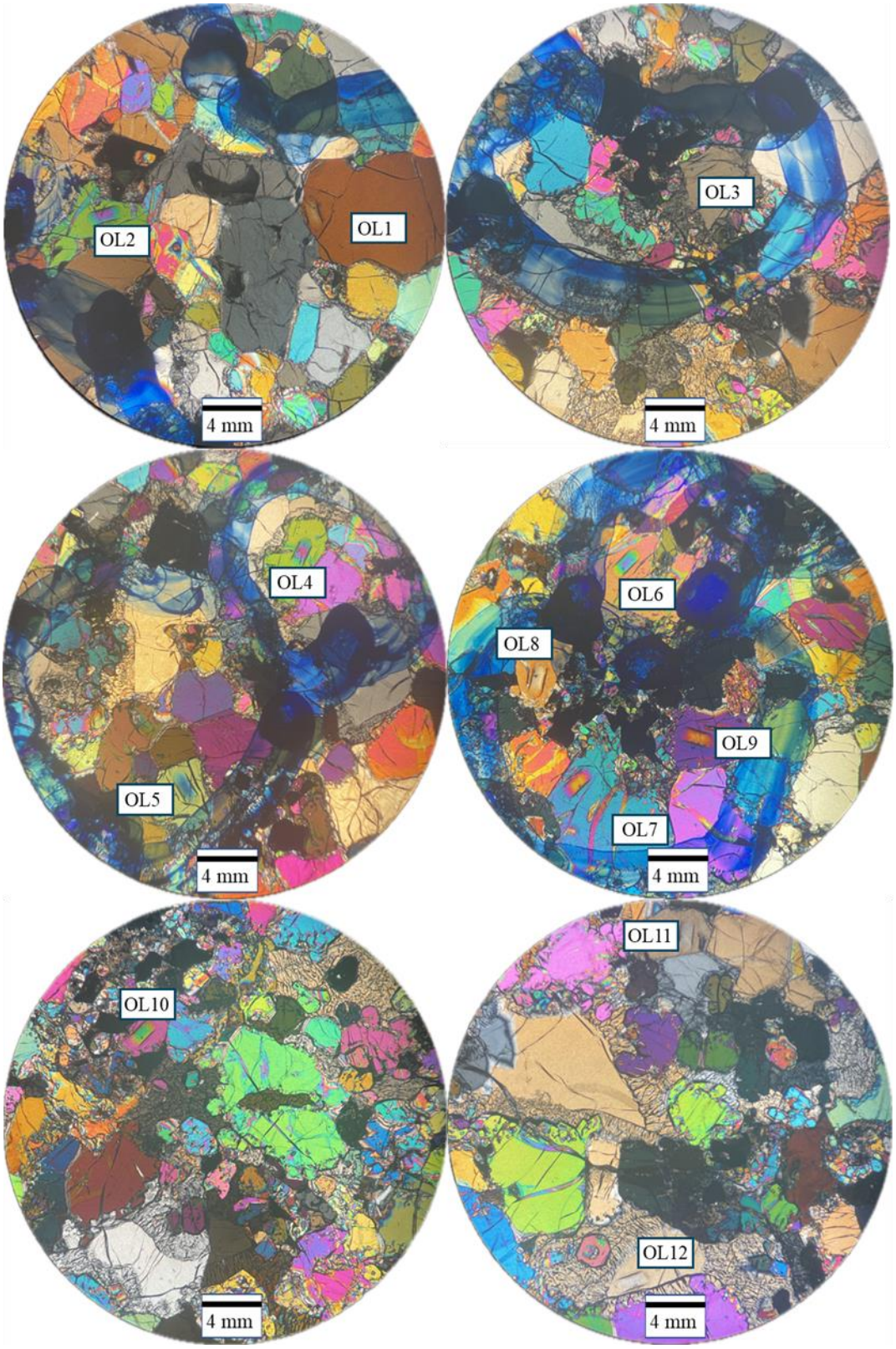

Appendix C (Figure C28): Analysis locations for sample MH-02-12

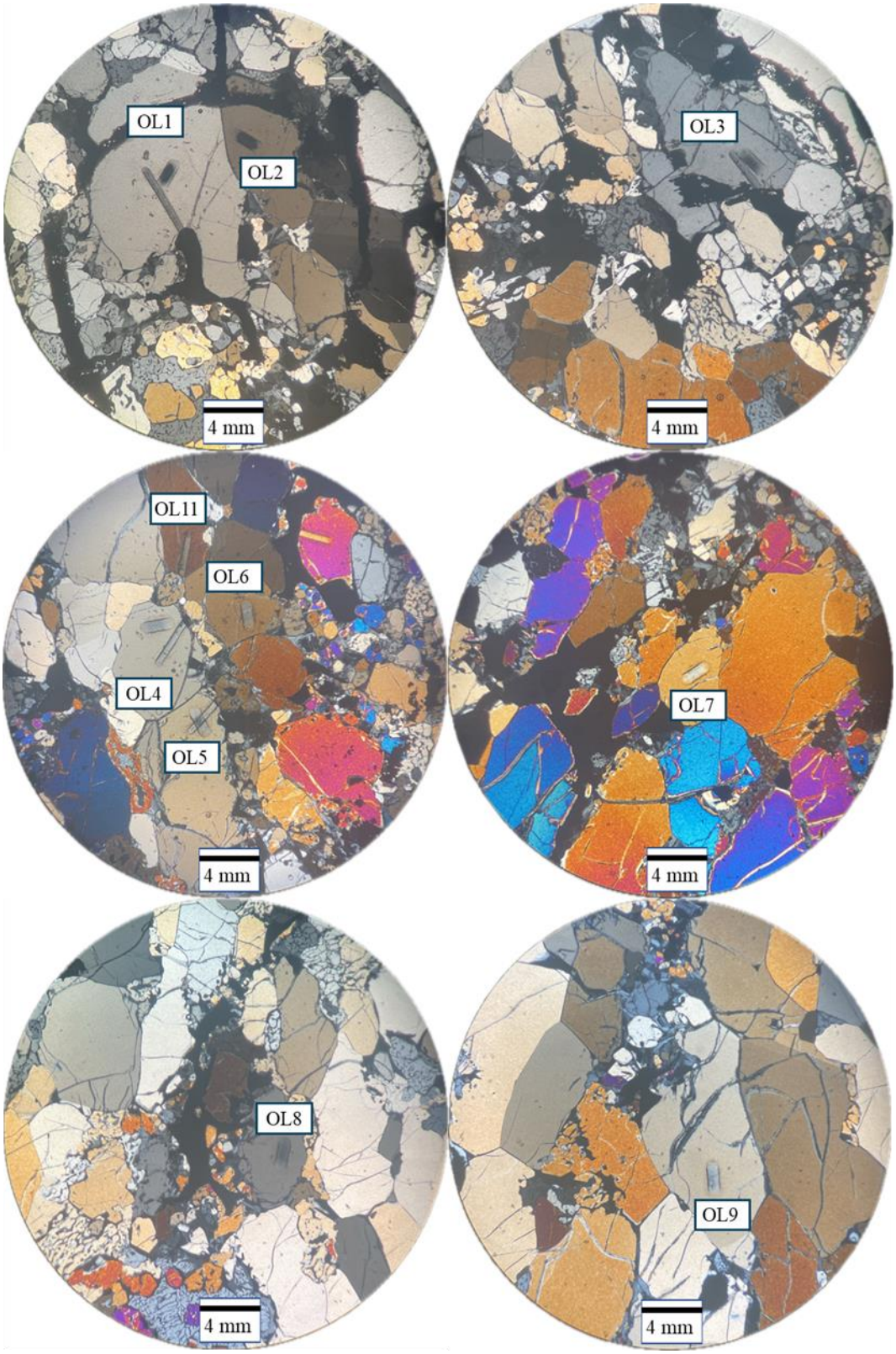

Appendix C (Figure C28): Analysis locations for sample MH-02-12 (continued)

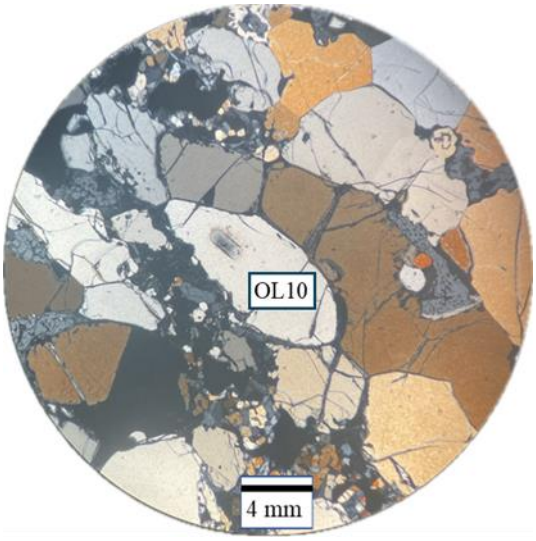

Appendix D: EPMA analysis locations.

Appendix D (Figure D1): Analysis locations for sample MH-02-115

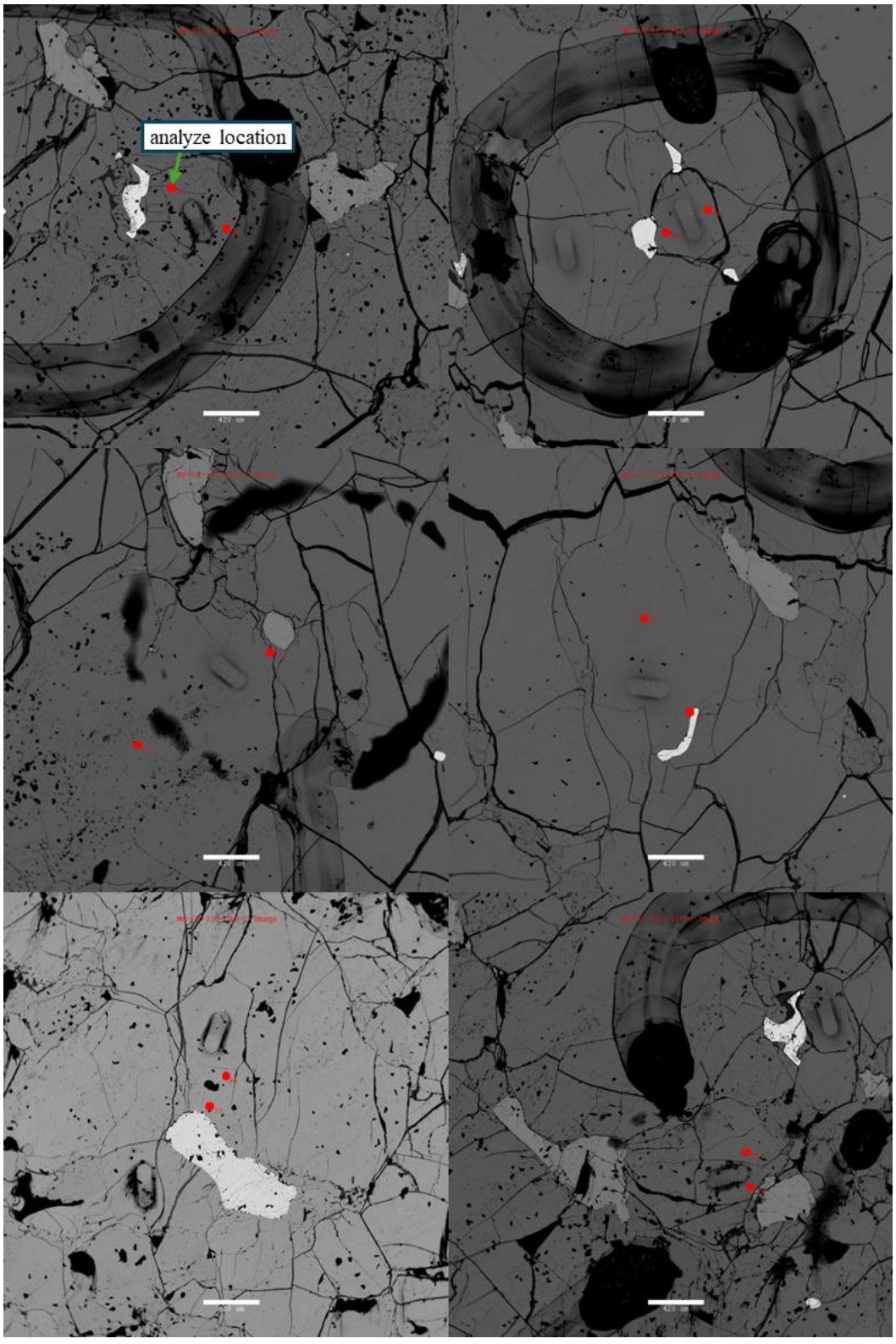

Appendix D (Figure D2): Analysis locations for sample MH-02-116

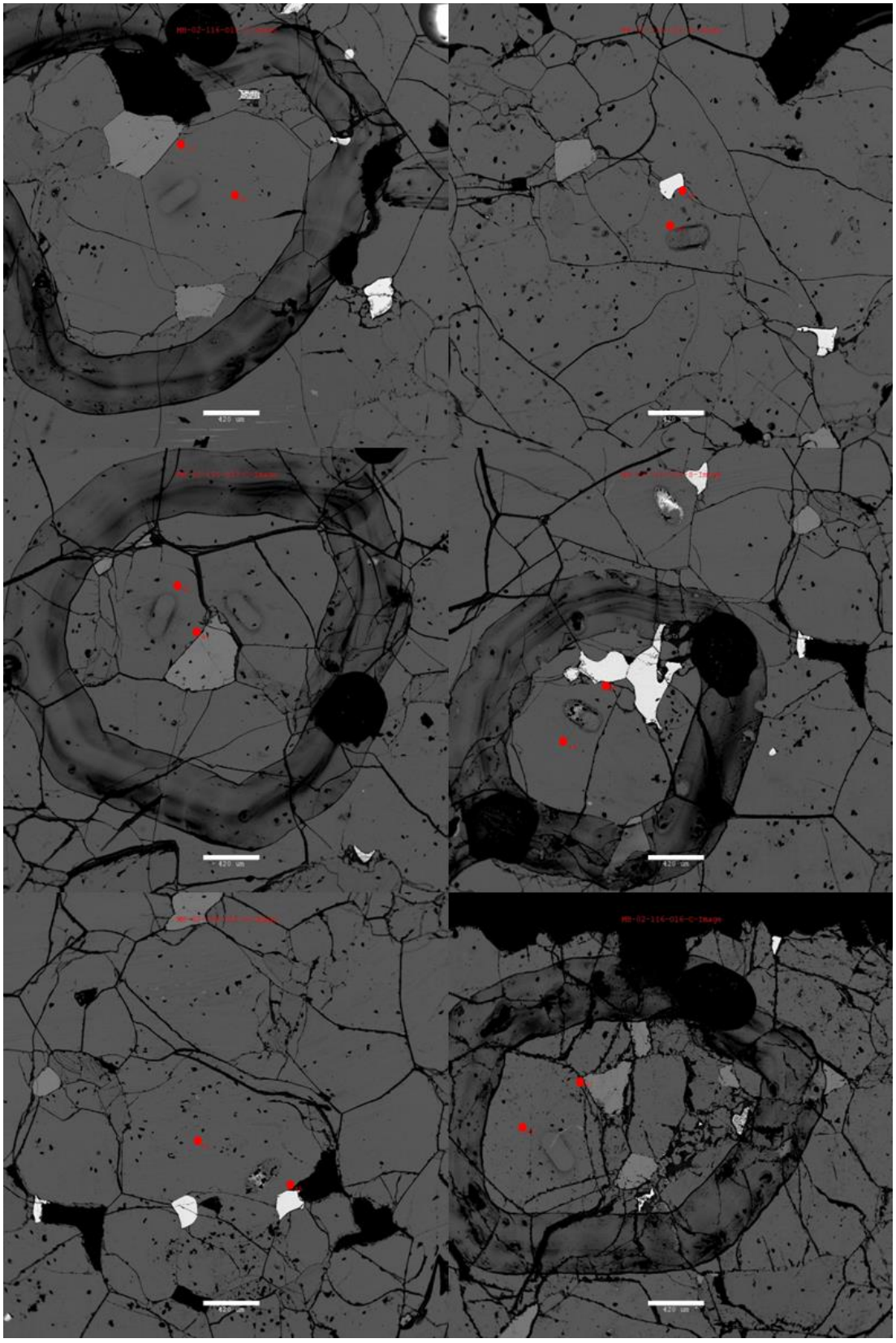

Appendix D (Figure D3): Analysis locations for sample MH-02-19

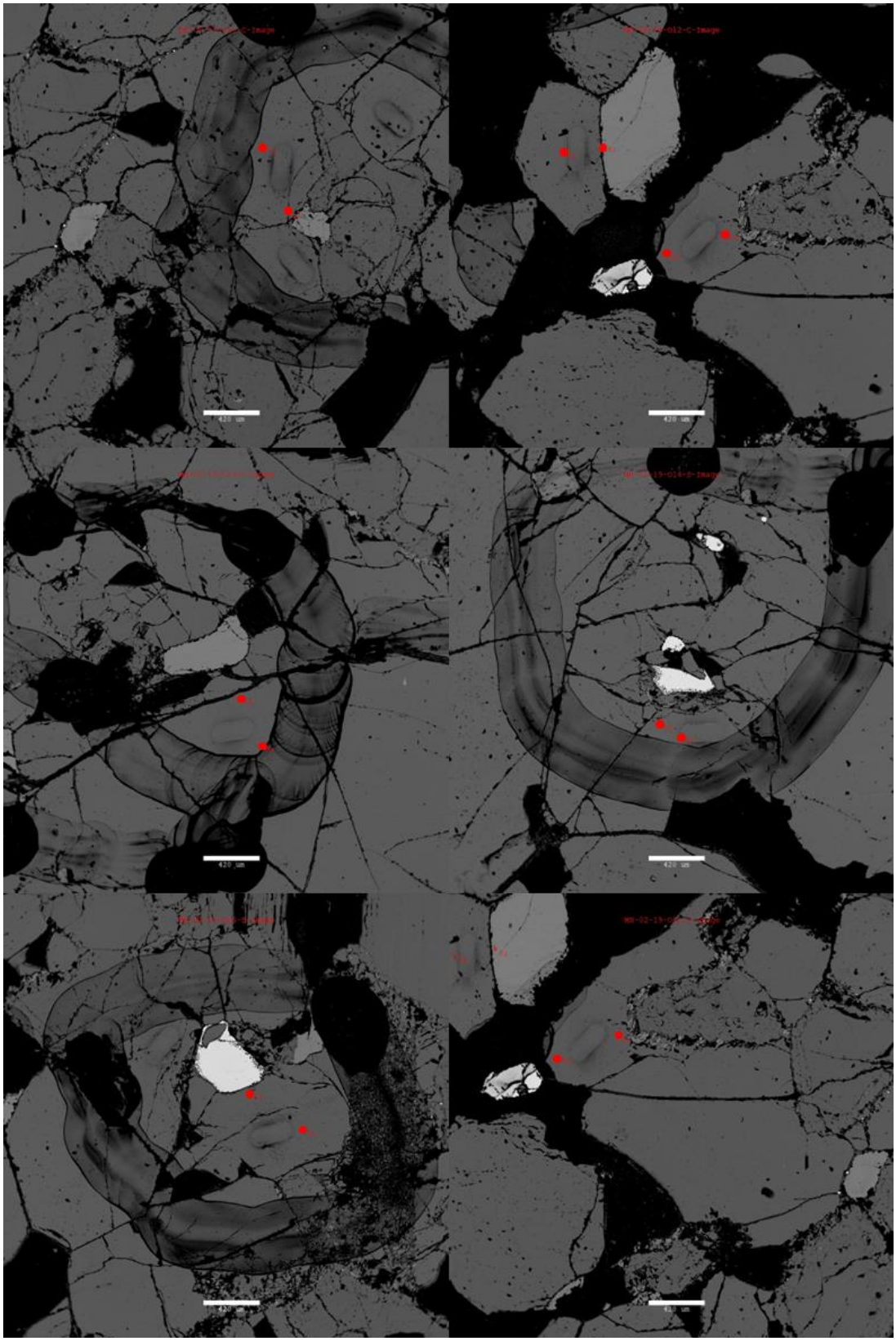

Appendix D (Figure D4): Analysis locations for sample MH-02-121

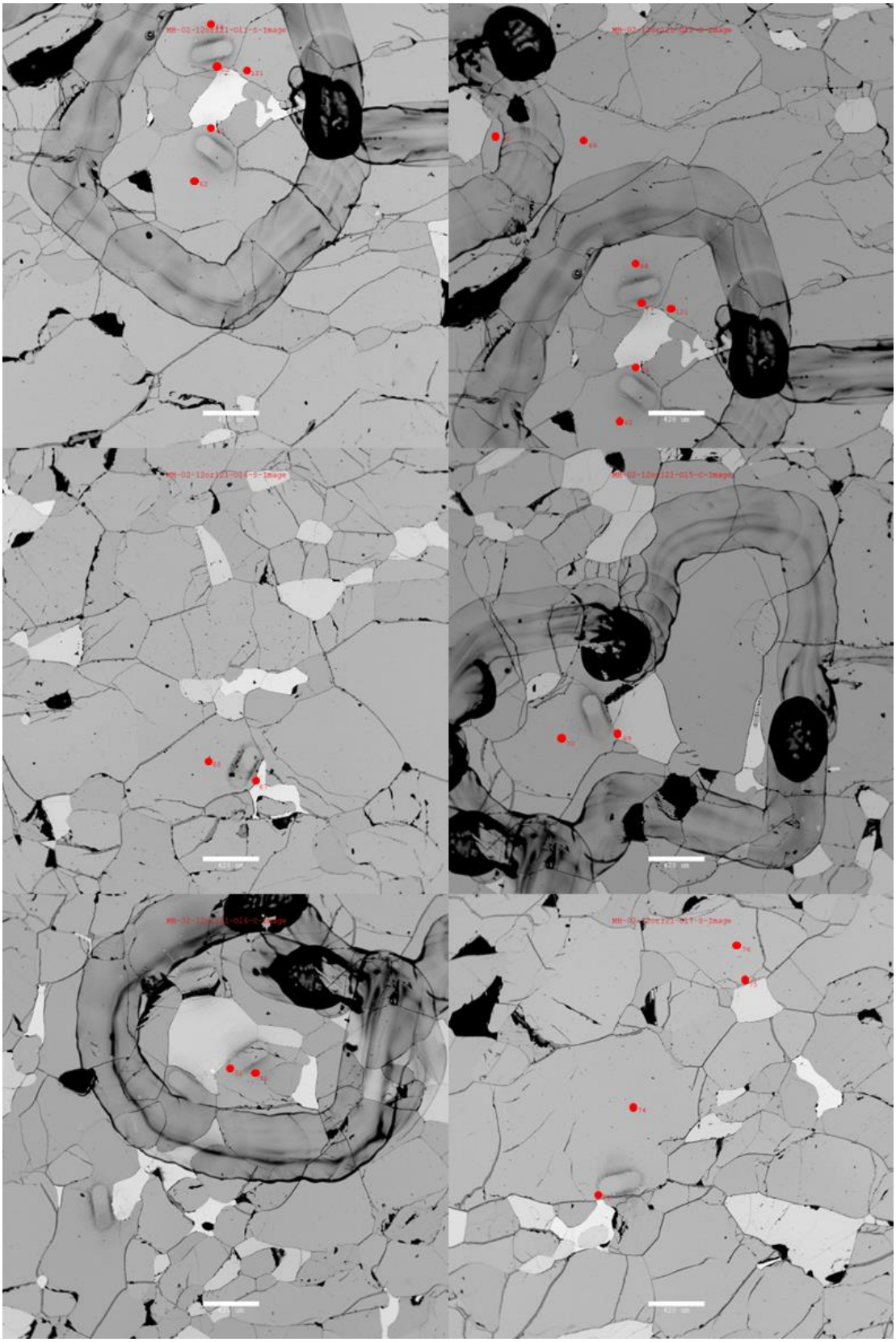

Appendix D (Figure D4): Analysis locations for sample MH-02-121 (continued)

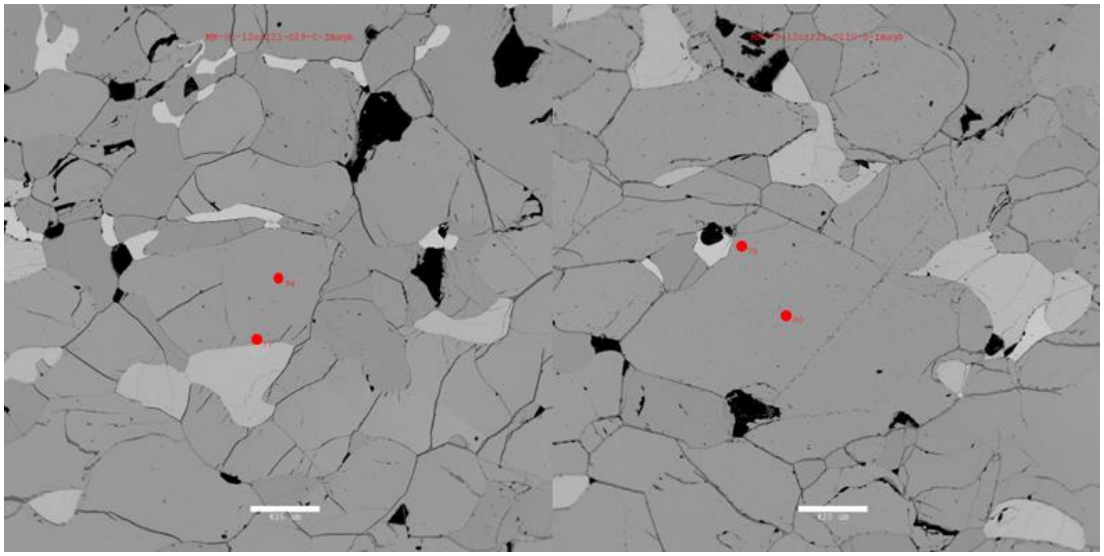

Appendix D (Figure D5): Analysis locations for sample MH-02-112

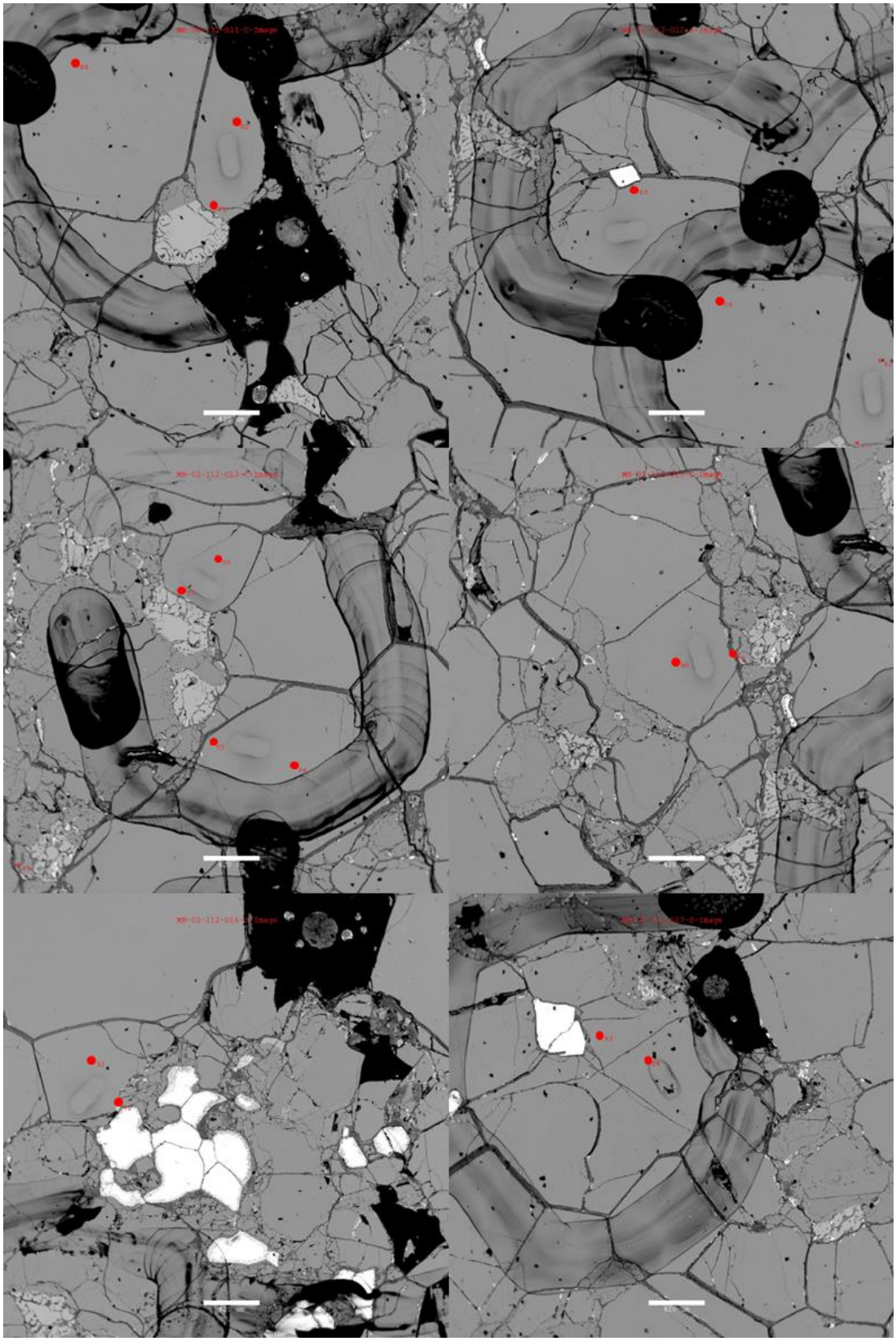

Appendix D (Figure D5): Analysis locations for sample MH-02-112 (continued)

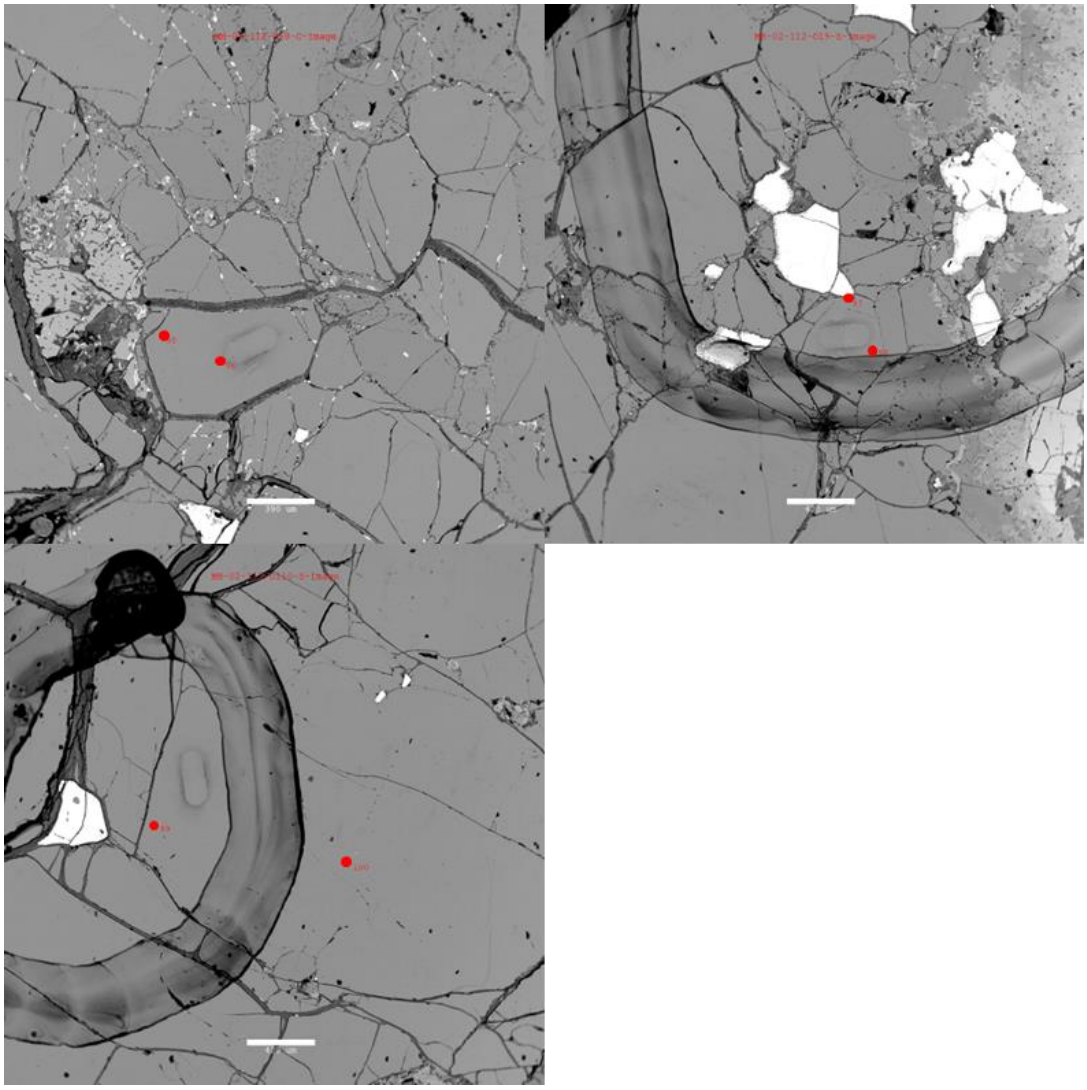

Appendix D (Figure D6): Analysis locations for sample MH-02-117-2

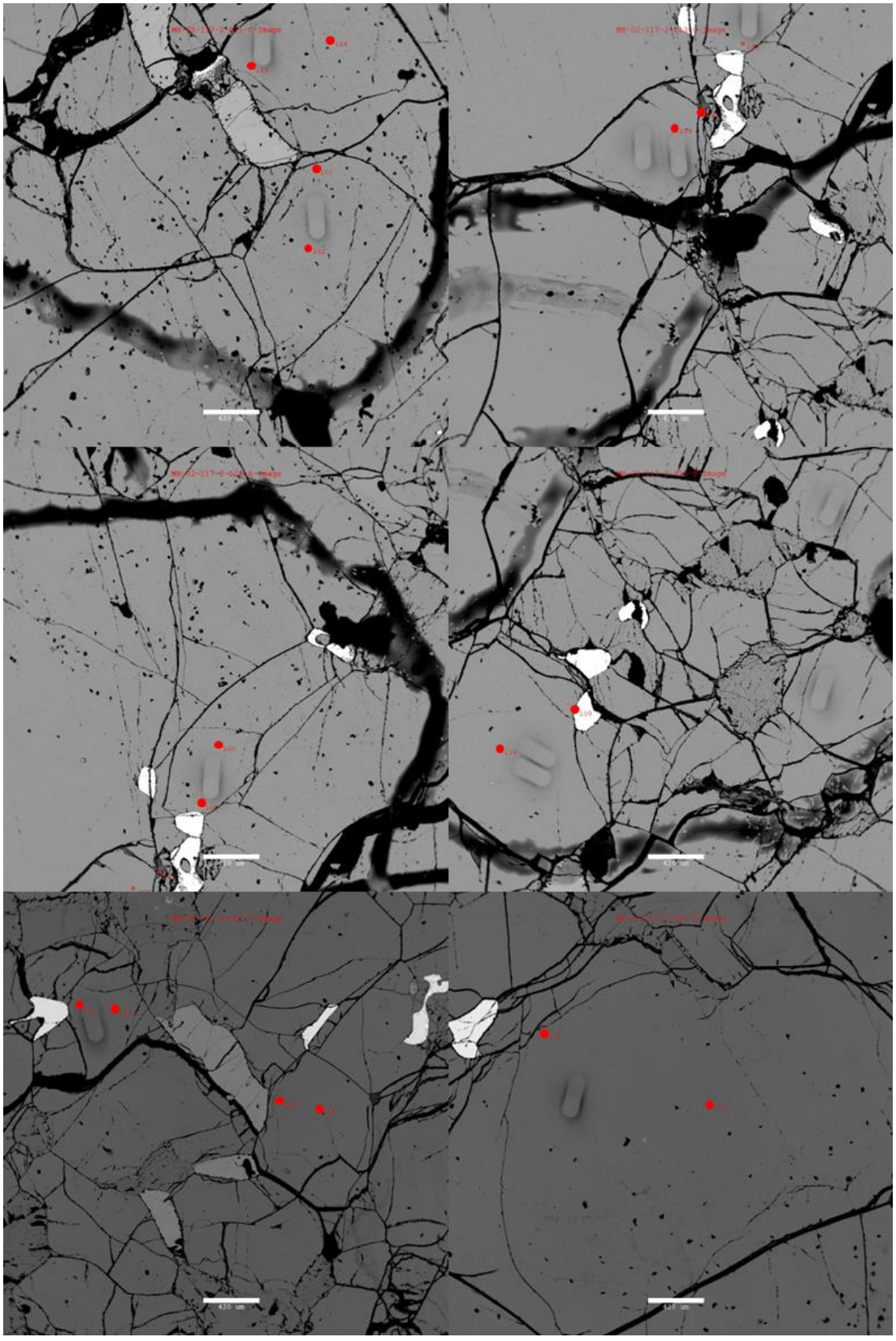

Appendix D (Figure D6): Analysis locations for sample MH-02-117-2 (continued)

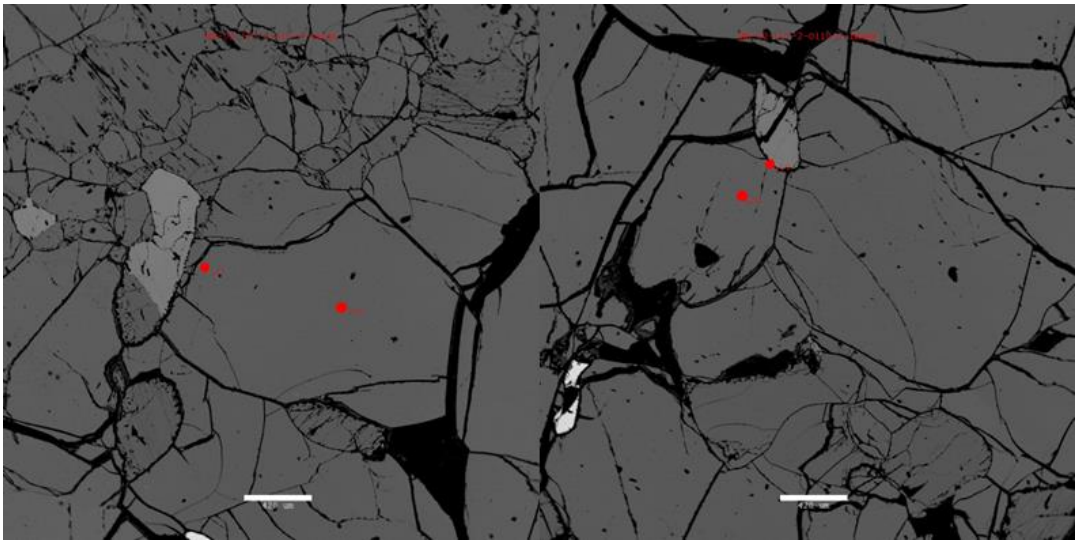

Appendix D (Figure D7): Analysis locations for sample MH-02-125

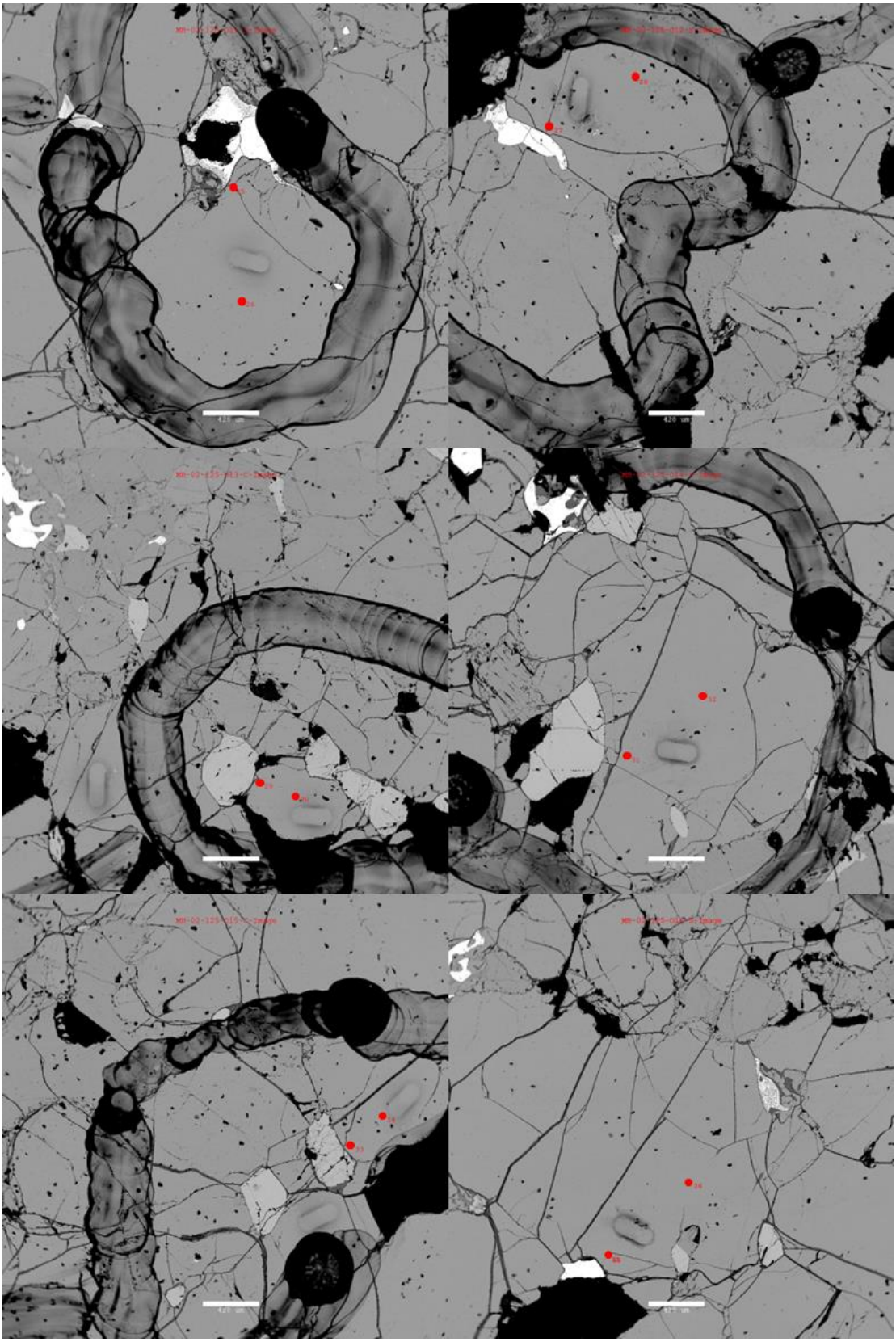

Appendix D (Figure D8): Analysis locations for sample MH-02-15

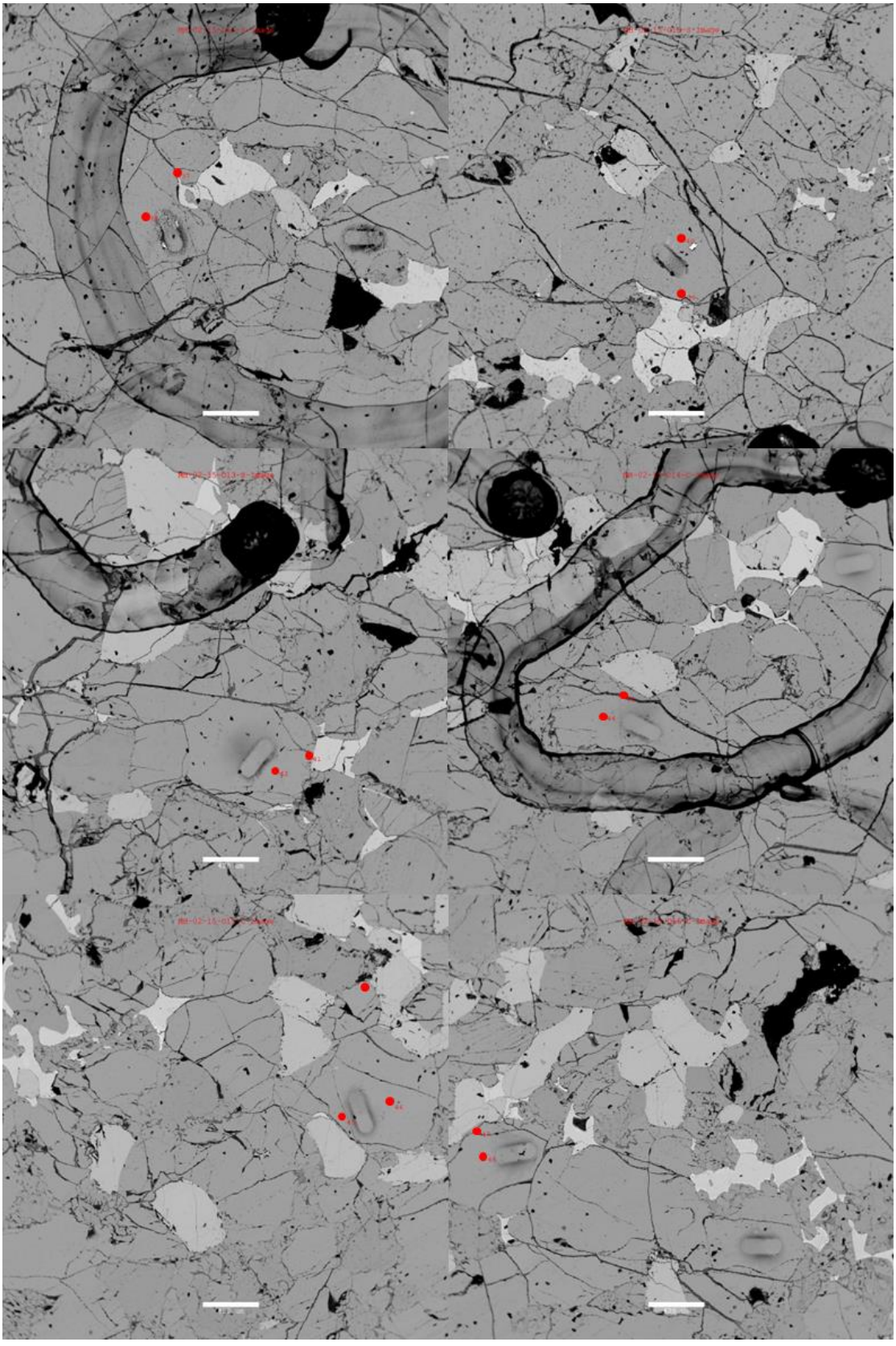

Appendix D (Figure D9): Analysis locations for sample MH-02-100

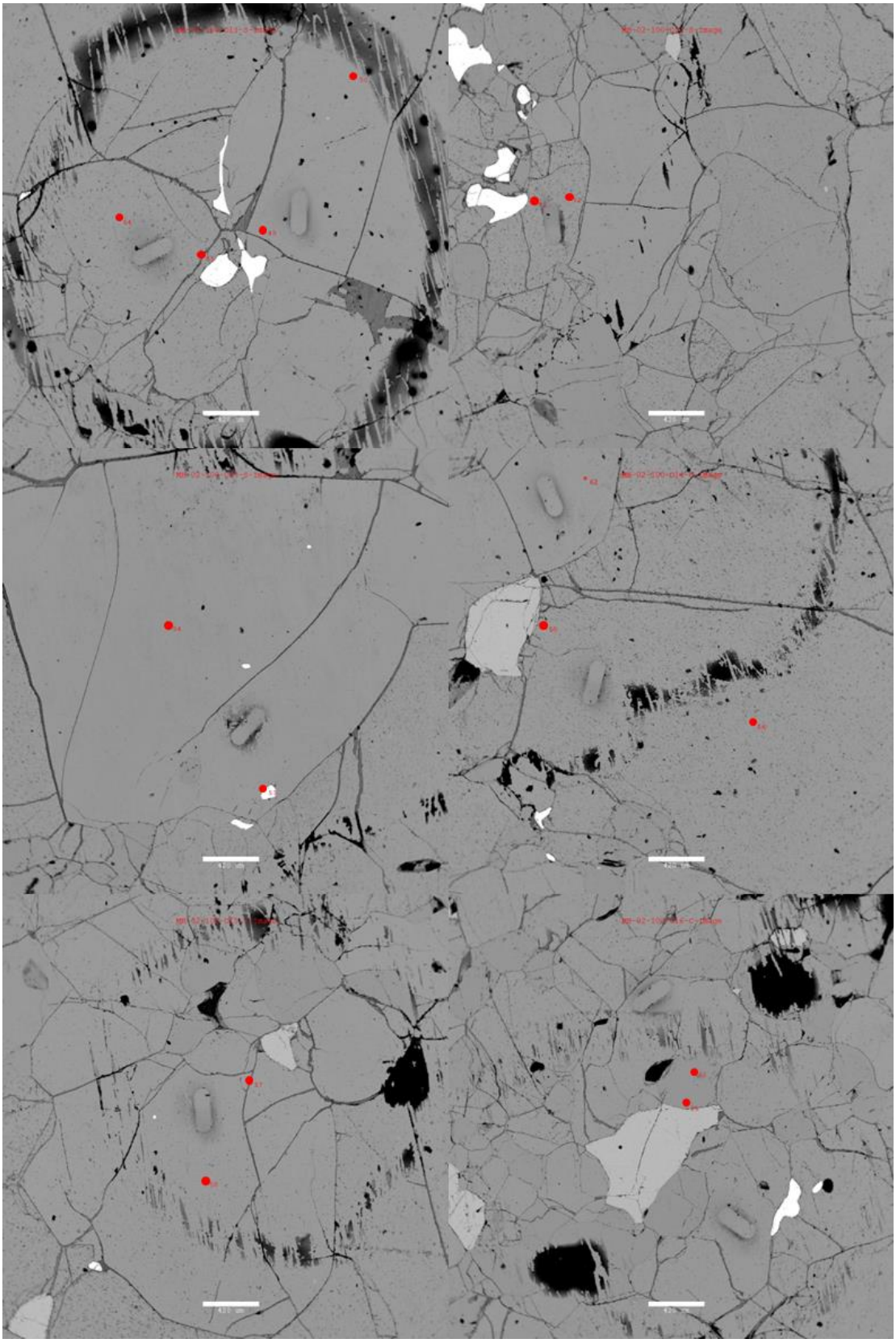

Appendix D (Figure D9): Analysis locations for sample MH-02-100 (continued)

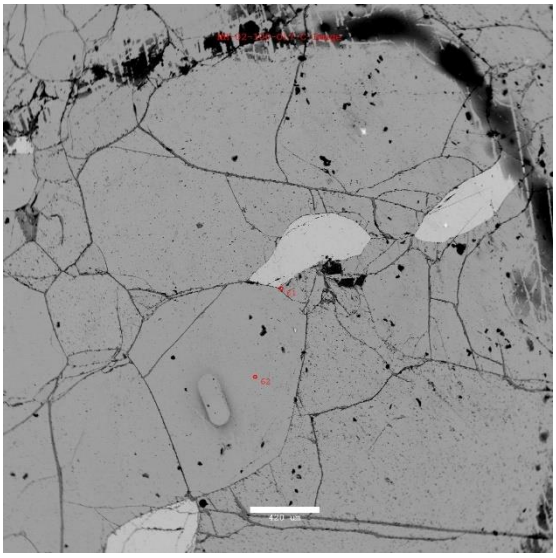

Appendix D (Figure D10): Analysis locations for sample 95LM1

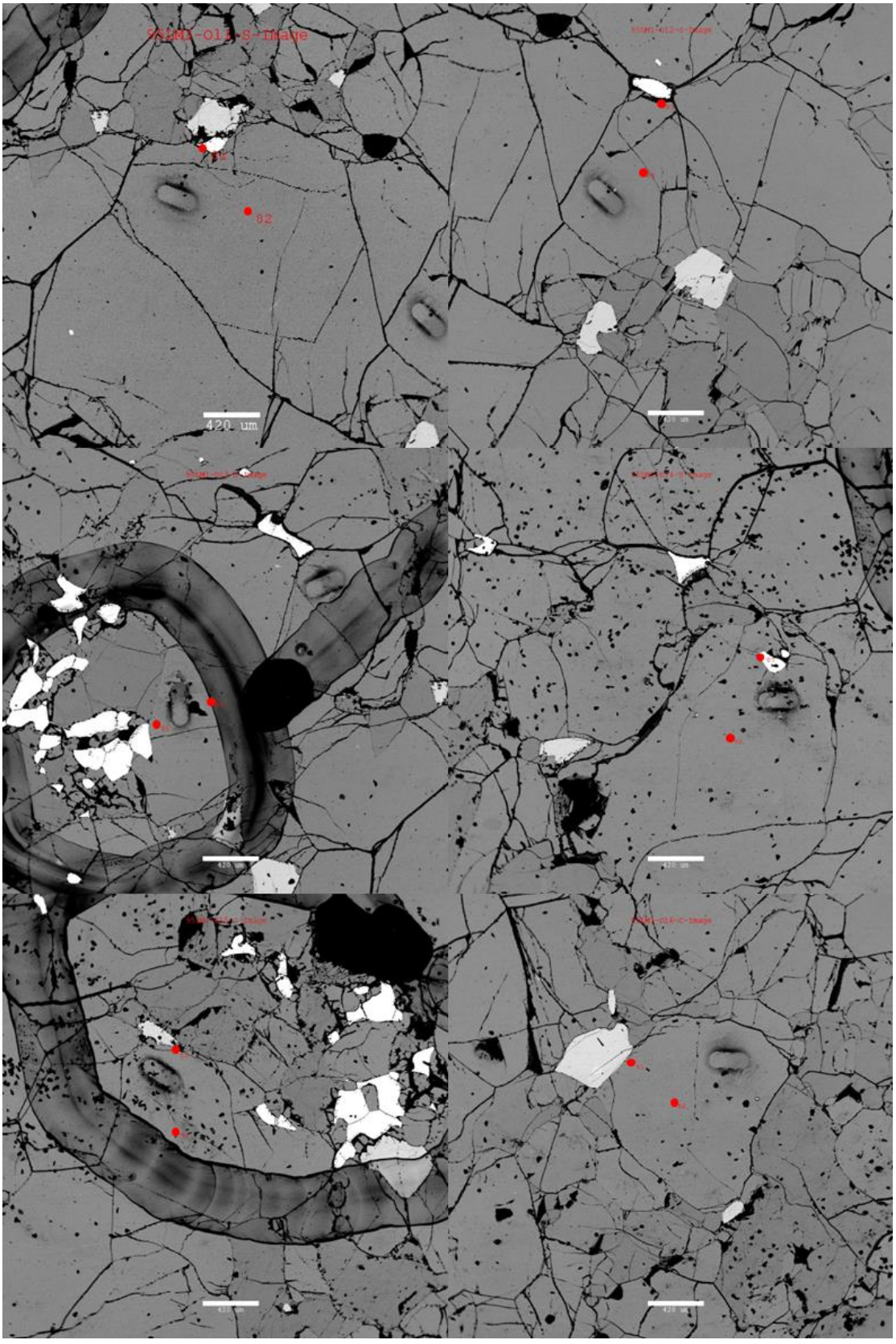

Appendix D (Figure D10): Analysis locations for sample 95LM1 (continued)

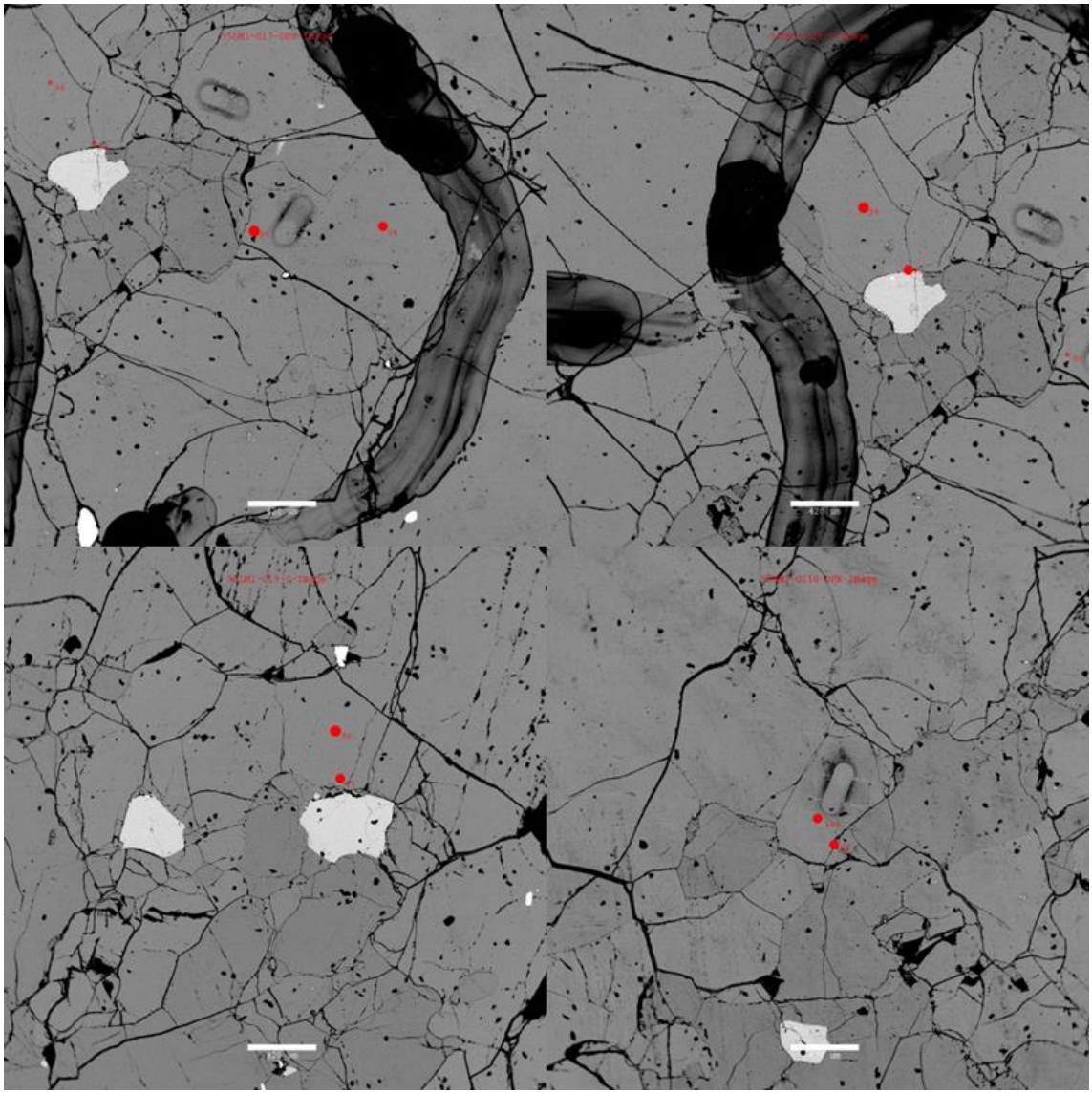

Appendix D (Figure D11): Analysis locations for sample MH-02-10C

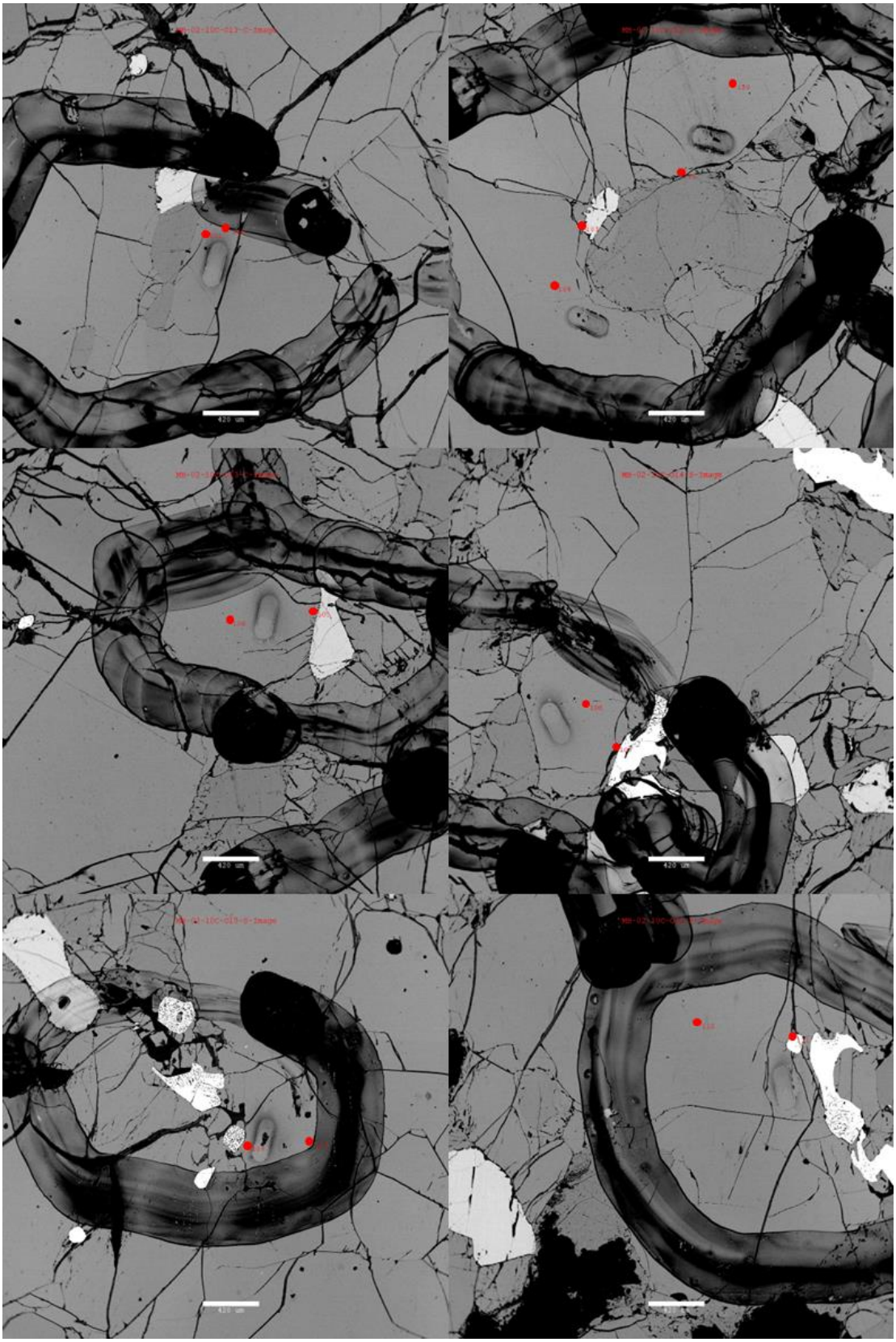

Appendix D (Figure D11): Analysis locations for sample MH-02-10C (continued)

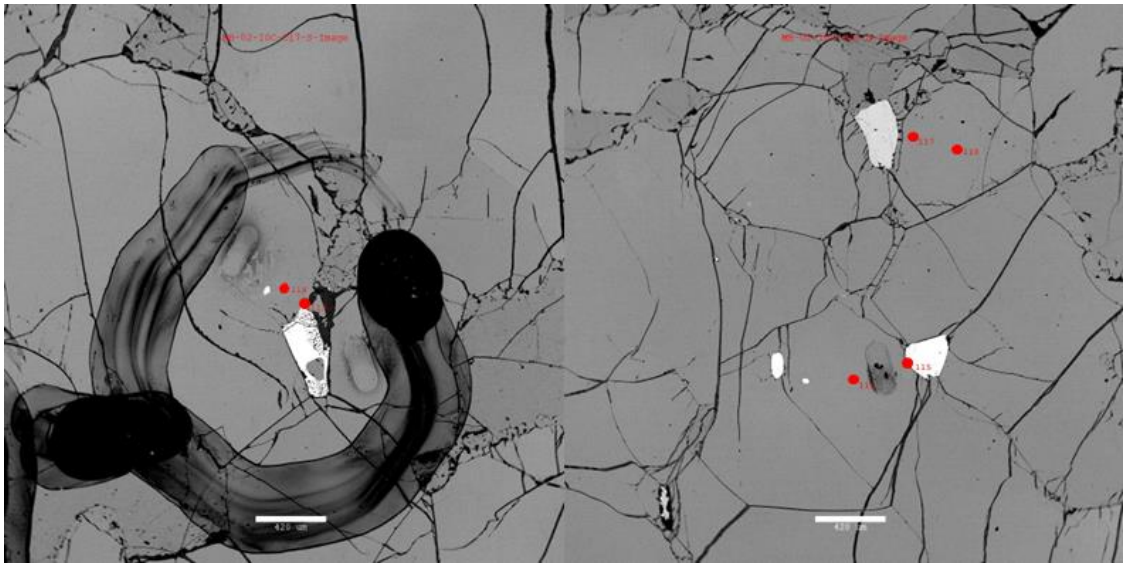

Appendix D (Figure D12): Analysis locations for sample MH-02-04

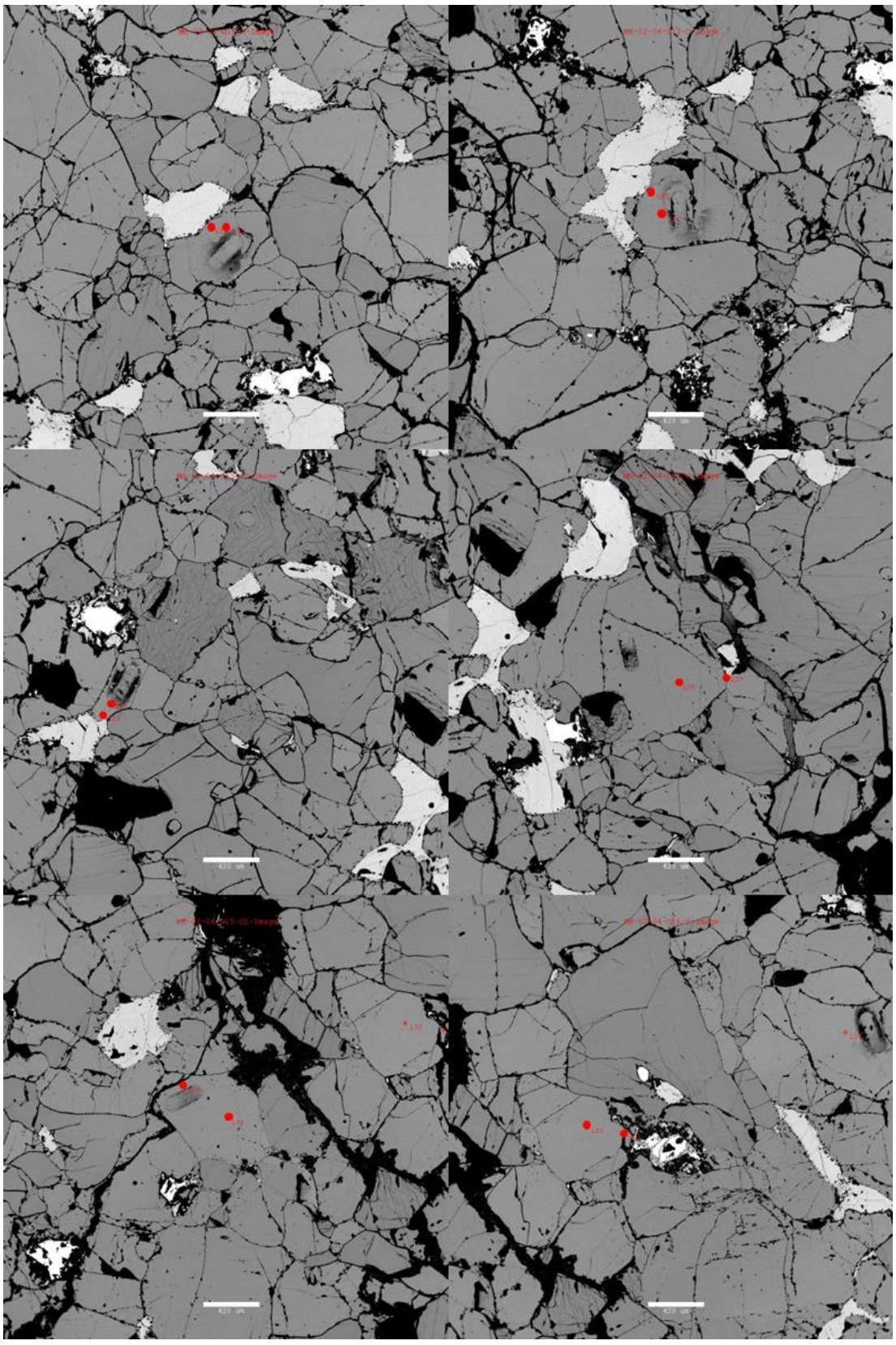

Appendix D (Figure D12): Analysis locations for sample MH-02-04 (continued)

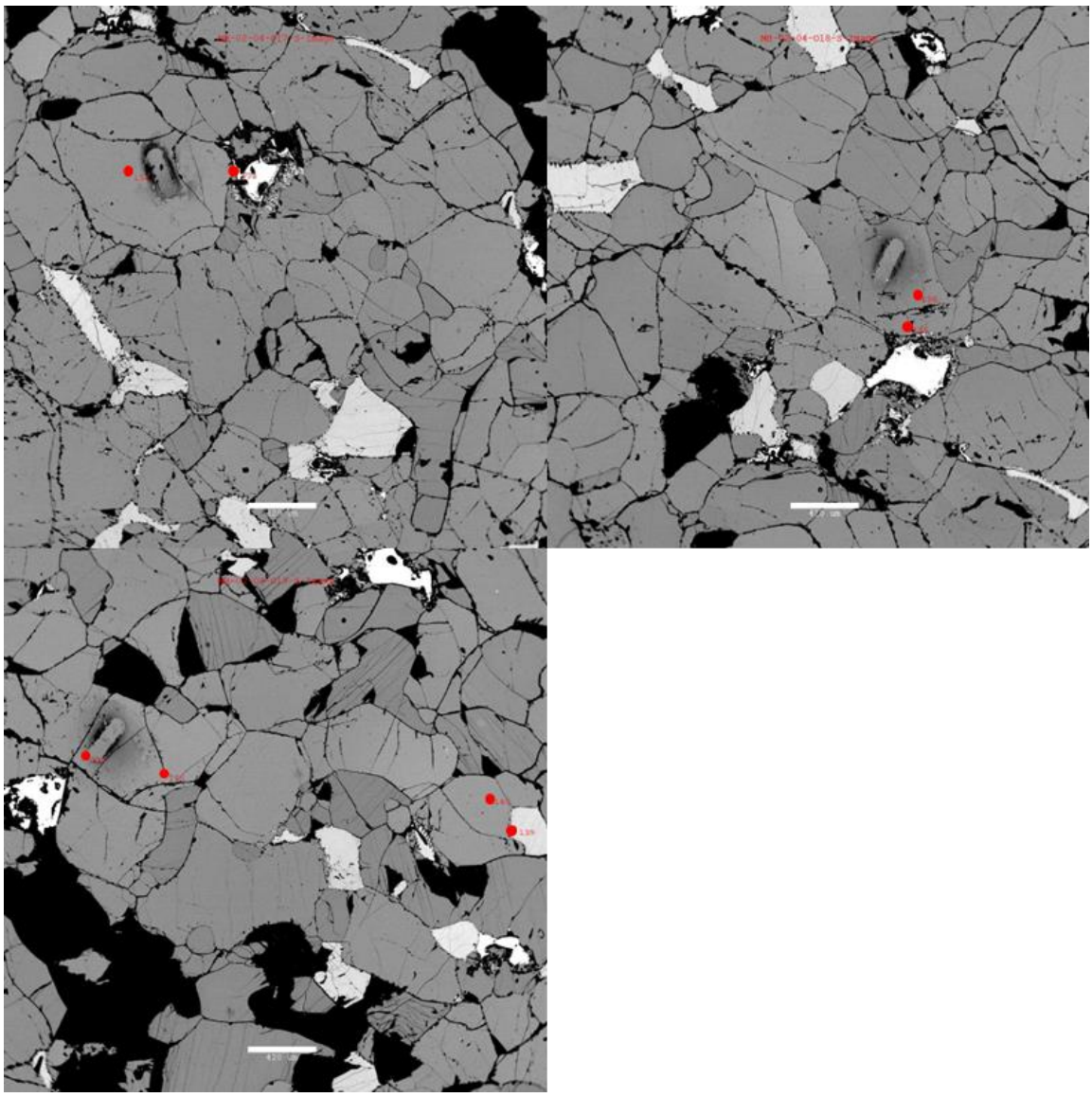

Appendix D (Figure D13): Analysis locations for sample MH-02-102

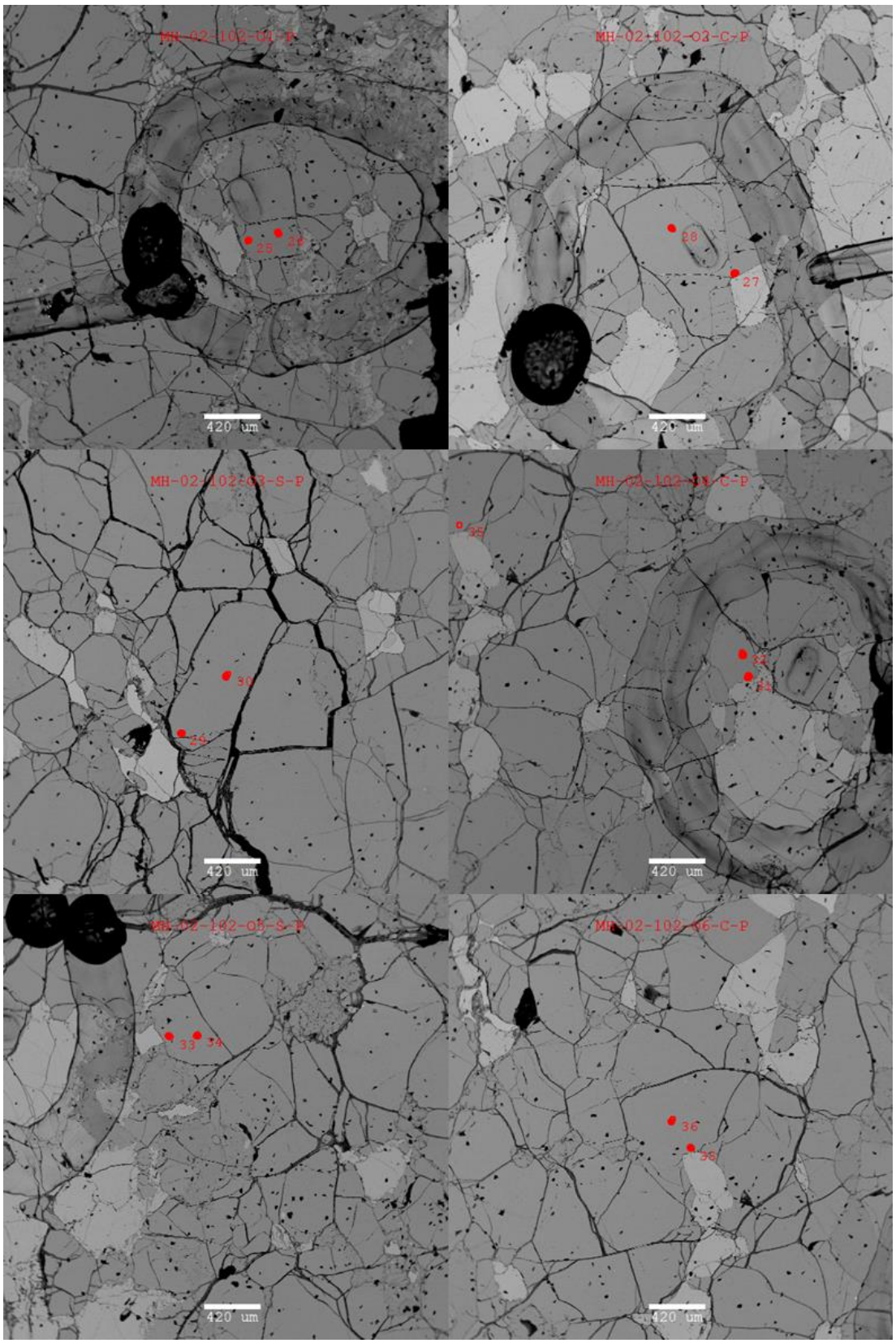

Appendix D (Figure D14): Analysis locations for sample MH-02-117-1

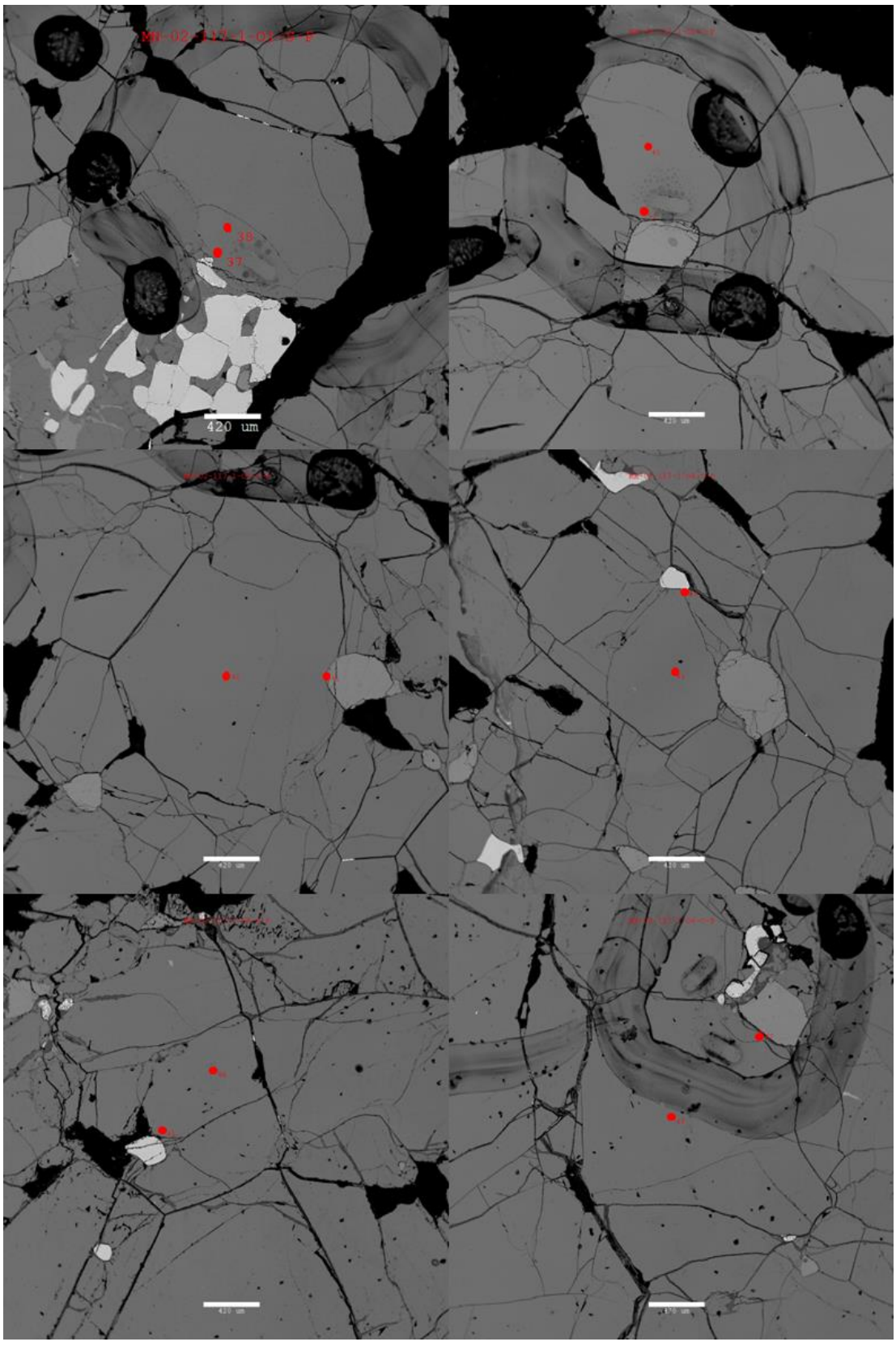

Appendix D (Figure D15): Analysis locations for sample MH-02-114

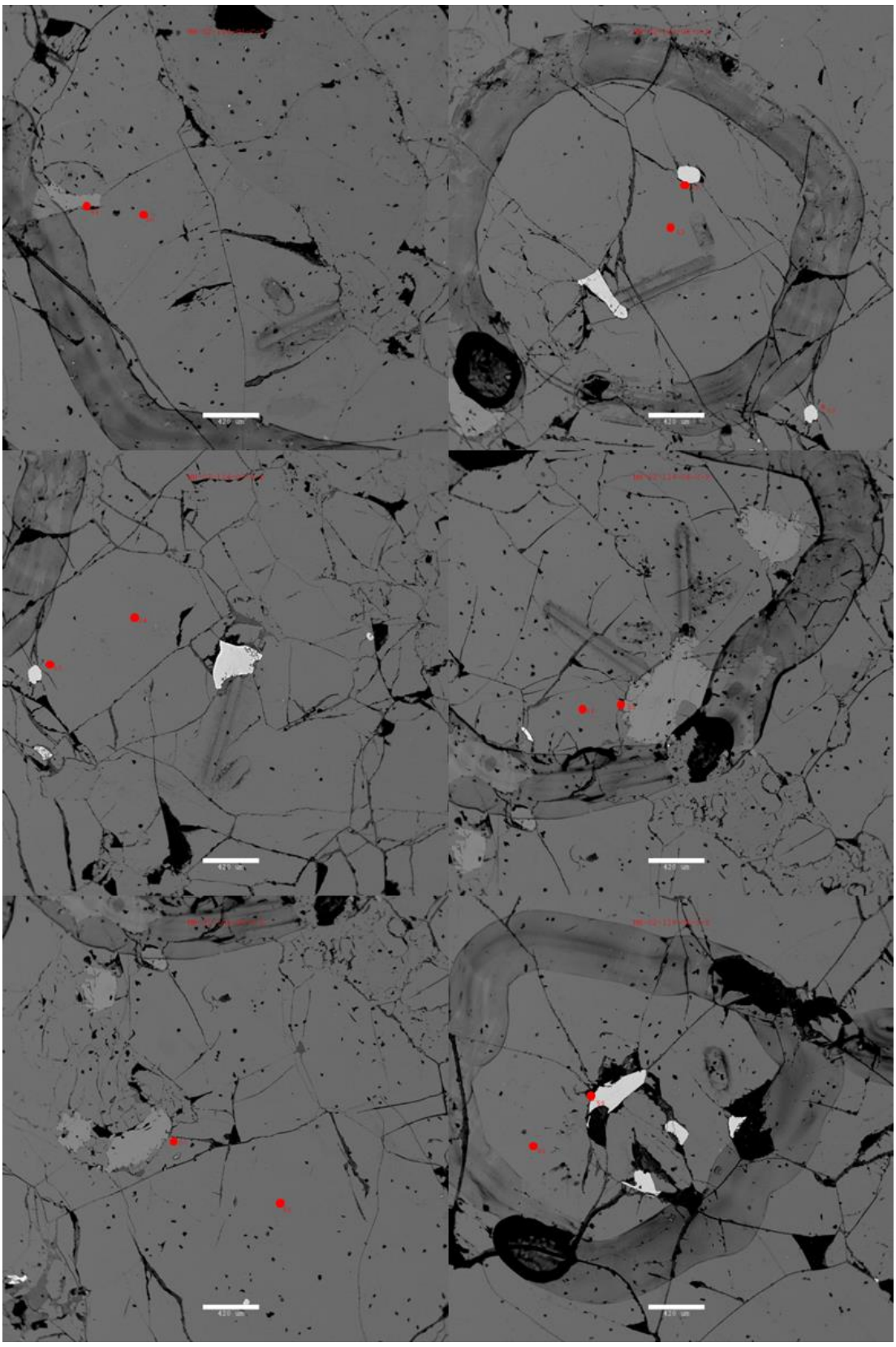

Appendix D (Figure D16): Analysis locations for sample MH-02-20

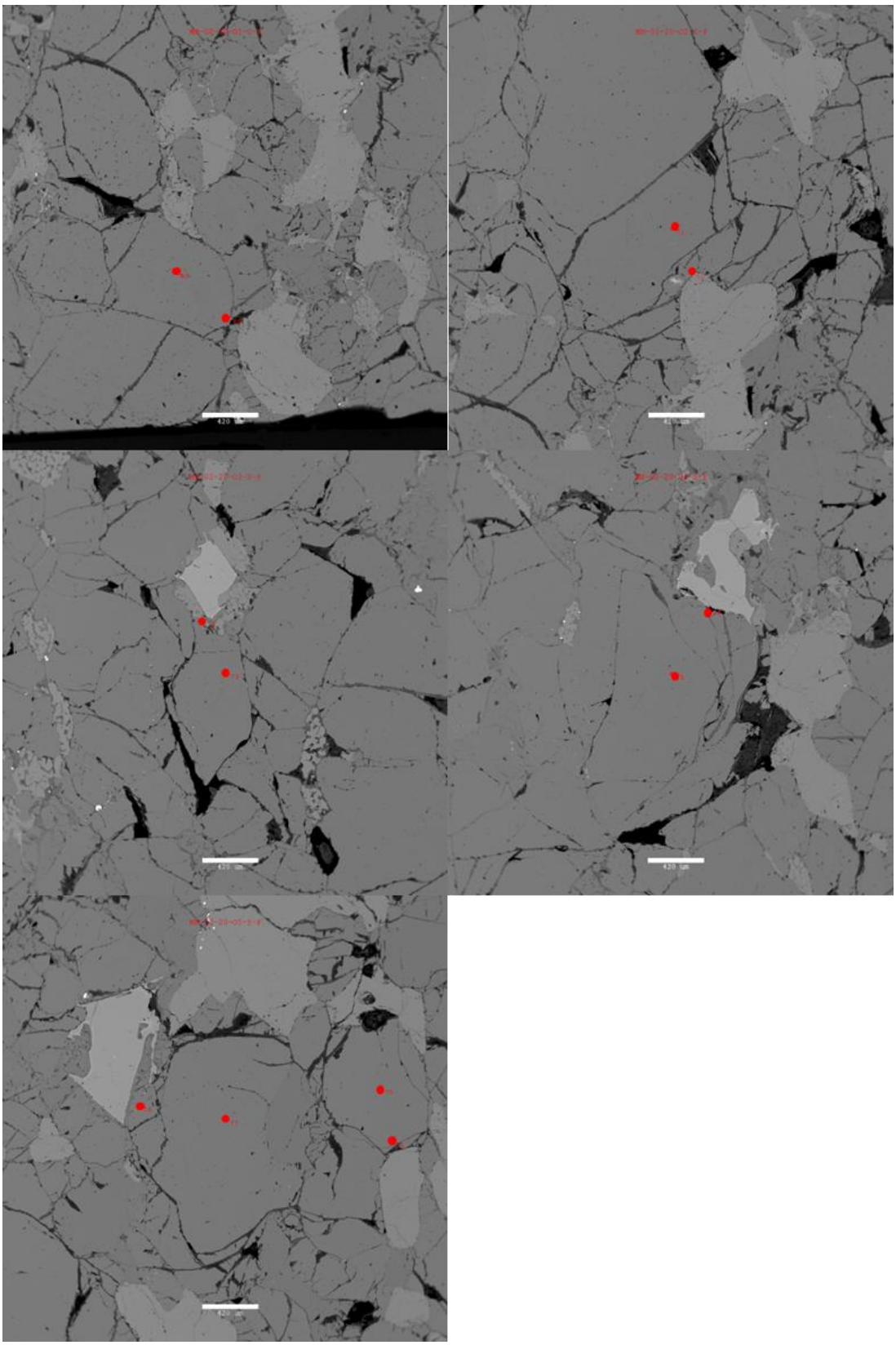

Appendix D (Figure D17): Analysis locations for sample MH-02-100B

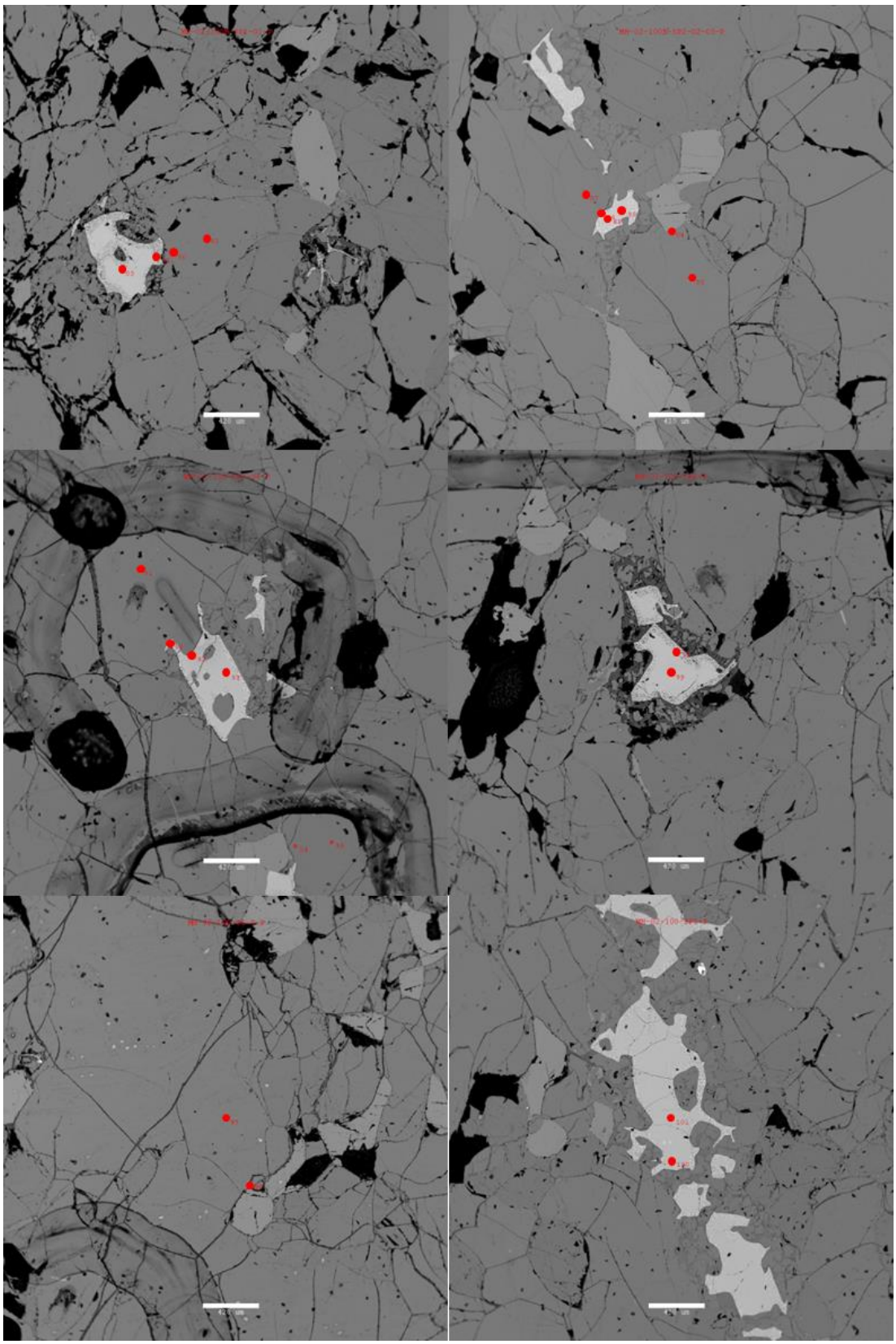

Appendix D (Figure D18): Analysis locations for sample MH-02-109

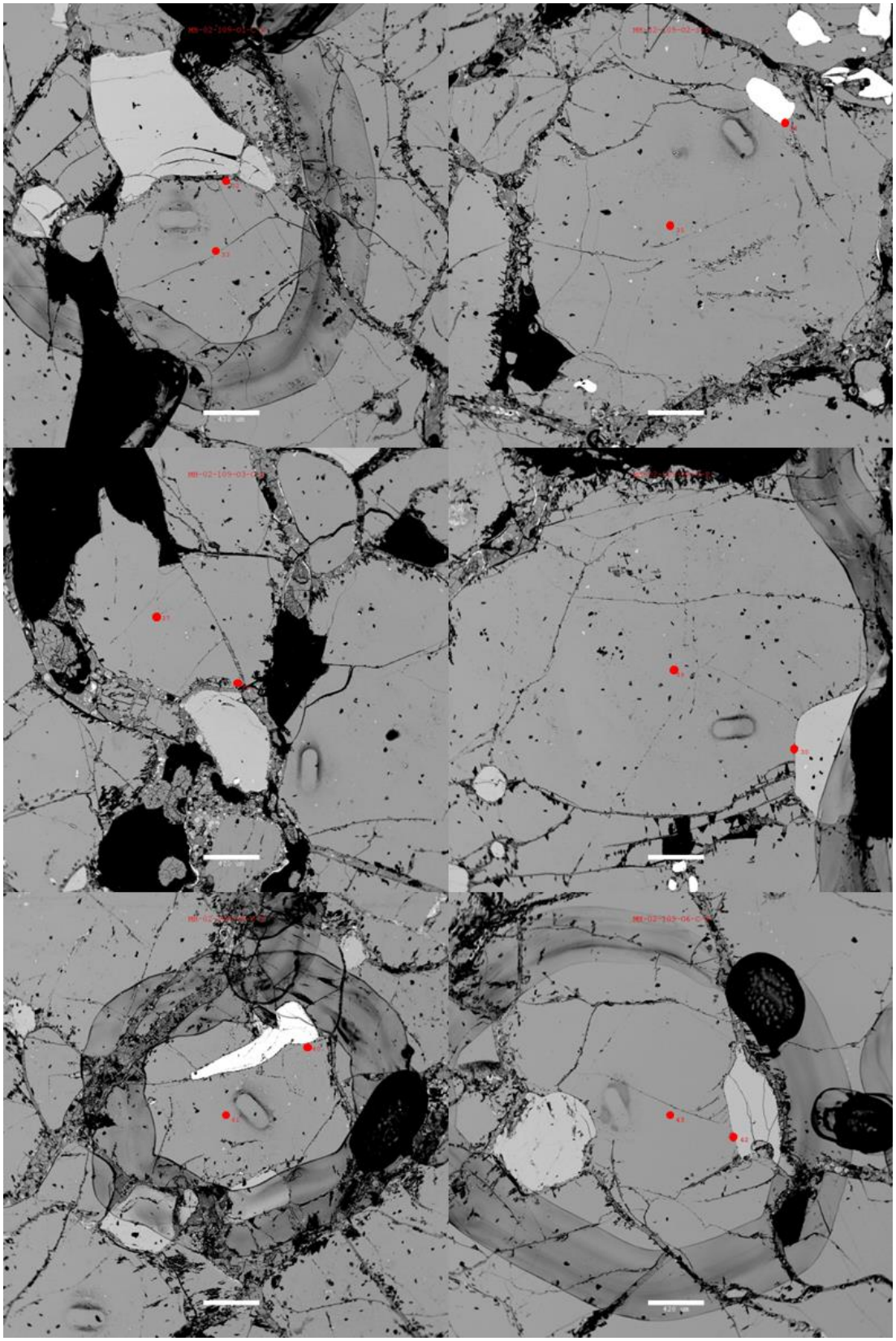

Appendix D (Figure D18): Analysis locations for sample MH-02-109 (continued)

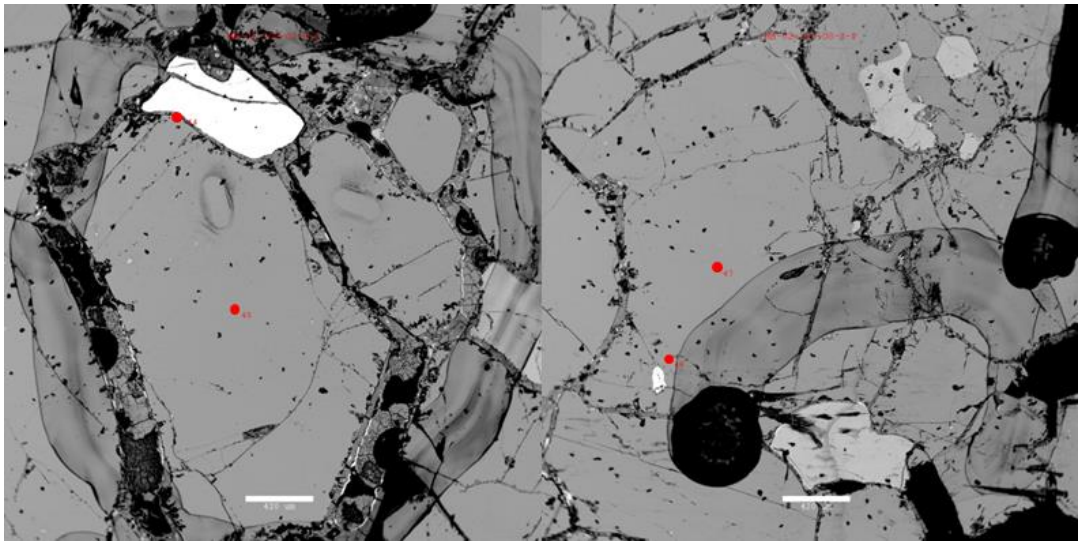

Appendix D (Figure D19): Analysis locations for sample MH-02-115B

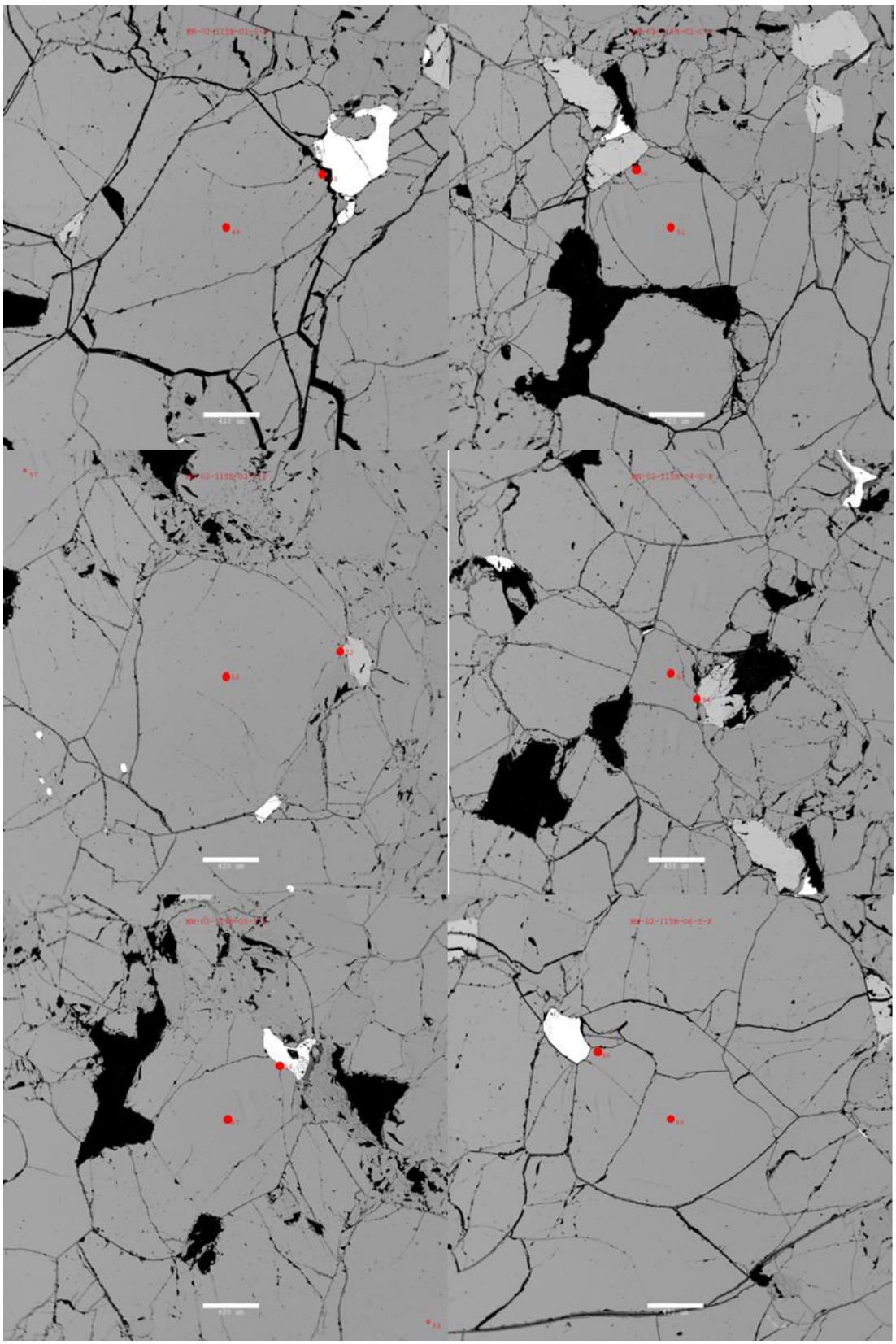

Appendix D (Figure D20): Analysis locations for sample MH-02-14

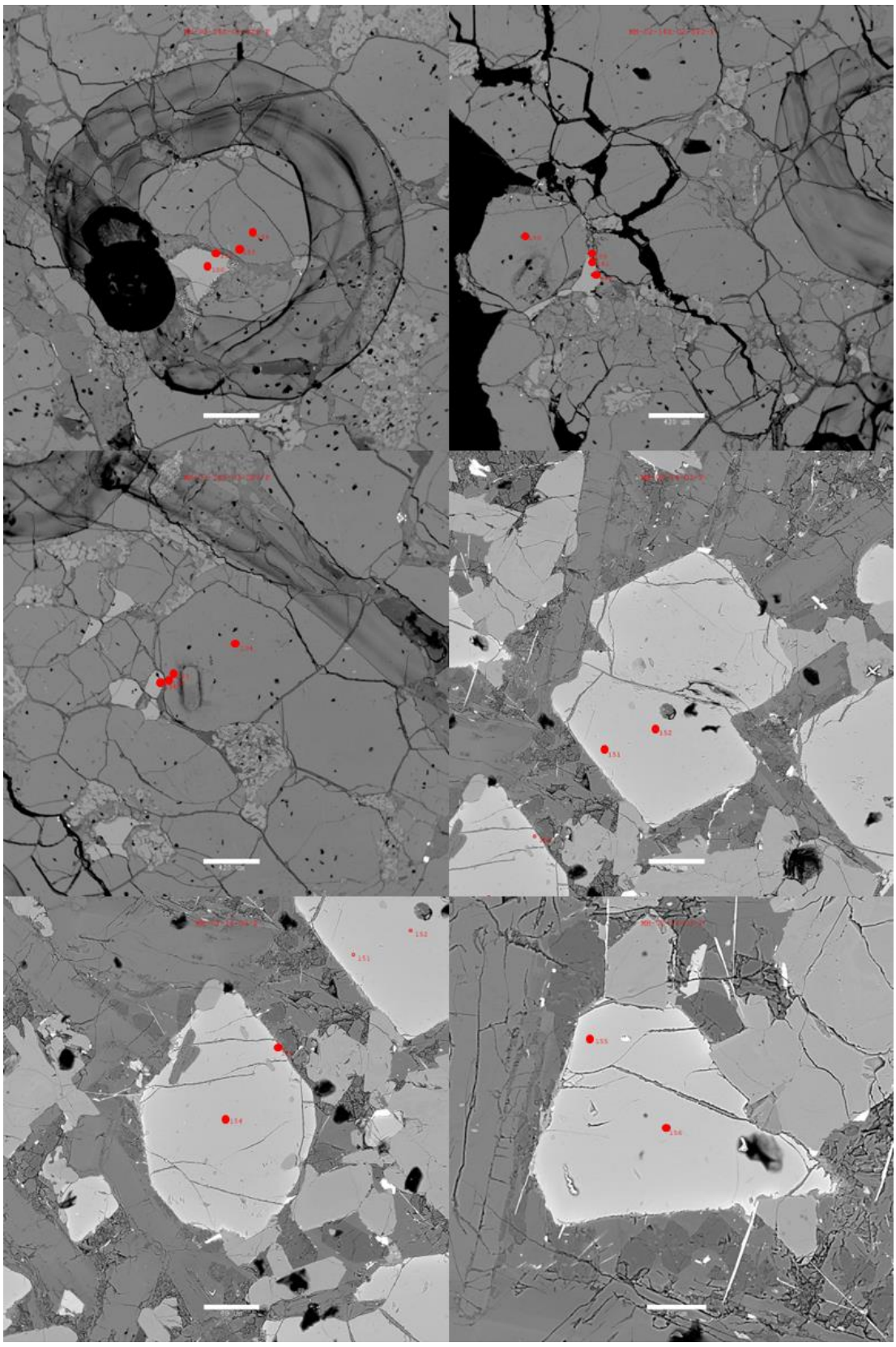

Appendix D (Figure D20): Analysis locations for sample MH-02-14 (continued)

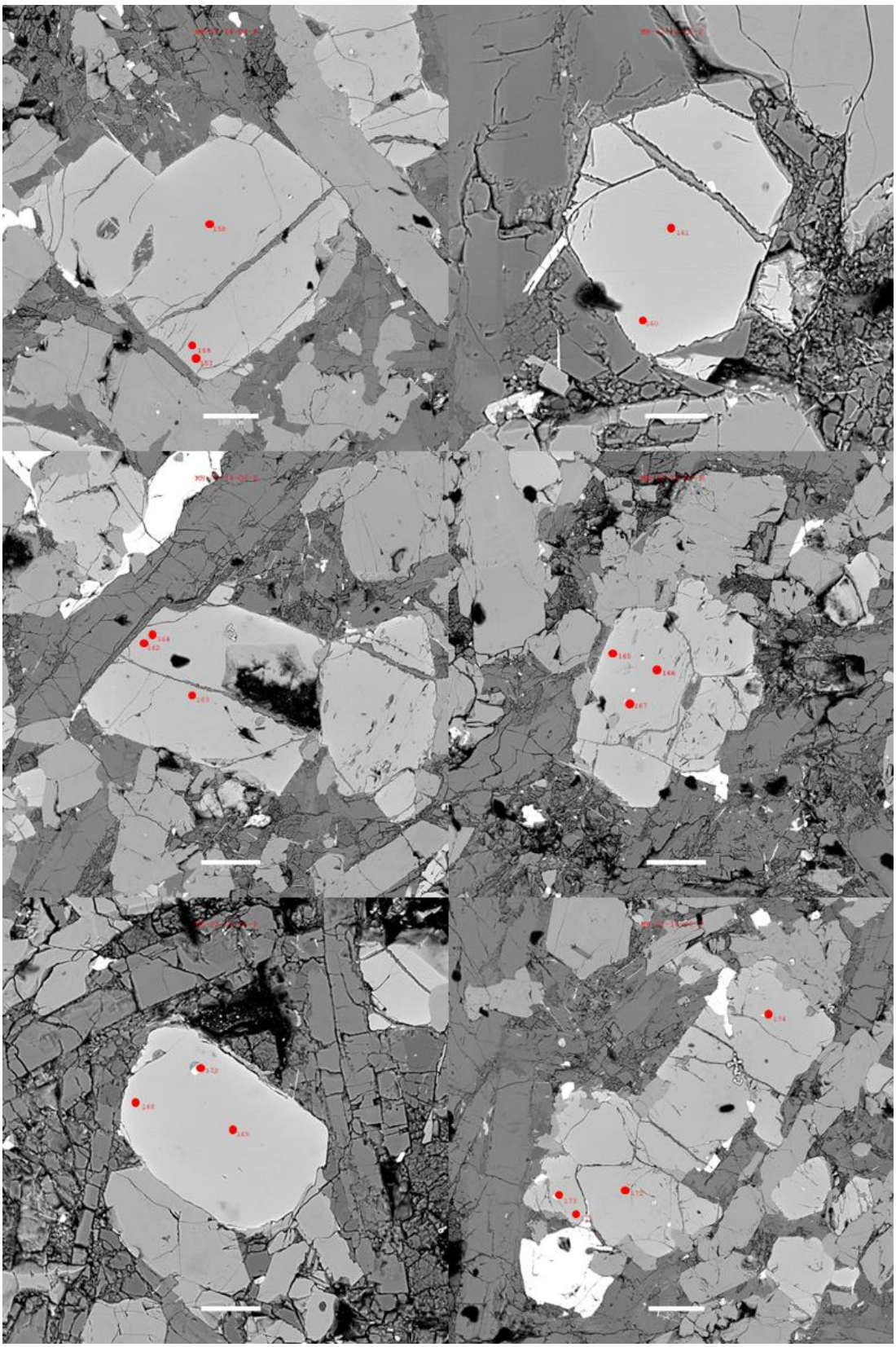

Appendix D (Figure D20): Analysis locations for sample MH-02-14 (continued)

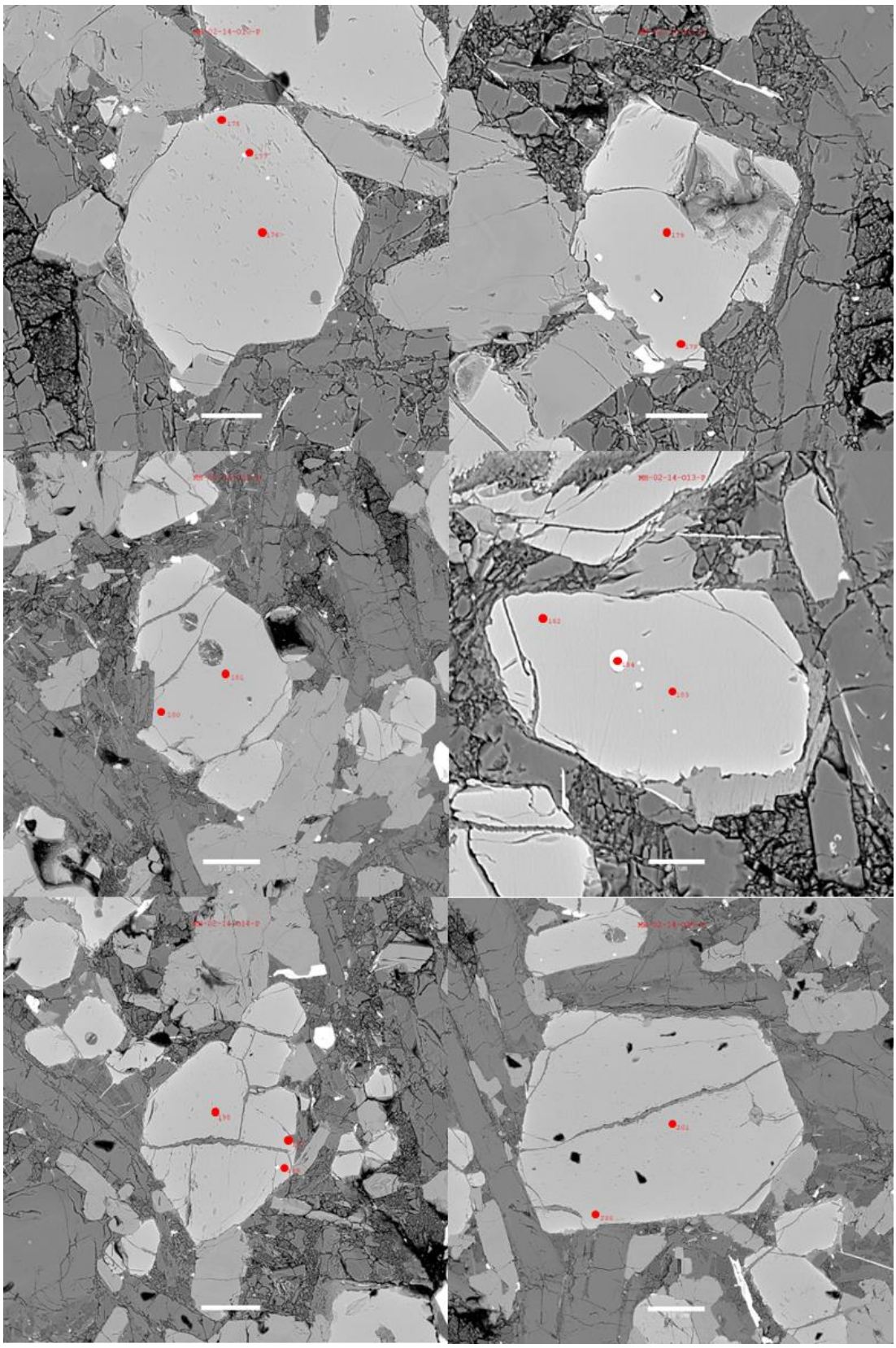

Appendix D (Figure D21): Analysis locations for sample MH-02-101

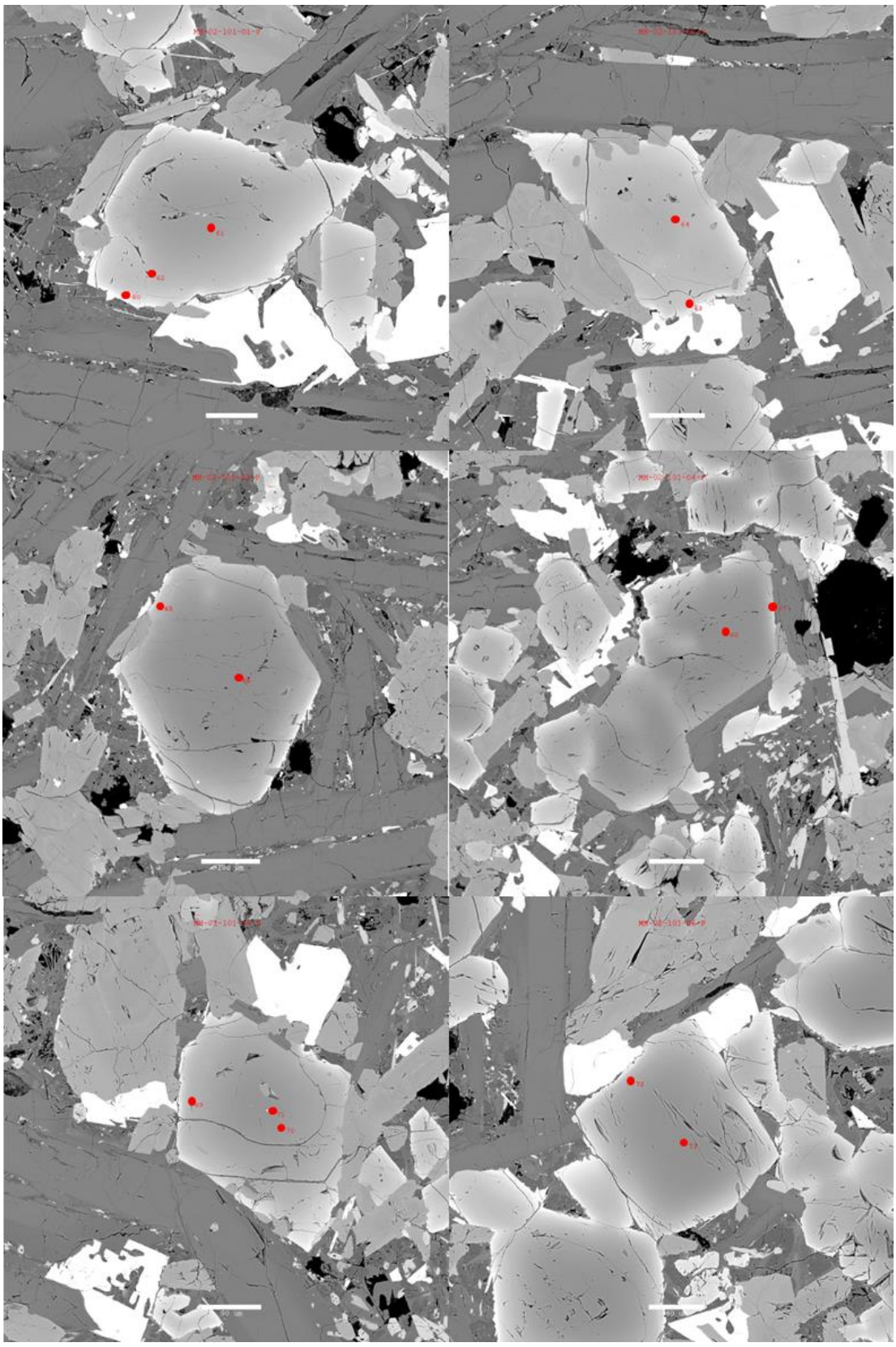

Appendix D (Figure D21): Analysis locations for sample MH-02-101 (continued)

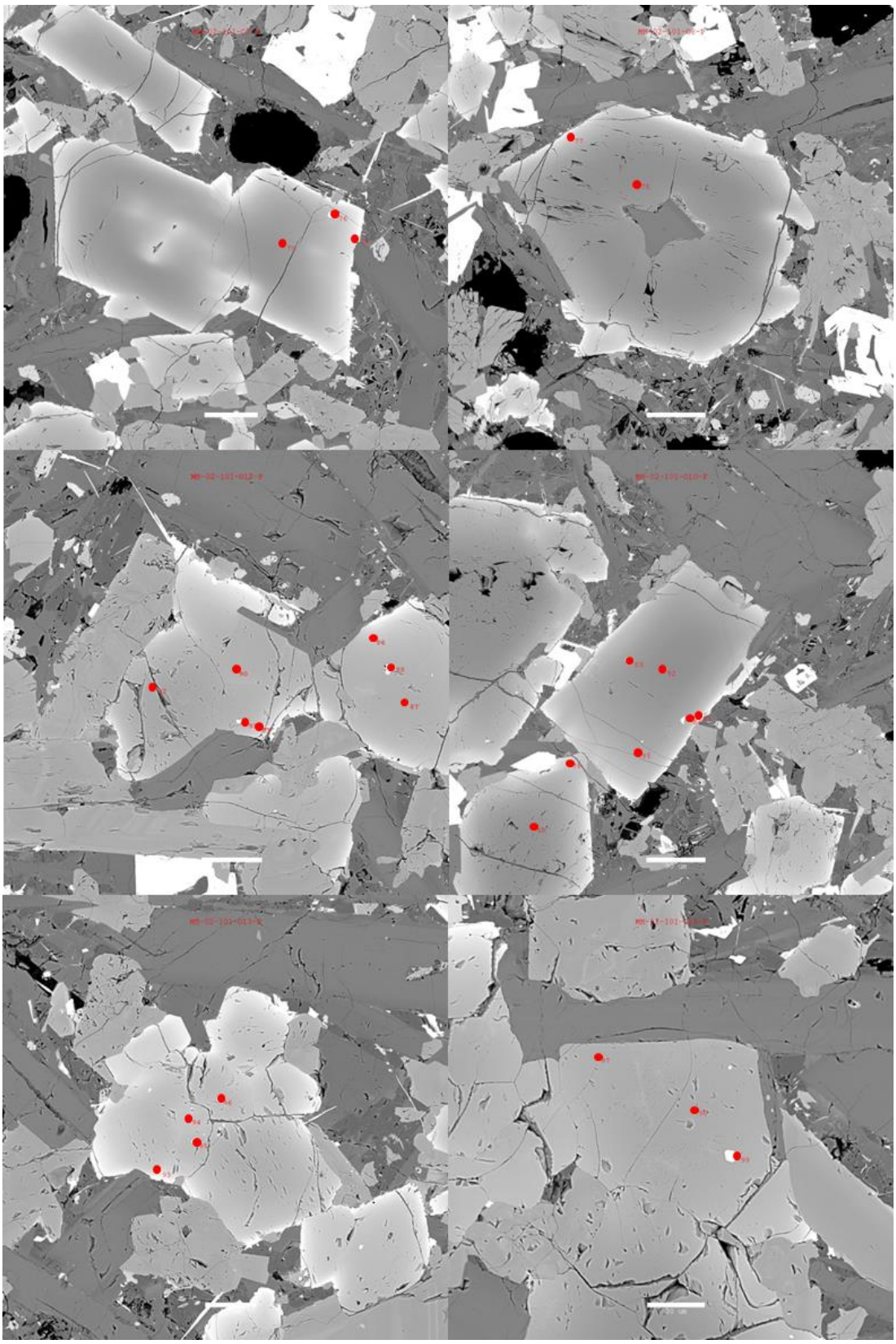

Appendix D (Figure D21): Analysis locations for sample MH-02-101 (continued)

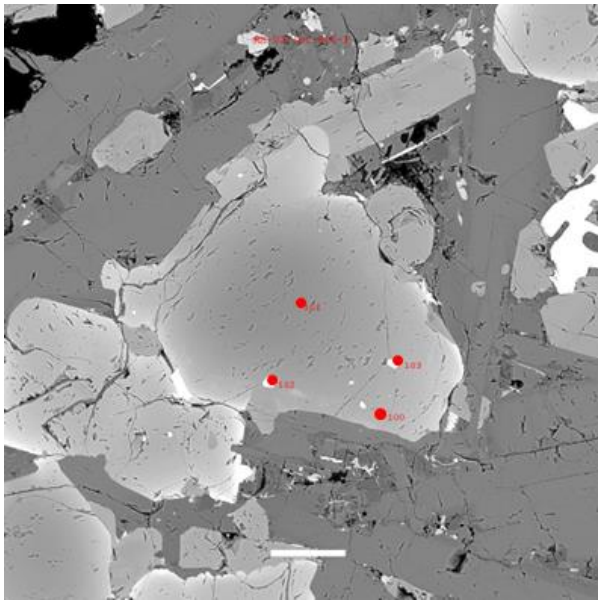

Appendix D (Figure D22): Analysis locations for sample MH-02-16

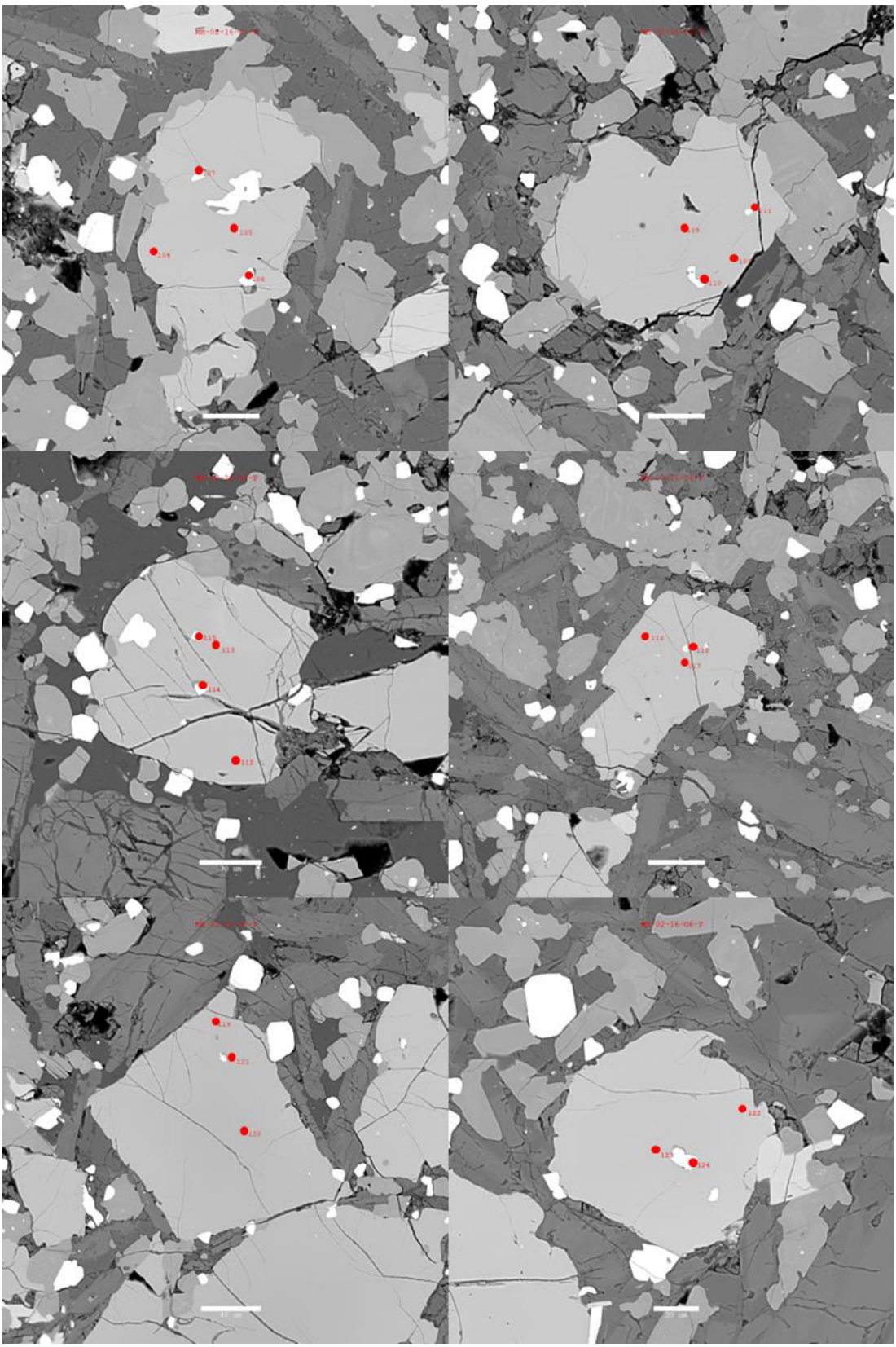

Appendix D (Figure D22): Analysis locations for sample MH-02-16 (continued)

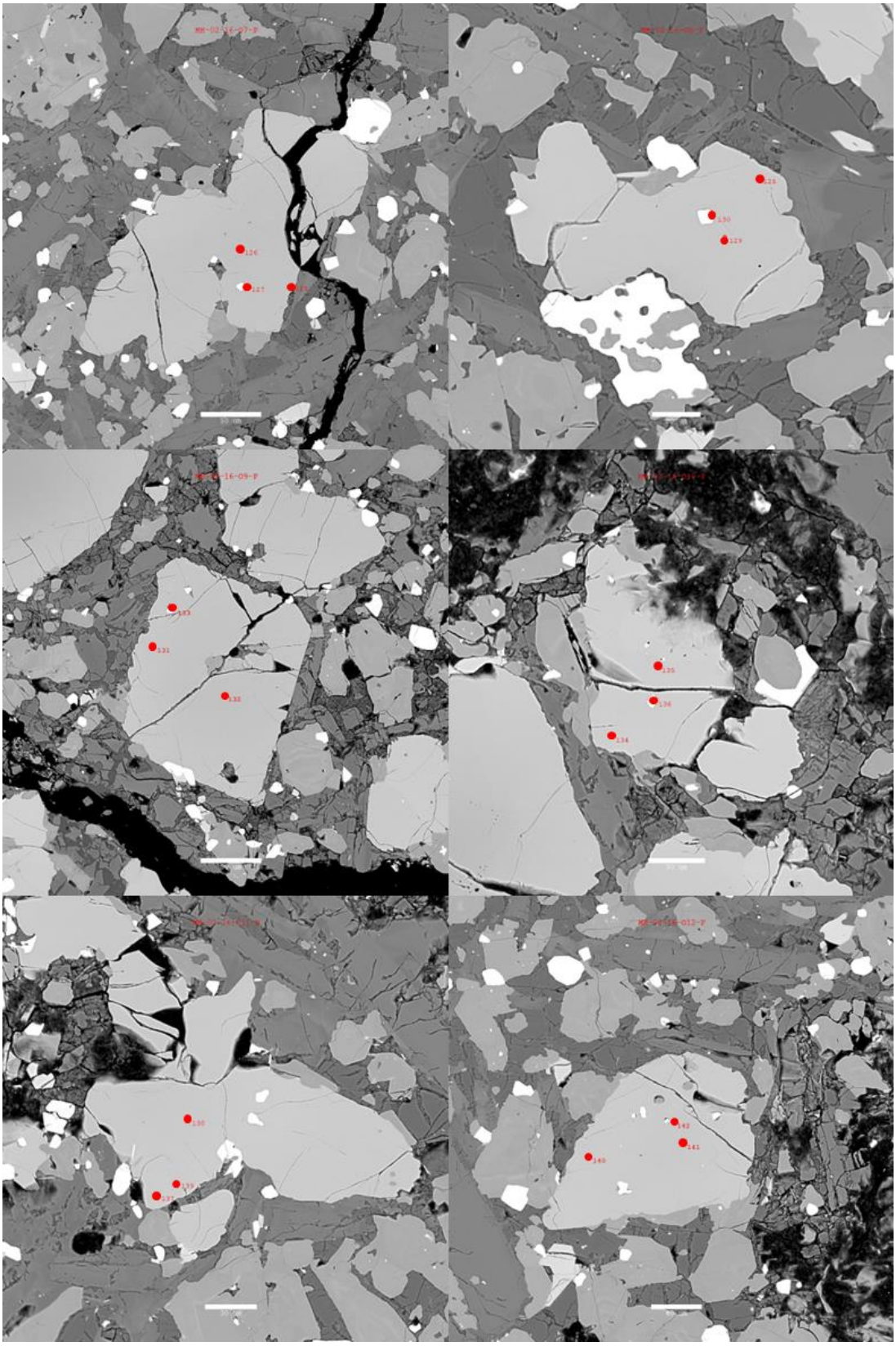

Appendix D (Figure D22): Analysis locations for sample MH-02-16 (continued)

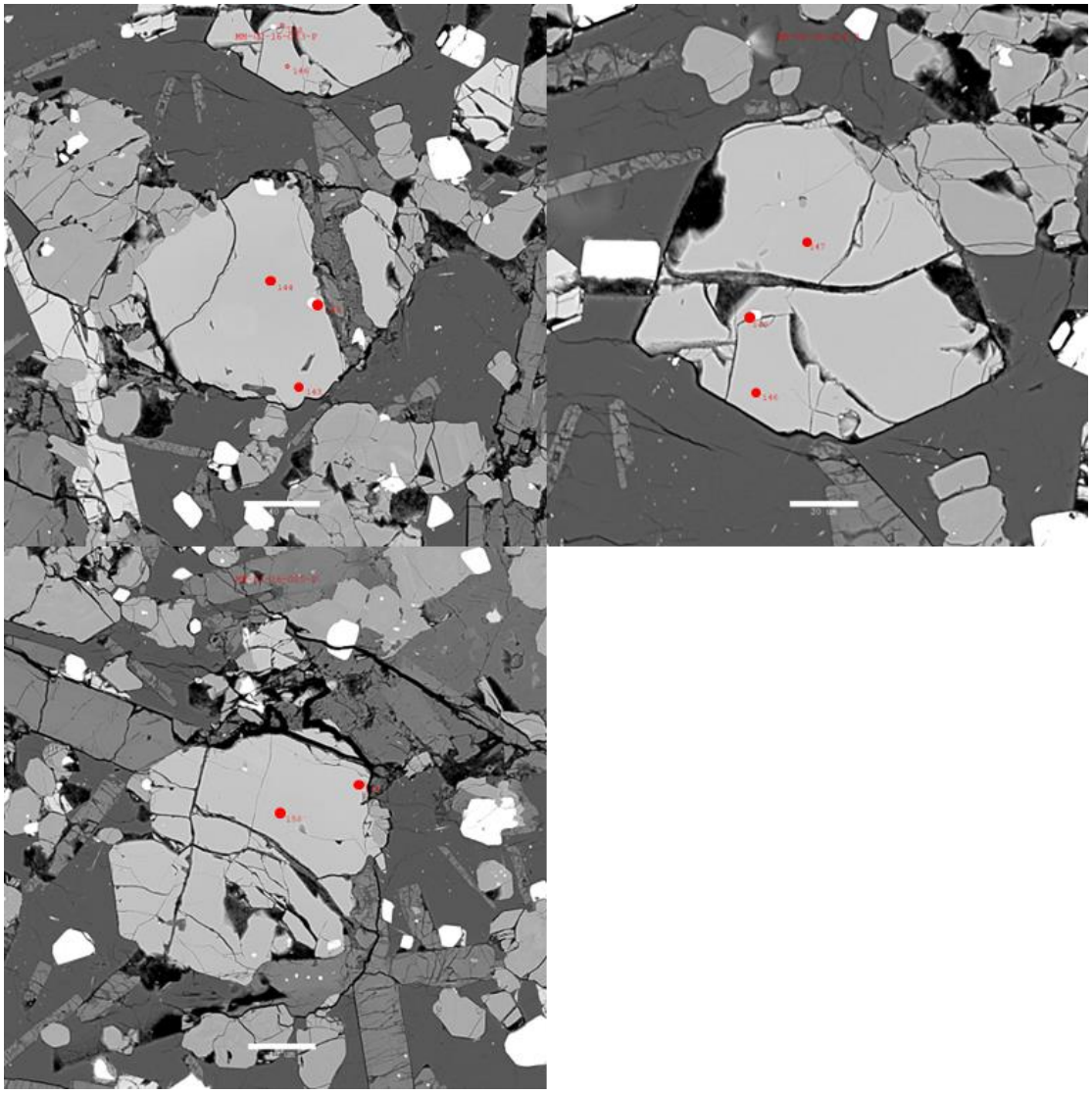

Appendix D (Figure D23): Analysis locations for sample MH-02-124A

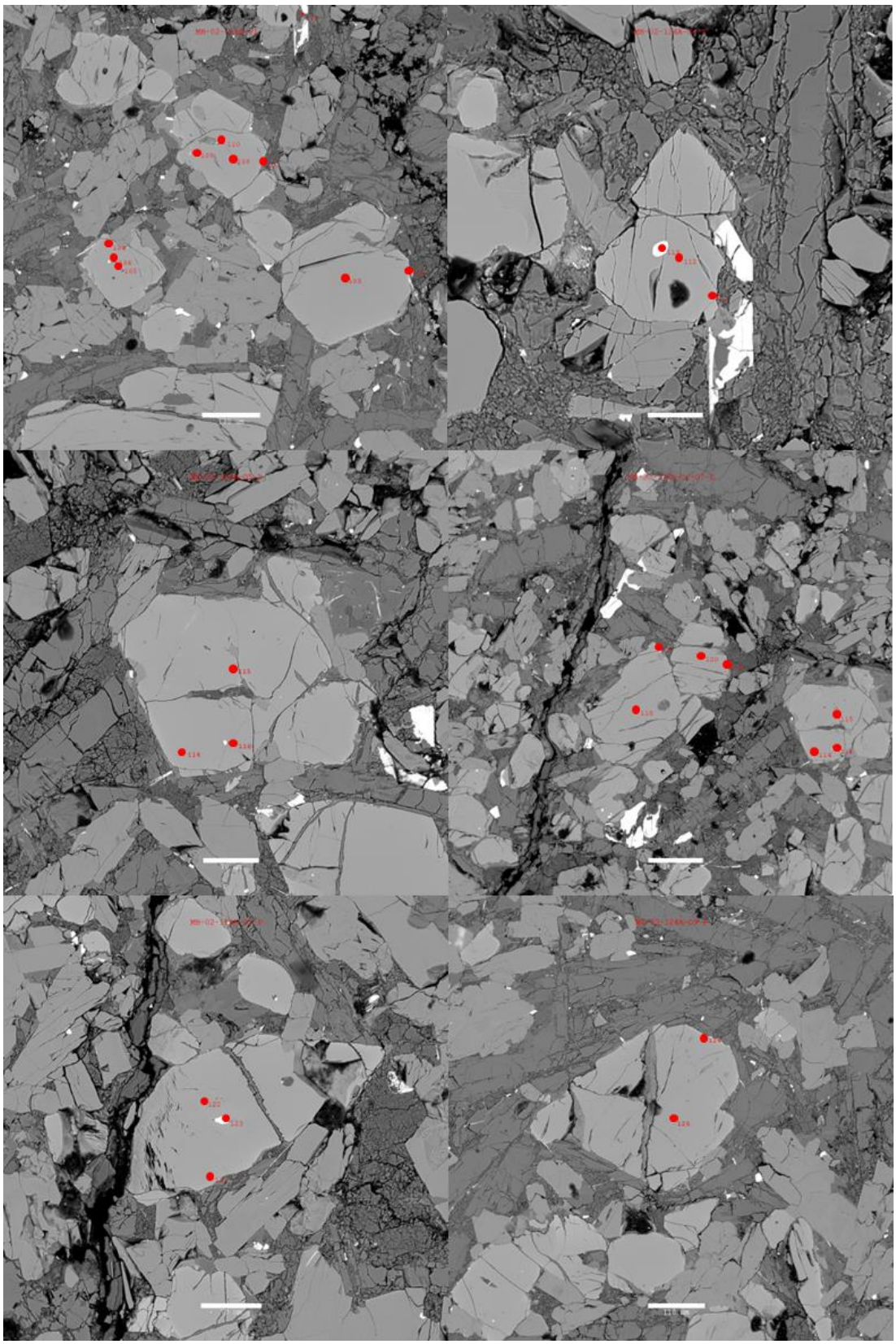

Appendix D (Figure D23): Analysis locations for sample MH-02-124A (continued)

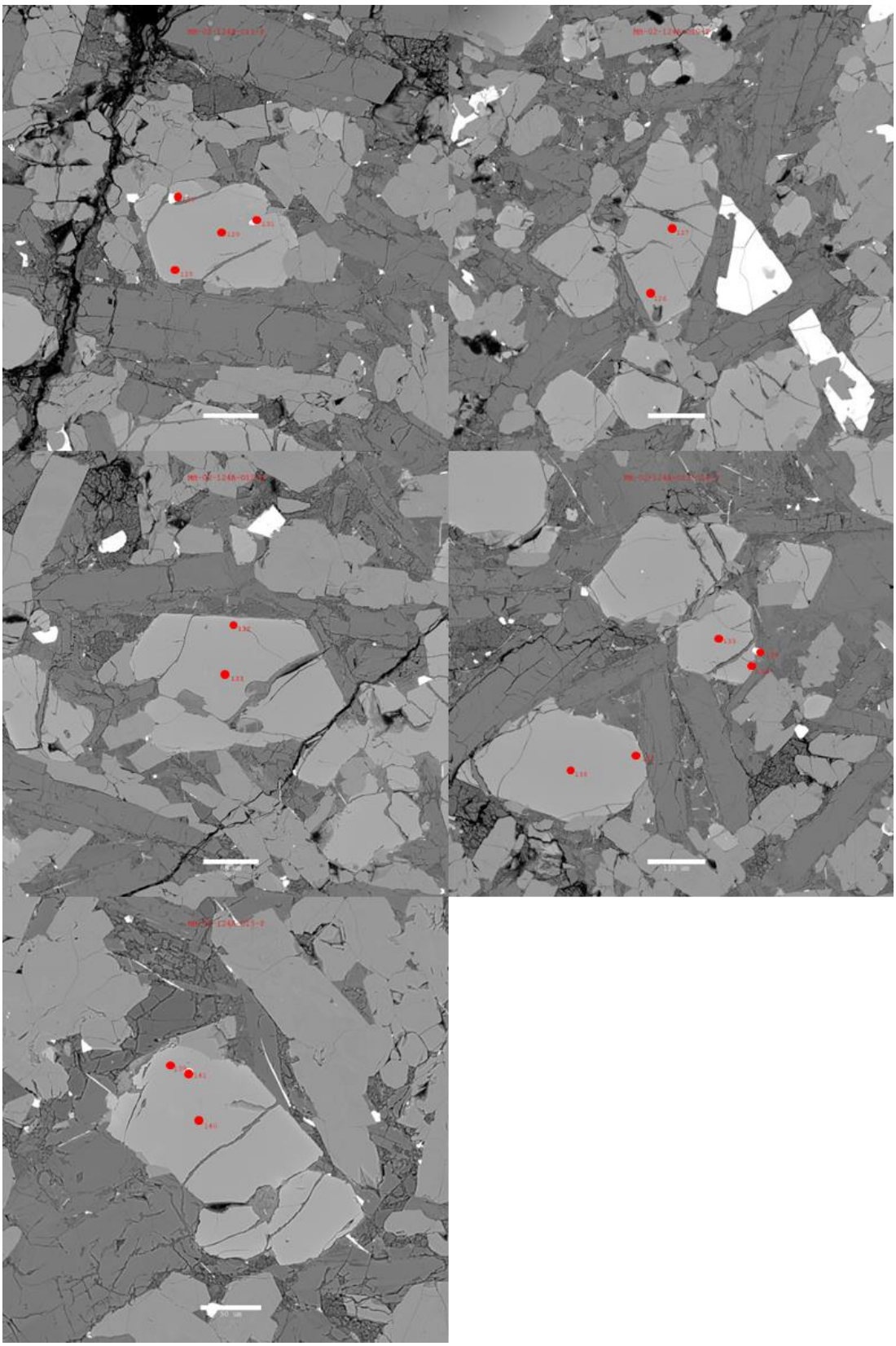

Appendix E: Olivine Al, Ca zoning profiles

(All zoning profiles are started from the core of the grain (0 micron) to the boundary of the grain then into adjacent pyroxene or spinel phases)

Appendix E (Figure E1): Olivine zoning profiles for sample MH-02-124A

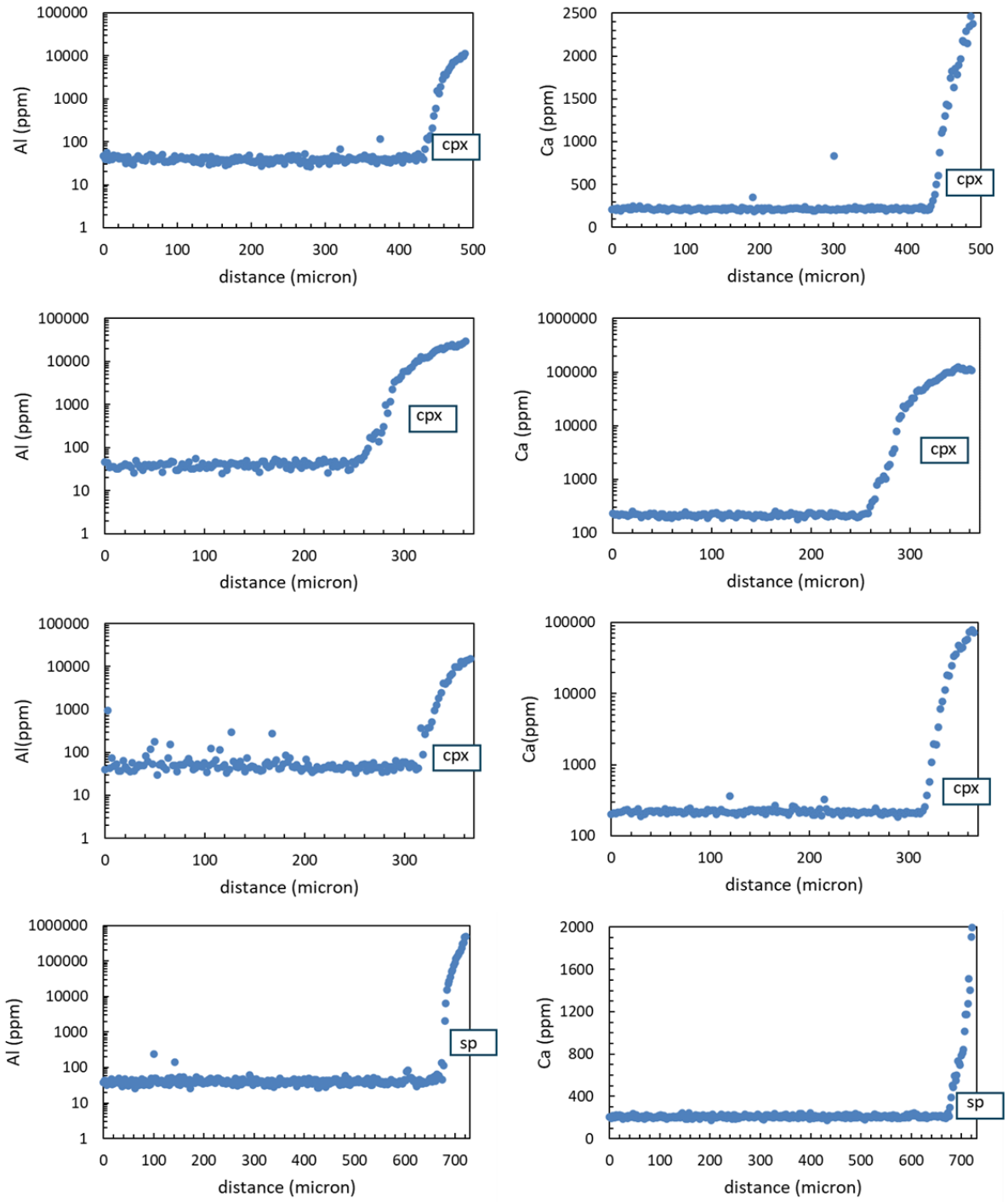

Appendix E (Figure E1): Olivine zoning profiles for sample MH-02-124A (continued)

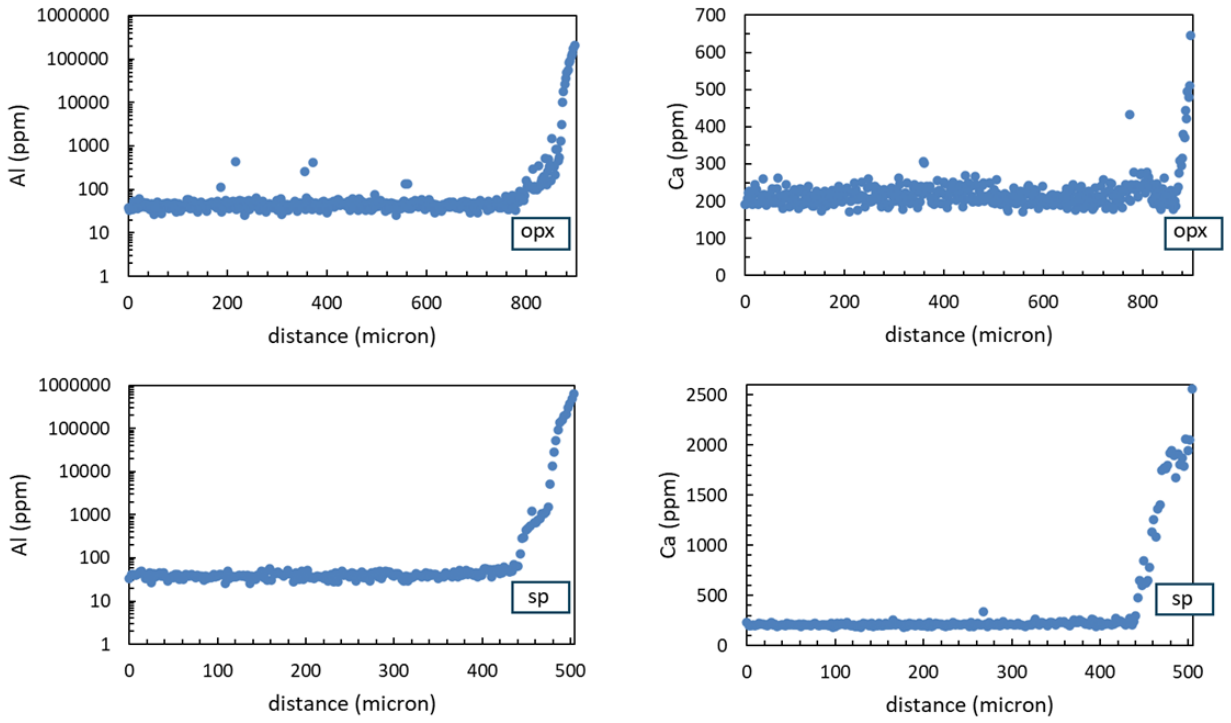

Appendix E (Figure E2): Olivine zoning profiles for sample MH-02-10B

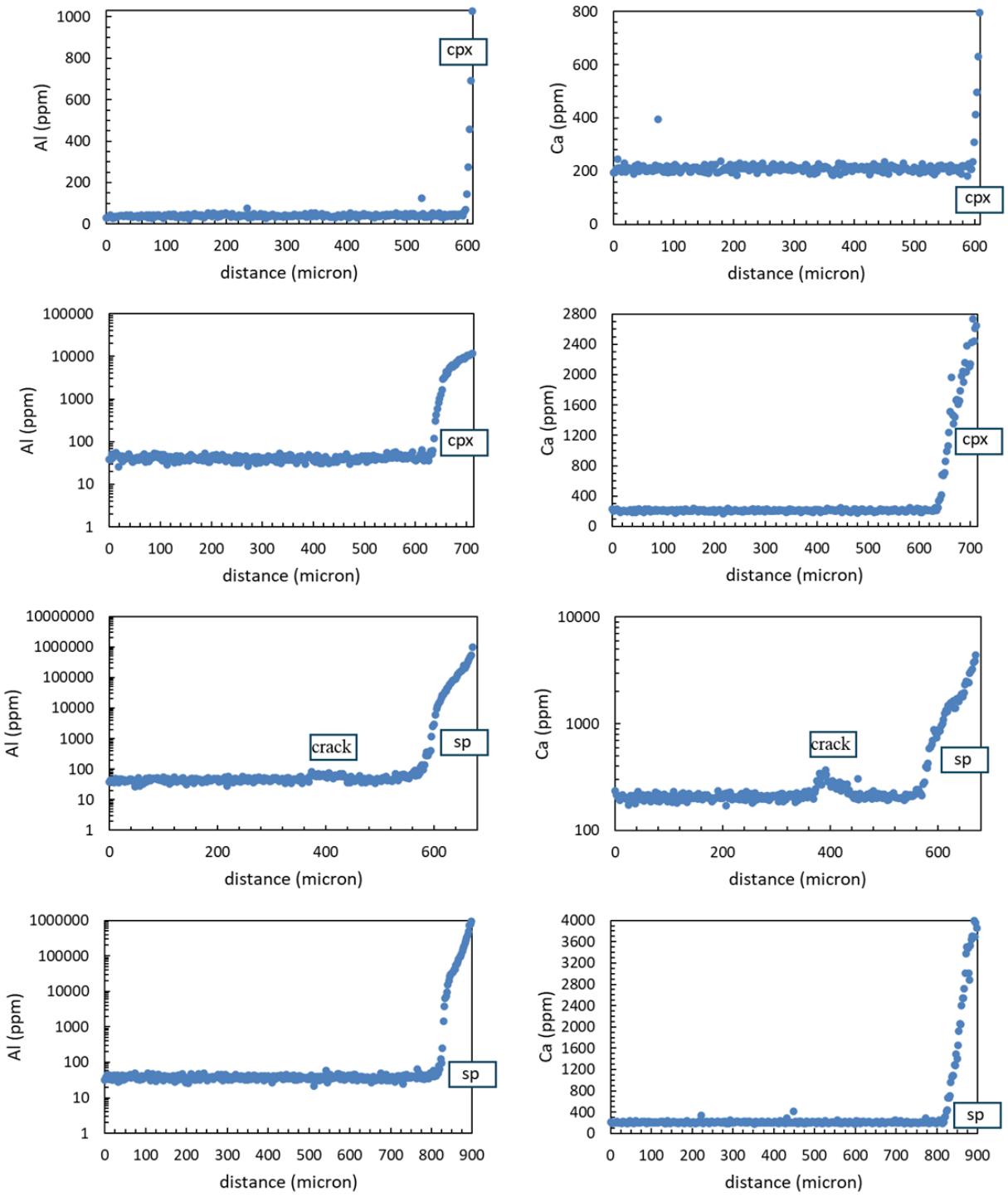

Appendix E (Figure E2): Olivine zoning profiles for sample MH-02-10B (continued)

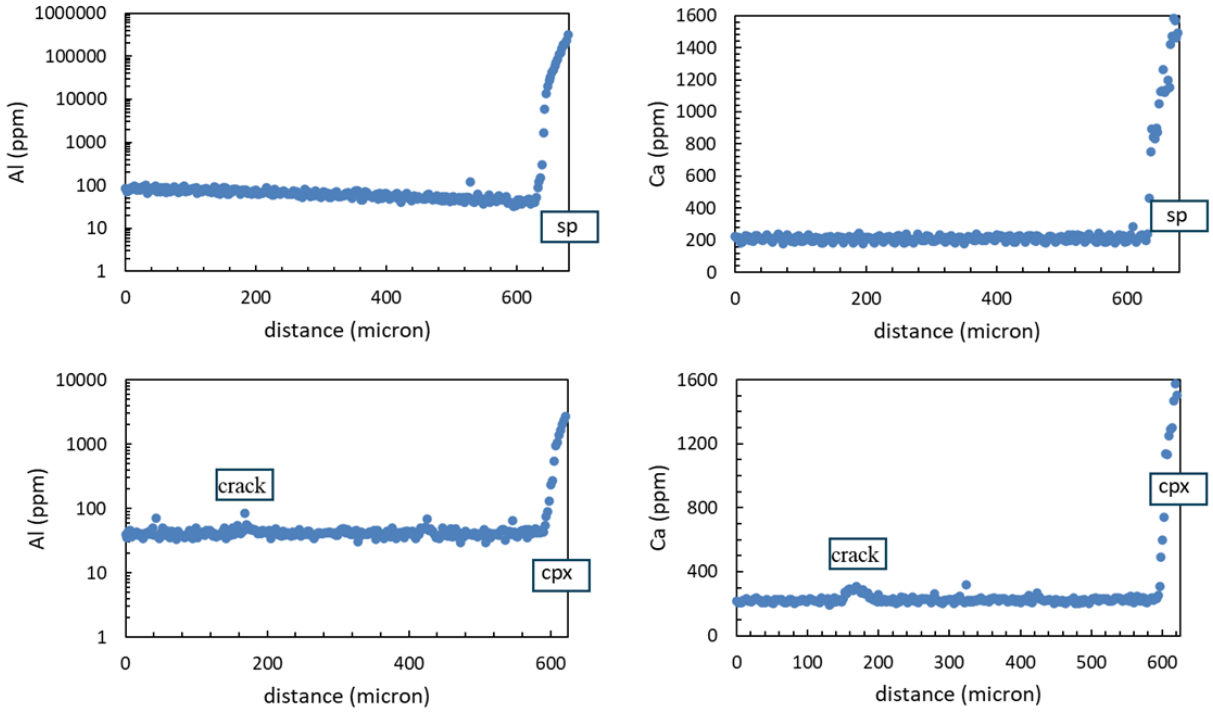

Appendix E (Figure E3): Olivine zoning profiles for sample MH-02-100B

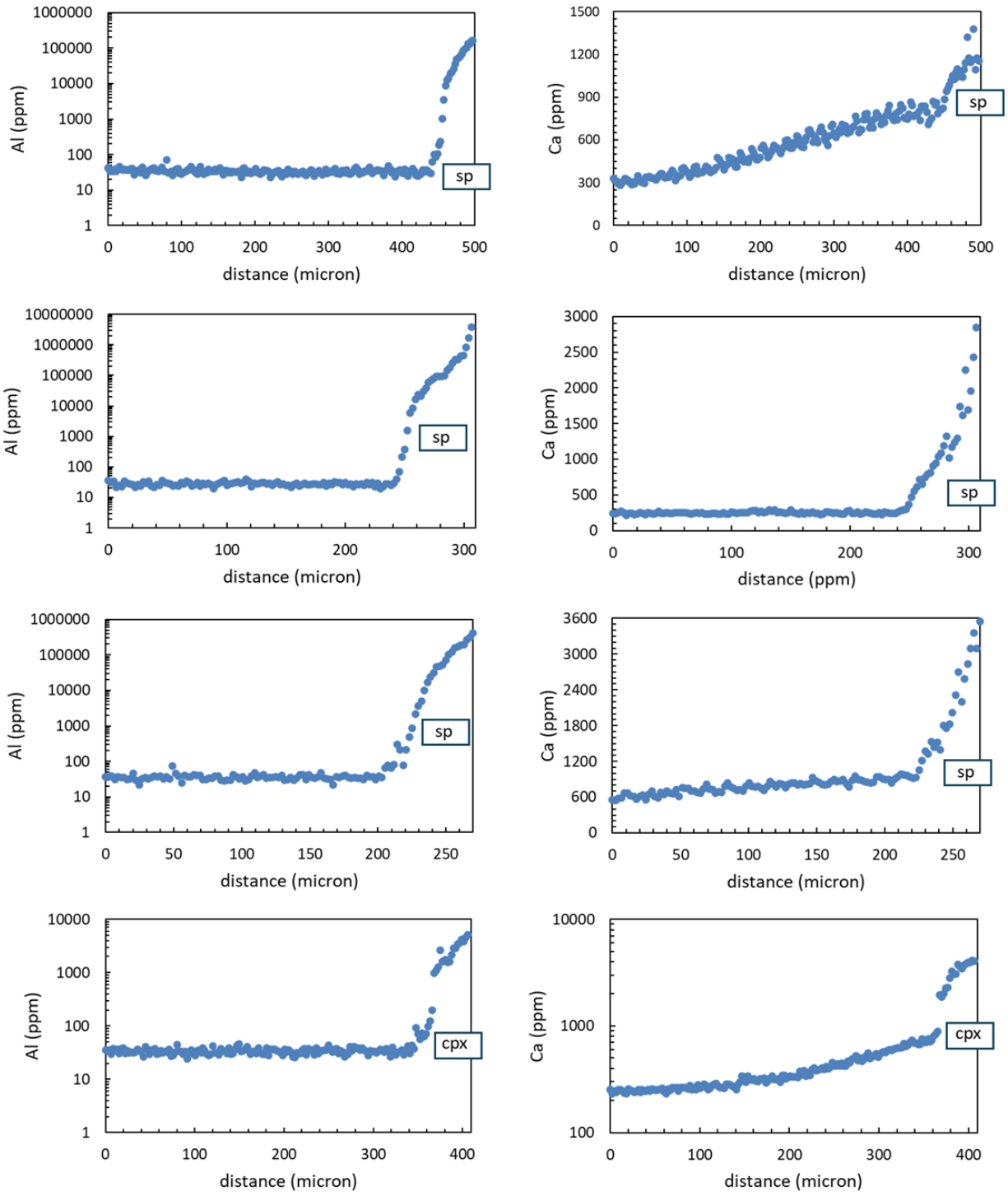

Appendix E (Figure E3): Olivine zoning profiles for sample MH-02-100B (continued)

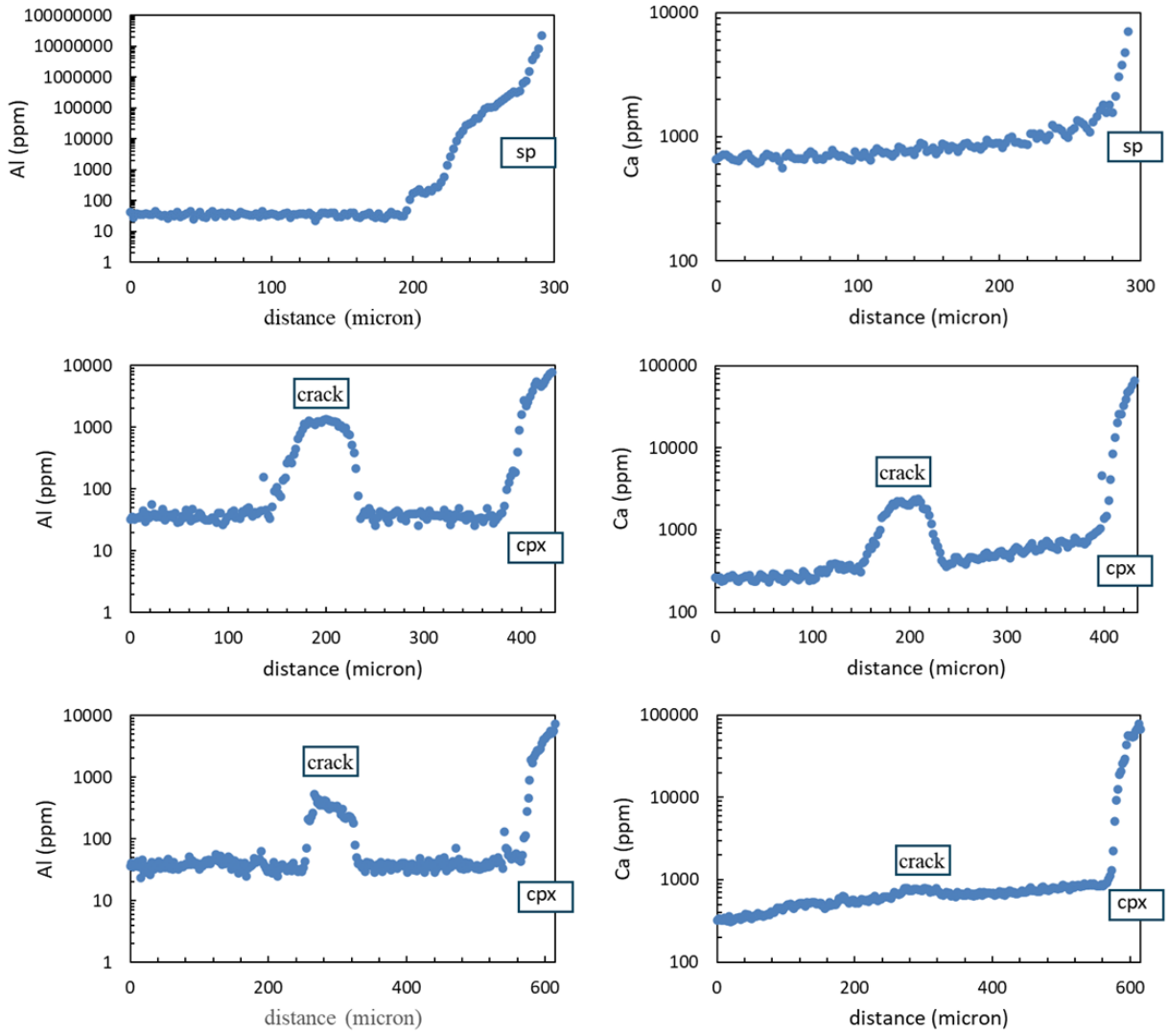

Appendix E (Figure E4): Olivine zoning profiles for sample MH-02-9B

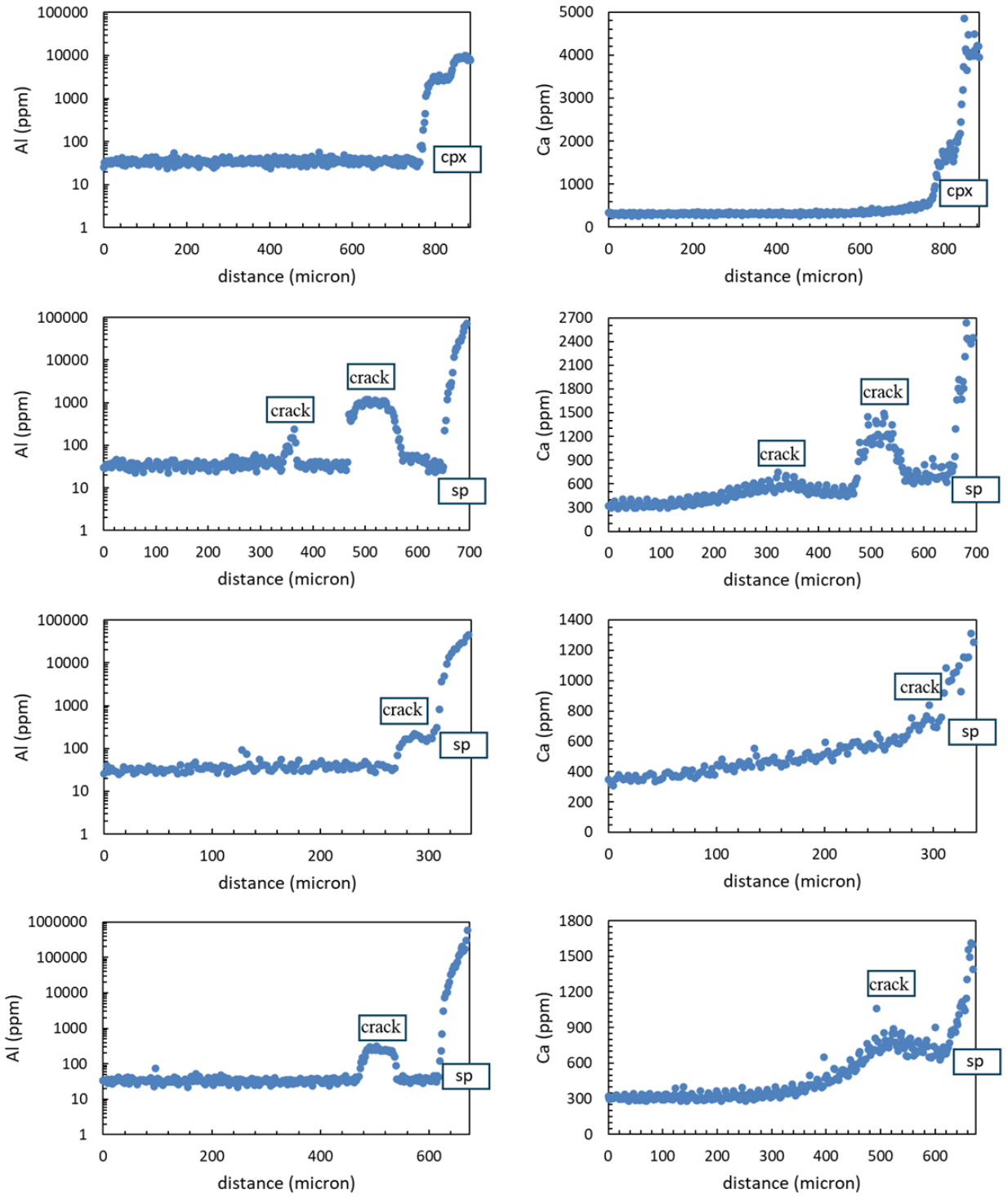

Appendix E (Figure E4): Olivine zoning profiles for sample MH-02-9B (continued)

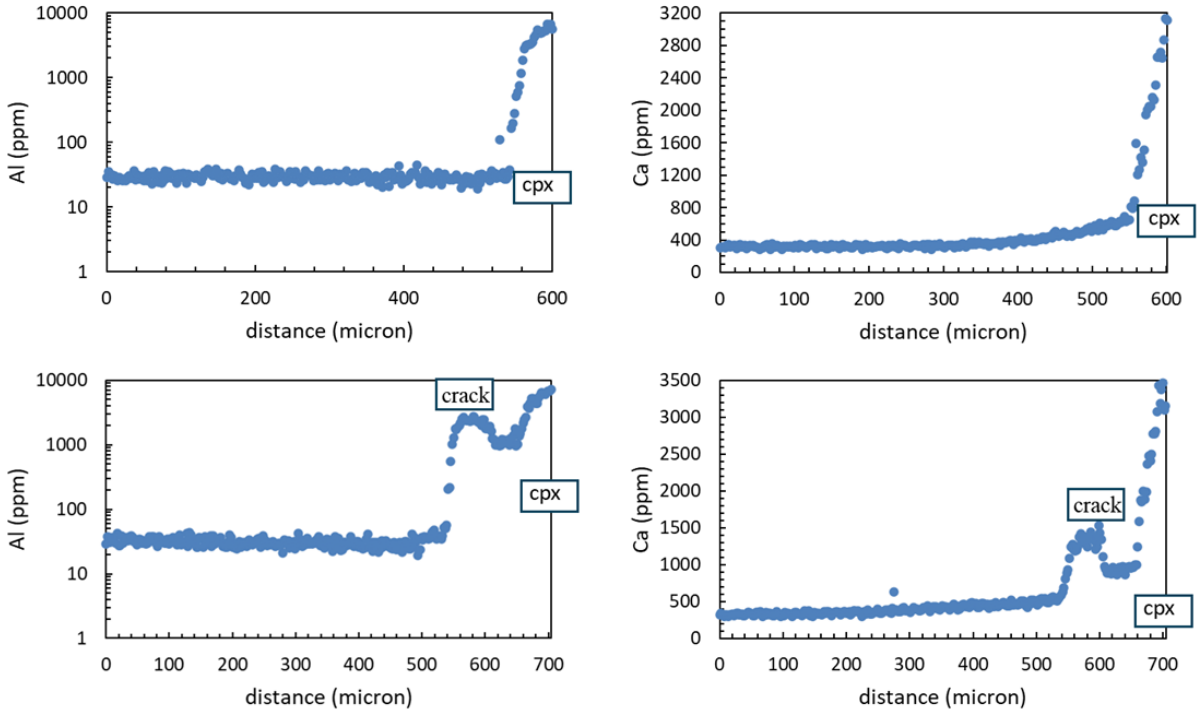

Appendix E (Figure E5): Olivine zoning profiles for sample MH-02-18B

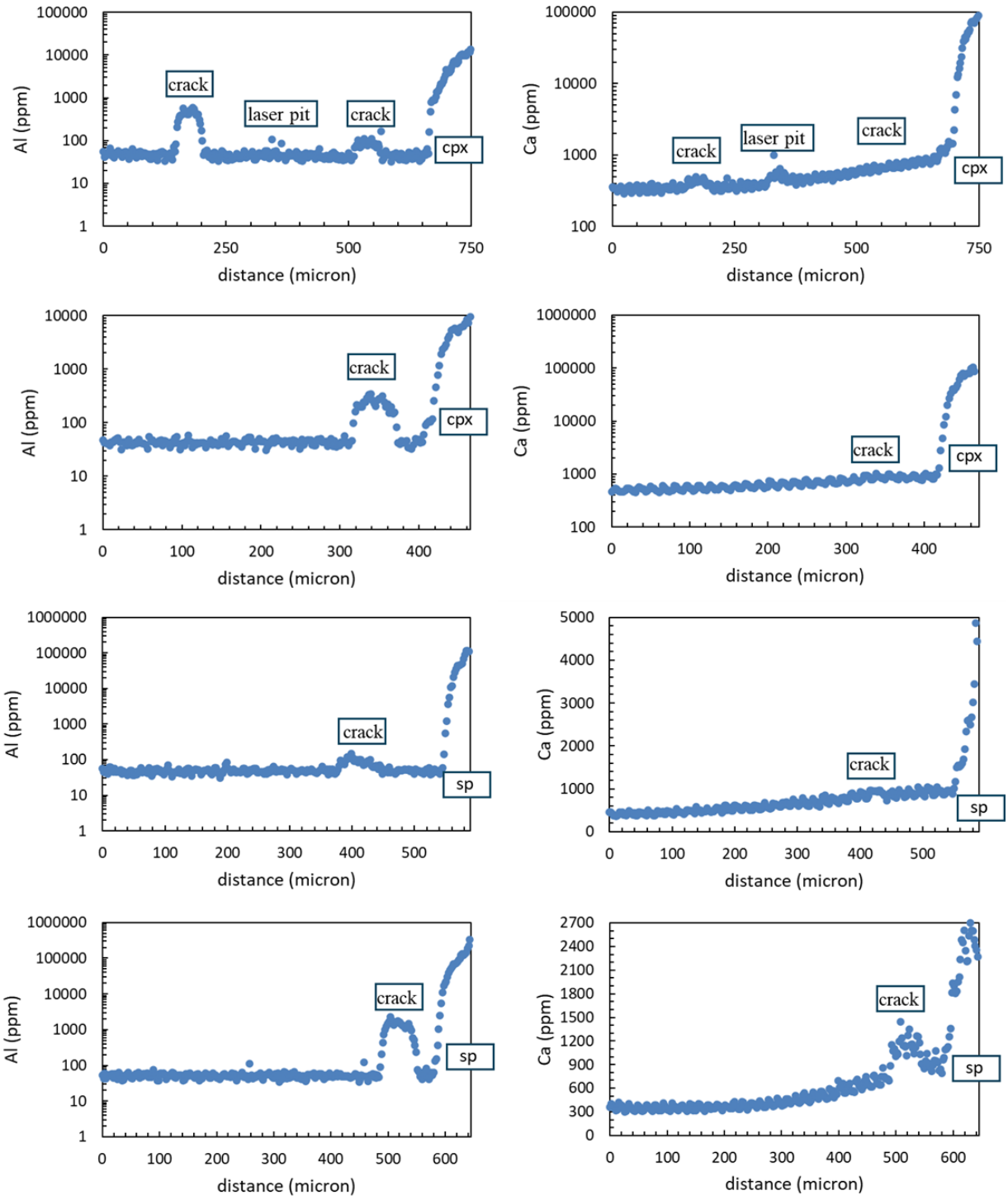

Appendix E (Figure E5): Olivine zoning profiles for sample MH-02-18B (continued)

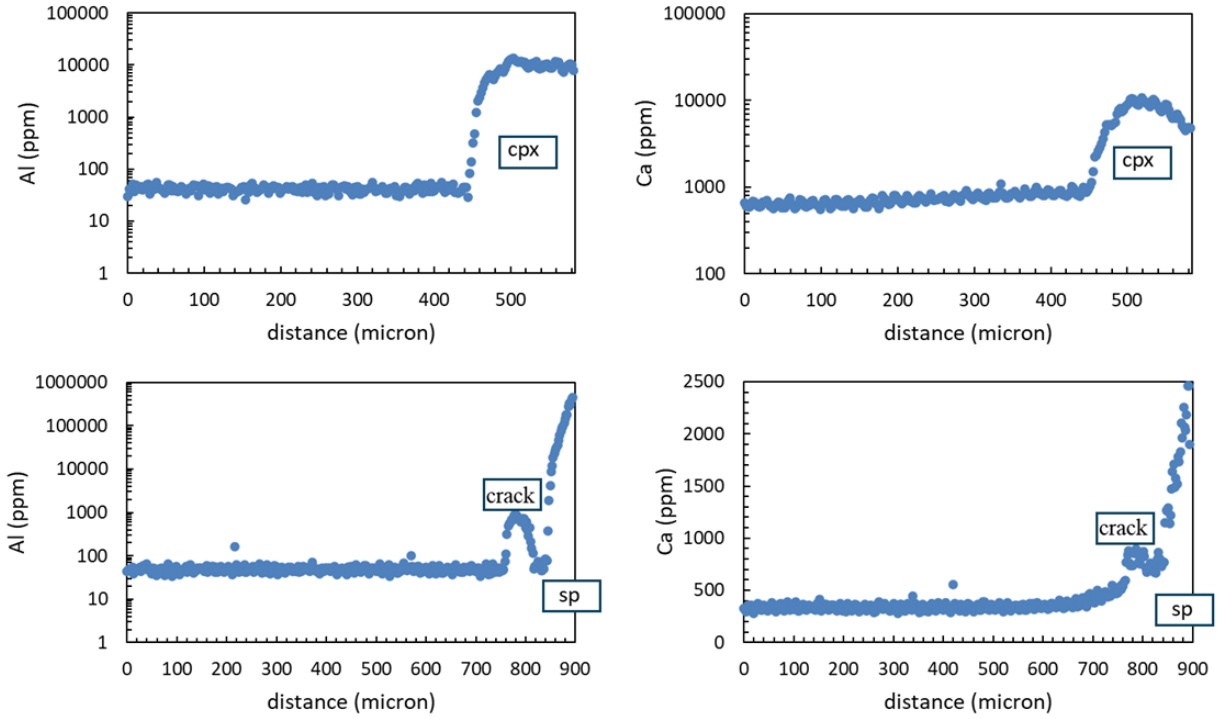

Appendix E (Figure E6): Olivine zoning profiles for sample MH-02-114

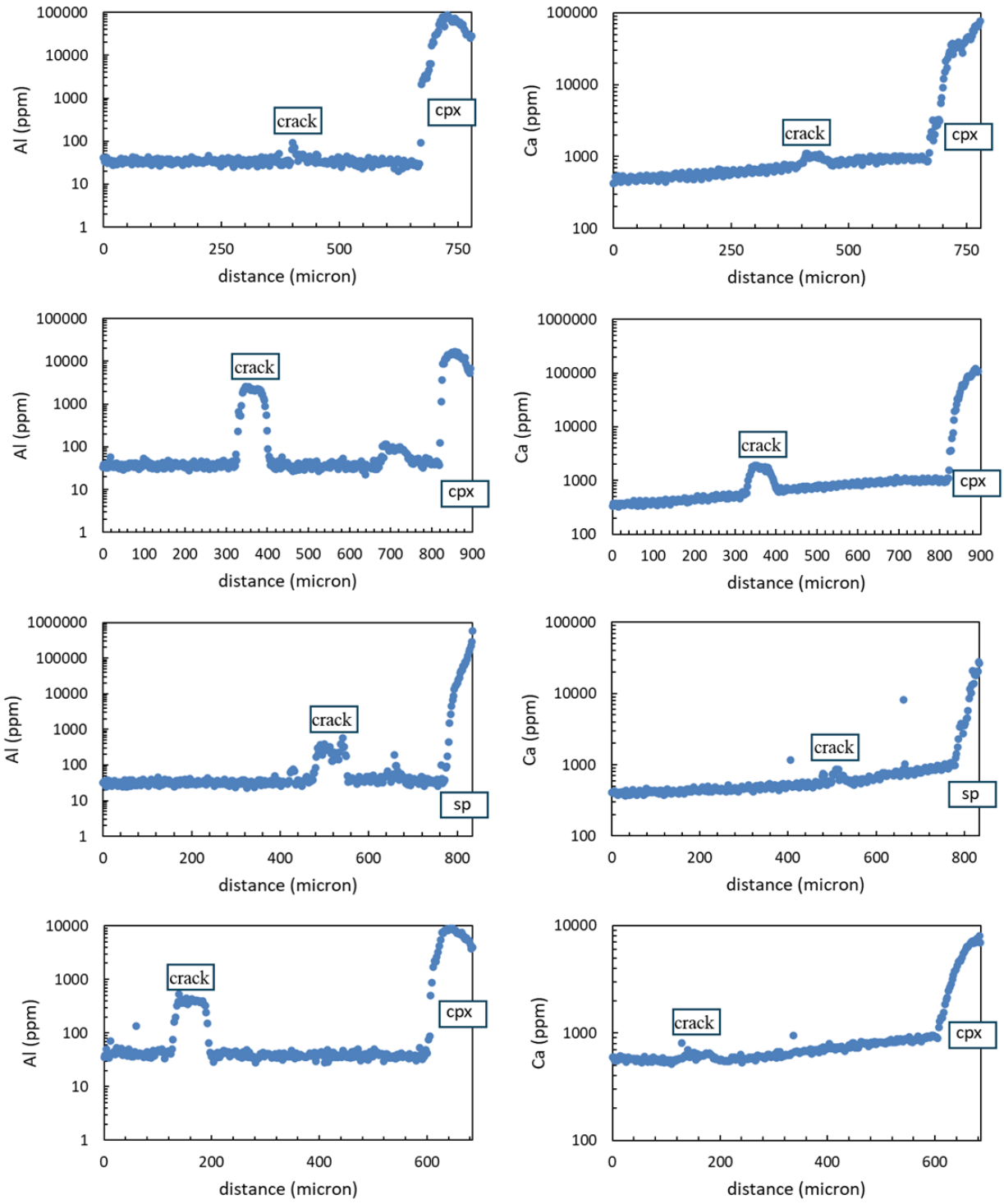

Appendix E (Figure E6): Olivine zoning profiles for sample MH-02-114 (continued)

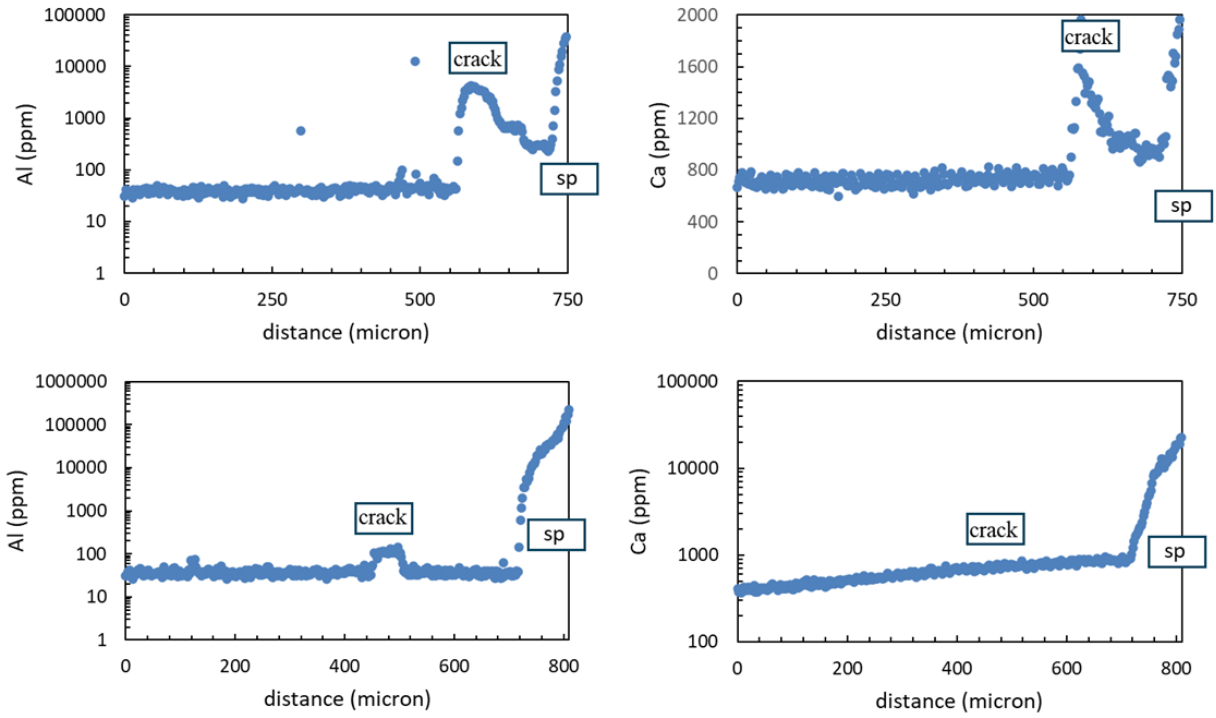

Appendix E (Figure E7): Olivine zoning profiles for sample MH-02-12

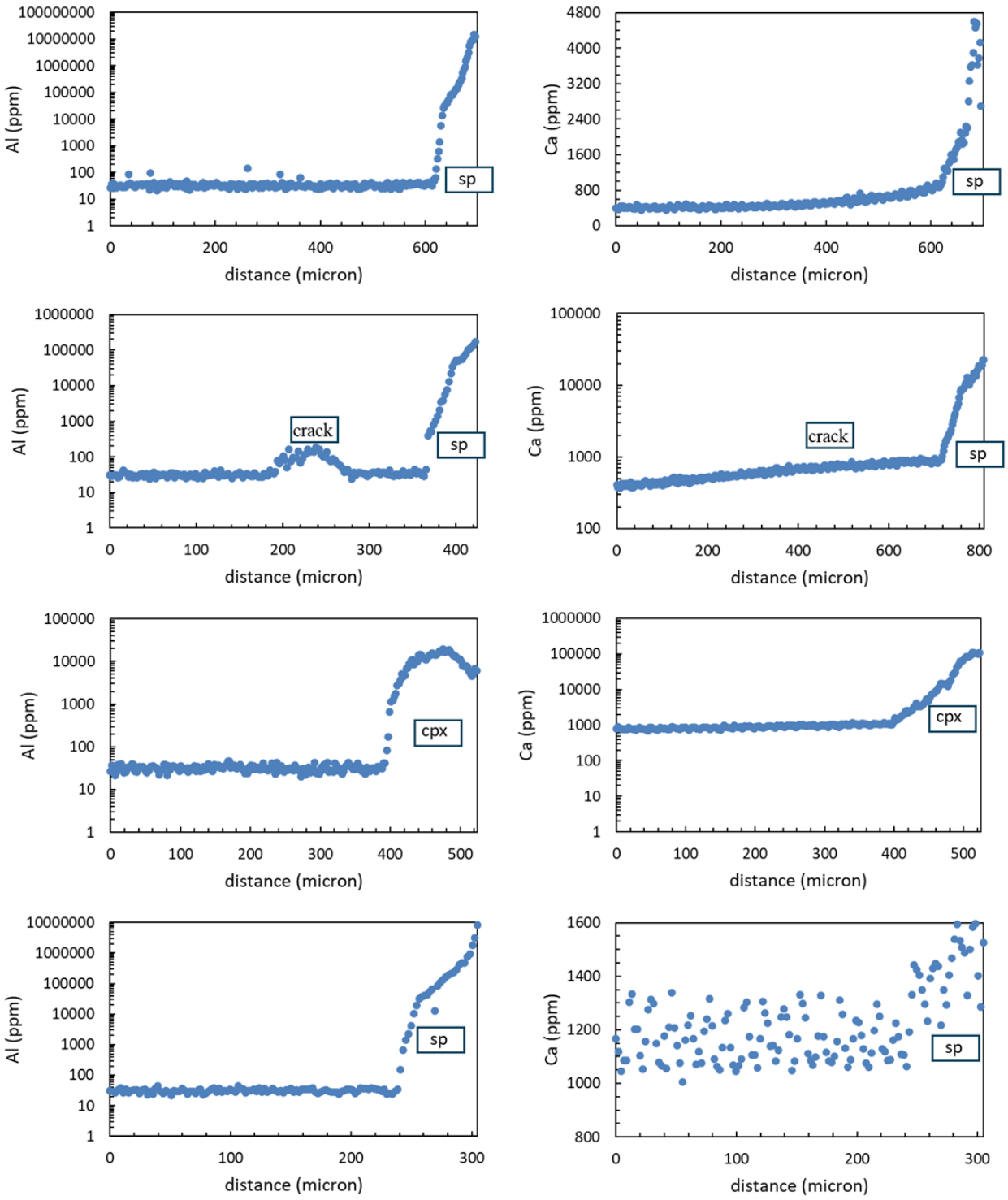

Appendix E (Figure E7): Olivine zoning profiles for sample MH-02-12 (continued)

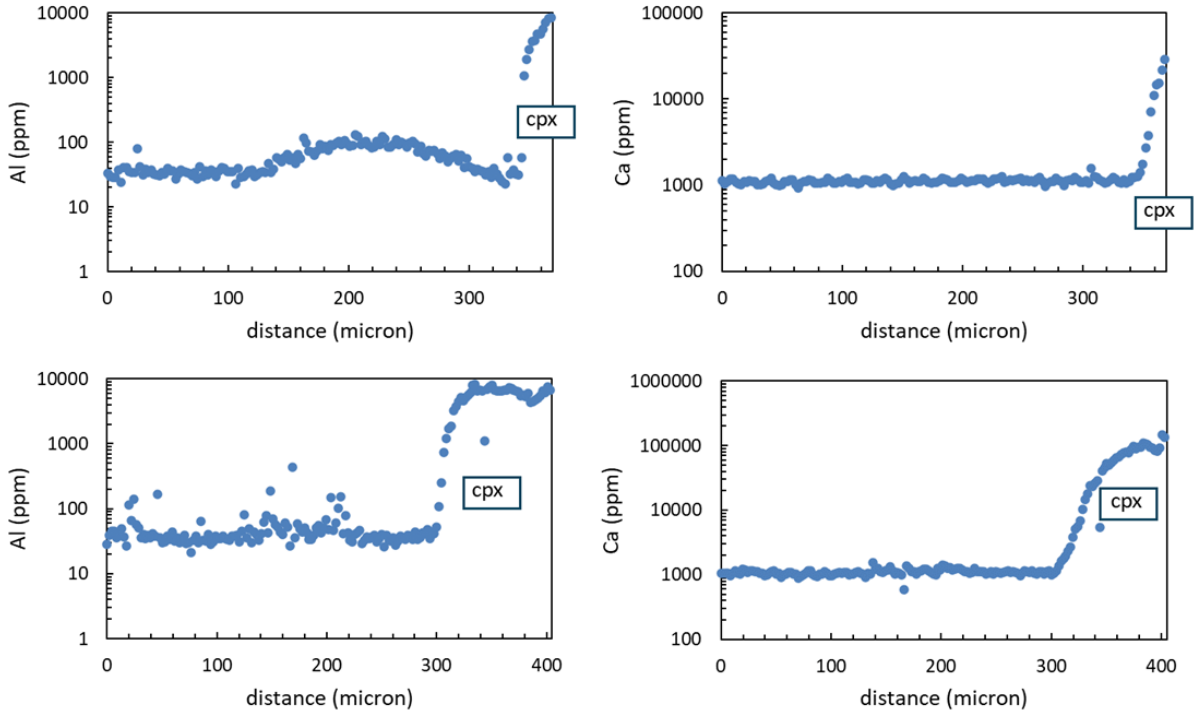

Appendix E (Figure E8): Olivine zoning profiles for sample MH-02-10C

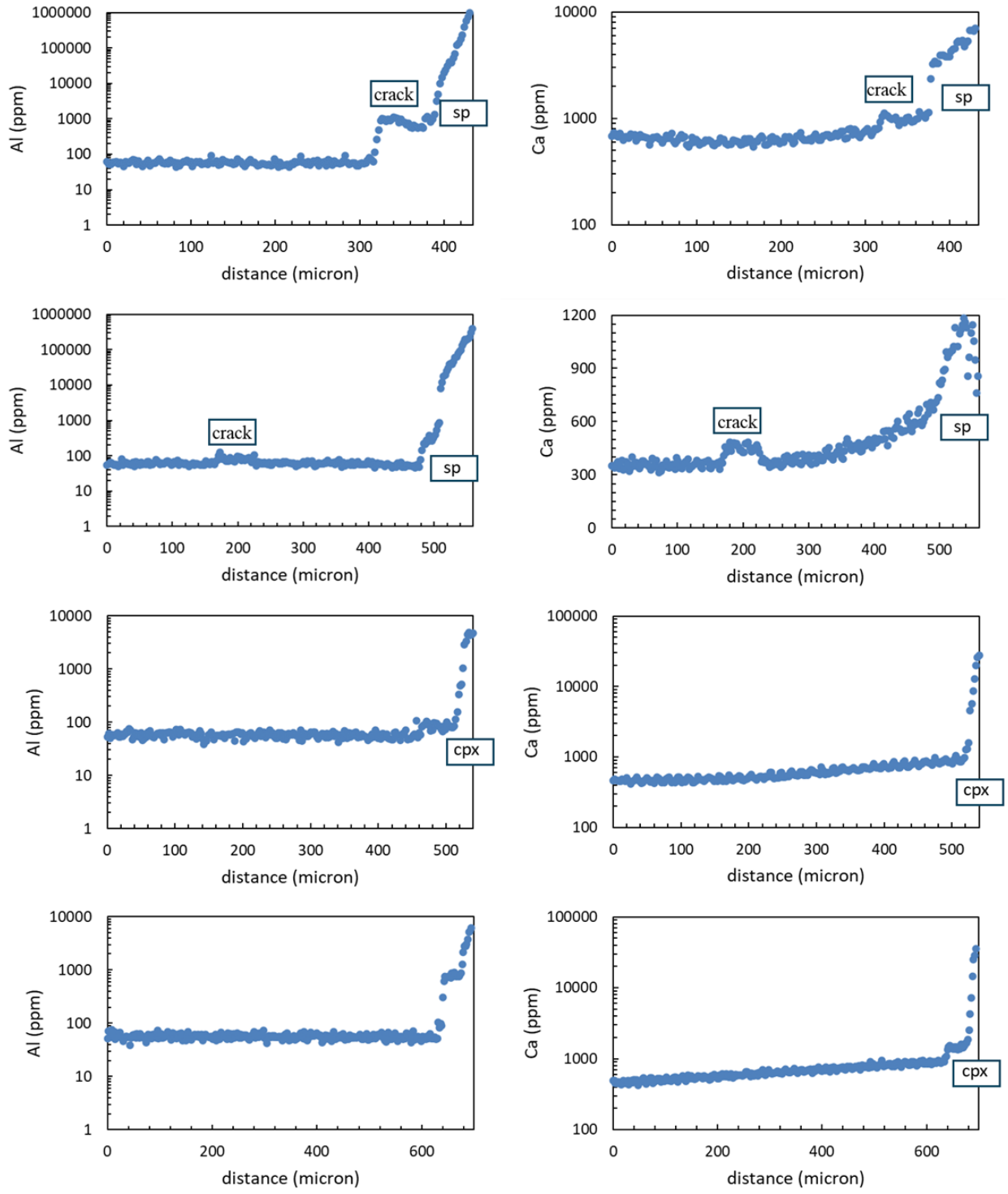

Appendix E (Figure E8): Olivine zoning profiles for sample MH-02-10C (continued)

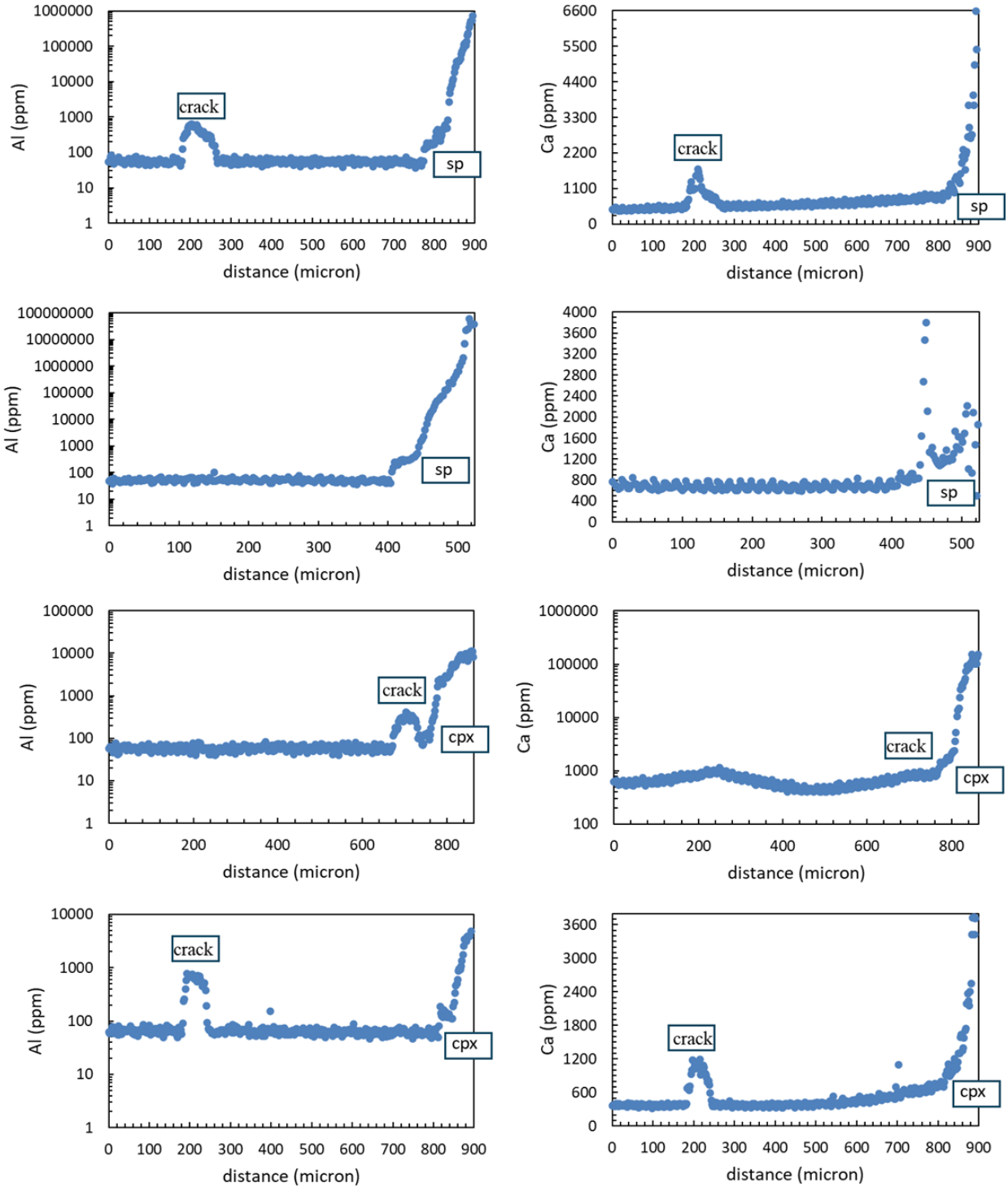

Appendix F: Best fitted olivine Ca zoning profiles

(All zoning profiles are started from the rim of the grain (0 micron) to the core of the grain)

Appendix F (Figure F1): MH-02-100B-3

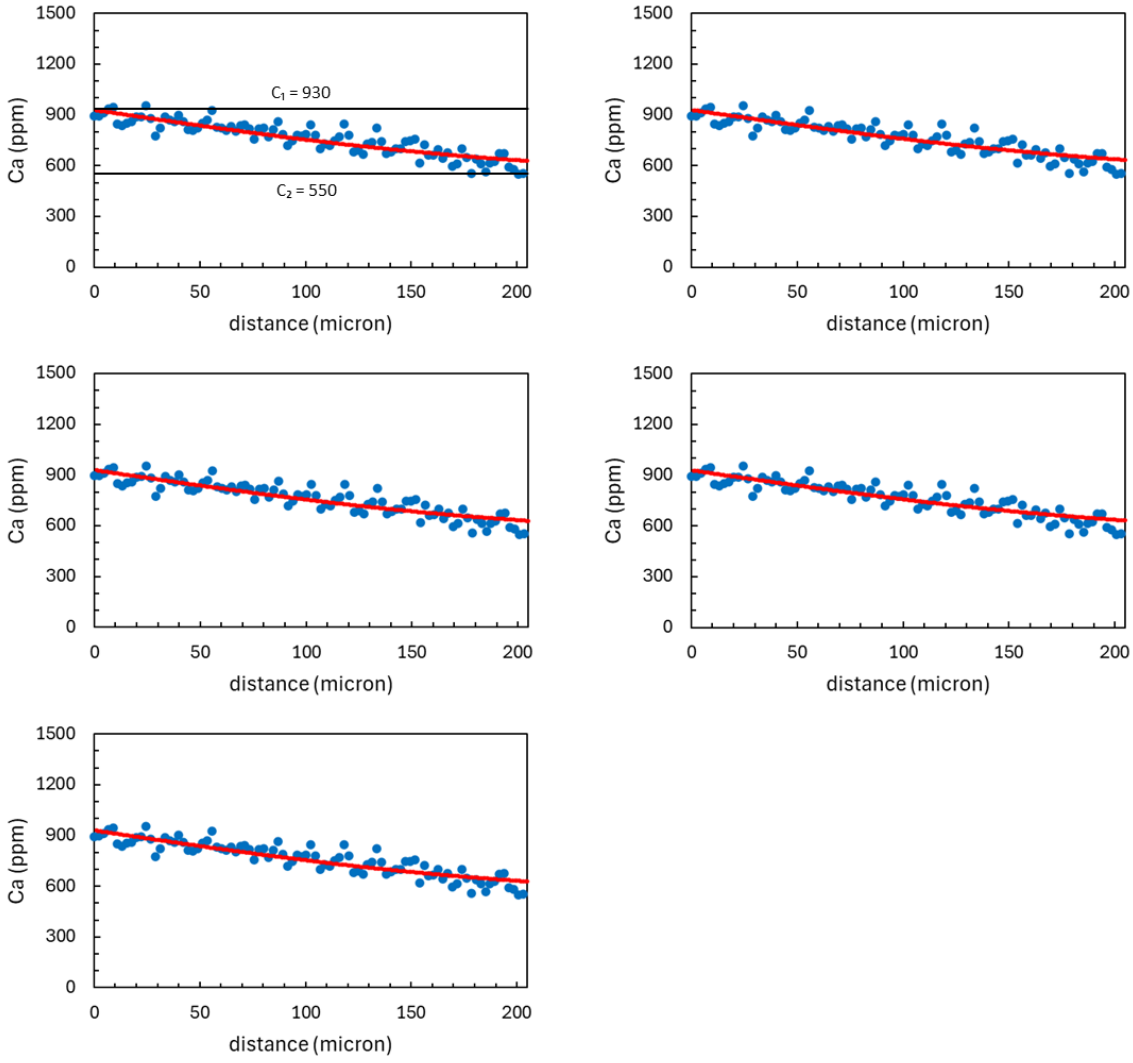

Appendix F (Figure F2): MH-02-100B-4

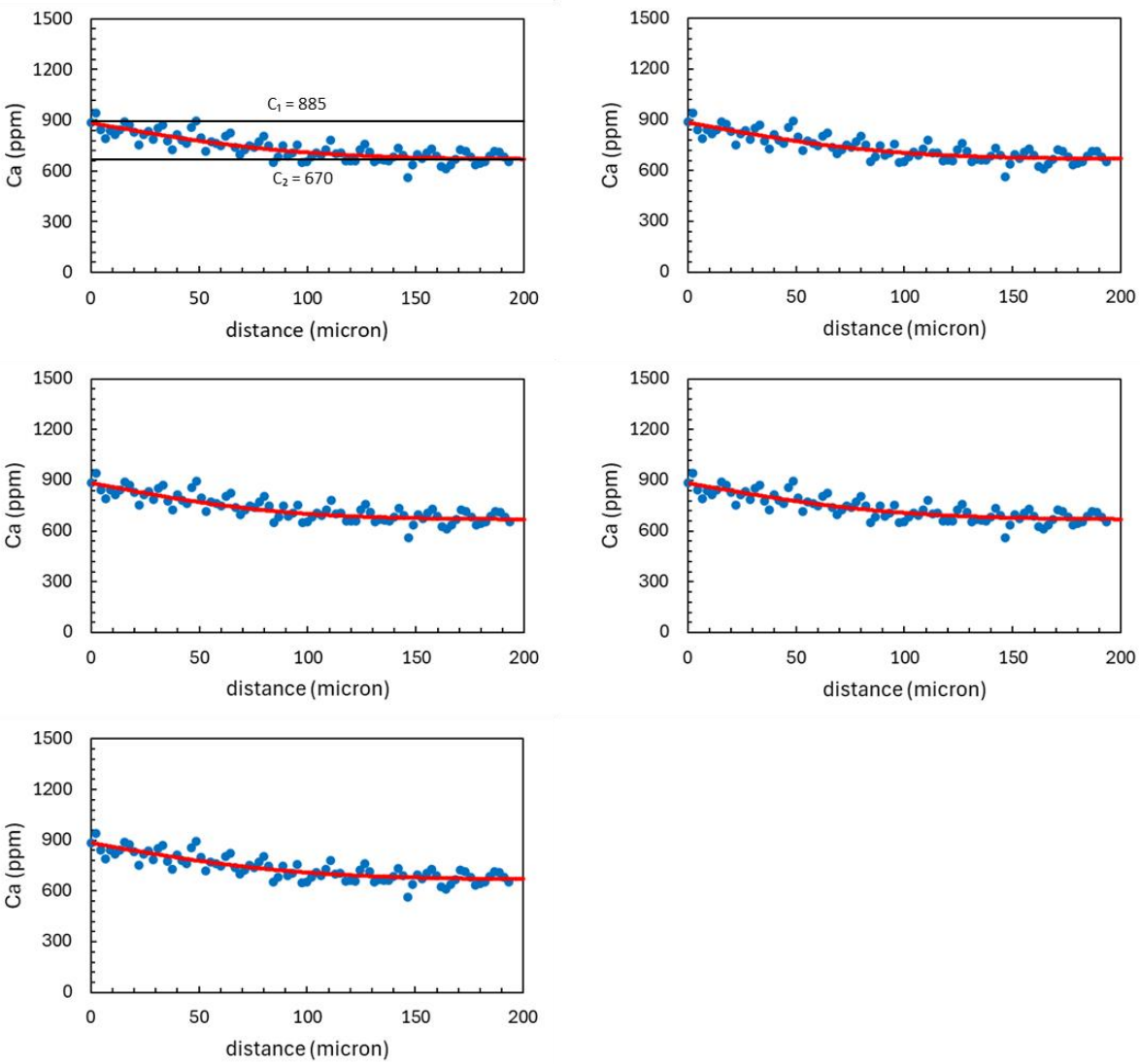

Appendix F (Figure F3): MH-02-100B-5

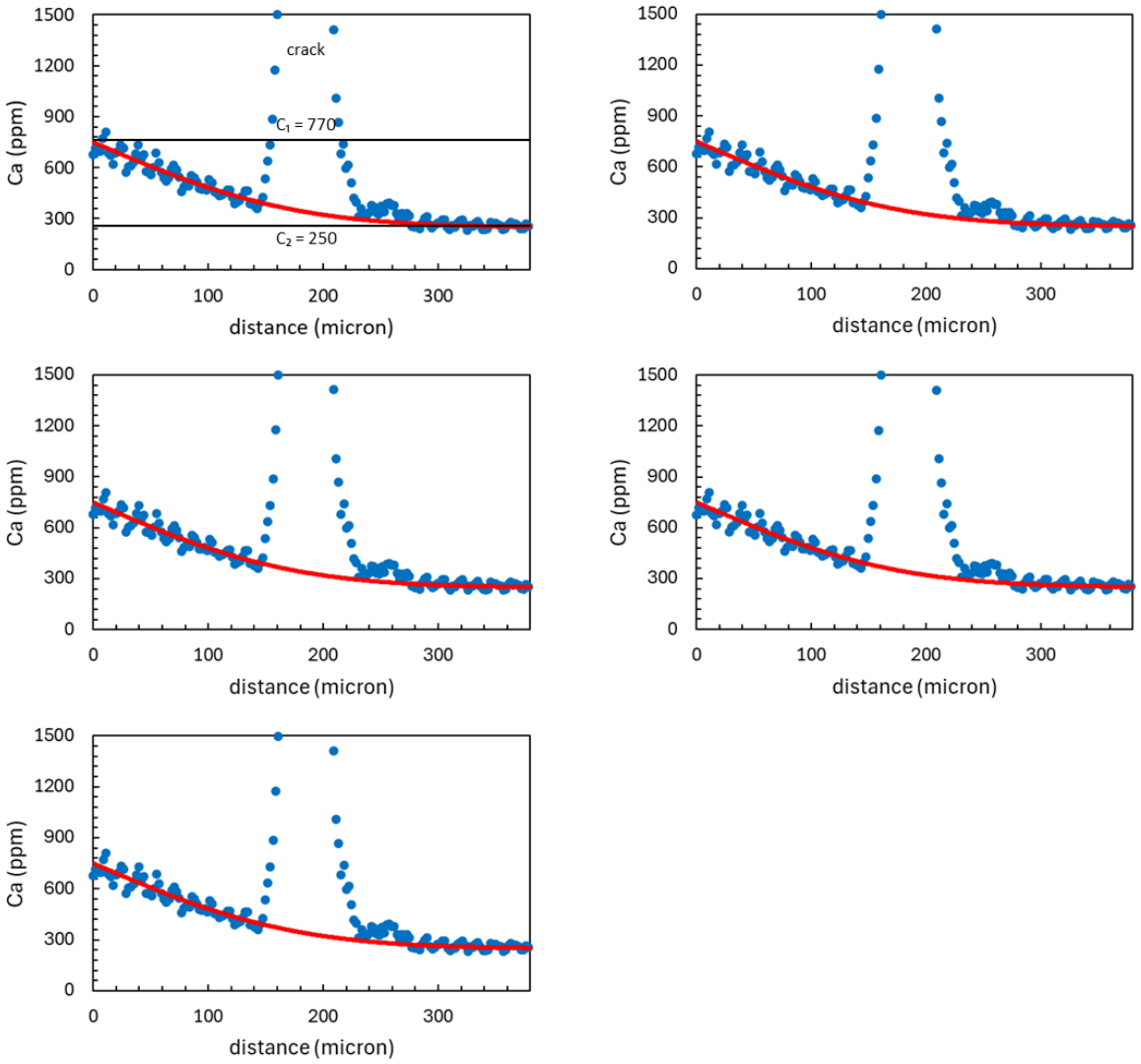

Appendix F (Figure F4): MH-02-100B-7

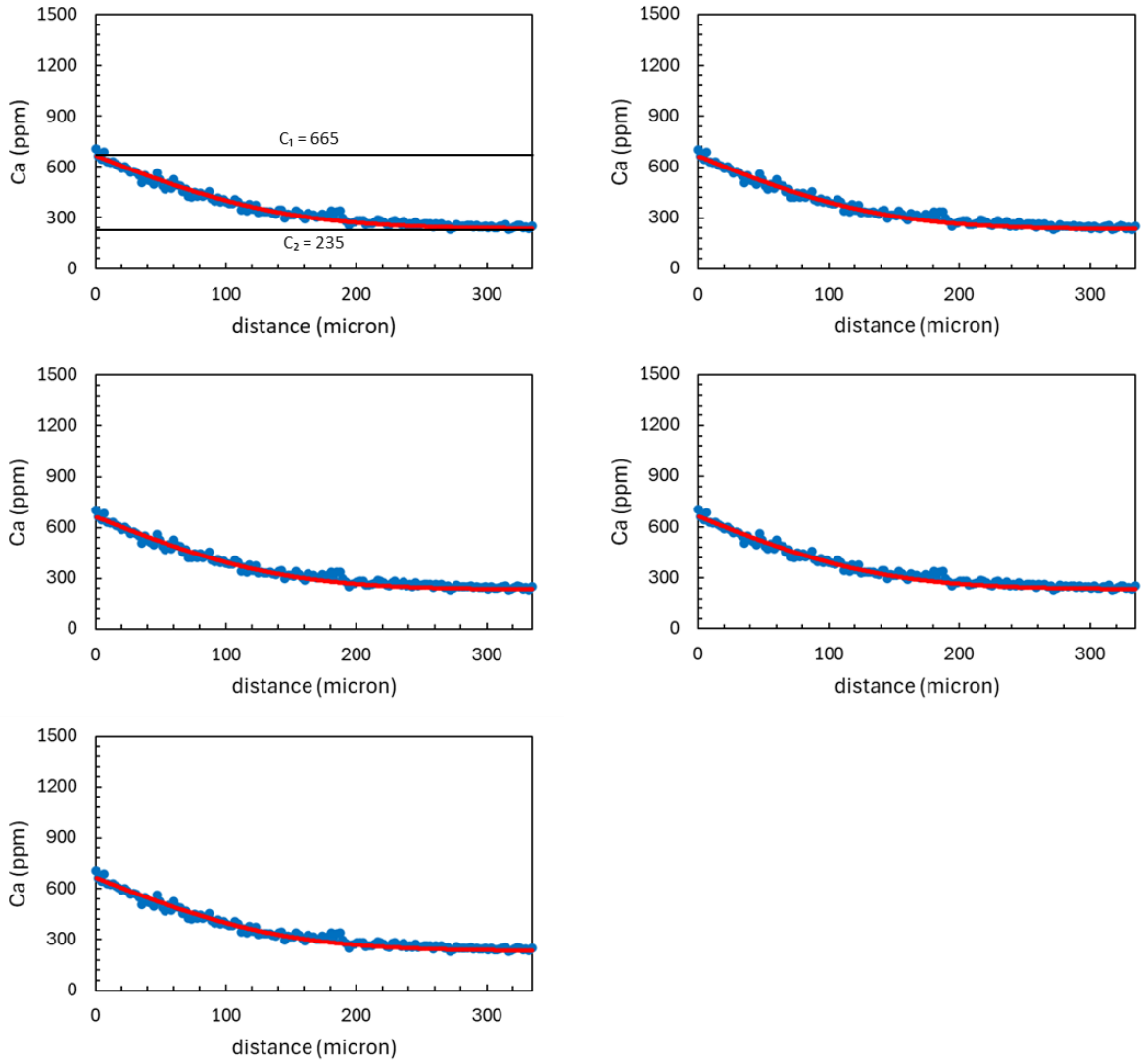

Appendix F (Figure F5): MH-02-9B-1

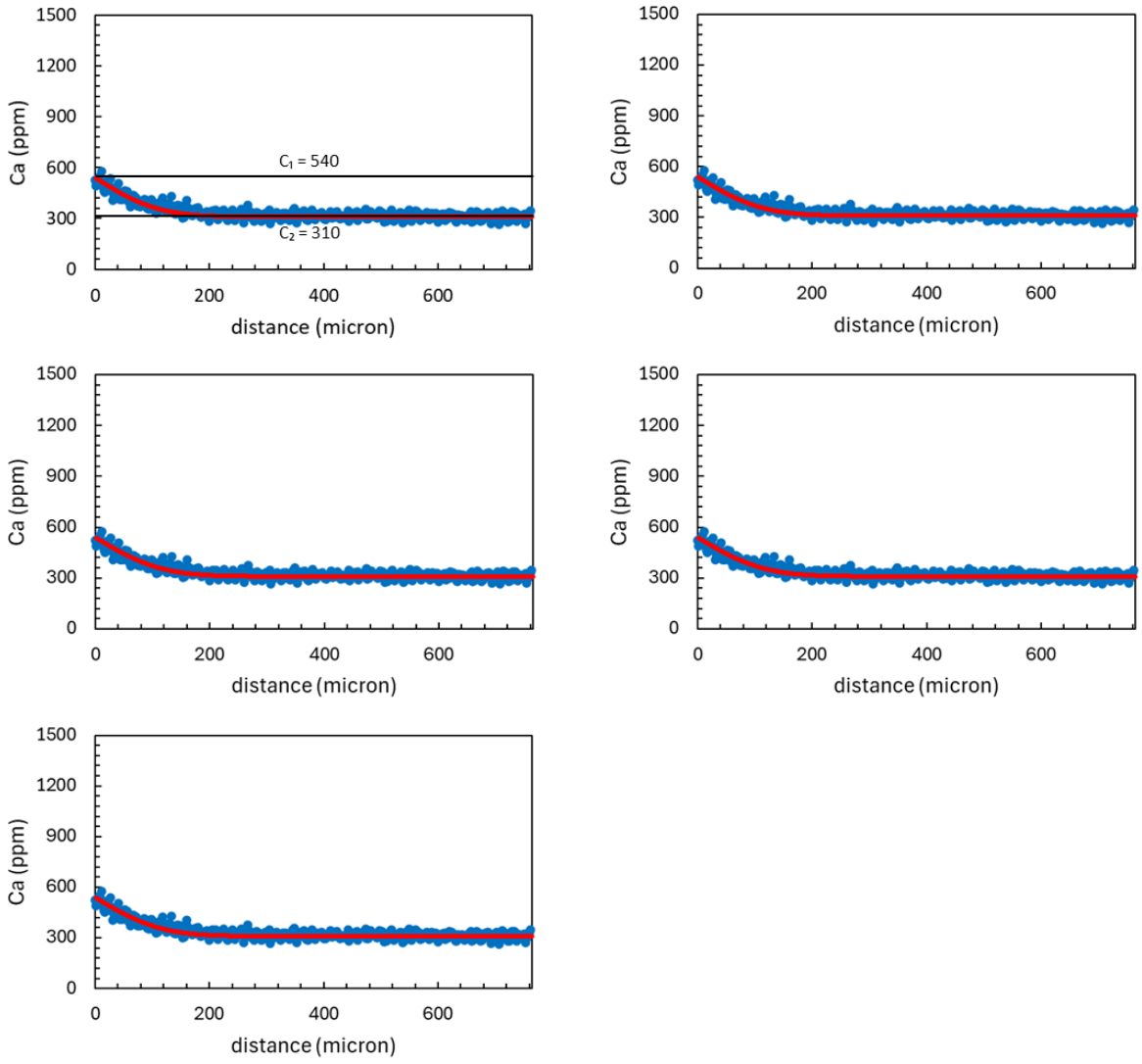

Appendix F (Figure F6): MH-02-9B-3

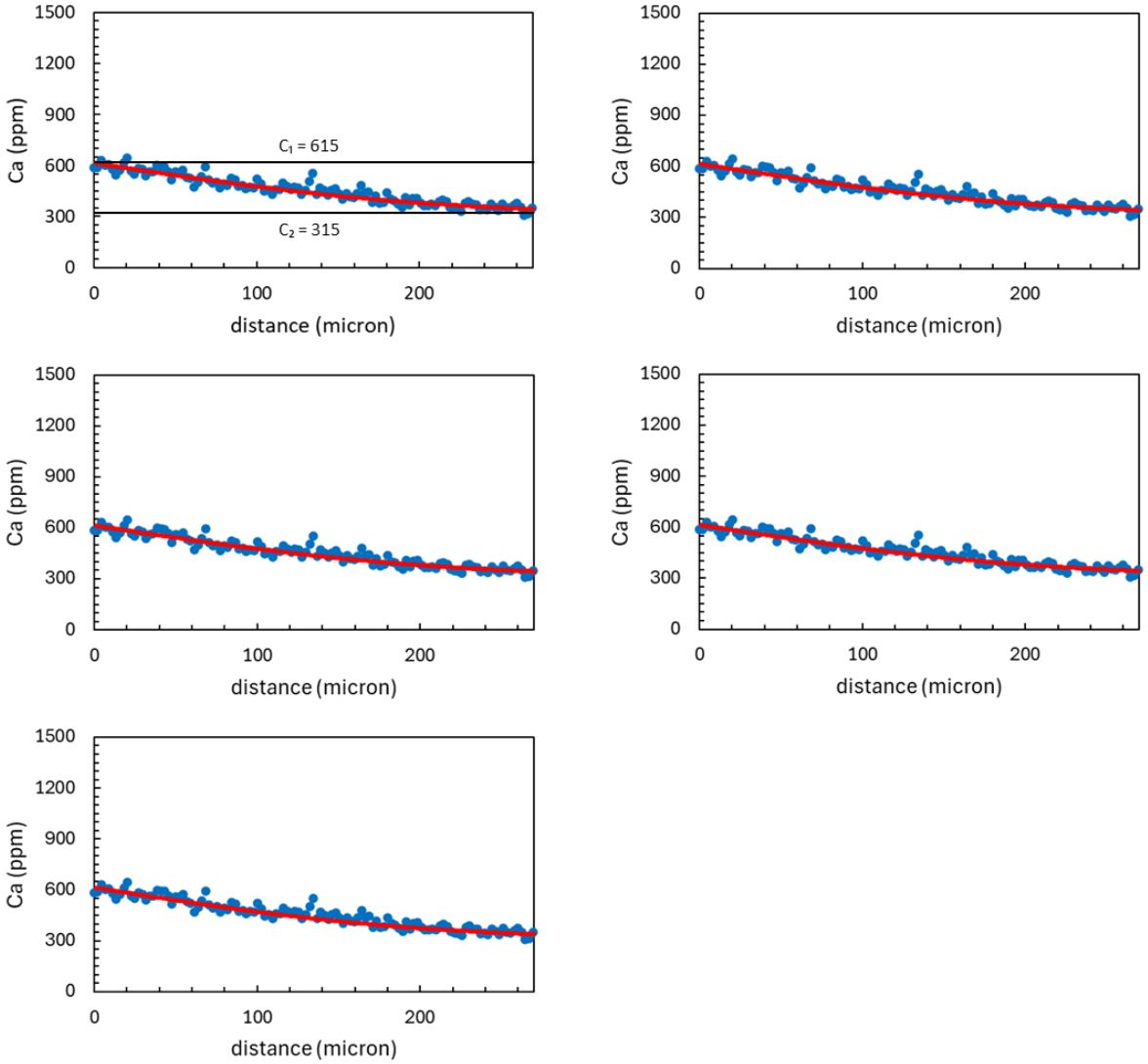

Appendix F (Figure F7): MH-02-9B-5

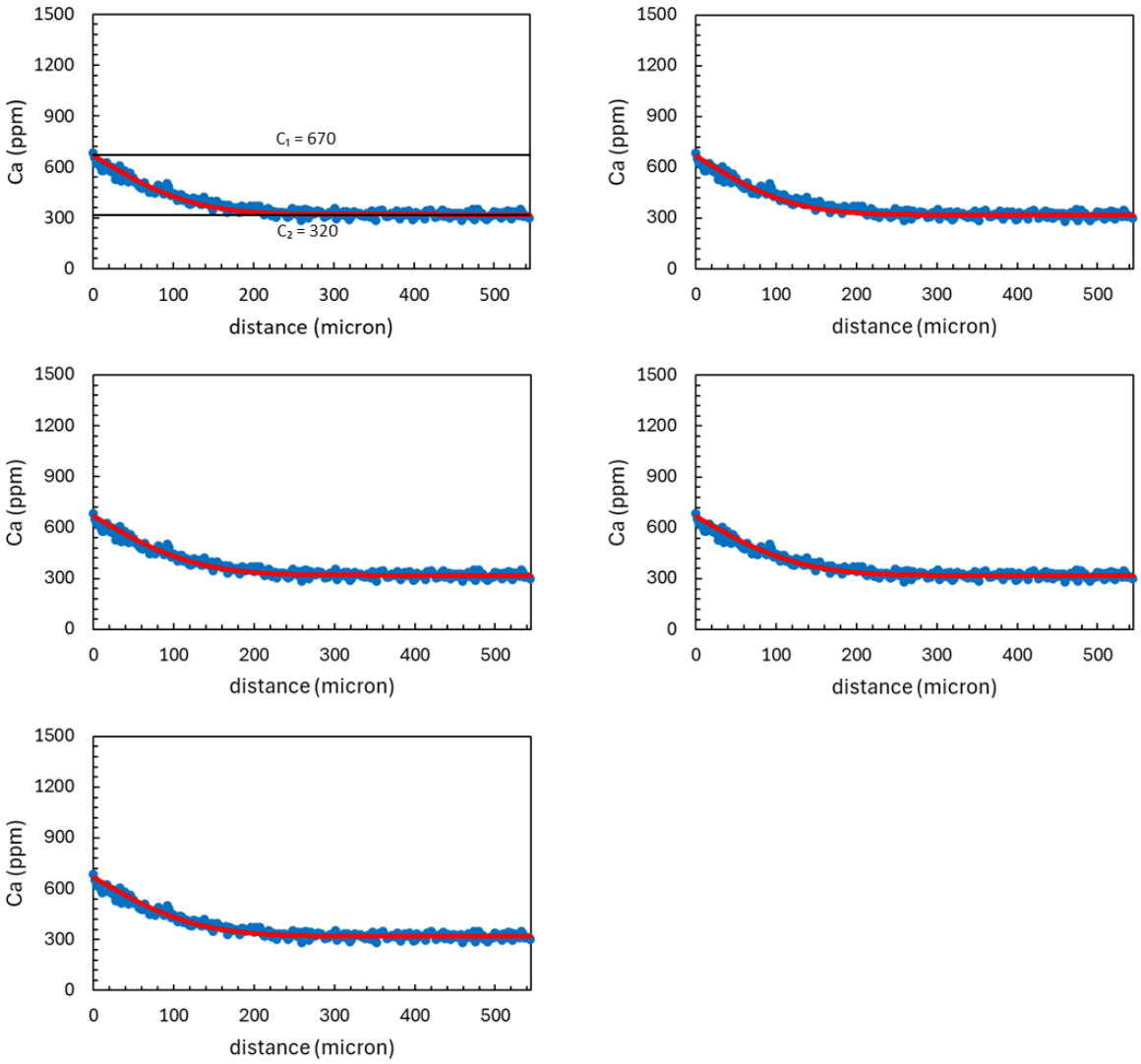

Appendix F (Figure F8): MH-02-18B-1

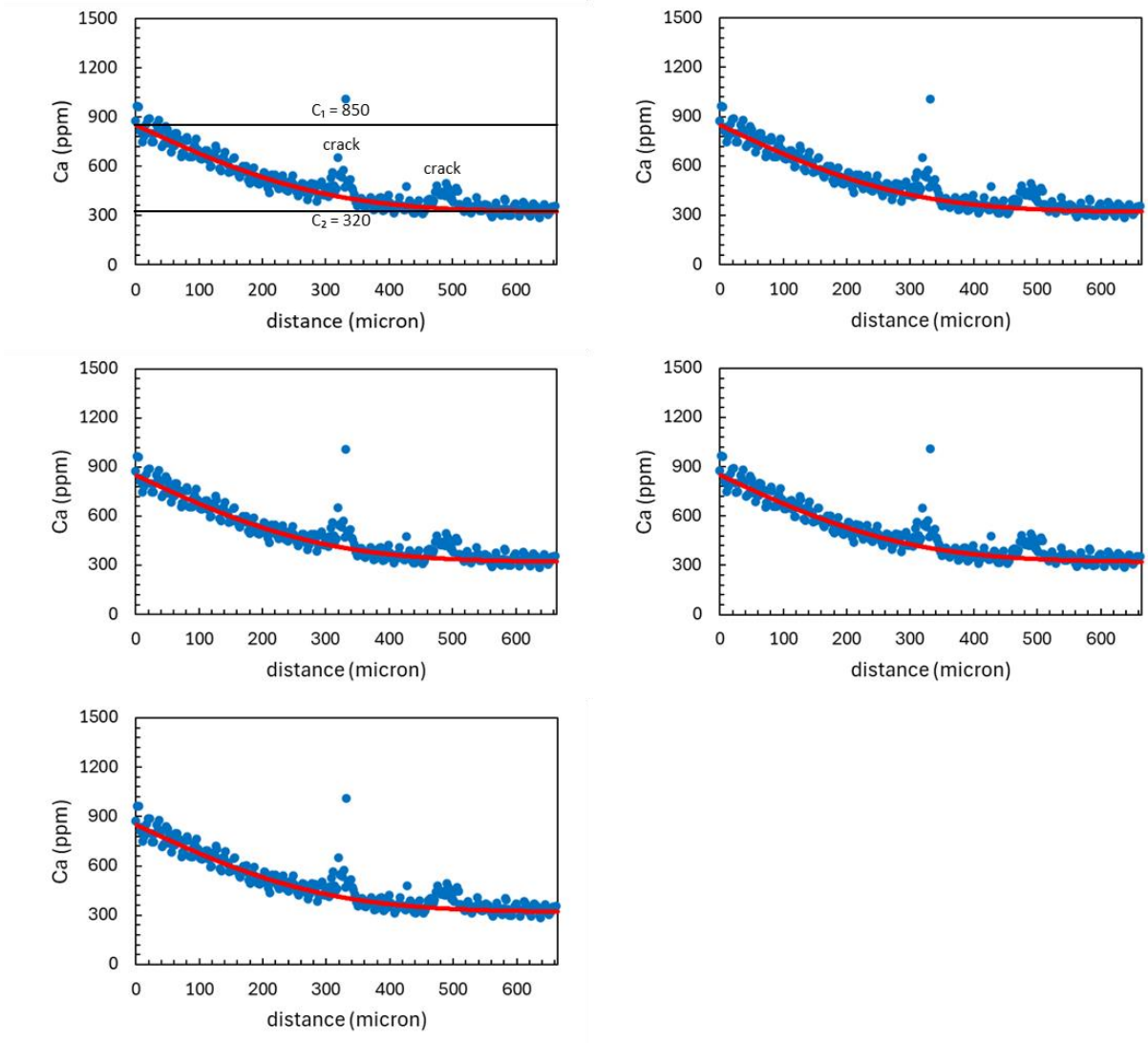

Appendix F (Figure F9): MH-02-18B-2

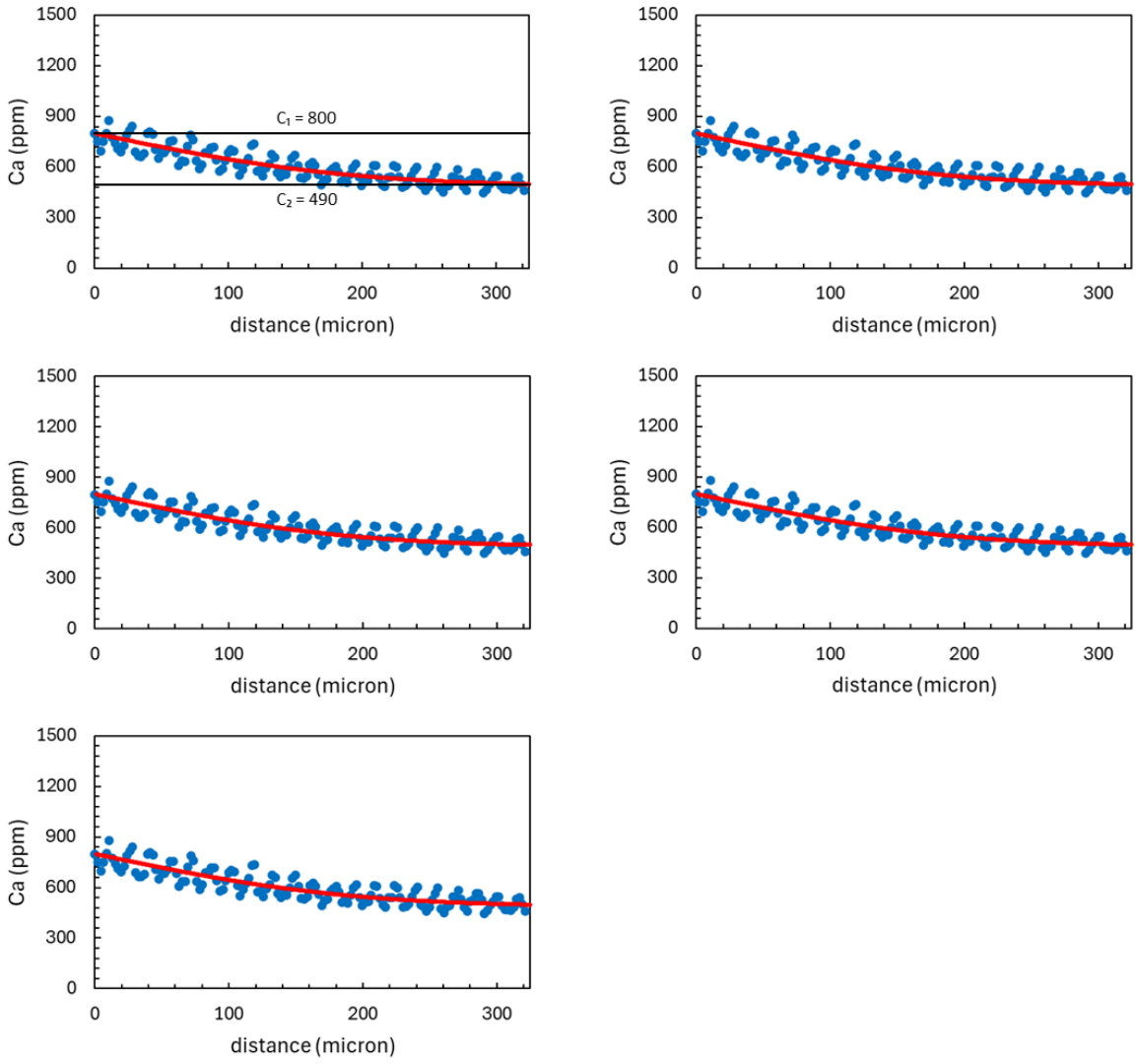

Appendix F (Figure F10): MH-02-18B-4

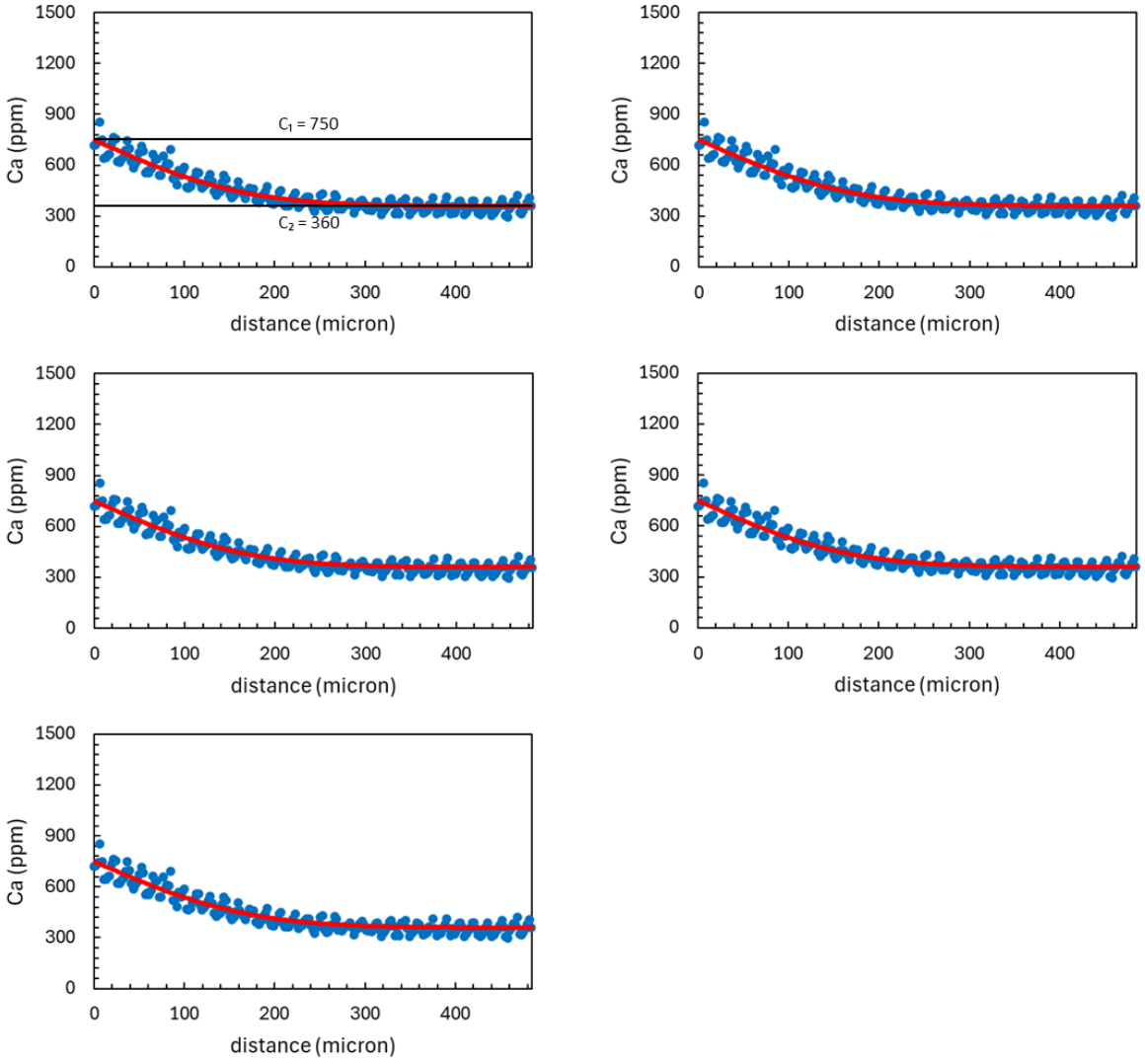

Appendix F (Figure F11): MH-02-18B-5

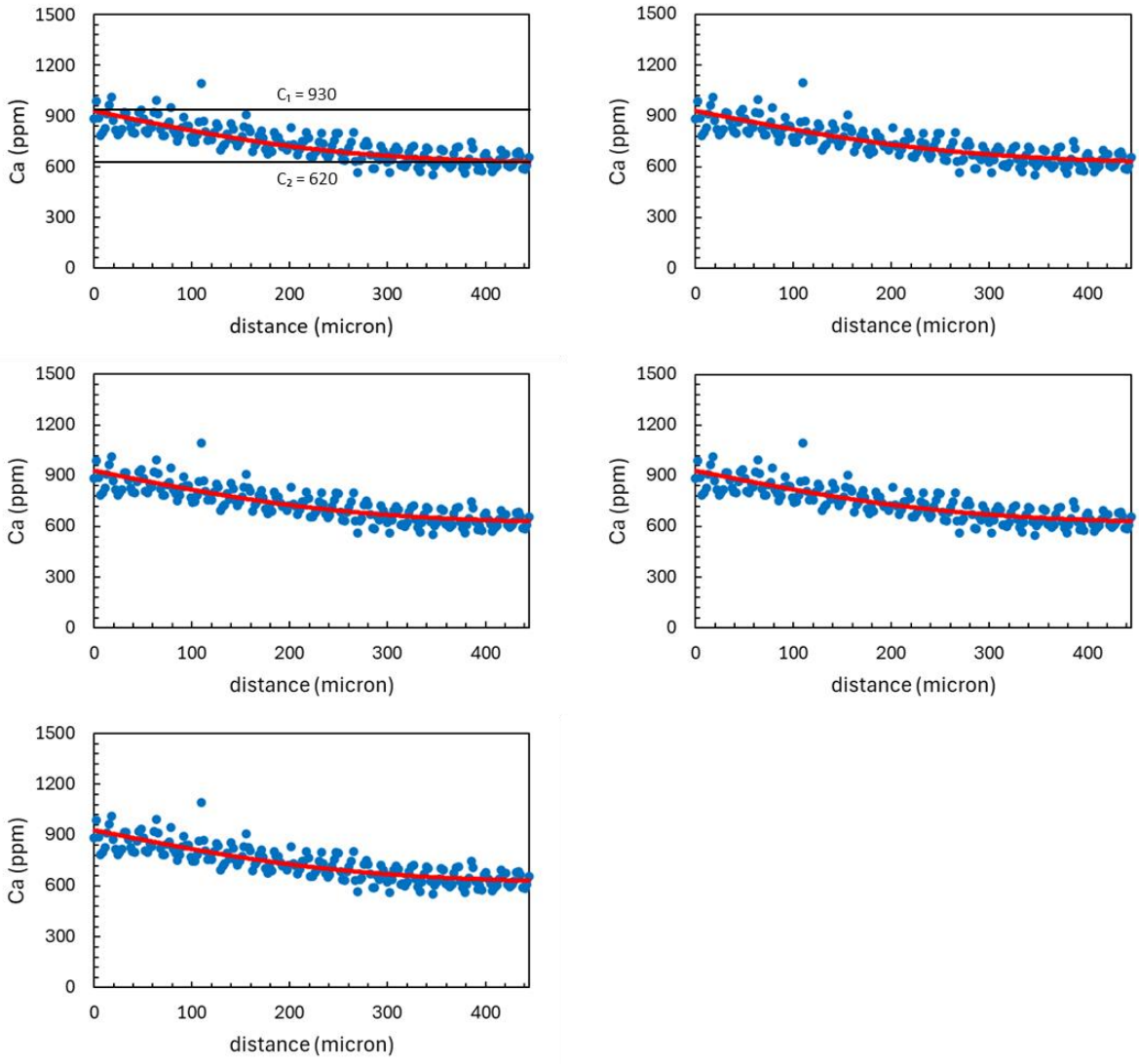

Appendix F (Figure F12): MH-02-18B-6

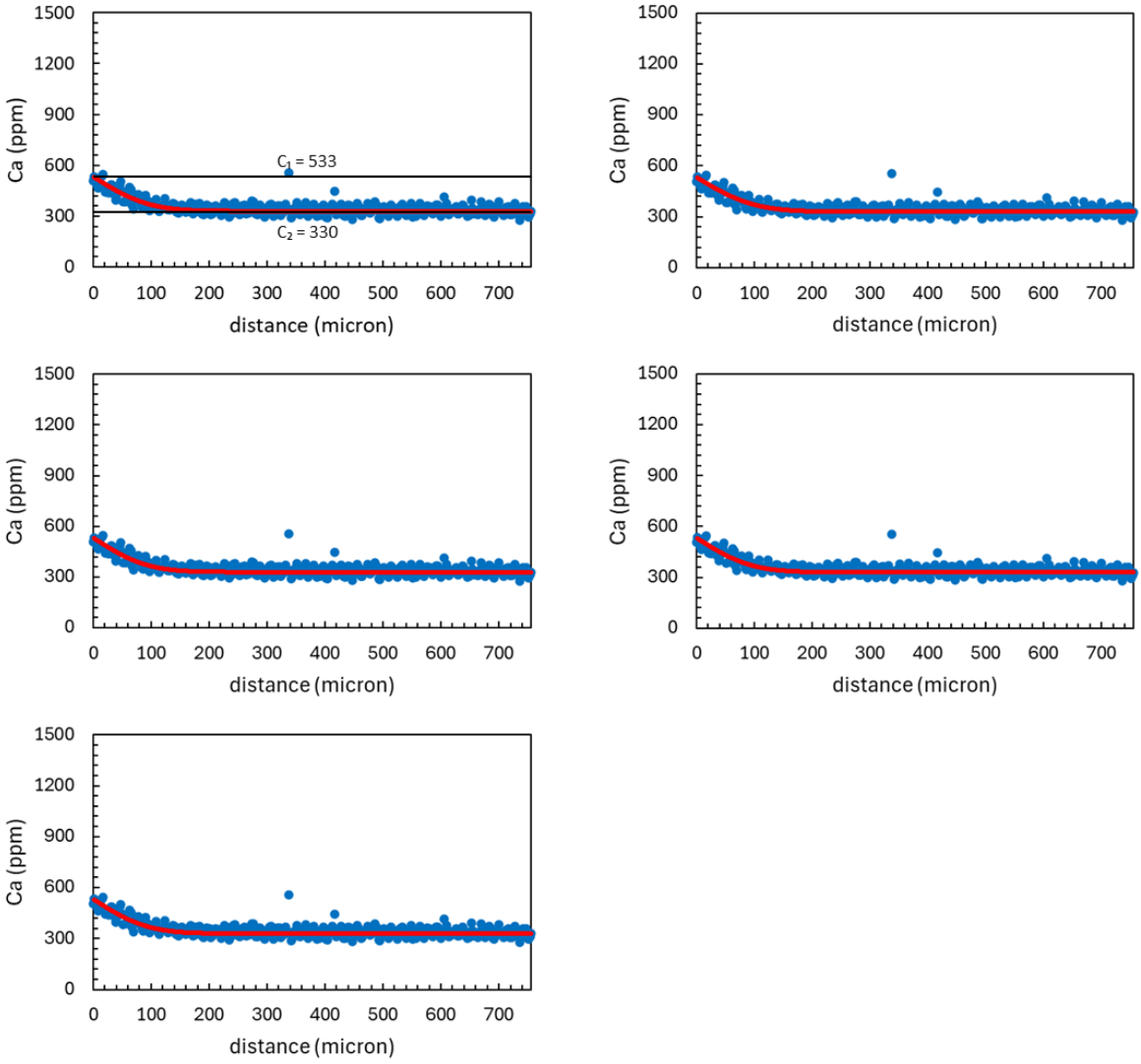

Appendix F (Figure F13): MH-02-114-1

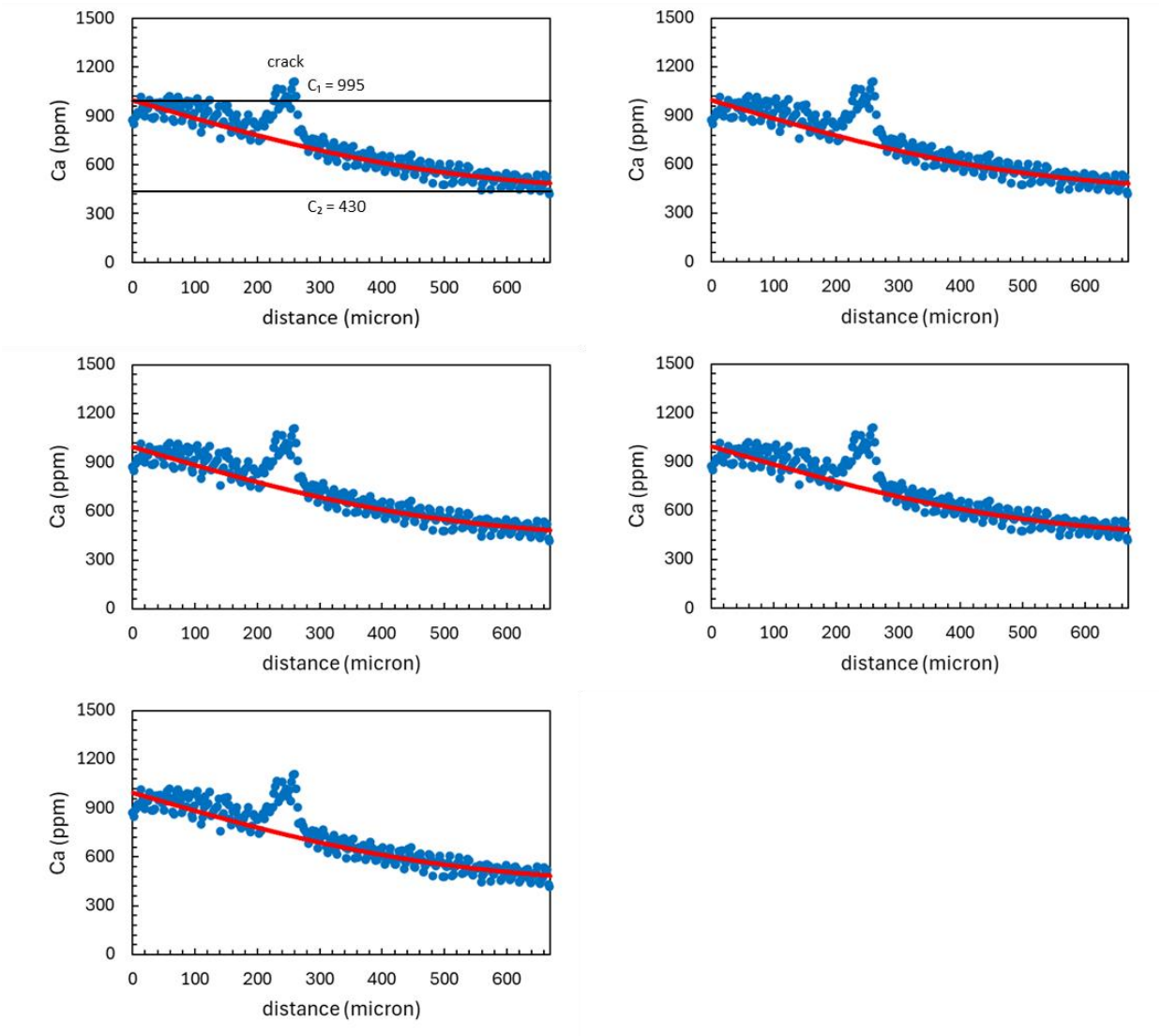

Appendix F (Figure F14): MH-02-114-2

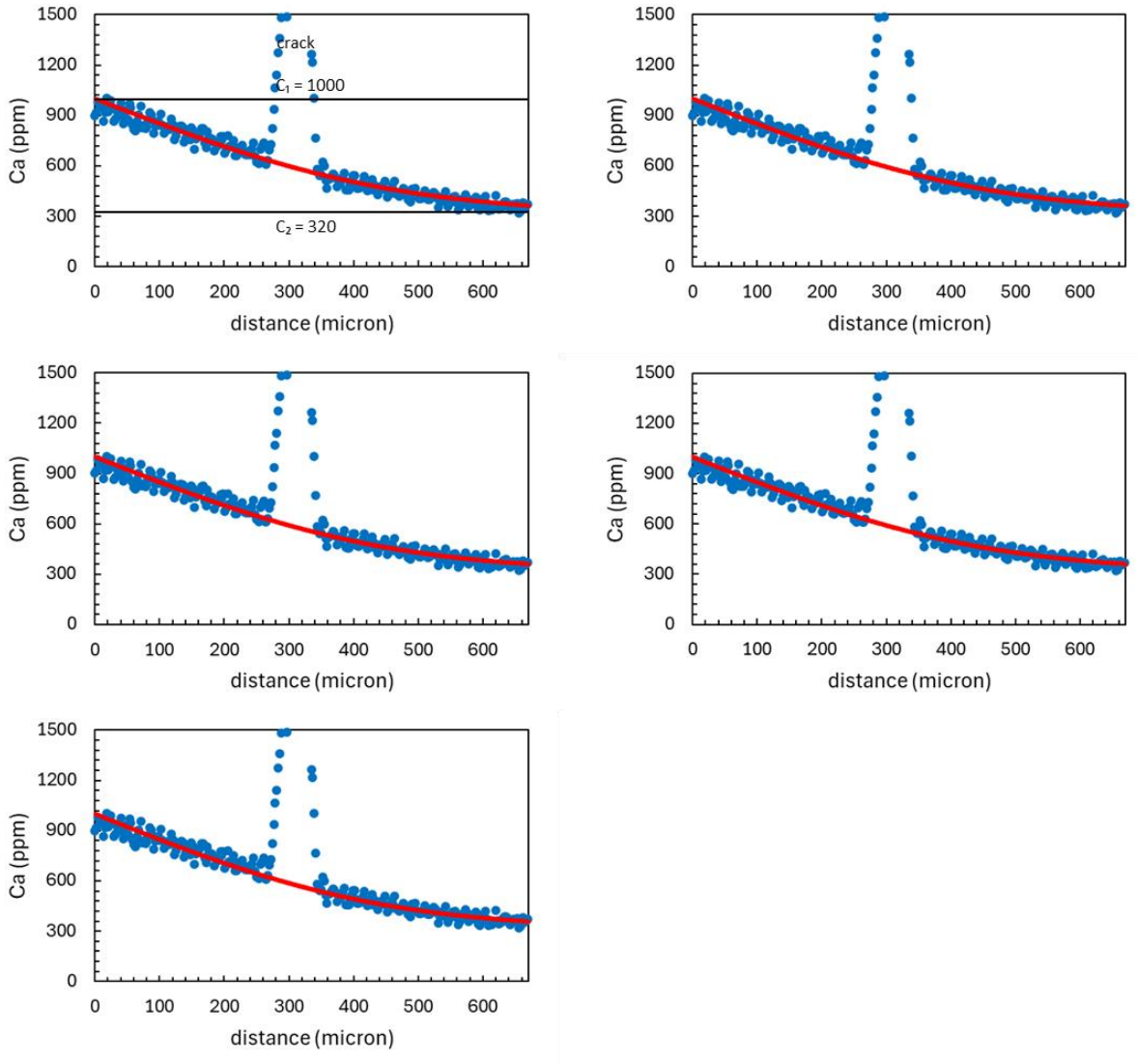

Appendix F (Figure F15): MH-02-114-3

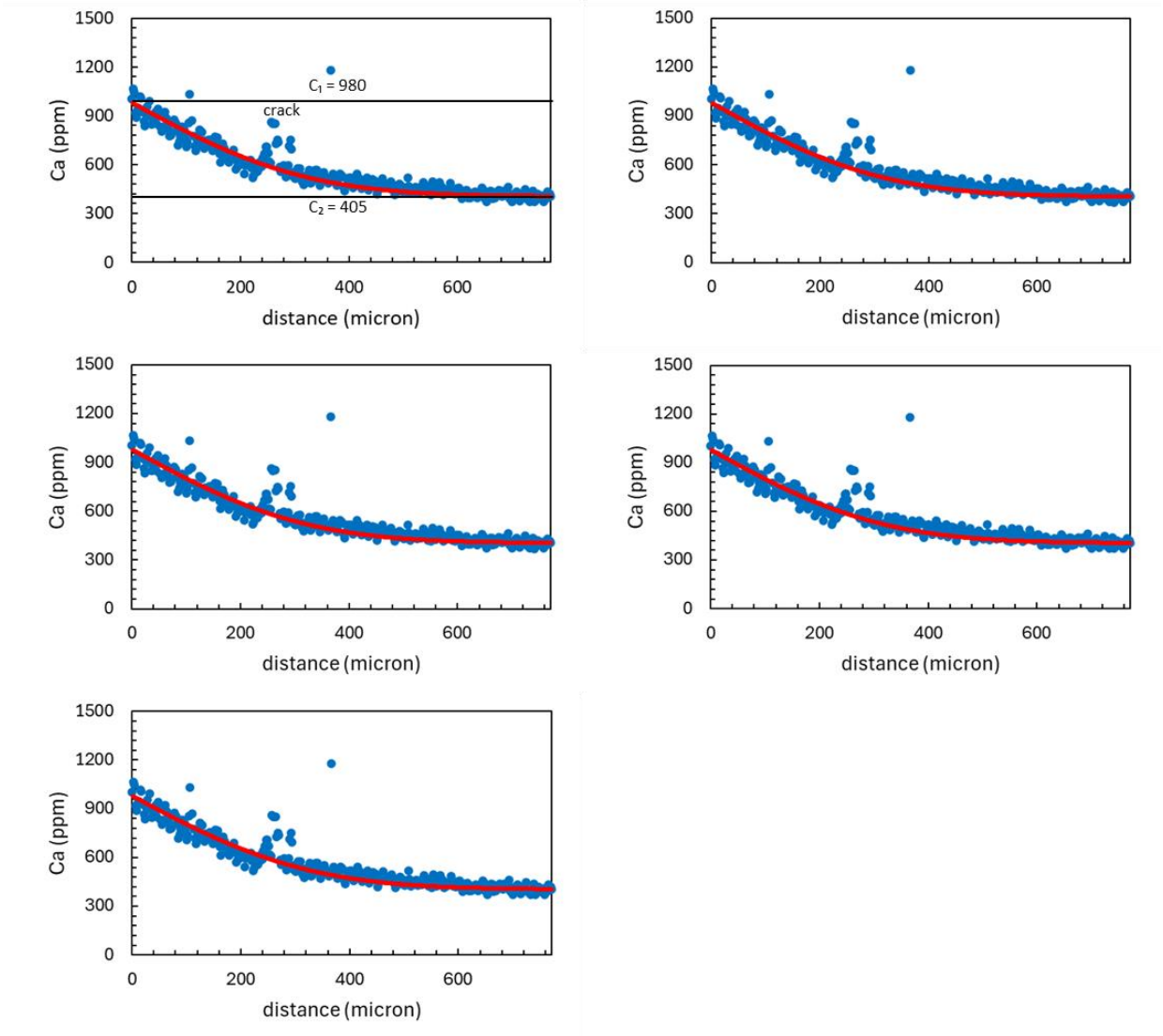

Appendix F (Figure F16): MH-02-114-4

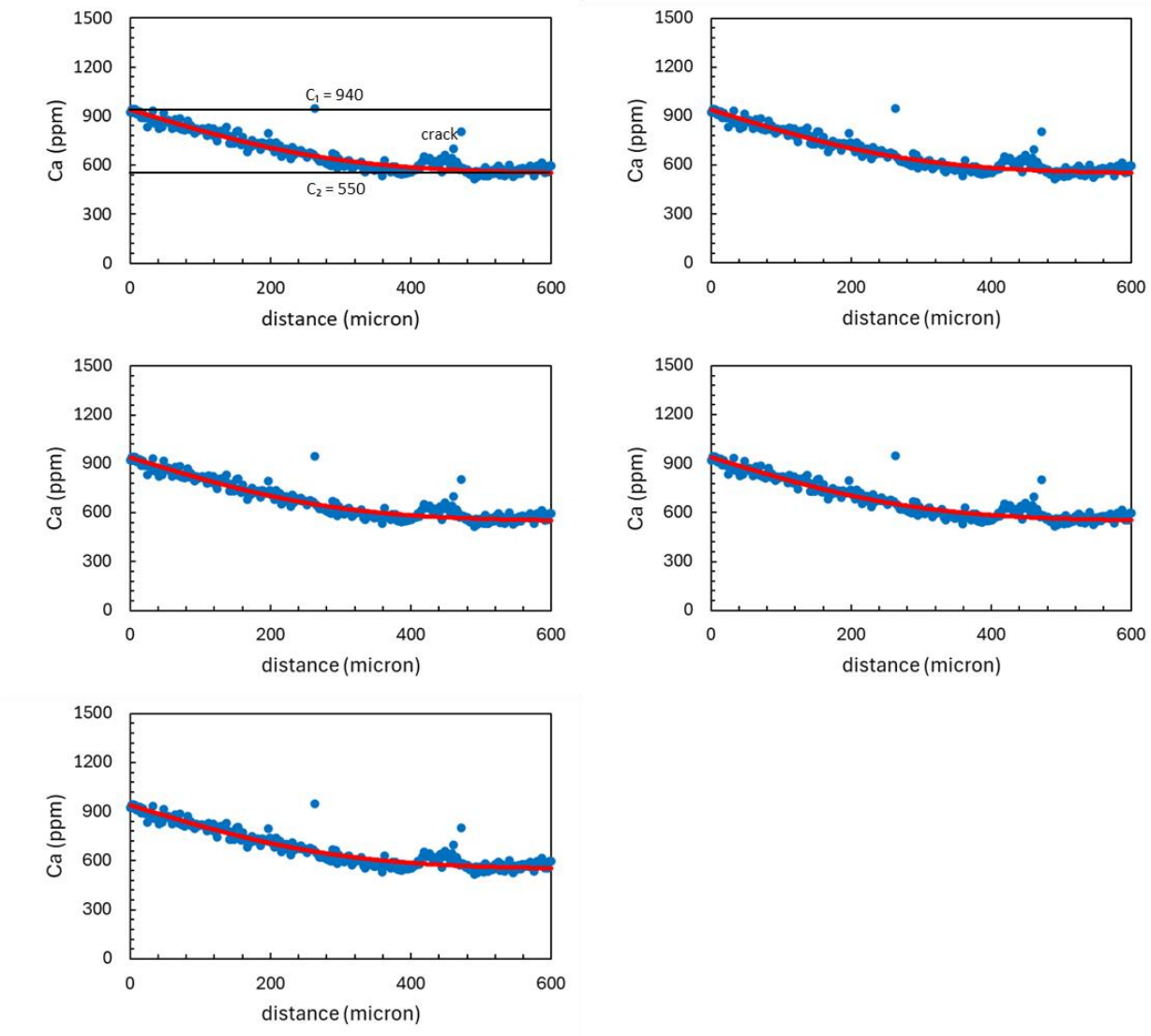

Appendix F (Figure F17): MH-02-114-6

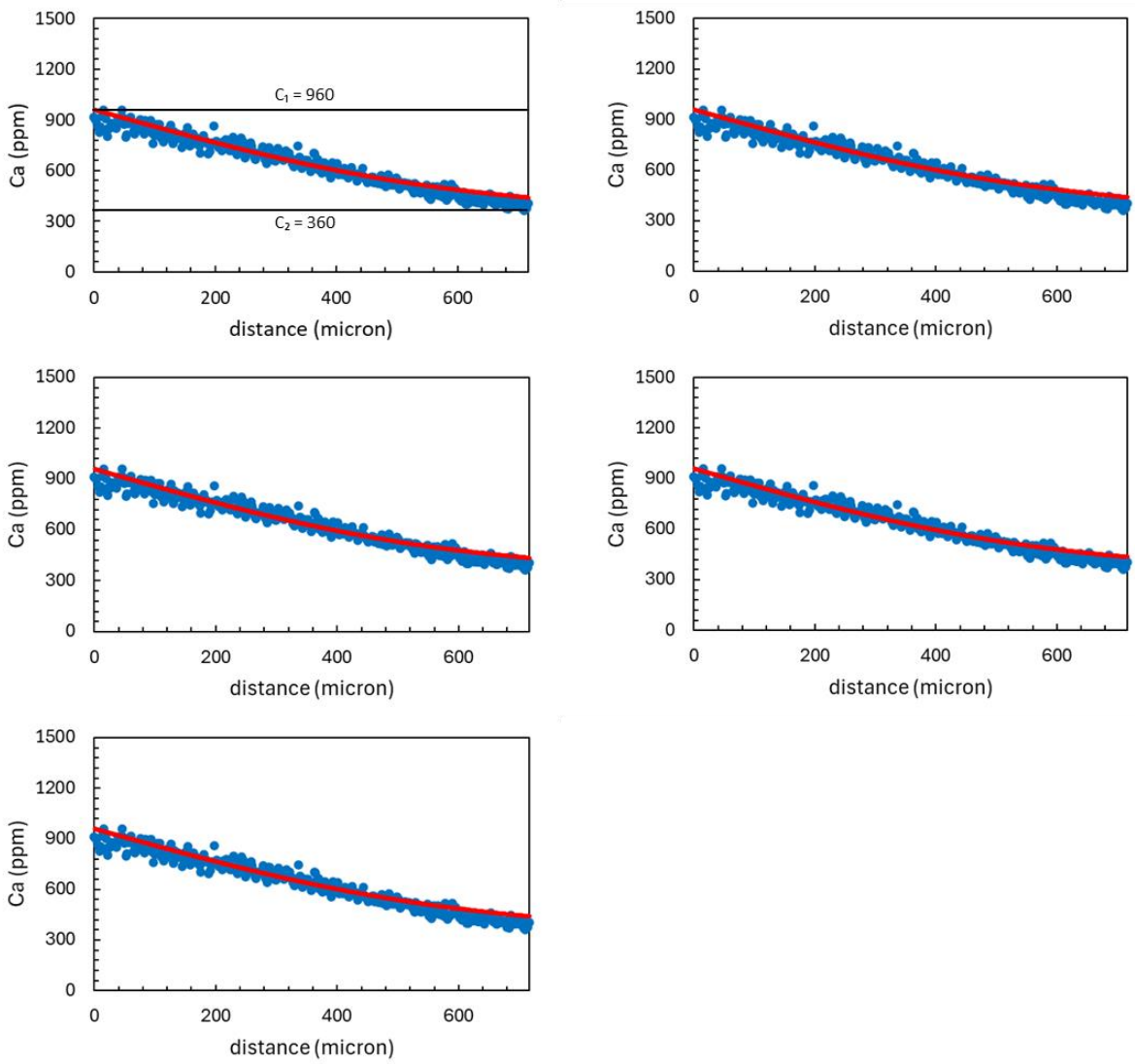

Appendix F (Figure F18): MH-02-12-1

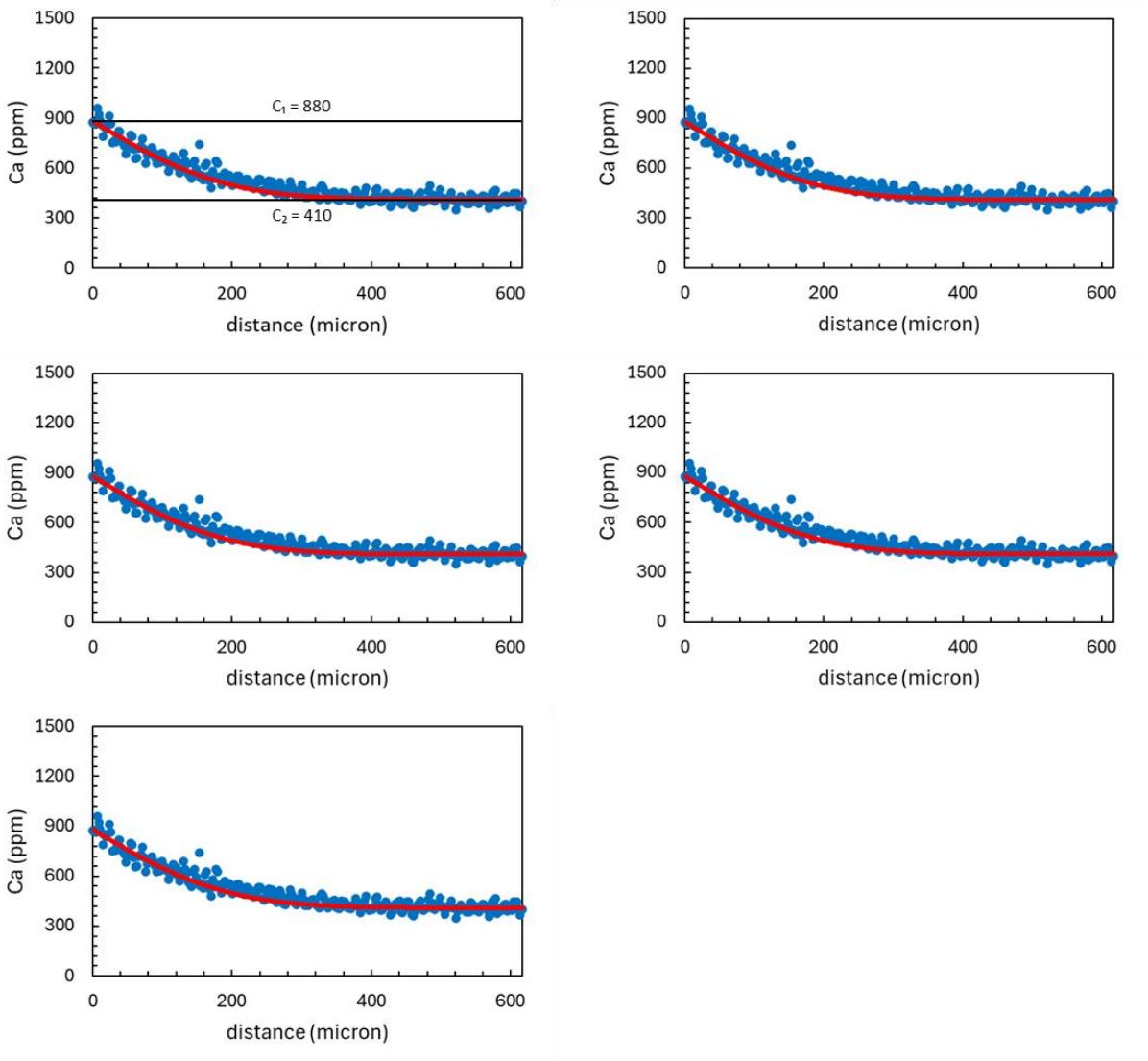

Appendix F (Figure F19): MH-02-12-2

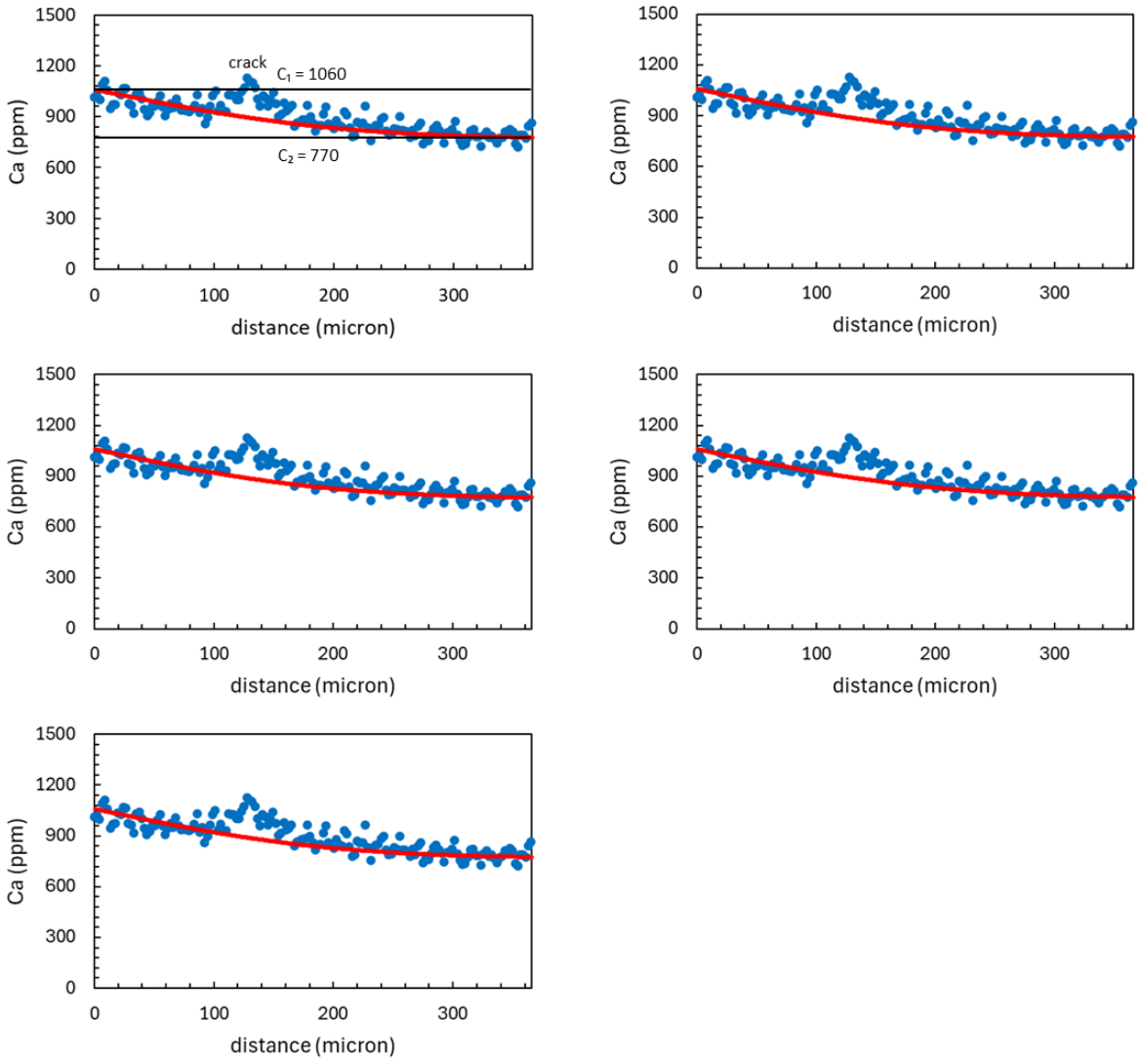

Appendix F (Figure F20): MH-02-12-3

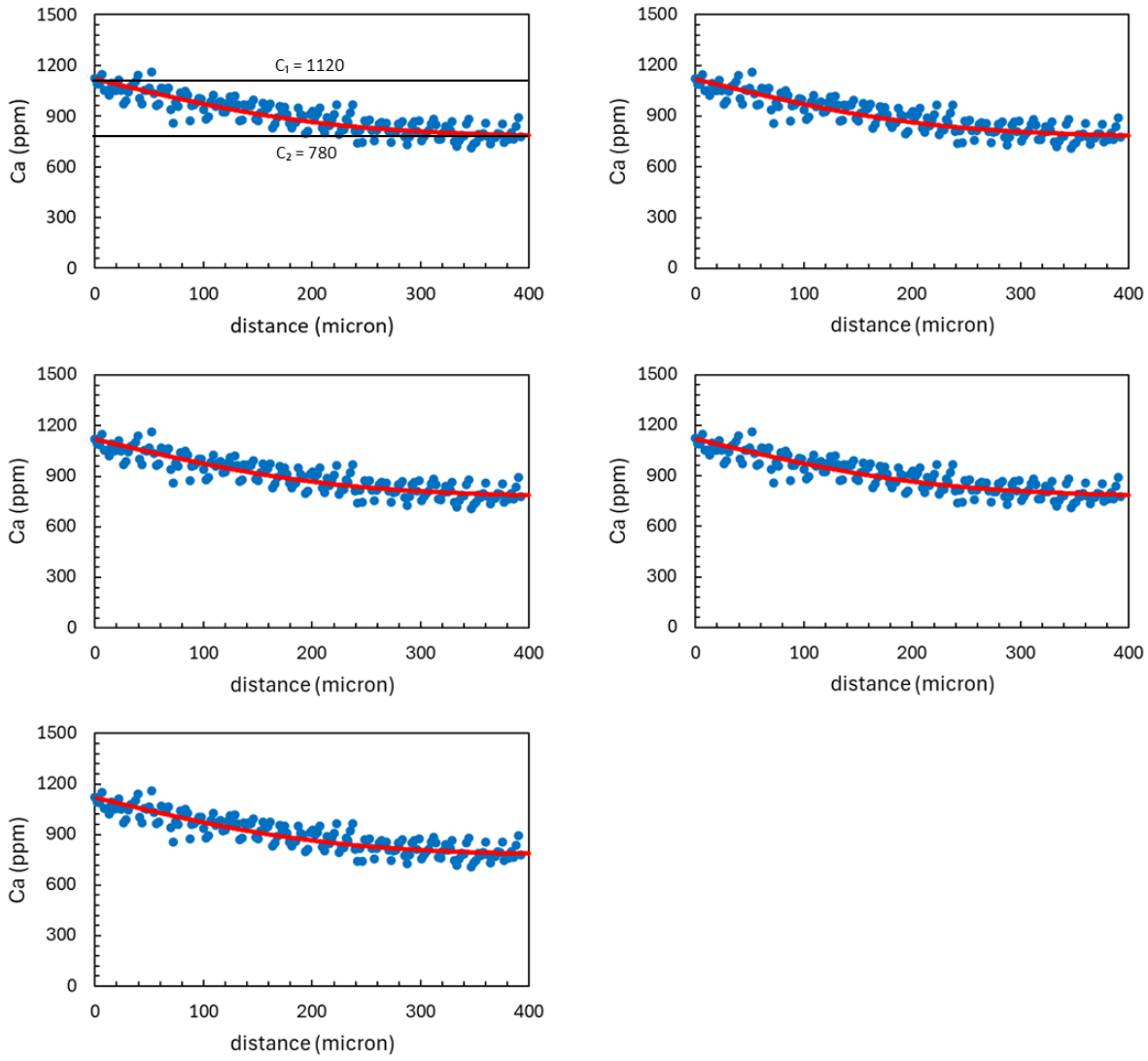

Appendix F (Figure F21): MH-02-10C-2

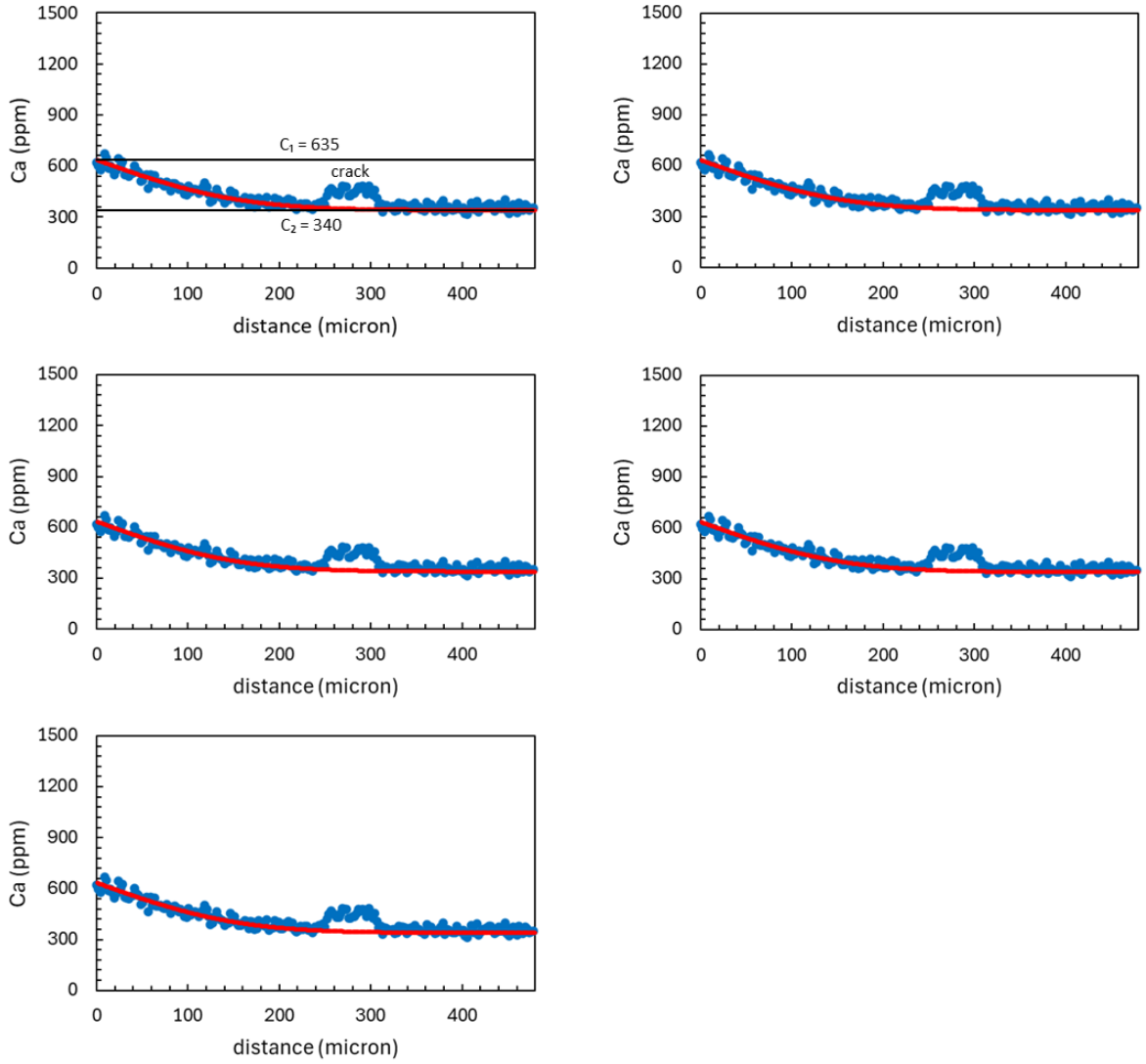

Appendix F (Figure F22): MH-02-10C-3

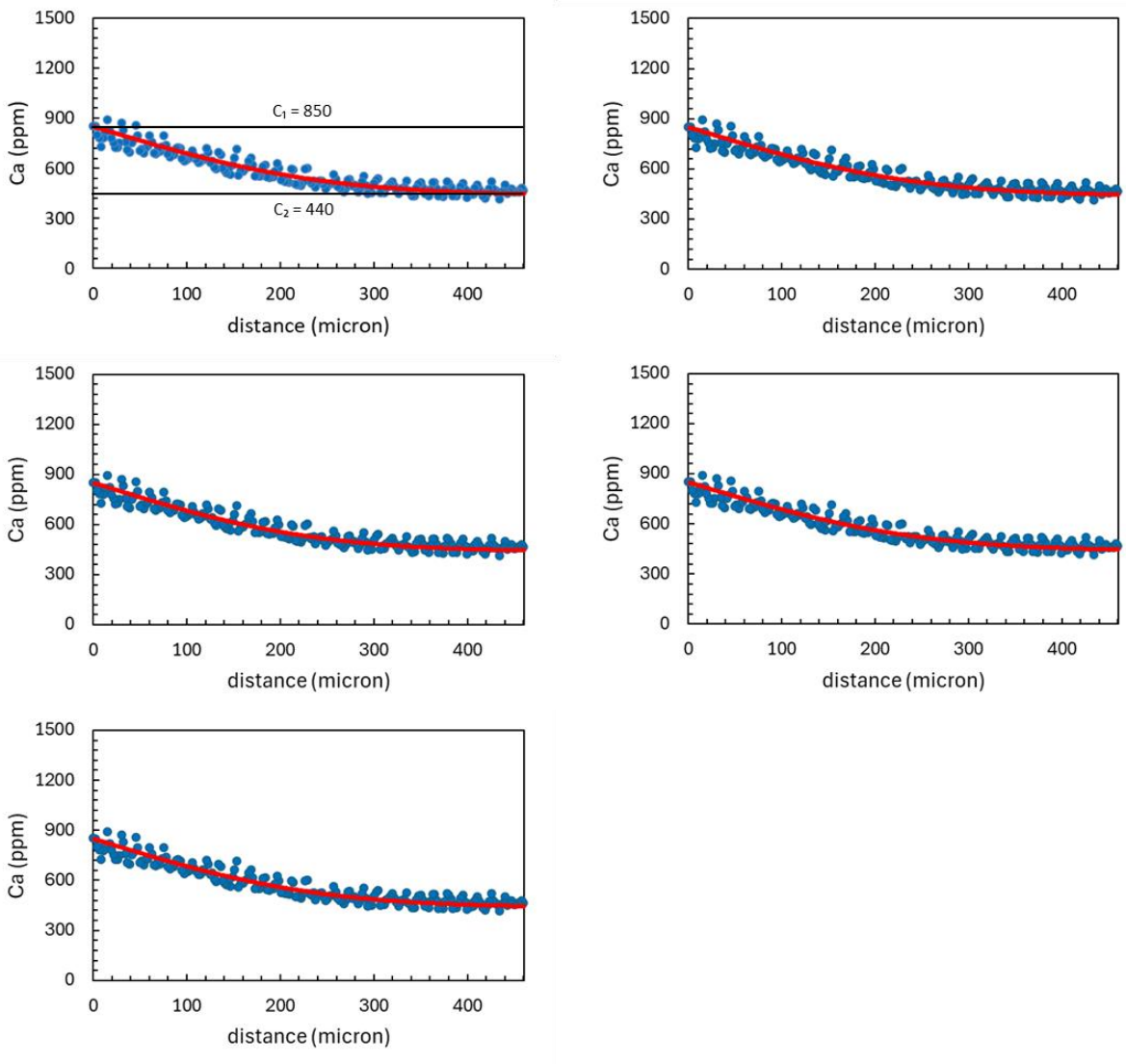

Appendix F (Figure F23): MH-02-10C-4

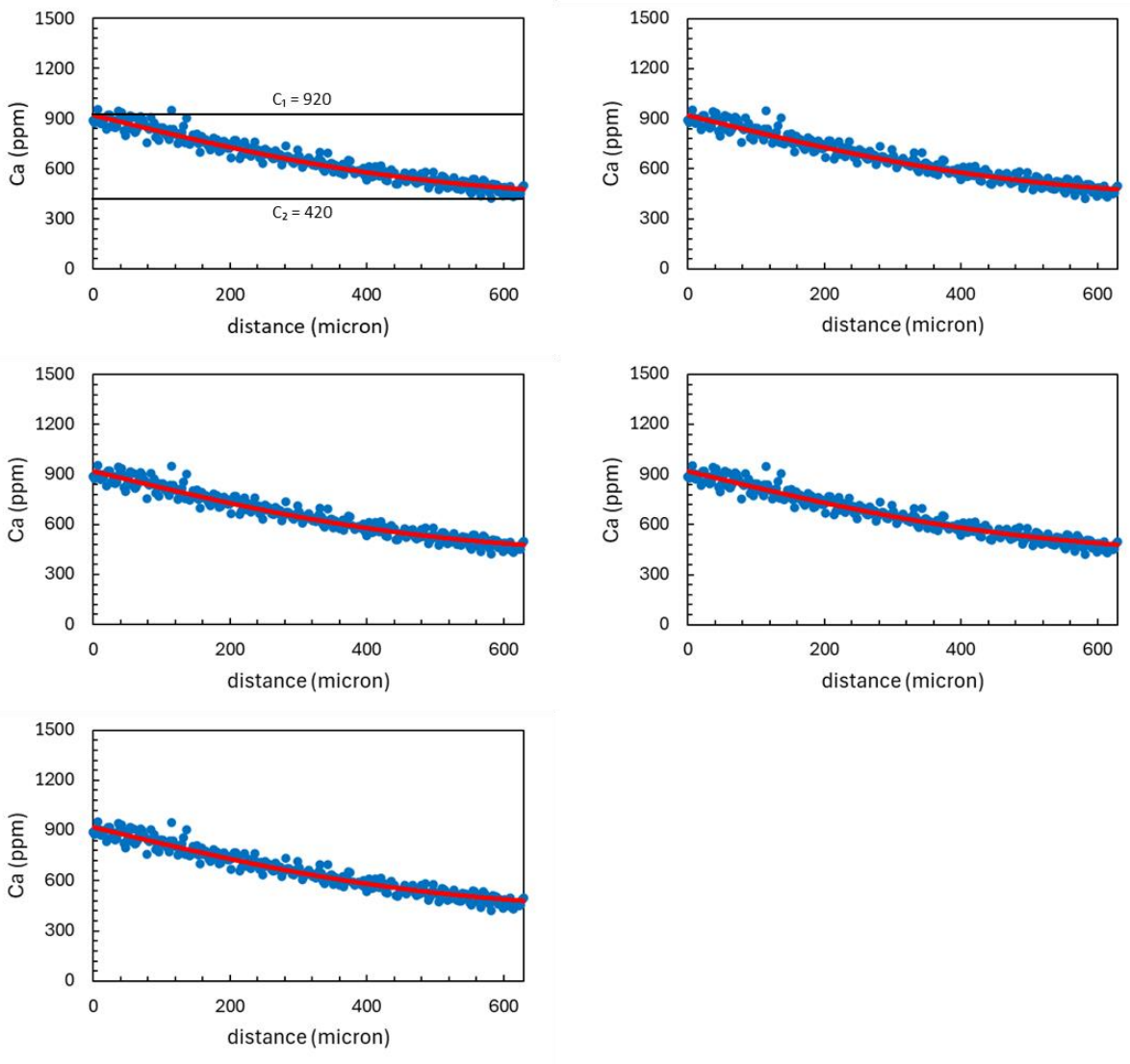

Appendix F (Figure F24): MH-02-10C-5

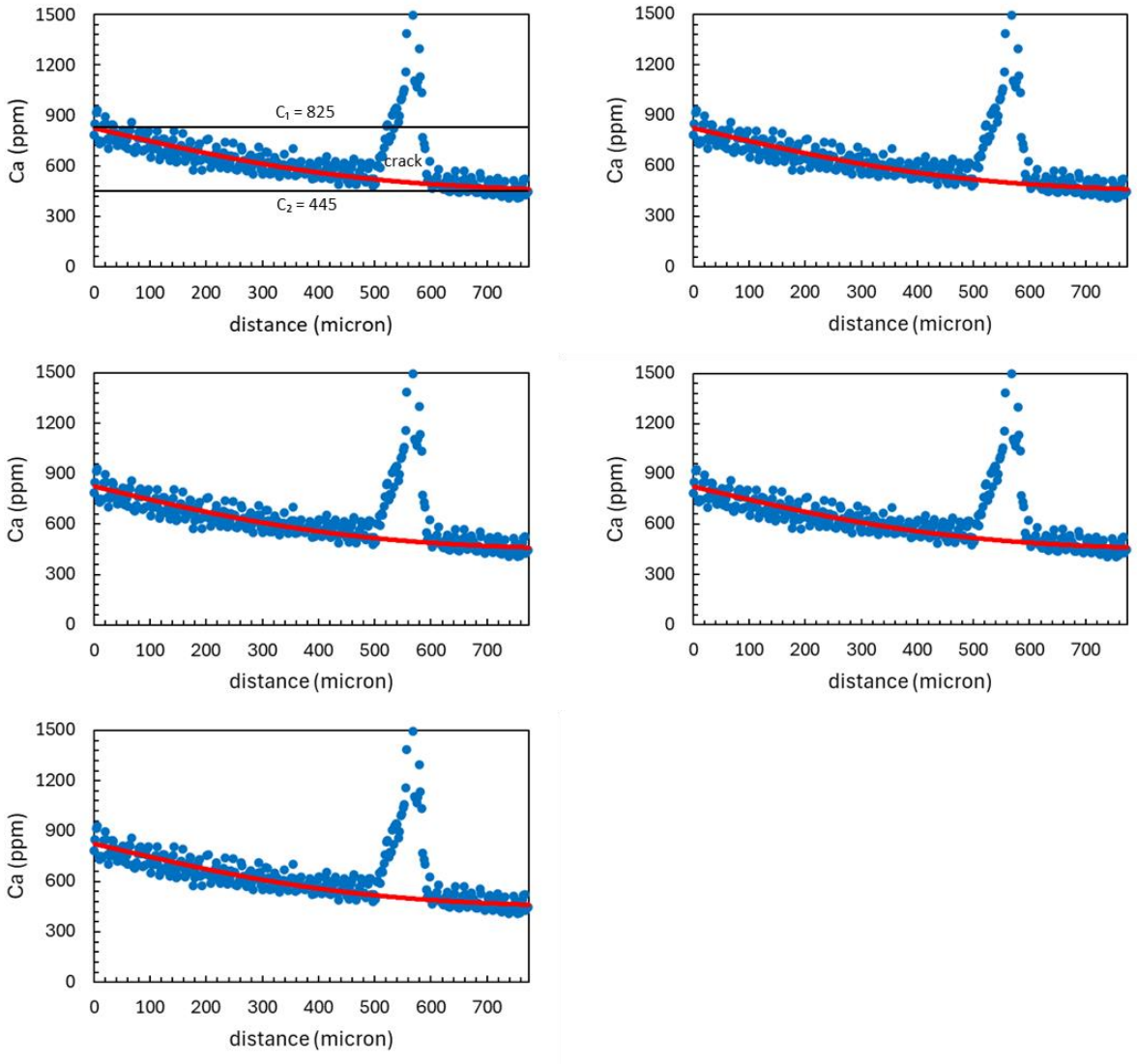

Appendix F (Figure F25): MH-02-10C-8